Variable Impedance Energy Dissipation on the Micro-Scale: Field Responsive Fluids in Novel Geometries

by

Ryan A. Griffin

B.S. Mechanical Engineering
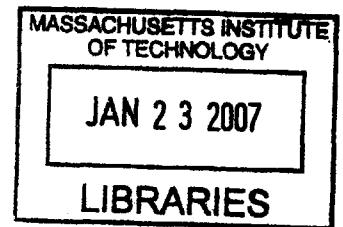University of Utah, 2004

SUBMITTED TO THE DEPARTMENT OF MECHANICAL ENGINEERING IN PARTIAL FULFILLMENT OF THE REQUIREMENTS FOR THE DEGREE OF
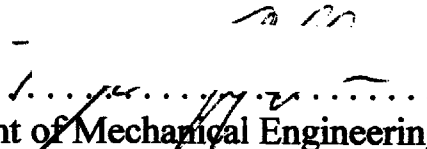
MASTER OF SCIENCE IN MECHANICAL ENGINEERING
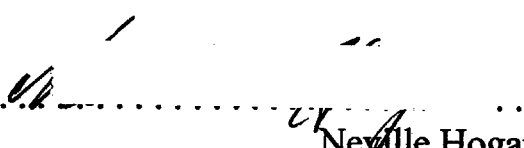AT THE
MASSACHUSETTS INSTITUTE OF TECHNOLOGY

JUNE 2006

Signature of Author . . . .
Department of Mechanical Engineering
May 19, 2006

Certified by . . . .
Neville Hogan
Professor, Mechanical Engineering; Brain & Cognitive Sciences
Thesis Supervisor

Accepted by . . . .
Lallit Anand
Chairman, Department Committee on Graduate Students

Variable Impedance Energy Dissipation on the Micro-Scale: Field Responsive Fluids in Novel Geometries

by

Ryan A. Griffin

Abstract

The aim of this thesis was to further characterize the effectiveness of field responsive fluids (FRFs) in geometries pertinent to the soldier and to examine the effects of specific geometric and kinematic parameters, including patterned surface geometry, electrode gap distance, and normal force on the performance of homogeneous ERF composites. Field responsive fluid composites designed for variable impedance energy absorption incorporated electrorheological fluid (ERF) and shear-thickening fluid (STF) in novel geometries to absorb compressive and tensile/shear forces. ER and ST fluids change their apparent viscosity in the presence of elevated electric and shear fields, respectively, and the magnitude of this effect can be adjusted using the magnitude of the input field, allowing variable impedance operation. Several test fixtures were developed to test these novel FRF composites. A compression apparatus was designed and constructed to test STF-filled foam over a range of strain rates not previously examined in the literature. Silicon-based microchannel devices with etched features on the order of 100 μm and etch depths of 7-90 μm were fabricated to test homogeneous ER fluids in small electrode gaps. Tests using these silicon devices allowed creation of 5 kV/mm (5 V/μm) electric fields across electrode gaps as small as 20 μm, with increases of measured shear force as high as 350% from no electric field to full 5 kV/mm operation. Production of these devices in bulk using established silicon processing techniques was demonstrated, and factors affecting the manufacture of these devices were investigated.

Thesis Supervisor: Neville Hogan
Title: Professor, Mechanical Engineering; Brain & Cognitive Sciences

Acknowledgements

To my family:
Thanks to my parents for their support and encouragement that helped me continue when I felt like giving up. It wouldn't have been nice, neat or complete without them.

To MIT:
Special thanks go to Neville Hogan for his patient, insightful help through the intricate twists and turns of this research project. I couldn't have finished without his optimism and encouragement. Thanks to Giorgia Bettin, Stephen Samouhos, and Doug Eastman, my long-distance labmates, for their advice and help. Thanks to all the members of the MTL staff, including Debb Hodges-Pabon, LiWen Wang, and Dennis Ward, for making the cleanroom not only bearable, but memorable. Thanks to my housemasters Terry and Ann Orlando for their hospitality and personal interest in my mental health. Thanks to professors Alex Slocum and Samir Nayfeh for their infusion of creativity and entrepreneurial spirit into my experience at MIT. Finally, thanks to Leslie Regan and Marjorie Joss, the wizards behind the curtain, for keeping things running so smoothly.

To my friends:
Not responsible for this thesis in any way, I blame the following people for distracting me from my work at MIT. Thanks to Alex Thiriez for tennis lessons and late nights spent scheming, Bridget Revier for our time on the road and on the ice, DQ for the old school education and anger management lessons, Theis for a little afternoon delight, Greg Pollock for the white-knuckle foosball and great Sox seats, Dave Cuff for six years of camaraderie, Biff for the sailing lesson and a clean slate, Kevin McComber for the red carpet treatment, the JeffDanielleCrispy trio for a memorable farewell, Dan Kluk and Ian MacKenzie for good times on and off the ice, Josh Young and Steven Charles for their big ideas, the underscore crew for Wednesday nights and an unforgettable orientation week, Resonance for a year spent making beautiful music and just as much noise, and Kara for something more than words.

Table of Contents

List of Figures

6 Results

7 Conclusion

7.1 External and internal elastic return mechanisms

7.2 Two potential solutions to prevent delamination

7.3 An idea for continuous thin film production with microscale features

7.4 Early conceptual drawing incorporating stacked microchannel shear pairs with an external elastic return mechanism and anchors for force transmission to the user

7.5 Three device cross-sections: (a) Electrode in channel, (b) continuous electrode, (c) channel sidewall contamination

7.6 Anisotropic material with (a) interlocked risers and (b) preferential shear directions

Chapter 1

Introduction and Overview

Imagine a set of army fatigues that moves with a soldier like normal fabric, but stiffens to absorb the impact of a bullet or bus like padded body armor. Imagine a helmet that not only stops bullets, but that absorbs the energy from a blast that could otherwise cause a concussion or traumatic brain injury. Imagine a piece of fabric that collapses down to the size of a folded t-shirt and can fold out into a rigid stretcher for a wounded solider or into a kayak to float supplies and soldiers across a river. This is the dream of researchers working on Institute for Soldier Nanotechnologies' (ISN) Project 4.3 under the title "Semi-active, variable-impedance materials: biomechanical design and control".

Applications like these are potentially made possible by composite materials incorporating field responsive fluids (FRFs), whose mechanical properties can change with an applied voltage or a collision. The two main FRFs researched for project 4.3 are electrorheological (ER) fluids and shear-thickening (ST) fluids. ER and ST fluids change their apparent viscosity in the presence of elevated electric and shear fields, respectively, and the magnitude of this effect can be adjusted using the intensity of the input field. By putting these fluids into novel geometries, composites can be made to absorb shear and compression energy to protect soldiers in applications like those shown in Figure 1.1 below.

Figure 1.1- Potential applications for variable impedance energy absorbing composites

Until now, ER and ST fluids have been characterized primarily in laboratory conditions where tight machining tolerances and careful rheometry have allowed researchers to study the basic properties of these fluids. Outside of the lab, ER fluid is used for energy dissipation in variable impedance dampers (such as tunable shock absorbers [Wereley, 2004]) and other precision applications, but its potential for energy absorption for the soldier extends beyond this highly constrained geometry. Previous work in ISN project 4.3 by Eastman [Eastman, 2004] has shown that ER fluid can absorb energy in geometries with unconstrained boundary conditions, much like those found in the fabric of a soldier's uniform, and current work has continued in this vein.

1.1 Variable Impedance Energy Dissipation

The use of electrorheological fluids (ERFs) in this research allows the mechanical impedance of composites to be tuned using the electric field input and the geometry in which the fluid is placed. This functionality allows for composites that can be selectively turned on, off, or at some percentage of the "on" state. One example of such a tunable ERF application is a shirt sleeve that is flexible to allow mobility in most situations but that stiffens to support a broken arm or absorb the energy from a fall or impact. Furthermore, the small time required for ER fluid to change from low viscosity to high, and from high back to low (as little as a few milliseconds) [Nava, 1997] theoretically allows for more exotic composite behaviors like suppression of vibration at specific frequencies. This capability could support accurate weapon aiming by allowing movement during low frequency, voluntary movements and preventing involuntary, high frequency motions caused by muscle tremor or heartbeat.

The variable impedance effect in shear thickening fluid (STF) is passive. No electric or magnetic field needs to be applied for STF to change its impedance and absorb mechanical energy. When a force is applied above a critical strain rate, the particles in STF begin to agglomerate into clusters capable of transmitting force, resulting in an increase in viscosity of the STF-based composite and higher absorption of the input mechanical energy [Bettin, 2005]. Applications of this effect could include elbow or knee pads that allow freedom of motion during normal movement (slow strain rate), but stiffen to absorb impact at high strain rate. Olympic slalom racers, for example, have recently adopted a similar rate-dependent technology (Figure 2) to protect skiers from collisions with slalom race gates [d3o, 2005].

Figure 1.2- Strain rate sensitive material d3o incorporated into ski suits to absorb energy during impacts with slalom race gates

1.2   Objective

The aim of this thesis is to further explore the use and effectiveness of field responsive fluids in geometries that are pertinent to the soldier, specifically geometries that promote ISN's goal of nanotechnology for the soldier by decreasing the characteristic length scale of this technology. Moreover, decreasing the length scale for ER fluids has been proposed as a way to increase the ER effect. The geometries under study include fabrics and energy absorbing layers on the order of the thickness and weight of the soldier's current uniform, unlike other FRF geometries (e.g. precision rheometers or bulky shock absorbers). Focus is placed on varying parameters like length scale, 2D layer geometry, and loading rates: parameters that can be tuned in design to maximize the effectiveness of these fluids at protecting and supporting the soldier.

The geometry and kinematics of force transmission in FRF composites were the two key factors examined in this work. Previous ISN research [Eastman, 2004] examined ERF composites with unconstrained boundary conditions and focused on characterizing the properties of two types of ER fluid, homogeneous and heterogeneous. However, other research [Kohl, 2000] had indicated that the ER effect was attenuated at small length scales, a potentially critical hurdle for creating high force-density ERF composites. The statement that caused the concern read, "*So far, the lack of appropriate fluids showing a pronounced ER effect in narrow flow channels has hampered the development of ER microactuators. Therefore, only a few reports*

have been published on this subject" [Kohl, p. 584]. Experiments were performed to confirm or refute this cursory observation.

The objective of this research was to examine the effects of specific geometric and kinematic parameters, including patterned surface geometry, electrode gap distance, and normal force on the performance of homogeneous ERF composites.

Testing of STF composites, specifically open-cell foam filled with shear thickening fluid was performed to examine the effect of strain rate on composite performance over a range of strain rates not previously examined in the literature [Bettin, p. 77]. Other experiments were carried out to examine the feasibility of using STF in a shear geometry, to characterize the baseline performance of the test apparatus used to test ER fluids in unconstrained boundary conditions, and to fabricate superior patterned-surface parallel plate shear devices (discussed in more detail in Sections 5.4, 5.3, and 5.9, respectively).

1.3 Methods

The hardware available for testing field responsive fluids for project 4.3 included a linear motion stage, several rheometers, and power supplies for high voltage experiments. The linear motion stage was originally instrumented for use as a tension tester for ER fluids in unconstrained boundary conditions (described in Section 3.2.3). Building on these resources, test fixtures were fabricated to test ERF and STF composites in shear and compression. The effect of the parallel plate electrode gap distance, patterned surface geometry and applied normal force were examined by modifying the linear motion stage to include a blade flexure fixture. Samples of STF-filled foam were tested at various strain rates in a compression fixture added to the linear stage, positioned vertically with a new test stand to support the foam samples on the lower compression surface.

The question of whether the ER effect disappears at small length scales [Kohl, 2000] was investigated using novel silicon-based devices fabricated using the same type of lithography and silicon processing techniques used to create many MEMS devices. These devices allowed homogeneous ER fluid to be tested in a parallel plate shear geometry with smaller electrode gaps than devices found in the literature; gap sizes ranging between 20 μm and 100 μm were implemented, but gaps between 0.5 μm and 0.5 mm could theoretically be achieved by the fabrication process laid out in Section 4.6. Parallel plate electrodes were chosen because they

generate a uniform electric field that scales linearly with the voltage applied across the electrodes and inversely with the distance between the electrodes, allowing control of the electric field through two inputs.

The concept implemented in these silicon microchannel devices was that of parallel plate electrodes separated by rigid spacers occupying a portion of the contact area (see Figure 3 below). This strategy was implemented by etching channels into planar silicon and depositing metal at the bottom of these patterned channels. The areas that were protected from the etch formed "risers" that prevented the countersunk electrode from coming into contact with a planar electrode in the presence of external and capacitive normal forces. The opposing planar and patterned electrodes were then set in a blade flexure fixture designed to approximate several degrees of freedom found in previous "unconstrained boundary condition" experiments. The electrodes were pulled past each other using the linear stage, creating a shearing motion that used the variable viscosity of ER fluid to modulate the force required to pull the plates past each other.
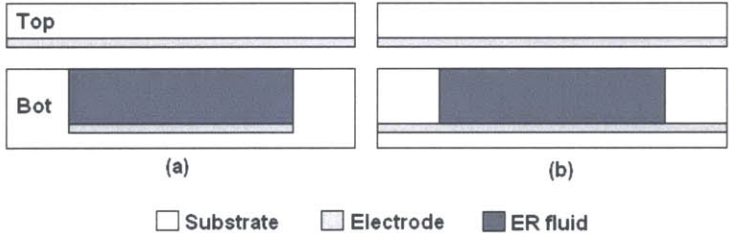
Figure 1.3- Two potential cross-sections for silicon-based ER microchannel devices

1.4   Overview

Chapter 2 presents a brief background on previous research performed in ISN project 4.3, as well as an introduction to the field responsive fluids on which this research is centered.

Chapter 3 discusses the design of new geometries to harness the potential of electrorheological and shear thickening fluids. Factors that affect the performance of the different geometries, including length scale, 2D layer geometry, and loading rates are discussed along with a plan to exploit these factors to improve composite performance.

Chapter 4 reviews the hardware designed and fabricated to test FRF composites with novel geometries. Testing fixtures include modification to the original shear testing setup, a new compression setup designed to test samples of STF-filled foam, and a blade flexure shear fixture

to test the novel silicon devices. The process steps taken in the Microsystems Technology Lab (MTL) to fabricate microchannel silicon devices are also detailed.

Chapter 5 relates the experimental procedure used to conduct experiments on samples in each of the three testing geometries, as well as to characterize several aspects of the silicon devices, including resistance and compatibility with homogeneous ER fluid.

Chapter 6 presents the results of the experiments performed during the course of this study of ER and ST fluids in novel geometries and correlates this data with the original questions about the effect of geometry and kinematics on composite performance.

Chapter 7 unites the ideas found throughout the other chapters to provide a discussion of the overarching trends and possible future direction of the research in ISN project 4.3.

Chapter 2

Background and Prior Work

Field responsive fluids are the key component used in this work to create tunable energy absorbing devices. Field responsive fluids come in three primary types: electrorheological fluids (ER fluids or ERFs), magnetorheological fluids (MR fluids or MRFs), and shear-thickening fluids (ST fluids or STFs) whose viscosities increase in elevated electric, magnetic and shear fields, respectively. The magnitude of this effect can be adjusted using the intensity of the input field over some finite range, allowing these fluids to be tuned to dissipate more or less energy depending on the control input.

ISN project 4.3 has focused exclusively on the use of ER and ST fluids to create useful composites for energy absorption. Both ER and ST fluids require only milliseconds [Nava, 1997; Bender, 1996] to change from a low viscosity to a high viscosity fluid state, and exhibit a large difference in energy absorption capability from an off state to an "on" state.

2.1 Introduction to Shear Thickening Fluid (STF)

Shear thickening fluids are a class of fluids composed of particles suspended in a liquid (a colloidal suspension). One popular example of a shear thickening fluid is corn starch in water, a substance also known as Oobleck. Oobleck, and shear thickening fluids in general, are characterized by their different responses to fast and slow shear or compression. An STF will flow like a viscous liquid when slowly poured from a jar, but will immobilize into a solid when stirred or struck. A classic demonstration of this property is for a demonstrator to briskly walk around on the surface of a pool of Oobleck without sinking, only to stand still and subsequently sink. The phenomenon that governs this behavior is based on interactions between particles suspended in the liquid.

The factors behind the underlying cause of shear thickening in colloidal suspensions are complex and are an active area of research [Catherall, 2000]. Two primary theories have been proposed: order-disorder transition [Hoffman, 1972] and hydrodynamic clustering [Brady, 1985].

The order-disorder transition theory asserts that colloidal suspensions form layers of organized particles until a critical shear rate is reached. Above this critical rate, instabilities in the flow move across layers and disrupt the organized flow resulting in increased viscosity. The theory of hydrodynamic clustering offers further explanation of the instability in the fluid by asserting that particles forced together by shear forces form particle cluster structures called "hydroclusters" where lubrication forces dominate the rheology, resulting in increased viscosity.

2.2   Introduction to Electrorheological Fluid (ERF)

Electrorheological (ER) fluids are a class of fluids whose viscosity rapidly and reversibly increases upon the application of an external electric field. This effect occurs above a certain critical electric field in the two primary types of ER fluids: heterogeneous and homogeneous. Heterogeneous ER fluids are a colloidal suspension of dielectric particles in an insulating fluid (often a non-conducting oil). The ER effect is also present in several types of fluids without a solid state (no particles). This set of fluids is grouped under the classification of homogeneous ER fluids.

With few exceptions, the two categories of ER fluids respond differently to standard rheometric tests at elevated electric fields. The overarching response to increasing electric field is shown in Figure 2.1 below. The shear stress versus shear rate plot for heterogeneous fluid shown in Figure 2.1a shows that at zero electric field, the fluid behaves like a viscous liquid, but at nonzero field the fluid behaves like a gel or Bingham plastic [Zhang, 2000]. The viscosity of the fluid remains constant with increasing field strength, but higher field strength leads to an increasing yield stress. Homogeneous fluid, on the other hand, shows an increasing viscosity with increasing electric field [Zhang, 2000]. This property of homogeneous ERF is similar to that of a variable damper. Based on the results of previous research for ISN project 4.3 [Eastman, 2004], this thesis focused solely on homogeneous ER fluid for its higher ratio of energy in to work absorbed and its potential for use at smaller length scales.
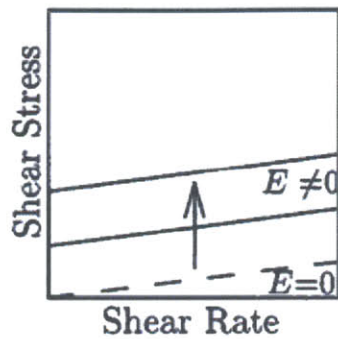
(a) Heterogeneous ERF response   (b) Homogeneous ERF response
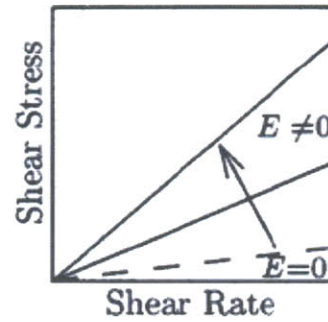
Figure 2.1- Shear stress versus shear rate for (a) Heterogeneous and (b) Homogeneous ER fluids [Zhang, 2000]

2.2.1 Heterogeneous

Particle-based ER fluids form fibrous structures that align with an applied electric field. This transition from particle suspension to fibrous structures is visible in the micrographs shown in Figure 2.2 below [Klingenberg, 1990]. When these particle chains in heterogeneous fluid are sheared, the fibers anchored to the opposing electrodes at each end elongate, break, and form new chains. The energy stored in stretching these chains and the energy dissipation incurred during the formation of new chains result in increased viscosity. Chains form due to dielectric polarization of particles in an external electric field. The separation of charge on individual particles results in a buildup of charge on opposing sides of the particles which are then attracted to one another, leading to formation of particle chains and large-scale fibrous structures.
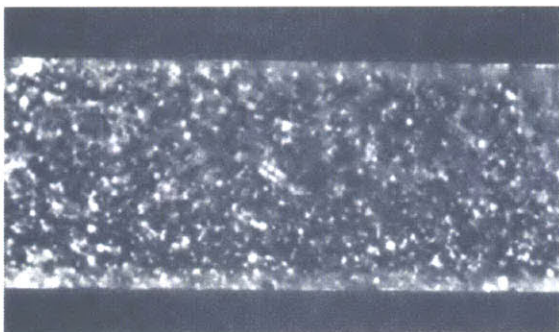
(a) Without electric field   (b) With electric field
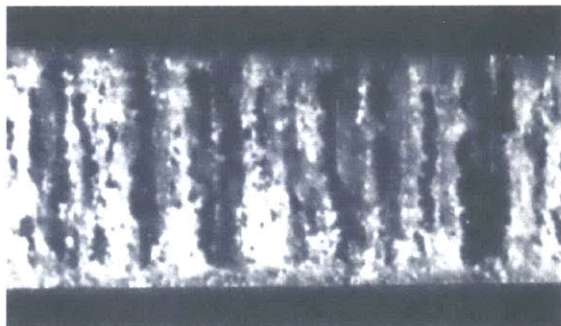
Figure 2.2- Heterogeneous ERF (a) with and (b) without an applied electric field [Klingenberg, 1990]

The microstructure of heterogeneous ER fluid can be seen in Figure 2.3 below. Individual particles can be seen in this scanning electron micrograph. These particles are often modeled as hard spheres in simulation, where the particle size distribution, carrier fluid viscosity, dielectric anisotropy between carrier fluid and particles and numerous other factors affect the performance of a given ER fluid. An informative simulation of the dynamic chain formation, breakdown, reformation and resulting viscous losses is given in [Bonnecaze, 1991].
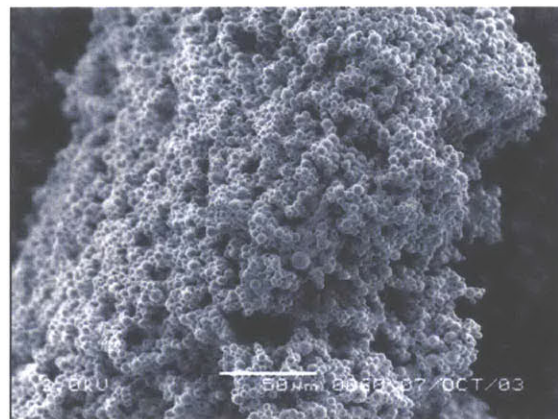
Figure 2.3- Scanning electron microscope (SEM) image of heterogeneous ER fluid

2.2.2 Homogeneous

The homogeneous ER fluid used in this research was an immiscible blend of liquid crystal polymer (LCP) and polydimethylsiloxane (PDMS or simply DMS) similar to the type described in [Orihara, 2001]. This ER fluid was graciously supplied by one of the authors of the Ohihara paper describing LCP/PDMS ER fluids, Dr. Akio Inoue. Orihara, Inoue, et al. concluded that the ER effect in this type of fluid occurs when higher viscosity LCP droplets elongate in an electric field and create bridges between the electrodes. These high viscosity bridges increase the effective viscosity of the fluid over the natural state of the fluid where LCP droplets are free to flow past each other in the low viscosity carrier PDMS liquid.

Orihara, et al. theorized that electrostrictive forces at the interface between the LCP and PDMS caused LCP droplets to elongate in an electric field. The definition of electrostriction is "a property of all electrical nonconductors, or dielectrics, that manifests itself as a relatively slight change of shape, or mechanical deformation, under the application of an electric field. Reversal

26

of the electric field does not reverse the direction of the deformation" [Britannica, 2006]. A familiar subset of this effect is the piezoelectric effect that occurs in dielectric materials without a centrosymmetric crystal structure [Kay, 1955]. A visual example of the elongation of LCP droplets in a PDMS matrix is shown in Figure 2.4 below.
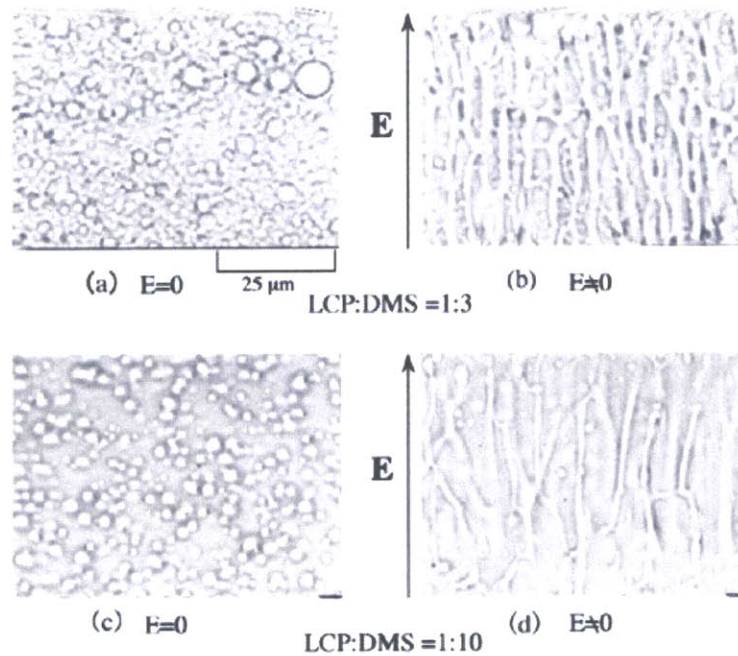
Figure 2.4- Elongation of liquid crystal polymer (LCP) droplets in polydimethylsiloxane (DMS) in an electric field for two ratios of LCP:DMS [Orihara, 2001]

Although heterogeneous ER fluid is more common than homogeneous ER fluid and there is a relative dearth of literature examining the properties of homogeneous ER fluid, previous research [Eastman, 2004] cited several benefits to using homogeneous ER fluid. Not only do homogeneous ER fluids not "suffer from the disadvantages in heterogeneous fluid such as particle settling, agglomeration and abrasion" (page 28), but their "coefficient of performance, defined as the ratio of the change in work done by the material to the electrical energy put into the material" (page 91) is observed to be about ten times higher than the COP of heterogeneous fluid (comparing Eastman's Figures 5-8 and 6-8). Homogeneous ER fluids also have the potential to work at length scales below 100 μm, where some particle-based fluids start to lose their potency due to decreased dipole energy (in electrode gaps less than ten particle diameters) [Dassanayake, 2000].

27

The ER response for the homogeneous ER fluid used in this research (donated by Dr. Akio Inoue from ERtec Co., Ltd.) is shown in Figure 2.5 below. A second type of homogeneous ER fluid (Type B) supplied by ERtec has the ER response shown below in Figure 2.6. Both figures are plotted on shear stress versus strain rate axes, where increasing field strength is observed to produce higher shear stress, τ, for a given shear rate, γ. The response for a given electric field is observed to peak and subsequently drop off after a critical strain rate. This critical strain rate increases with increasing electric field, allowing the fluid to absorb energy over a higher range of speeds at higher electric fields.
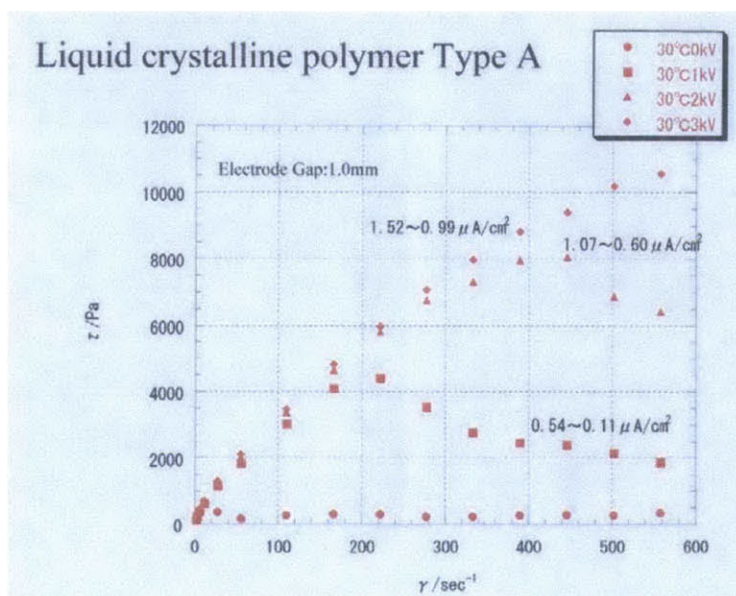
Figure 2.5- Shear stress versus strain rate plot for type A homogeneous ER fluid supplied by ERtec, Co. at electric fields of 0, 1, 2, and 3 kV/mm

The two ER fluids produce similar responses, although type A shows a larger ER effect with a shear stress roll-off at higher "critical strain rate". The maximum shear stress reported for the two fluids were 10.5 kPa and 8 kPa for type A and B respectively. The tradeoff for the higher shear stress produced by the type A ERF is the lower freezing point of type B (0 °C) over type A (10 °C), making type B more versatile at low temperatures. The viscosity of the two fluids at room temperature was similar, although not measured directly.
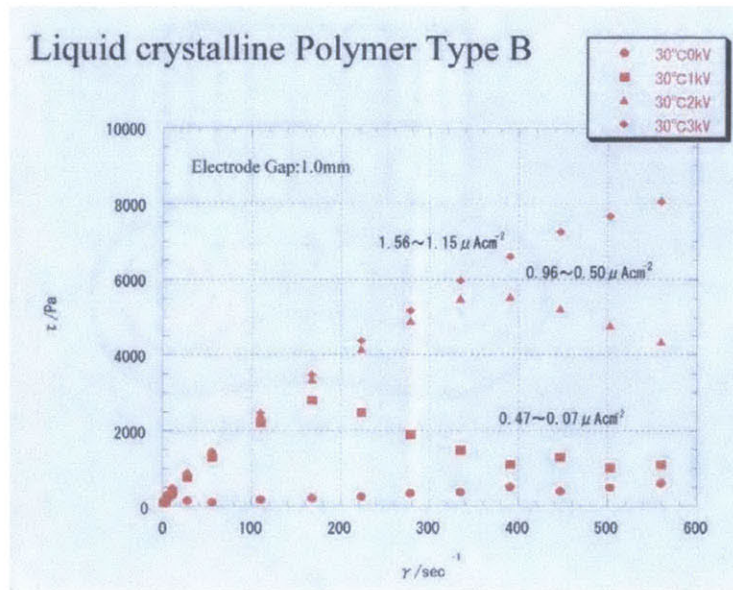
Figure 2.6- Shear stress versus strain rate plot for type B homogeneous ER fluid at electric fields of 0, 1, 2, and 3 kV/mm

2.3   Energy Dissipation and Force Transmission

Three modes of force transmission have been suggested for ER fluid between parallel plates: shear, valve, and squeeze modes (illustrated in Figure 2.7 below). Shear mode, illustrated in Figure 2.7a, transmits force perpendicular to an applied field and dissipates energy as the fluid is sheared between two parallel plates. Squeeze mode, illustrated in Figure 2.7b, forces fluid to flow out from between two plates and the resulting fluid motion dissipates energy in the same way a linear Couette flow does. Valve mode, illustrated in Figure 2.7c, relies on the viscous losses in flow between parallel plates (linear Couette flow) to create a pressure drop from a high pressure source to a low pressure sink. Previous ISN work has focused on the shear mode of force transmission, while applications like ER valves and haptic feedback devices utilize valve and squeeze modes, respectively.

(a) Shear mode   (b) Squeeze mode   (c) Valve mode
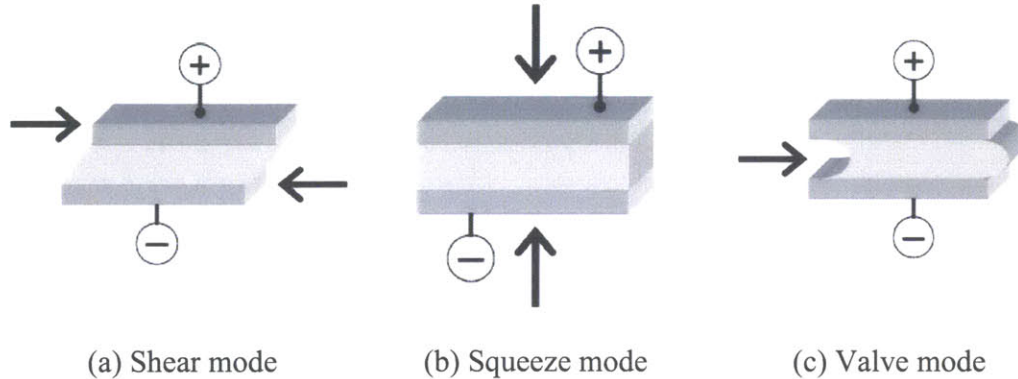
Figure 2.7- Shear, squeeze, and valve modes of force transmission

The desirable high ER effect produced at high electric field requires a combination of high voltage and low inter-electrode distance in a parallel plate geometry. STF does not need either of these conditions to exhibit a dramatic change in viscosity, leading to other potential energy dissipation modes. One of these modes occurs when STF is put into open-celled foams (compressible porous media). Compression of an STF-filled foam forces the fluid to flow through the many small passages that make up the foam. Flow through these narrow passages creates higher strain rates than direct compression of STF, and gives the STF a "foothold" on the cell walls that allows forces to be transmitted through the foam matrix. Previous ISN research examined this type of energy absorbing composite in detail [Bettin, 2004].

2.4 Applications of ST and ER Fluids

The high-performance variable properties of FRFs make them ideal candidates for solutions in several areas of energy dissipation and fluid motion control. Several practical applications of STF have made it to market, and several more are in development. Applications of STF include hip protective garments [Hayes, 1995], improved Kevlar composites for ballistic and stab protection [Lee, 2002; Egres, 2004], and STF-impregnated foams for absorption of impact energy [Bettin, 2004]. The hip protective garment, and STF-impregnated foams are discussed in Sections 3.3.3 and 3.3.4.

Practical applications of ER fluid include variable dampers [Makris, 1996, Zhang, 2000], clutches [Nakamura, 2002], valves [Yoshida, 2002], robotic actuators [Kondoh, 1997, Kohl, 2000], brakes [Webb, 1998, Choi, 2005], shock absorbers [Wereley, 2004], and haptic interfaces

(tactile arrays) [Taylor, 1998]. Each application generally focuses on one of the three force transmission modes of ER fluid: shear, valve, or squeeze. Two devices that use the shear mode of force transmission are shown in Figure 2.8 below. Figure 2.8a shows an ER clutch designed to transmit a portion of the torque from an input shaft to an output shaft. Figure 2.8b shows an ER damper used to suppress vibration in robot arms. Both devices shown in Figure 2.8 shear a thin layer of ER fluid between several concentric rotating cylinders (Taylor-Couette flow) to transfer force from one cylinder to the other.

(a) ER clutch, [Nakamura, 2002]   (b) ER damper, [Zhang, 2000]
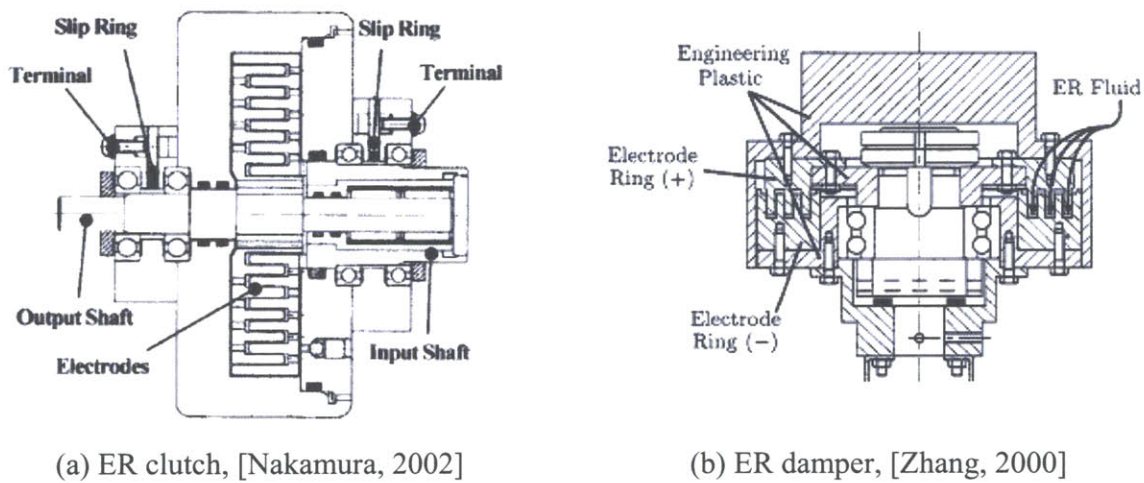
Figure 2.8- ER clutch and ER damper utilizing the shear mode of force transmission

ER fluid used in shock absorbers, robotic actuators, and other common ER applications use ER fluid in valve mode. The flow of ER fluid passing through an orifice can be controlled using an applied voltage (in the case of a shock absorber), or the flow to a small bellows can be controlled to extend or retract a piston. An example of fluid actuation using ER valves is shown below in Figure 2.9, where 5 small bellows are used to incrementally walk this miniature robot down the length of a pipe. Switching times as low as 20 ms and linear velocities as high as 0.9 mm/sec have been demonstrated with this type of actuation [Kondoh, 1997].
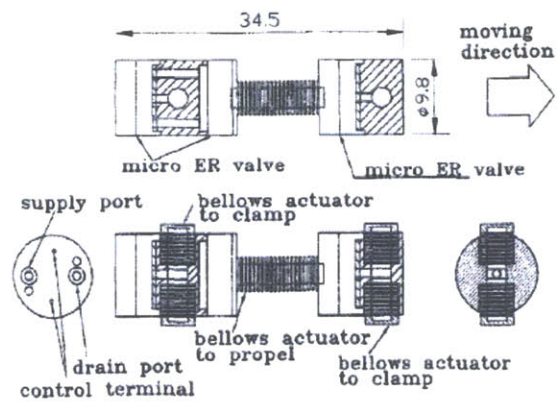
Figure 2.9- Micro in-pipe mobile machine using ER valves [Kondoh, 1997]

Chapter 3

Material Design

One of the conclusions of the research discussed in Chapter 2 motivated the use of homogeneous ER fluids over heterogeneous ER fluids for their superior performance in tests with unconstrained boundary conditions. The following chapter presents further motivation for the continued testing of FRFs in unconstrained boundary conditions, and discusses the design parameters that were thought to have an effect on the performance of FRF composites. This chapter also includes descriptions of the geometries, new and old, that have been designed to transform the change in fluid properties of FRFs into a change in the mechanical impedance of human-scale energy absorbing materials. Calculations of several relevant parameters including fluid shear stress, external and capacitive normal forces, and resistances of different ER device compositions are also presented.

3.1 Customer Requirements

While the prototypes developed in this thesis are several generations away from being field deployable, it is important to keep in mind the overarching performance measures of energy absorbing materials in the military. One significant requirement of the U.S. Army and the individual solider for new technologies involves lightening the load on soldiers, who currently carry on average between 63 lbs (fighting load) and 131 lbs (emergency approach march load) [Devil CAAT, 2003] of ammunition, food/water, body armor, and gear. Such high loads have been shown to negatively impact both soldier health and performance [Knapik, 2004; Johnson, 1995]. The focus on reducing combat load is echoed in both the redesign of the carrying equipment issued to soldiers (from the ALICE pack to the MOLLE pack shown below in Figure 3.1) and in the importance of weight reduction in the new Future Force Warrior program at the U.S. Army Natick Soldier Center.

33

Figure 3.1- ALICE (All-purpose, Lightweight, Individual Carrying Equipment) and MOLLE (Modular Lightweight Load Carrying Equipment) pack designs

3.2   Design Considerations

Several factors that govern the fundamental performance of ER prototypes must also be taken into account. These factors include the applied voltage and resulting leakage current, the normal force between electrodes, the degrees of freedom used for energy absorption, and the onset of electrical breakdown in ER composites. Previous research has shown that factors like the distance of the gap between the electrodes [Dassanayake, 2000], the magnitude of the electric field [Choi, 2001], the surface properties of the electrodes [Otsubo, 1998; Hanaoka, 2002] and the macro-scale geometry [Nakamura, 2002 (Clutch); Takesue 2002 (One-sided electrodes); Kohl, 2000 (Microchannels); Zhang, 2000 (Multiple concentric cylinders); Makris, 1996 (Damper)] also affect the performance of ER devices. Additionally, practical requirements dictate that useful prototypes need to be flexible in the off state to allow mobility, reinforcing the motivation behind running experiments with devices in unconstrained boundary conditions.

3.2.1 Research Plan

A plan to test the factors affecting the performance of ER composites listed above was outlined at the beginning of the project with three primary design iterations. The first iteration was designed to test the effect of inter-electrode spacing on the ER effect using a rigid substrate, to

either confirm or refute the comment made in the literature [Kohl, 2000] (see Section 1.2). If the remark were correct, it would prevent the use of ER fluids in the envisioned microchannel geometries. The second iteration was designed to test the effect of surface geometry on composite performance by introducing several patterned surface geometries including parallel channel, diagonal channel, and dot array designs, again based on rigid substrates. The third iteration planned to transfer the most effective combination of electrode gap and surface geometry to a flexible substrate. The iteration to a flexible substrate was deferred for future research because of the relatively large number of unknowns in the kinematics of this geometry and some unanticipated manufacturing challenges.

3.2.2 Electrode Separation

The shear force exerted by ER fluid in an electric field theoretically increases with increasing voltage and decreasing electrode gap up to the point of dielectric breakdown. Interestingly, no reference could be found in the literature to any research testing this theory between moving electrodes with gaps below 0.25 mm (250 μm) at its logical upper limit. One of the goals of this work was to extend the study of homogeneous ER fluids to length scales smaller than those reported in the literature, in the range of 1-100 μm. At this length scale, the required voltage to create the typical minimum electric field for ER experiments, 1 kV/mm, is between 1 and 100V, a much more manageable voltage than 1000 V typically used. This step toward smaller electrode gaps and substrate thicknesses has the potential to increase the ER effect, increase the number of shear layers in a stack of a given thickness, and to address the troubling question of whether the ER effect disappears at small length scales discussed in Section 1.2.

3.2.3 Unconstrained Boundary Conditions

A fabric designed to allow mobility and maneuverability for a soldier in the off state has to be flexible. Unconstrained boundary conditions (UBCs) mimic the conditions that will likely be seen in actual use, where energy absorbing materials could potentially be subjected to any combination of bending, tangential tension and normal compression (e.g. fabric wrapped around a bent elbow undergoing an impact). Previous ISN research [Eastman, 2004] has shown that ER fluid works well in UBCs and the designs implemented in this thesis, though based on rigid substrates, are intended to advance the understanding of the corresponding flexible prototypes.

35

To make the testing of rigid prototypes as relevant to the project goal as possible, test fixtures were designed to mimic several degrees of freedom of UBC tests. These fixtures were based on blade flexures that allowed movement in the roll, pitch, and lift of each rigid device, without the complicating factor of local variation in electrode gap. The "float" between chips allowed relative motion between the devices to be governed by the fluid, much like in the case of UBCs. The blade flexure fixtures (discussed in more detail in Sections 3.4.3 and 4.5) also allowed a first order characterization of the normal force applied between the moving devices and allowed estimation of the relative effects of the shear force due to friction and due to the ER effect.

3.2.4 Breakdown

The critical failure mode of ERF-based devices is dielectric breakdown. This important aspect of device performance had not been characterized for homogeneous ER fluid on the length scales needed for this research, and represented an important piece of information for future prototypes. The question of whether ER fluid could support a field of the needed magnitude at such small electrode gaps, although unexamined with moving electrodes in the literature, was presented in analogous work with stationary electrodes at 200 μm [Kondoh, 1997] and 80-150 μm [Yoshida, 2002], where field strengths of up to 5 kV/mm were reported. Another issue raised during experiments with flexible electrodes was the possibility of decreasing inter-electrode spacing over time [Eastman, p. 105], with the effect of bringing the device closer to electrical breakdown at progressively lower applied voltages. This thesis proposes a solution to this issue in the form of a channel/riser geometry that imposes a minimum inter-electrode gap (discussed in Section 3.4).

3.3   Previous Geometries

3.3.1   Unidirectional Shear Between Flexible Electrodes

The primary geometry/loading scheme previously examined for project 4.3 was designed to absorb mechanical energy by shearing ER fluid between two flexible electrodes as shown below in Figure 3.2.
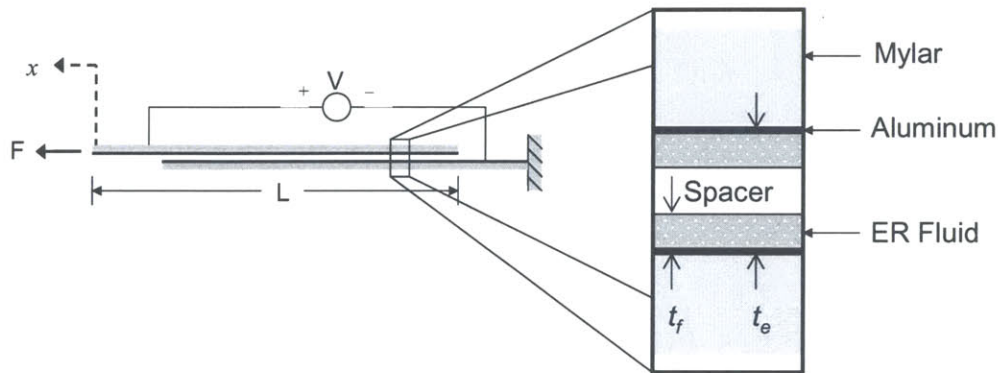
Figure 3.2- Parallel electrode shear geometry [Eastman, p. 37]

The electric field generated between the two flexible electrodes activated the ER effect, with the spacer material inserted to prevent contact and discourage electrical breakdown between the electrodes. Several different spacers were examined in this geometry, including tissue paper, Kraft paper, polypropylene film, materials traditionally used as dielectrics in capacitors (the flexible electrode geometry is essentially a parallel plate capacitor). A fourth option, designed as a baseline, used no spacer. The best performance, measured by the "ratio of the change in work done by the material to the electrical energy put into the material" [Eastman, p. 91], turned out to be the case where no spacer was used with homogeneous ER fluid. The downside to the use of flexible electrodes with no spacer was the increased tendency for failure due to electrical breakdown.

3.3.2 Channel and Grid Designs

Two other designs that were suggested, but not implemented, in previous research for project 4.3 were channel and grid geometries that relied on the valve and squeeze modes of force transmission through a viscous liquid, respectively. The channel geometry shown in Figure 3.3 below uses input voltage to control the pressure drop between two fluid reservoirs (top and bottom) by altering the effective viscosity of the ER fluid in the channels. If the figure below is a plan view of a thin device, this design could theoretically absorb compression energy into the page over one of the reservoirs, assuming that the object compressing the reservoir doesn't simply shift the fluid to the other side of the reservoir. Compression of the device over the channels would also absorb energy by causing fluid to flow away from the point of compression,

assuming that the electrodes are significantly compliant into the page to allow the compression. This device was considered to be a subset of the flexible electrode design with multiple layers.
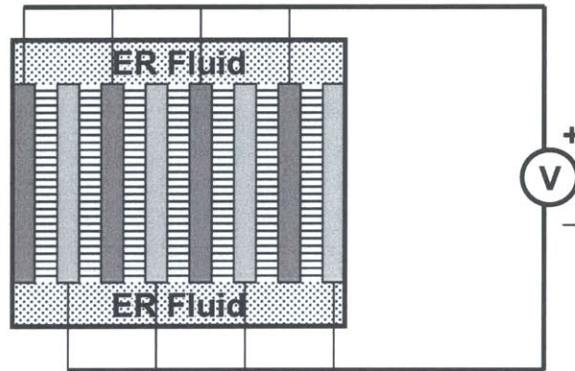
Figure 3.3- ER channel design utilizing the pressure drop between two fluid reservoirs

The grid design shown below in Figure 3.4 allows specific regions of the device to be activated depending on which panels are energized. The squeeze mode of force transmission is activated when the panels are compressed toward the ground electrode. This causes fluid to flow out from under the panels, absorbing energy through viscous losses in the fluid, much like compressing the channel design perpendicular to the channels. The range of motion of this design is limited to the space between the electrodes; research [Taylor, 1998] indicates that the small force capability and limited range of motion of this device may limit its use to applications like haptic devices (forces on the order of 1.5 N). Applications larger than fingertip feedback, like those designed to absorb energy from movement at the elbow or knee, may be better suited to a scalable technology with a larger range of motion and higher force capacity like the flexible electrode geometry.
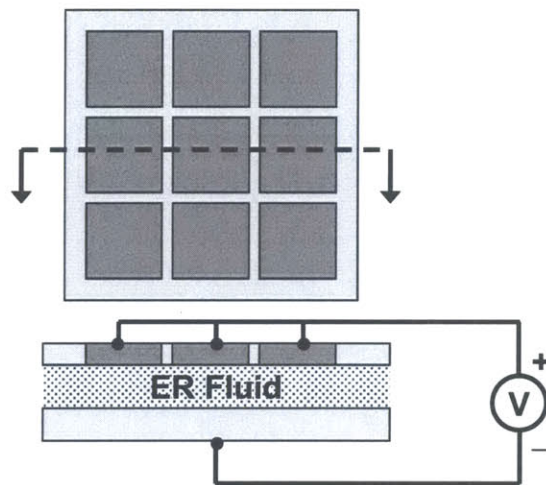
Figure 3.4- Grid design utilizing fluid flow due to fluid compression between two electrodes

3.3.3 Shear Thickening Fluid-Filled Pouches

One patented application of shear thickening fluid used STF in pouches to attenuate the peak femoral force during a fall that would otherwise fracture an elderly person's hip [Hayes, 1995]. This patent quoted a decrease in the femoral load by 68-88% during a hip impact test with a surrogate pelvis matching the stiffness of an actual pelvis (see Figure 3.5). The performance of this hip protection device was stated to have superior impact attenuation properties to all other patented designs at the time of publication, with the nearest competing technology attenuating a mere 20% of the femoral load during impact tests on surrogate pelvises.
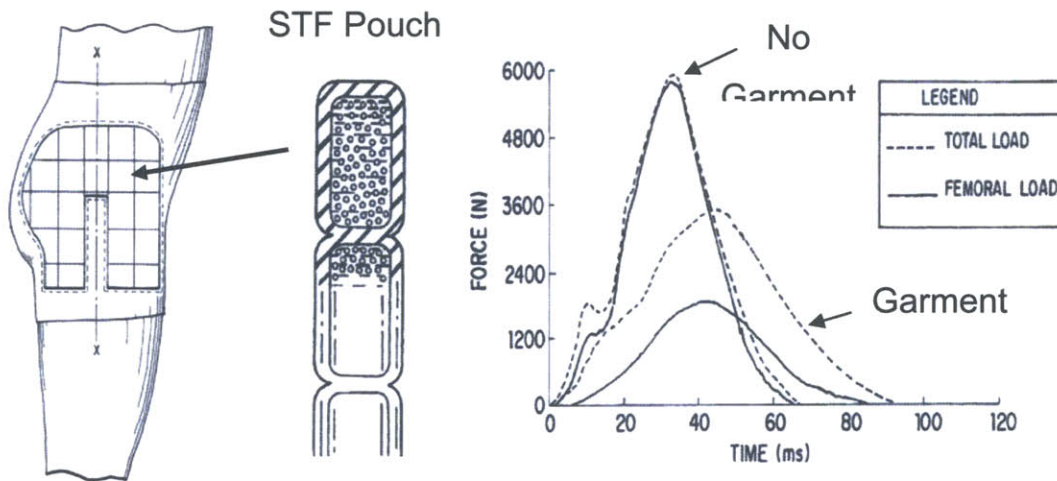
Figure 3.5- Shear thickening fluid pouches used to cushion hip impacts [Hayes, 1995]

3.3.4 Shear Thickening Fluid-Filled Foam

A new energy dissipation scheme developed at ISN [Bettin, 2004] used open cell reticulated foam to retain STF. When cylindrical samples of this foam were compressed, the fluid was forced to flow radially outward through the many small pores in the foam. The high strain rate flow through these pores caused the shear thickening fluid to solidify. The pores in the foam impeded the fluid flow and increased the amount of energy absorbed over empty foam or unimpeded fluid flow. Figure 3.6 below shows two sets of high speed photographs taken during impact tests on foam filled with glycerol (top) and STF (bottom) in a Dynatup drop tower. The corresponding kinetic energy absorbed by the filled foam samples was reported to be 55% and 85% for the glycerol and STF foams, respectively. The energy absorbed per unit volume in the STF foam was reported to be 1.5E6 J/m^3.
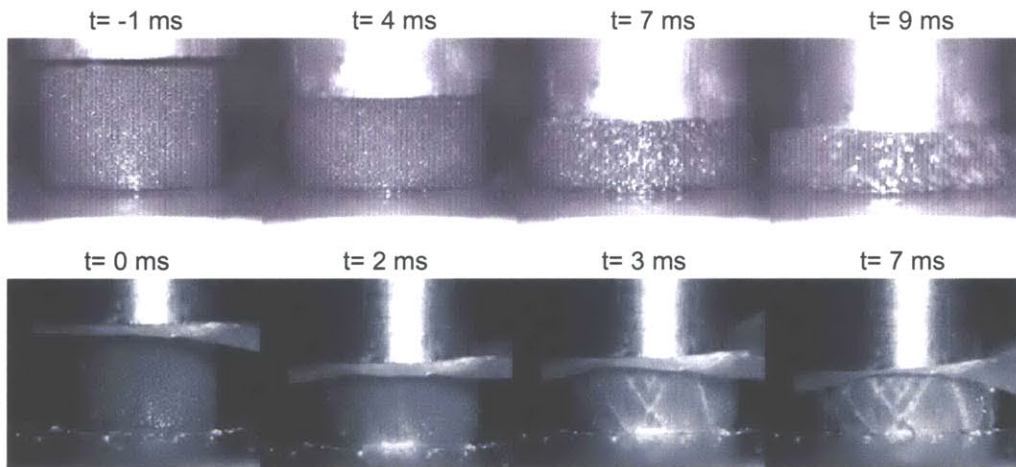
Figure 3.6- Dynatup impact tests on foam filled with glycerol (top) and STF (bottom)

3.4 New Geometries

3.4.1 Silicon Microchannel ER Devices

The results from the original flexible electrode shear experiments showed that homogeneous ER fluid with no spacer produced the highest ratio of output work absorbed to input electrical energy of any tests performed [Eastman, 2004]. Using this result as a starting point, a concept was envisioned to use discrete spacers over a fraction of the electrode to separate the electrodes without using a conventional continuous spacer material. This concept allowed small electrode

gaps to be maintained with a continuous layer of ER fluid between the electrodes, unbroken by a layer of spacer material. Two cross-sections describing the basic premise and two possible implementations of this design are shown below in Figure 3.7.
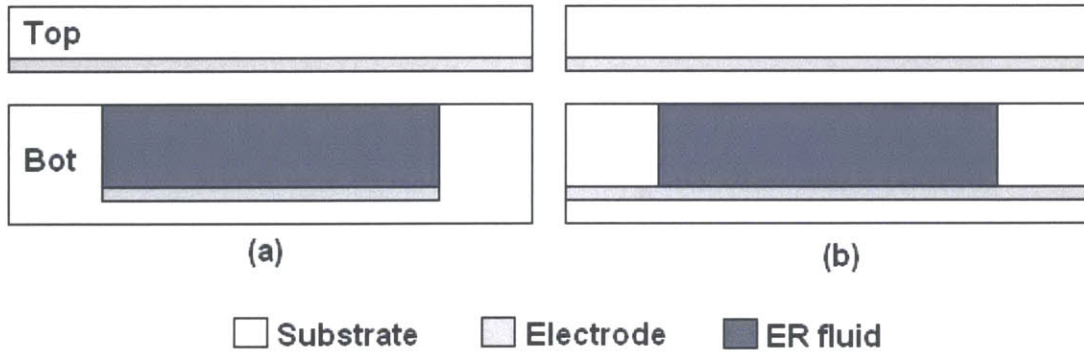
Figure 3.7- Device cross-sections with parallel electrodes separated by channels and risers

While only one "unit cell" of the device is shown, this geometry tessellates left and right to form a series of channels that run into the page. Figure 3.7a shows a device with electrode material only at the bottom of the channels, while Figure 3.7b shows two continuous electrodes separated by risers deposited on the lower electrode. A basic understanding of silicon processing technology prompted the selection of the first device cross-section (electrodes in channels), using photolithography, deep reactive ion etching (DRIE), and physical vapor deposition (PVD), among many other processes, to pattern and etch channels, deposit metal over the entire wafer, and selectively remove metal in areas other than the channel bottoms. The processing details, along with general descriptions of the processes listed above are given throughout Chapter 4.

The first iteration of this design resulted in devices very similar to the cross-section shown in Figure 3.7a, but first pass tests drew attention to the previously unnoticed low resistivity of the silicon substrate. These devices had resistance that was too low to support the voltage required to activate the ER effect without excessive current requirements. To compensate for this low resistivity, a layer of insulating silicon dioxide (SiO_2) was added on top of the risers to increase the resistance between the upper and lower devices. The final design (shown diagrammatically in Figure 3.8 below) used a 1 μm thick layer of silicon dioxide, which was sufficient to insulate the devices, and a 1 μm layer of aluminum with 2% silicon in the bottom of the channels. Al-2%Si was used instead of pure Al to prevent a common source of defects in

microchips; the high solubility of Al in Si can lead to formation of localized "spikes", where aluminum atoms migrate into the silicon crystal structure, leaving areas of lower resistance that can fail under normal current flow.

Silicon (Si)   Silicon Dioxide (SiO2)
Aluminum (Al-2%Si)   ER fluid
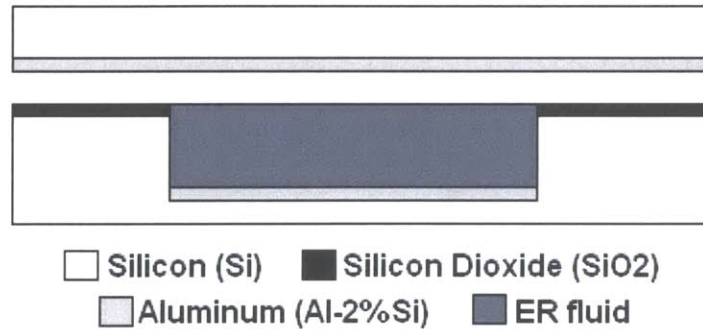
Figure 3.8- Diagram of the basic composition of silicon-based ER channel designs

3.4.2 Silicon Device Fabrication

The appeal of using silicon-based manufacturing techniques for the first two design iterations (before introducing a flexible substrate) was based on the perceived level of control of the channel depth available with these techniques and the design flexibility of photolithography. Photolithography is a technique that uses a thin layer of photosensitive polymer (photoresist, or simply resist) that is resistant to chemical attack to mask selected regions of a silicon wafer during etching processes.

A sample process is outlined in Figure 3.9 below where: (a) Si with a layer of SiO_2 is covered with a layer of photoresist (b), which is selectively exposed to light (c) through the non-opaque areas of a mask. Areas of "positive" photoresist exposed to light dissolve in photoresist developer (d), leaving the SiO_2 (e) and Si substrate (f) underneath these exposed areas open to attack during etch processes before the resist is stripped (g). By changing which areas of the wafer are exposed to light, any 2D design can be etched into the silicon substrate. This design flexibility allowed the creation of three device surface geometries, including devices with parallel channels, diagonal channels, and arrays of freestanding pillars, discussed in Sections 3.4.4, 3.4.5, and 3.4.6 below.
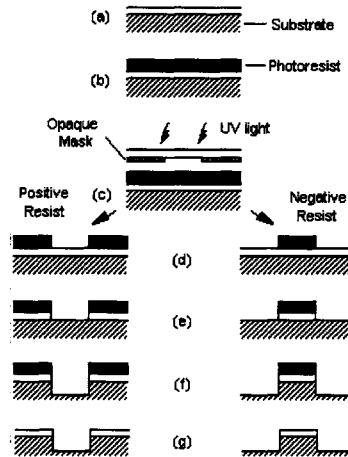
Figure 3.9- Photolithography process diagram

3.4.3 Blade Flexure Test Fixture

As discussed previously in Section 3.2.3, one goal of this project was to advance the understanding of devices with unconstrained boundary conditions. The first two design iterations, intended to study the effect of inter-electrode spacing and surface geometry on ER composite performance, were based on rigid silicon substrates to take advantage of existing silicon processing techniques and well-defined boundary conditions before attempting to understand the performance of more complicated flexible prototypes. To make the testing of these rigid prototypes as relevant to the project goal as possible, blade flexure test fixtures were implemented to mimic several degrees of freedom of unconstrained boundary condition tests.

The term "blade flexure" in the context of this project refers to a flexible piece of metal that has one characteristic dimension much smaller than the other two. In this case, the thickness of the blade flexure was thin with respect to the width and length of the beam as shown below in Figure 3.10. One end of the blade was rigidly clamped between two blocks of aluminum, forming a cantilevered beam whose relative dimensions led to low stiffness in the vertical direction and in lengthwise torsion (roll). Silicon devices were bonded to the other end of the blade with a uniform layer of cyanoacrylate (superglue) applied with a very thin, flexible plastic "squeegee".

43
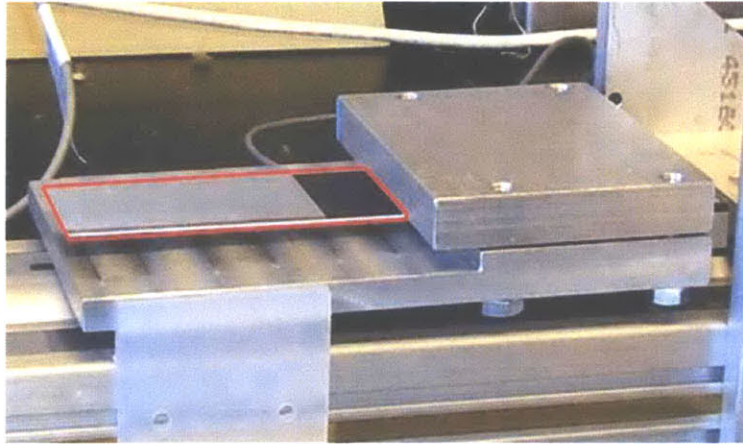
Figure 3.10- Cantilevered blade with thickness << length and width

The flexure constrained motion along the stiff axes (yaw, and horizontal motion), and imposed motion along the axis of translation. This set of degrees of freedom corresponded closely to those found in the flexible electrode tests. Two differences were that it added a normal force between the devices and prevented variation in the local radius of curvature of the device (due to the rigidity of the devices). The normal force applied by the blades was calibrated at the beginning of each experiment by plastically deforming the two opposing blades to overlap each other by the thickness of the blade and device (described in Sections 3.7.2 and 5.6). This imposed a known deflection on the end of the cantilevers that allowed calculation of the normal force between blades using the width and height of the blade to determine the moment of inertia and modulus of elasticity and length of the blade to calculate the force.

3.4.4 Parallel Channel Device Geometry

The first surface geometry produced with photolithography was the parallel channel geometry shown in Figure 3.11 and Figure 3.12 below. Figure 3.11 shows a close-up plan view of a single parallel channel device, with comments denoting the different regions visible from the top including the "high" SiO_2 insulating layer, the channels, and the Al-2%Si metallization layer in the bottom of the channels. This surface geometry was chosen for its simplicity, allowing flow to develop along the channels without interruption. As a simple design, this geometry became the baseline for comparing other geometries.

44
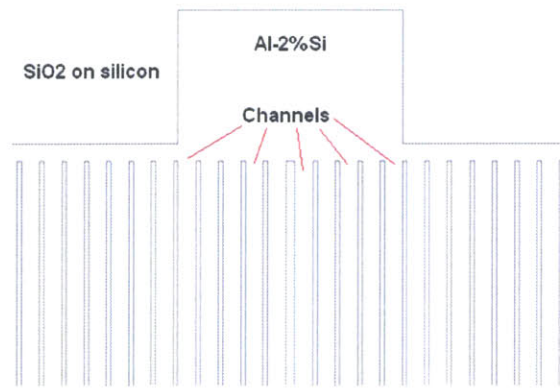
Figure 3.11- Close-up of the parallel channel device geometry

Figure 3.12 below shows several of the features required to integrate several parallel channel devices into a wafer level package including electrode contact terminals, device division marks, and mask alignment marks. Once fabricated, the four devices per wafer were cut apart on a die saw with a rotating cutting blade and a small width of cut. Each device was designed to measure 37mm x 64mm, with an active area of 35mm x 60mm. The contact terminals measured 3mm x 5mm. Each channel was 400 μm wide and between 20 and 100 μm deep and each riser was 100 μm wide. The theoretical limits for minimum channel depth approach 0.5 μm and the maximum channel depth is limited by the thickness of the substrate.
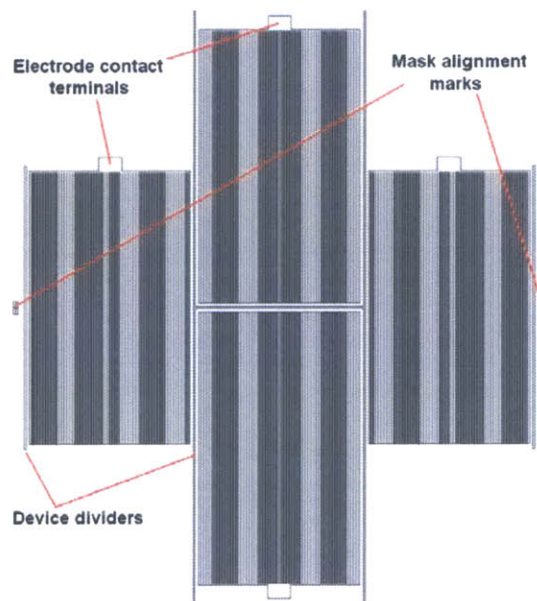
Figure 3.12- Top view of the parallel channel device and wafer layout

45

The device composition implemented in this work (Figure 3.7a) uses a pseudo-infinite electrode on top and strip electrodes on the bottom. Rigorous analysis of this electrode geometry would show some charge buildup at the edges of each riser with a corresponding non-uniform electric field. To minimize the impact of this edge effect, the channels in all the new geometries were designed with aspect ratios in compliance with Saint-Venant's principle. By designing the width of the channels to be at least 3-5 times as wide as the risers and the channels to be 3-5 times as wide as they were deep, the edge effects could be neglected via an order-of-magnitude argument. This simplification allowed calculation of properties like capacitance, capacitive normal force, and electric field to be performed using the equations for a simple parallel plate capacitor, taking into account the reduction in total electrode area.

3.4.5 Diagonal Line Device Geometry

After the process plan was iterated to yield high quality, low defect devices, two new masks were implemented to examine the effect of 2D device geometry on the magnitude of the ER effect and to showcase the design flexibility of photolithography. The second surface geometry implemented diagonal channels that would theoretically induce off-axis fluid motion to increase the distance ER fluid would move for a given device translation distance. Channels were arranged at 30° in two devices per wafer and 45° to the axis of symmetry in the second two devices. Wafer and device numbers were also introduced to allow better tracking of device defects and to allow batch processing of tens of wafers at a time. Figure 3.13a and b below show the two device designs incorporated onto the diagonal line wafers.

The theoretical increase in the viscous losses could be estimated by multiplying the ER shear force by a multiplier corresponding to $1/\cos(\theta)$, where θ is the angle between the diagonal channels and the normal. However, the exact fluid flow pattern is unknown a-priori due to factors such as the vertical float between the blade flexures, which might allow ER fluid to flow across the tops of the channels. By comparing the theoretical increase in ER shear force to the measured increase in simple geometries, a relative effect of the surface geometry may be discerned.

(a) 30° Diagonal line design   (b) 45° Diagonal line design
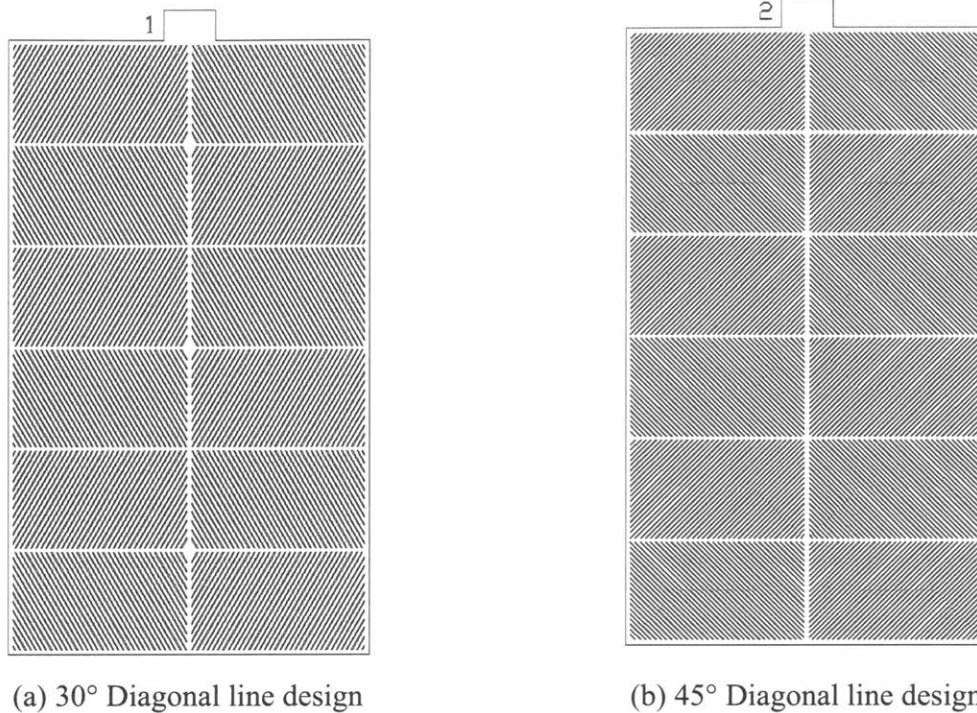
Figure 3.13- Two device designs incorporated on diagonal line device wafers

Several of the negative aspects of the original parallel channel design were improved on in the second set of masks. For example, the parallel line device routed voltage along serial paths where a single defect in a line would result in loss of continuity to the rest of the line downstream. The diagonal line design allowed single defects on any given line without loss of current flow, making this design far more robust to contamination and defects common in silicon processing. Unlike the first mask design, which used two masks to first remove photoresist over channel areas and second to leave photoresist over the channel electrodes, the new process plan used a single mask (each mask cost about $500 to make) to do both functions. This streamlining was achieved by using image reversal resist (discussed in more detail in Sections 4.6.17 and 5.9.1.3) during the second photolithography step to protect the Al in the bottom of the channels from being etched.

The diagonal line wafers were designed with the same channel and riser widths as the parallel line design (400 μm channels and 100 μm risers), and used a symmetric, cell based design to discourage parasitic off-axis forces and encourage fluid recirculation. Conversely, a single area of hatched lines at an angle to the axis of motion would tend to pull to one side and force the fluid to the opposite side during a run. This parasitic asymmetry would potentially

47

degrade the performance of a device and confound the effect of simply increasing the length of travel of a single fluid particle.

3.4.6 Dot Array Device Geometry

The third and final surface geometry implemented in this research was a patterned array of posts designed to redirect fluid flow impinging on each post, increasing the viscous losses over flow in parallel channels. Flow through this geometry can be compared to flow through a pebble-bed reactor, where obstructions are introduced to slow the flow of fluids and increase mixing and surface area. Like the diagonal line geometry, the dot array wafers consisted of two types of devices (shown below in Figure 3.14). The first type was designed with rows of dots spaced with 500 μm offset to make any line along the direction of device motion run into at least one post. The second type of device (Figure 3.14b) was designed with same area of risers and channels as the parallel line geometry (416.5 mm^2) using 100 μm diameter posts. These devices were designed to increase the isotropy over the diagonal line design, with higher viscous absorption than parallel channels.

(a) 500 μm pitch lines offset at 100 μm   (b) 100 μm diameter dots, A= mm^2
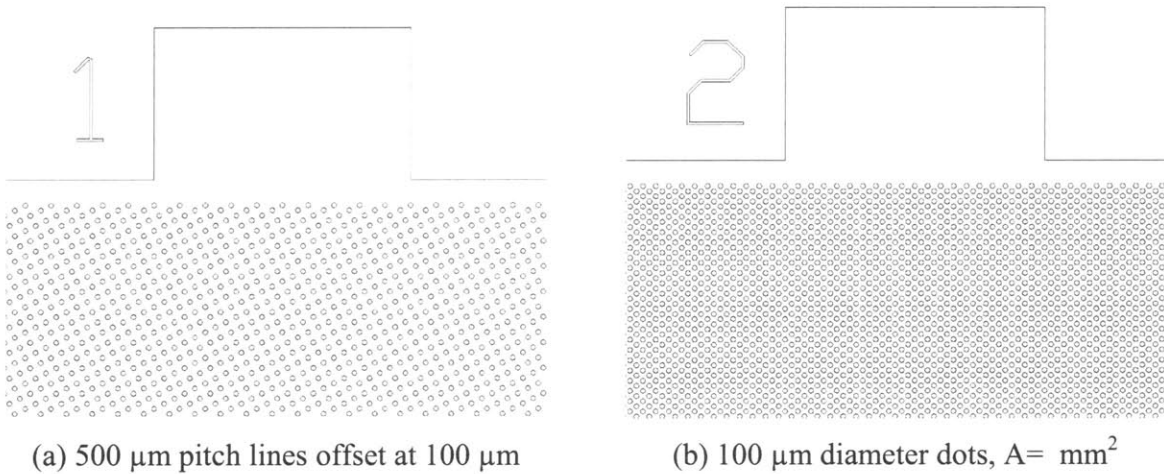
Figure 3.14- Two dot array device geometries for increasing energy absorption

3.5   Calculations

Several effects were involved in energy absorption in these micro-scale silicon devices including shear resistance exerted by the fluid, frictional force between opposing devices created by applied and capacitive normal forces, and capacitive forces incurred by decreasing the overlap between the capacitor plates. Simple models and the specific values for the geometries developed in this thesis are presented for each of the listed effects along with other relevant calculations for the performance of these devices.

3.6   Viscous Shear Force Exerted by Moving Fluid

There is a relative dearth of research in the literature into homogeneous ER fluid that makes analytical calculations of the shear stress difficult to come by. Previous researchers at ISN have suggested a parameterized model in the form of a power law relationship in Equation 3.1 below [Eastman, p. 29],

$$\tau = \left(\eta_0 + f_c E^n \right) \dot{\gamma} \tag{3.1}$$

where τ is the shear stress (Pa), η_0 is an initial viscosity (Pa-s), f_c is a measure of the magnitude of the ER effect, E is the electric field, and $d\gamma/dt$ is the shear rate (s^{-1}). This model reflects the trend presented in Figure 2.1b, where the slope of the shear stress versus strain rate curve increases with increasing electric field. A more generalized model has also been suggested [Eastman, p. 40] to generalize the shear stress in all ER fluids using Equation 3.2,

$$\tau = c(V) + b(V)\dot{x} = \left(a_0 + a_1 V^{n1} \right) + \left(a_2 + a_3 V^{n2} \right)\dot{x} \tag{3.2}$$

where c and b are nth order functions of V, a_1 through a_3 and n1 and n2 are constants, and dx/dt is the relative velocity of the shearing surfaces. This result with specific values from the original shear design with homogeneous ER fluid and no spacer was reported [Eastman, p. 85] to follow Equation 3.3,

$$\tau = 140 \pm 40 + \left(100 \pm 1600 + (1.1 \pm 14)V \right)\dot{x} \tag{3.3}$$

49

Again, the amount of uncertainty in the constants presented in previous work leaves something to be desired in terms of repeatability and accuracy. One reason these values may have had such large tolerances is the use of unconstrained boundary conditions combined with a new sample for every test. Deployed prototypes would contain and reuse the same fluid sample for the lifetime of the device, where fluid containment measures would prevent evaporation of any ER fluid components. Combined with the concept of using a bidirectional prototype (discussed in Section 7.8.3), this containment could lead to much more repeatable performance.

The research presented in this thesis has removed several confounding factors from this area of inquiry. For example, a normal force whose magnitude can be estimated from kinematic and capacitive models has been added to the analysis, the device cross-section has been designed to enforce a lower bound on the electrode gap using risers, and the amount of fluid injected into the test apparatus has been more closely calibrated through various means.

3.7 Normal Force and Friction

3.7.1 Blade Deflection Force Model

An external force is applied by the blade flexures to keep the silicon devices in contact. The magnitude of this force was calculated using beam bending theory applied to a composite beam (see Figure 3.15 below). The moment of inertia of the rectangular section of 5005 Alloy Aluminum used in the blade was calculated to be I_b=3.2 mm^4 (w=37 mm, h=1.01 mm, E=68.9 GPa), while the composite moment of inertia for the silicon device (w=37 mm, h=0.675 mm, E=170 GPa in the [110] direction) and aluminum blade was calculated to be I_c=22.1 mm^4 using the parallel axis theorem. The neutral axis of the composite section of the beam was found to lie within 20 μm of the interface between the Aluminum and the Silicon. This small value was neglected in the calculation of the moment of inertia of the composite beam, where the neutral axis was taken to lie exactly at the Si/Al superglue interface.

50
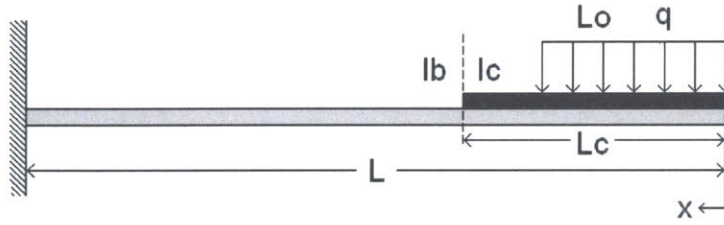
Figure 3.15- Cantilevered blade with composite moment of inertia, Ic

Using the calculated moments of inertia and the lengths of the cantilever and silicon device (L=123 and Lc=65 mm), the equation for beam bending (Equation 3.4) was applied to derive the slope and deflection of the cantilever in the three regions of the beam. The first pair of equations (Equations 3.5 and 3.6) applies to the region of length Lo in contact with the opposing blade. The second pair (Equations 3.7 and 3.8) applies over the remaining length of the silicon device, Lc, not in contact with the opposing blade. The third pair (Equations 3.9 and 3.10) applies over the remaining length of blade, L, with moment of inertia Ib.

$$\frac{d^2 y}{dx^2} = \frac{M}{EI} \tag{3.4}$$

Region 1 $\qquad \dfrac{dy}{dx} = \dfrac{qx^3}{6EI_C} + C_1 \tag{3.5}$ $\qquad y = \dfrac{qx^4}{24EI_C} + C_1 x + C_2 \tag{3.6}$

Region 2 $\qquad \dfrac{dy}{dx} = \dfrac{ql}{2EI_C}\left(x^2 - lx\right) + C_3 \tag{3.7}$ $\qquad y = \dfrac{ql}{2EI_C}\left(\dfrac{x^3}{3} - \dfrac{lx^2}{2}\right) + C_3 x + C_4 \tag{3.8}$

Region 3 $\qquad \dfrac{dy}{dx} = \dfrac{ql}{2EI_B}\left(x^2 - lx\right) + C_5 \tag{3.9}$ $\qquad y = \dfrac{ql}{2EI_B}\left(\dfrac{x^3}{3} - \dfrac{lx^2}{2}\right) + C_5 x + C_6 \tag{3.10}$

The boundary conditions at the wall allowed for the constants C_5 and C_6 to be solved, and the boundary conditions between sections 3 and 2, and 2 and 1 allowed the other four constants of integration to be solved. These boundary conditions and the corresponding constants of integration are given below in Equations 3.11- 3.16,

$$\left[\frac{dy}{dx}\right]_{x=L} = 0 \rightarrow C_5 = \frac{ql}{2EI_B}\left(L^2 - Ll\right) \tag{3.11}$$

$$\left[y\right]_{x=L} = 0 \rightarrow C_6 = \frac{ql}{2EI_B}\left(\frac{2L^3}{3} - \frac{L^2 l}{2}\right) \tag{3.12}$$

$$\left[\frac{dy}{dx}\right]_{CB+} = \left[\frac{dy}{dx}\right]_{CB-} \rightarrow C_3 = \frac{ql\left(l_C^2 - ll_C\right)}{2E}\left(\frac{1}{I_B} - \frac{1}{I_C}\right) + C_5 \tag{3.13}$$

$$\left[y\right]_{CB+} = \left[y\right]_{CB-} \rightarrow C_4 = \frac{ql\left(2l_C^3 - 3ll_C^2\right)}{12E}\left(\frac{1}{I_B} - \frac{1}{I_C}\right) + l_C\left(C_5 - C_3\right) + C_6 \tag{3.14}$$

$$\left[\frac{dy}{dx}\right]_{BA+} = \left[\frac{dy}{dx}\right]_{BA-} \rightarrow C_1 = C_3 - \frac{ql^3}{6EI_C} \tag{3.15}$$

$$\left[y\right]_{BA+} = \left[y\right]_{BA-} \rightarrow C_2 = C_4 - \frac{ql^4}{8EI_C} + l\left(C_3 - C_1\right) \tag{3.16}$$

These equations were programmed into Matlab, where the deflection and slope of the composite beam could be calculated for any input overlap distance and distributed load. Figure 3.16 below is an example of the deflection (a) and slope (b) curves that could be generated with this model. Specifically, these plots were generated with a combination of overlap and distributed load that made the deflection at x=Lo/2 equal to half the thickness of the blade and device for reasons that are explained below.

(a)   (b)
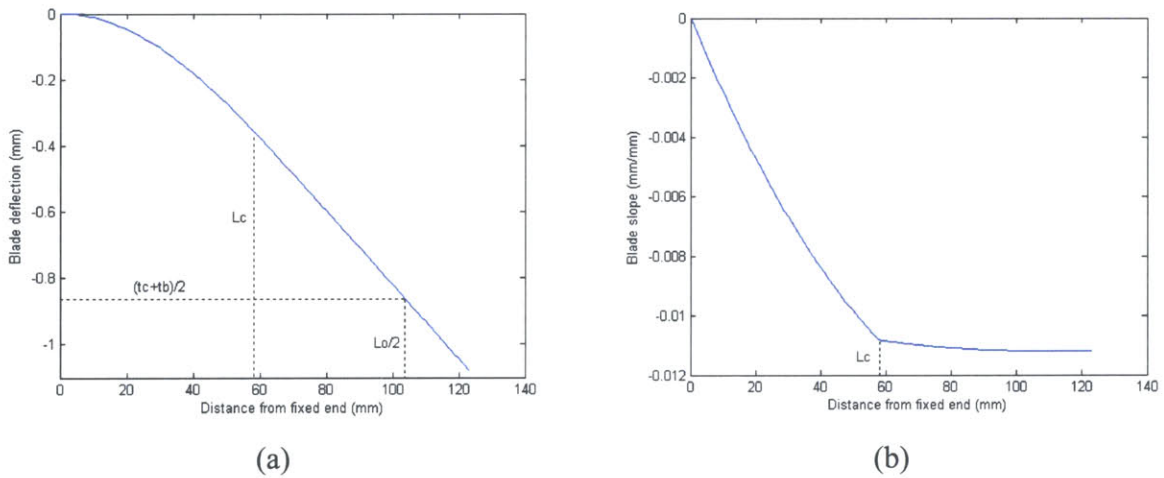
Figure 3.16- Deflection and slope for the composite blade loaded with 0.56N over 42 mm

52

3.7.2 Calibrating Blade Normal Force

The factor that determined the deflection of the blade was not a known distributed load; rather, the factor that determined the distributed load was a known deflection. In essence, the deflection profiles of the blades were such that the deflection at the center of the contact area was the same for both blades (by symmetry). The way that the blade normal force was calibrated in experiments (the full procedure is described in Section 5.6) was to line up the end of the blades as shown in Figure 3.17 below. To maintain symmetry, each blade deflected half of the vertical overlap at the center of the contact area. The resulting displacement, y, evaluated at the center of the contact area is half of the total thickness of the beam as given in Equation 3.17 below,

$$y\left(x = \frac{L_0}{2}\right) = \frac{\left(t_B + t_c\right)}{2} \tag{3.17}$$

where x is the distance from the constraint, tb is the blade thickness, and tc is the chip thickness. Matlab was used to iteratively find the force required to deflect this point on the blade the required distance, to create a plot of the normal force at every point in an experiment. The result of this calculation is displayed in Figure 3.18 below.

Figure 3.17- Calibrating the normal force between blades

(a)   (b)
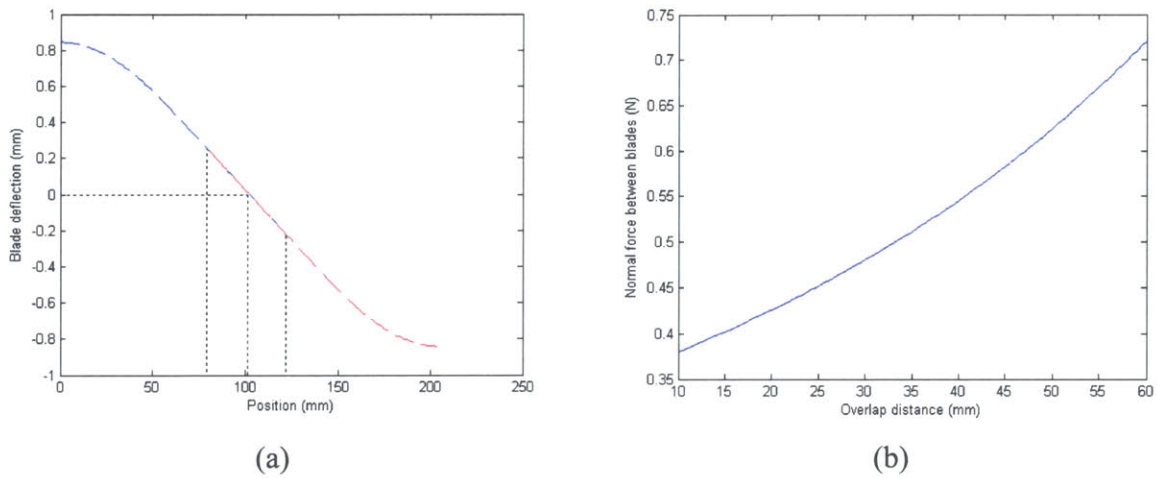
Figure 3.18- (a) Deflection of two opposing blade flexures in contact, (b) Normal force between blades versus overlap distance.

As shown in Figure 3.18b above, the normal force was calculated to decrease as the overlap area between devices decreased. This confirms the intuitive notion that as the spatial interference between the blades decreased, the forces exerted between the two should decrease. Figure 3.19 below shows that not only did the normal force applied by the blades decrease over the course of an experiment, the normal force decreased faster than the contact area did, resulting in a decreasing contact pressure with decreasing overlap.
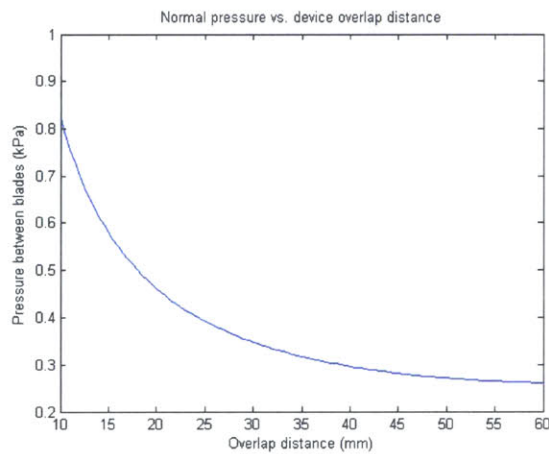
Figure 3.19- Contact pressure between blades versus overlap distance

54

As the devices were pulled past each other, the normal force changed as the imposed deflection decreased and the contact area decreased. Drag forces due to friction in this system were expected to follow Equation 3.18,

$$F_f = \mu F_n \tag{3.18}$$

where F_f is the frictional force, μ is the coefficient of friction (dynamic), and F_n is the normal force between the two friction surfaces. The maximum frictional force generated by the cantilever preload was expected to fall in the range of 0.21 to 0.35 N based on an estimated coefficient of friction, μ of 0.3 to 0.5. The normal forces in Figure 3.18 above were calculated for 153 mm long blades with 30 mm of the blade clamped in the fixture. Early device tests clamped the same length blade over the first 60 mm of the blade, with predicted normal forces in the range of 1.1 to 2.6 N. The higher preload in these tests was expected to produce frictional forces in the range of 0.78 to 1.3 N, which matched the experimental results in Section 6.4.

3.8 Capacitive Force

The electric field, capacitance and pull-down force of a parallel plate capacitor are given by Equations 3.19- 3.21 below,

$$E = \frac{V}{t} \quad (3.19) \qquad C = \frac{\varepsilon_0 kA}{t} \quad (3.20) \qquad F_n = \frac{1}{2}QE = \frac{1}{2}CVE = \frac{\varepsilon_0 kA}{2t^2}V^2 \quad (3.21)$$

where E is the electric field, V is the voltage across the capacitor plates, t is the electrode gap, ε_0 is the permittivity of free space (8.854E-12 F/m), k is the dielectric constant of the material in the electrode gap, A is the area of the capacitor plates, Q is the charge, and C is the capacitance.

3.8.1 Electrode-in-Channel Devices

Neglecting edge effects caused by the non-infinite nature of the patterned electrode using Saint-Venant's principle, the capacitive force was calculated using equations for a parallel plate capacitor with an area equal to the average of the areas of the patterned electrode and the top

electrode. Table 3.1 below displays the results of this calculation and also for the same calculation performed with the area of the patterned electrode and with the area of the top electrode (not including the contact pad). Values of V=100 volts, t=100 μm, and k=5 [Adolf, 1995; Wen, 1998] were used.

Table 3.1- Capacitive normal force varying with area

	$A_{eff}=A_{patt}$	$A_{eff}=0.5(A_{patt}+A_{top})$	$A_{eff}=A_{top}$
Area	1684 (mm^2)	1892 (mm^2)	2100 (mm^2)
Capacitance (nF)	0.745	0.837	0.926
Normal force (mN)	37.3	41.8	46.5

The difference between using the average capacitor area and the patterned area is 12%, and the linearity of the normal force with capacitor area makes the force response to this parameter less sensitive than to the applied voltage or the electrode gap. The same normal force calculation repeated for V= 500 volts and A=A_{ave} gives an electric field near the breakdown of ER fluid at 5kV/mm and a normal force of 1.05 N, 25 times the normal force at the standard minimum electric field at 1 kV/mm.

3.8.2 Continuous Electrode Devices

The second device cross-section (Figure 3.7b and Figure 3.20) has two parallel electrodes with ER fluid and two dielectric layers separating the electrodes. In retrospect, this design (design B) has several features that have the potential to make a superior prototype than the design using electrodes in channels (design A). Design B wasn't conceptualized until after several drawbacks of design A were discovered, including process problems like non-uniform DRIE etch rate and photoresist thickness. It is recommended that future researchers use design B where possible.

The non-uniform DRIE etch rate resulted in channel depth that varied across the surface of the wafer by as much as 50% of the maximum depth. This non-uniformity was repeatable (discussed in Section 6.8), but undesirable for parallel electrodes and could be prevented by the implementation of design B. One such implementation might call for successive layering of Si, conductor, SiO_2, and spacer. With these layers in place, DRIE (preceded by the appropriate channel defining photolithography) could be run down through the spacer to the layer of SiO_2

which would serve as an etch stop (DRIE has high selectivity of Si to SiO_2). The SiO_2 could then be etched in a buffered oxide etch (BOE, discussed in Section 4.6.10), leaving the planar channel bottoms with a uniform layer of conductor.

This fabrication process would also solve the problems encountered during the second photolithography step. The most difficult step in the implemented device fabrication plan was the application of photoresist to the uneven wafer surface of channels and risers. Photoresist is traditionally spun onto a substrate at speeds ranging from 500-5000 RPM. The centripetal forces that spread photoresist into a uniform layer on planar surfaces result in non-uniform coverage of steps, especially when these steps become much larger than the intended layer of photoresist. In the implemented fabrication process, photoresist was observed to flow along channels and pool in the corners of the etched channel area, thickly coat inward facing channel walls, and undercoat other areas. Numerous approaches were tried to achieve good photoresist coverage in the bottom of channels without photoresist coverage on the walls of the channels, with varying success. The sensitivity of the device resistance to any photoresist masking Al-2%Si on the channel walls (shorting the countersunk electrode to the planar electrode), was a significant issue that would be entirely avoided with an implementation of design B.

Design B, while more complicated in terms of capacitance calculations, also eliminates the electrical field edge effects of design A (along with the added manufacturing benefits). Analyses of the capacitance, normal force, and electric field distribution in the second cross-section are presented below for future reference. The cross-section of Design B can be thought of as a combination of capacitors in series and parallel described schematically in Figure 3.20b below.

(a)   (b)
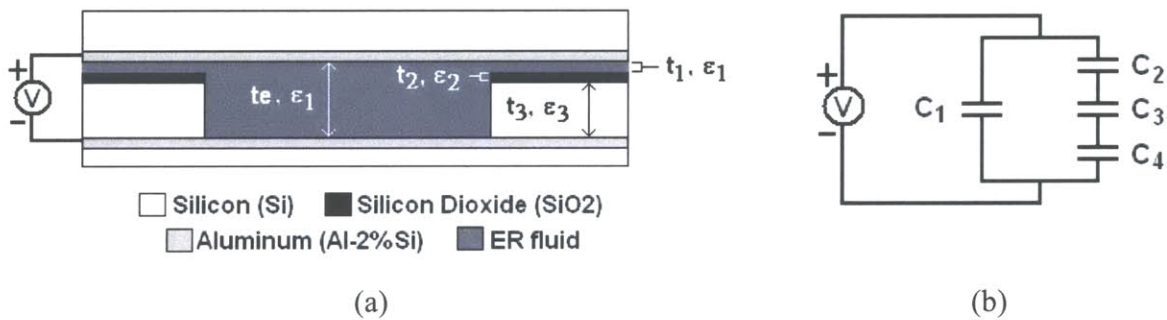
Figure 3.20- Diagrams of (a) the variables used in the capacitance calculation for potential future devices and (b) the equivalent capacitor network

Using the rules for calculating equivalent capacitance (capacitors in parallel add, capacitors in series add as inverses), the equivalent capacitance of the capacitor network of Figure 3.20b above was derived and is given in Equation 3.22 below,

$$C_{TOT} = \frac{A_C k_1 \varepsilon_0}{t_e} + \frac{A_R \varepsilon_0 k_1 k_2 k_3}{t_1 k_2 k_3 + t_2 k_1 k_3 + t_3 k_1 k_2} \qquad 3.22$$

where A_C is the total channel area, A_R is the total riser area, and the other variables are shown in Figure 3.20a above. Using the actual channel and riser areas from the calculation above (1684 and 416 mm^2), $t_1 = t_2 = 1$ μm, $t_3 = 100$ μm, $k_1 = 5$, $k_2 = 4.5$, and $k_3 = 11.7$, the total capacitance can be calculated to be 410 μF.

The electric field in each layer can be found using Gauss's law, which states that the total electric flux out of a closed surface is equal to the charge enclosed, divided by the permittivity. Since the flux is constant through all three layers, the relative electric field in each layer is given by Equation 3.23 below,

$$E_n = \frac{Q}{\varepsilon_n A} = \frac{CV_0}{\varepsilon_n A} \qquad 3.23$$

Since the charge across the capacitor is the same for all the layers, the relative electric field in the Si, SiO$_2$, and ER fluid are inversely proportional to the dielectric constant of each material. Thus, the electric field in the silicon and ER fluid are similar, while the field in the silicon dioxide is about half as large.

3.9   Resistance calculations for SiO$_2$

The first set of devices designed to test the effect of electrode gap on homogeneous ER fluid did not take into account the low resistivity of the silicon substrate used to fabricate the devices. The resistivity of silicon can range anywhere from 10e-4 to 10e4 Ω-cm depending of the concentration of p- or n-type dopants. The resistivity of wafers used for the first devices was quoted by the manufacturer to fall in the range of 6.0-12.0 Ω-cm. In a dry resistance test with the

full area of the raised silicon in contact (contact area = 43.57 mm^2) and a channel depth of 50 µm, the resulting resistance calculated using Equation 3.24 below would fall in the range of 20-45 mΩ. With a required voltage operating range of 50-250 Volts to generate a 1-5 kV/mm electric field, this resistance would allow upwards of 12500 Amps of current to flow.

$$R = \frac{\rho L}{A}$$ (3.24)

where R is the resistance of a wire, ρ is the resistivity given in Ω-cm, L is the length, and A is the cross sectional area (43.57 cm^2 in this calculation).

The high voltage supply used in this project was not capable of such extreme currents or power output, and the devices were redesigned to decrease the leakage current to a much more reasonable value. This was achieved by adding the layer of silicon dioxide to the top of the risers. This added a resistor in series with the silicon riser to bring the total resistance for the same example above (with a 1µm thick layer of SiO$_2$) to 2.3- 230 GΩ. This high resistance is due to the high resistivity of silicon dioxide (1e14 to 1e16 Ω-cm) and results in a lower current leakage, which is important when mobile power demands are taken into account. This lower leakage current could also improve the ratio of the energy cost per unit work absorbed in the final design, a performance measure presented in previous ISN research [Eastman, 2004].

3.10 Deflection Calculations for Substrate Bending

In future versions of this technology when the weight and thickness of shear-based prototypes are optimized, the substrate has to support the forces acting on it. The capacitive normal force discussed in Section 3.8 acts to pull the electrodes toward each other, potentially causing bending of the substrate if each layer is made thinner to fit more layers in a given total thickness. The length spanned by each electrode was designed to be 400 µm (the channel width).

The span is currently overbuilt due to the thickness of the silicon used for the devices, but future prototypes would ideally shrink the thickness of each layer to allow more layers and more shear area for a given stack thickness. With a wafer thickness of 550 µm, and a maximum channel depth of 100 µm, the minimum thickness of the span was 470 µm. The equation for the maximum deflection in a simply supported beam (Equation 3.25) is,

$$\delta_{MAX} = \frac{5}{384} \frac{FL^3}{EI} \quad \text{(3.25)} \qquad\qquad I = \frac{bd^3}{12} \quad \text{(3.26)}$$

where F is the total force, L is the span of the beam, E is the modulus of elasticity (107 GPa for silicon), and I is the moment of inertia of the rectangular beam, given by Equation 3.26 above where b is the thickness and d is the height of the rectangular beam. Plugging in the specific numbers for the current span (with beam height 470 mm, thickness 1 μm and the total force given by Equation 3.21 above for a single channel span), the results are as follows: F=0.22 μN, I=8.65e-18m^4, δ_{max}=2e-13m.

With flexible substrates, the value of E is expected to drop significantly and the bending strength of the channel bottom will have to be optimized. Another Alternatively, one could balance the attractive forces on the channel bottom by adding an electrode to the back side of the channel bottom. This would balance the capacitive forces on the electrode and yield a more robust solution while minimizing the overall thickness of a fabric layer. However, this presumes the availability of a manufacturing process to create such two-sided patterned devices on flexible substrates. This process is beyond the scope this thesis and is deferred as a topic for further research.

Chapter 4

Hardware Design and Fabrication

4.1 Hardware Overview

Several new pieces of hardware were designed and fabricated to further the research into field responsive fluids in novel geometries including a compression fixture, a blade flexure fixture, and silicon-based microchannel devices. The compression fixture, discussed in Section 4.4, was designed to test samples of open-cell reticulated foam filled with STF over a range of strain rates not initially available to ISN project 4.3 researchers. The silicon microchannel devices were designed to allow parallel plate shear tests with electrode gaps less than the typical minimum allowed by conventional rheometers. These small electrode gaps (on the order of 1-100 μm) were achieved by separating two planes of deposited aluminum with risers of silicon/silicon dioxide (Si/SiO2) (discussed in Sections 3.4). This chapter reviews the existing hardware and discusses the design and fabrication of new hardware, including the compression apparatus, the blade flexure fixtures, and novel silicon devices.

4.2 Linear Stage

The central piece of testing hardware used for this project was a Parker Daedal 404XR linear motion stage originally instrumented to approximate a linear tensile tester. All the fixtures fabricated for testing FRF composites were designed around this platform, shown below in Figure 4.1. This linear stage was driven by a Parker Compumotor VS23B-DFR10 stepper motor with a torque speed curve shown in Figure 4.1 below. Voltage to the motor was provided by a Parker Gemini GT6K controller/drive unit. The stepper motor drove a ballscrew with a 20mm lead that allowed the carriage to translate at up to 1 m/s over the 500mm travel of the stage.
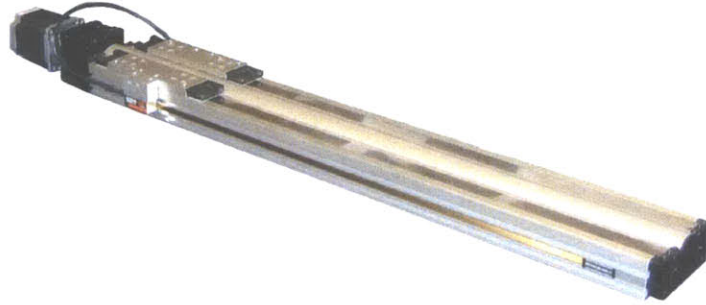
Figure 4.1 - Parker Daedal 404XR linear motion stage

The GT6K microstepping controller provided closed loop position control using the signal from a linear encoder on the side of the linear stage for position feedback. The linear encoder had a 1 μm resolution that gave the linear stage a bidirectional positioning repeatability of ±5 μm. Commands to the GT6K could be sent from a host computer via Ethernet or from programs loaded directly onto the controller for higher performance. A more detailed discussion of the programs implemented on the GT6K is presented in Section 5.5.4.

A Transducer Techniques MLP-10 force transducer (rated to ±10 lbs) was used to acquire force data during tests. The MLP-10 was powered by a DPM-3 digital panel mount meter that also scaled the force signal from the transducer into a 0-10 V output based on calibration values for the specific transducer. The DPM-3 could be programmed with calibration values for the transducer in tension, compression, or both, and could output the scaled 0-10 V signal corresponding to any force range. For example, the DPM-3 could be set to output 0 V when the force was zero and 10 V when the force was 10 lbs tension or could be set to output 0 V when the force was 10 lbs compression and 10V when the force was 10 lbs tension. The DPM-3 also conditioned the force signal with an adaptive auto filter designed to reject noise. The output of the DPM-3 was fed to a United Electronic Industries PDL-MF multifunction DAQ board with an input range of 0-10 V. The complete set of components is shown in Figure 4.2 below.
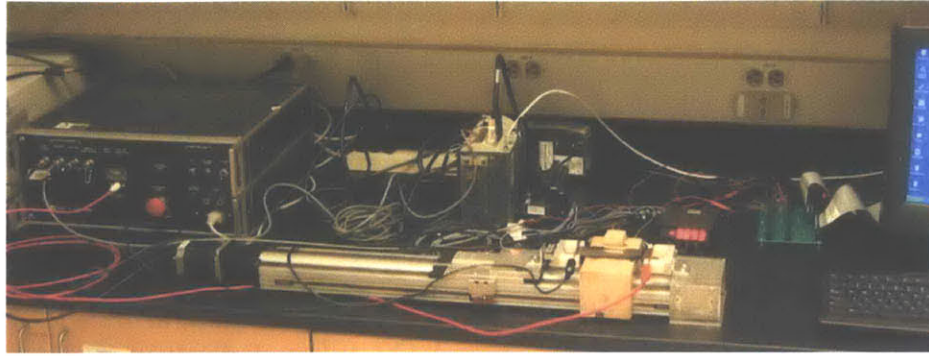
Figure 4.2- Shear testing setup with 404XR linear stage, GT6K controller, MLP-10 load cell, DPM-3 signal conditioner, DAQ board and high voltage amplifier

4.3 Original Shear Testing Setup

Previous experiments were run using a fixture that attached to the frame of the linear motion stage on one end and the moving carriage on the other end. Although the basic premise behind this fixture was good, the implementation (shown in Figure 4.3 below) left some room for improvement. As shown in Figure 4.3b, the fixed side of the fixture was held to the linear stage by friction, since the screw holes drilled to secure the fixture to the slots in the side of the linear stage didn't line up with the corresponding slots in the side of the linear stage. At higher loading rates, the friction holding the fixed end of the fixture was inadequate to support the forces created by the moving strips and the fixture tended to slide or rock forward. A lack of alignment features on the nylon sample holders also made it difficult to ensure that samples were parallel or even at the same height.
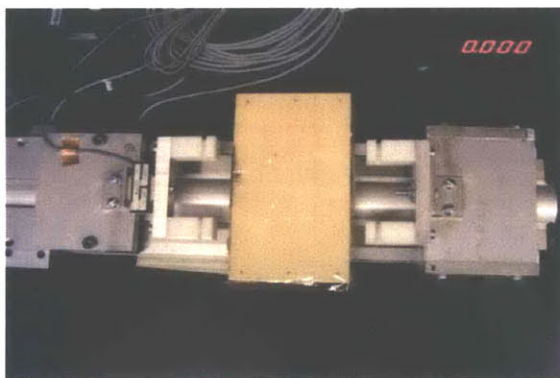
(a)
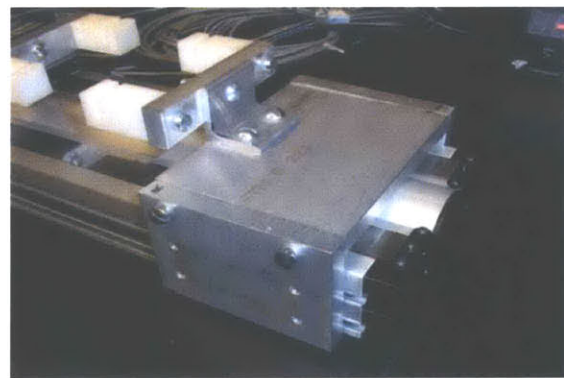
(b)

Figure 4.3- (a) Table to support aluminized Mylar electrodes, (b) Tension apparatus "fixed" end

A wooden table (shown in Figure 4.3a above) was included in the original design to support the aluminized Mylar electrodes. This table kept the electrodes from drooping, but introduced a problem in several tests when the moving electrode stuck to the table, producing incorrect force readings. Careful positioning of the table later solved this problem, but care had to be taken to ensure that the electrodes overlapped exactly and that the table was entirely under the stationary electrode. The table was also notoriously hard to clean and was not always at the height of the stationary electrode, which may have introduced variations in the data taken using this setup. Although the use of the table was discontinued with the introduction of the blade flexure fixture, future work with flexible electrodes could use this type of table with the addition of a cleanable surface (plastic, etc.), aligned at a known height relative to the linear motion stage.

Another possible source of misalignment in the original shear testing setup was the fixture on the moving carriage. Screws used to hold the moving fixture and the force transducer were passed through holes that were too large. This unnecessary clearance allowed the force transducer and fixture to rotate through approximately 20° and translate by roughly 2mm in each direction, which made it difficult to repeatably position the electrode during each test. This lack of repeatability had the potential to change the overlap between opposing electrodes when the sample was changed, which may have affected the force data. Care also had to be taken to tighten the screws with the angle bracket pulled toward the fixed end of the stage. If the screws were tightened without this precaution, the locking friction of the screws may have been insufficient to prevent the fixture from suddenly shifting under testing forces.

Although the original shear testing fixture was used to provide a baseline comparison with previous results, many improvements were made to the apparatus for subsequent experiments. These improvements were intended to expand the force and speed capability of the apparatus, enhance the rigidity of the fixture, and increase the positional repeatability of samples. The following sections explain in further detail the fixtures designed and fabricated to test new samples of field responsive fluids in novel geometries.

4.4   Compression Apparatus

A new fixture was designed and built to test samples of open-cell reticular foam, both empty and filled with glycerol or STF in compression at strain rates not available to ISN team 4.3 before the

creation of this hardware. Previous experiments performed on STF-filled foams were limited to constant strain rate tests at low strain rates (results were reported at rates between 10^{-2}-10^0 s^{-1}) and high energy impact tests at non-constant strain rate (1.3 x $10^5 \leq$ e $\leq$2.3 x 10^6 J/m^3) [Bettin, 2004]. The constant strain rate experiments were performed using a Texture Analyzer (TA.XT Plus) manufactured by Stable Microsystem, while the high energy impact tests were performed using an Instron Dynatup 9850 drop tower with a 7.4 kg crosshead moving at up to 20 m/s.

The desire to test STF-filled foams at higher strain rates stemmed from the incomplete data for this type of composite at intermediate strain rates. Instead of purchasing new equipment to test STF-filled foam samples at intermediate strain rates, it was suggested that the linear stage be modified for this purpose. A quote from the thesis that reported the foam compression results shows the perceived need for this new piece of testing equipment, "*Because of apparatus limitations constant strain rates testing was not possible with the texture analyzer for strain rates greater then 1 s^{-1}*" [Bettin, p. 79]. Any additional data at rates higher than 1 s^{-1} was desirable, and an initial goal of running tests at 2 s^{-1} was set for the modified linear stage. The first step in the conversion of the linear stage into a compression tester was to check the theoretical capability of the linear motion stage against the 2 s^{-1} strain rate design requirement.

4.4.1 Anticipated Torque and Speed Requirements

Tests at a constant strain rate of 2 s^{-1} were calculated to require speeds and forces within the limits of the linear stage. For a 10mm thick sample, a constant strain rate of 2 s^{-1} required a maximum velocity of 20 mm/s (V_0 in Equation 4.2 below). This requirement was well within the 1000 mm/s theoretical limit of the stage. Stresses as high as 0.2 MPa were reported for STF-filled foam samples tested at 1 s^{-1} [Bettin, p. 77], corresponding to a force of 100 N for a 8 mm diameter cylindrical sample. The force requirement for tests at 2 s^{-1} was expected to be on the same order as tests at 1 s^{-1}, or around 100-150 N.

Based on the torque speed curve for the stepper motor powering the linear stage shown in Figure 4.4 below, the amount of force theoretically available at the maximum stage velocity (50 RPS or 1 m/s) was calculated to be 150N (assuming a drive efficiency of 80%) using Equation 4.1 below,

65

$$F = \frac{2\pi T}{L}\eta \qquad\qquad (4.1)$$

where F is the linear force created by a ballscrew (in Newtons), T is the torque in N-m, L is the lead in m (0.02 m for the ballscrew in the 404XR), and η is the drive efficiency (the value used for calculations was 80%). The stall torque for the stepper motor was quoted at a maximum of 267.5 oz-in (1.88 N-m) [Eastman, 2004], but the torque speed curve suggested a more conservative torque of 1.2 N-m. Equation 4.1 predicted a corresponding force of between 301 N and 474 N, which was considered to be sufficient for these compression tests.
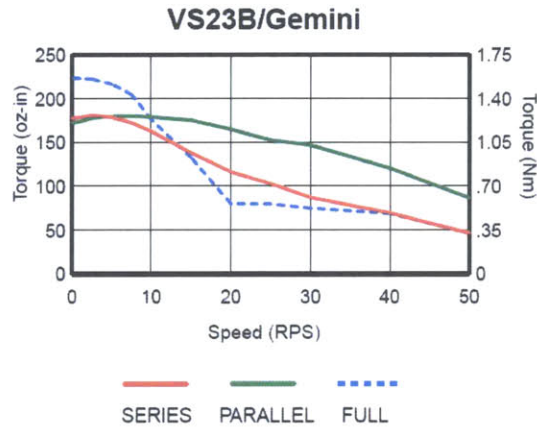
Figure 4.4- Torque speed curve for a VS23B stepper motor driven by a GT6K controller [Parker Catalogue, 2005]

4.4.2 Constant Strain Rate Compression

Constant strain rate compression tests were desirable because they matched the test conditions presented in previous ISN research [Bettin, 2004]. Constant strain rate compression requires an exponentially decreasing velocity profile of the form given by Equation 4.2 corresponding to a sample height given by Equation 4.3,

$$V = -\dot{\varepsilon}H_0 e^{-\dot{\varepsilon}t} = V_0 e^{-\dot{\varepsilon}t} \qquad\qquad (4.2)$$

$$H = H_0 e^{-\dot{\varepsilon}t} \qquad\qquad (4.3)$$

66

where V is the velocity in mm/s, H_0 is the sample size before compression in mm, $\dot{\varepsilon}$ is the strain rate in s^{-1}, t is the time in seconds, and V_0 is the equivalent initial velocity in mm/s. Although the linear stage was "not designed to be a data collecting device" (to quote a technical support representative from Parker Automation), the velocity of the carriage could be changed "on the fly", and exponentially decreasing velocity profiles were successfully implemented on the 404XR. Since the linear stage satisfied the theoretical requirements for velocity, force, and functionality, work progressed to construct the required fixtures to perform compression tests.

4.4.3 Hardware Implementation

The next step was to design and fabricate a test fixture capable of withstanding the forces created by the linear motion stage at these speeds while maintaining adequate structural stiffness to measure the strain of the sample with relatively high accuracy. A deflection of 0.1mm was deemed an acceptable error. Aggressive tests at the theoretical maximum of the linear stage, 300N, thus required a stiffness of 3000 N/mm. Based on the required stiffness and location of mounting points on the moving carriage and the frame of the linear stage, the compression fixture shown below in Figure 4.5 was designed.
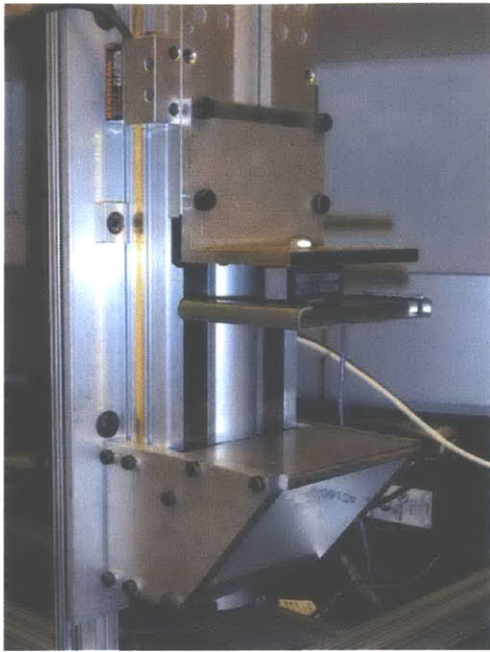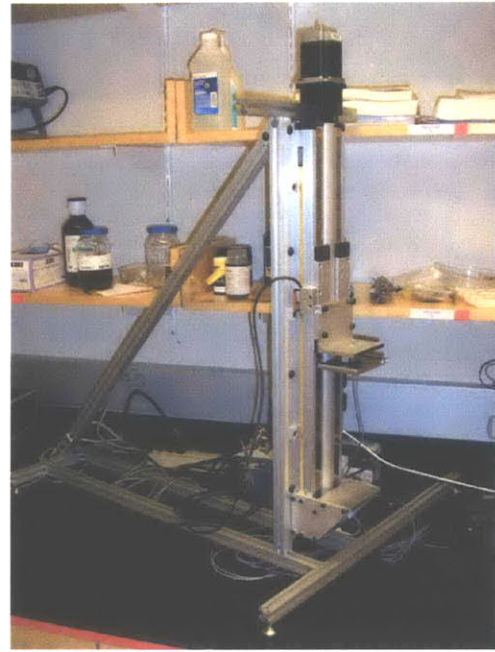
<center>(a)   (b)</center>

Figure 4.5- (a) Compression fixture close-up, (b) Vertical test stand and compression fixture

As shown in the figure, four bolts were used to secure the upper platen, force transducer and compression surface to the moving carriage (top). The lower subassembly was bolted to the frame of the linear stage using eight machine screws and custom nuts machined to fit into the slots in the side of the frame. The curved piece of stainless steel that served as the upper compression surface was introduced to cover the hole needed to bolt to the underside of the force transducer. This piece was assembled (slid) onto the lower plate after the force transducer had been bolted to the l-shaped upper bracket and the flat lower plate.

The stiffness of the upper bracket (the less stiff of the two brackets) was calculated to be 11,850 N/mm using a simplified cantilevered beam model with beam length of 33mm, thickness of 6.35 mm, and width of 95 mm. This first order calculation was a simplification over other more accurate calculations (plate bending or full FEA), but the resulting deflection of 0.025 mm under a 300 N load was considered to be sufficiently low to proceed without further calculations. The total deflection of the upper and lower platens, the force transducer, and the flex of the linear stage were assumed to be less than the desired $\delta=0.1$ mm.

In order to accommodate samples of various shapes and sizes, the compression apparatus was oriented vertically (as shown above in Figure 4.5) using extruded aluminum framing

<center>68</center>

manufactured by 80/20 Inc. This orientation allowed samples to be held in place by gravity on the lower compression surface, but required some additional hardware to hold the linear stage vertically. The stage itself was toe clamped to a slab of aluminum using toe clamps supplied by the manufacturer of the linear stage. These toe clamps (shown in Figure 4.6 below) were inserted into the same slots in the frame used to secure the lower subassembly of the compression fixture. The aluminum slab, in turn, was bolted to two vertical extruded aluminum struts using standard 80/20 fasteners. The vertical struts were supported by a diagonal brace that tied the vertical part of the assembly to a base structure with a large footprint. The large footprint prevented the linear stage from tipping over under normal operating conditions and included adjustable feet so the entire assembly could be easily leveled on most surfaces.
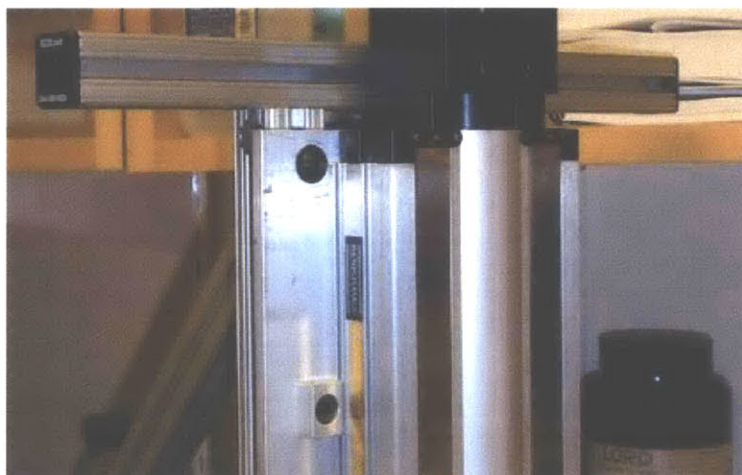
Figure 4.6- Close-up of vertical stand

4.5   Blade Flexure Fixture

As discussed in Section 3.2.3, previous ISN research [Eastman, 2004] has shown that ER fluid works well in unconstrained boundary conditions and the silicon devices implemented in this thesis, though based on rigid substrates, were intended to advance the understanding of the corresponding flexible prototypes. To make the testing of rigid prototypes as relevant to the project goal as possible, test fixtures were designed to mimic several degrees of freedom of unconstrained boundary condition experiments. These fixtures were based on blade flexures (shown edge-on in Figure 4.7) that allowed movement in the roll, pitch, and lift of each rigid

device. Another way to think about blade flexures is to compare the moment of inertia of such a beam in several directions. Using the coordinate frame shown in Figure 4.8 below, the moments of inertia about the x and y axes are much lower than about the z axis. This makes it difficult to move the end of the beam in the x and y directions, but not in z. Torsion of the end of the blade about the x axis is also easier than torsion of the blade about the z axis.
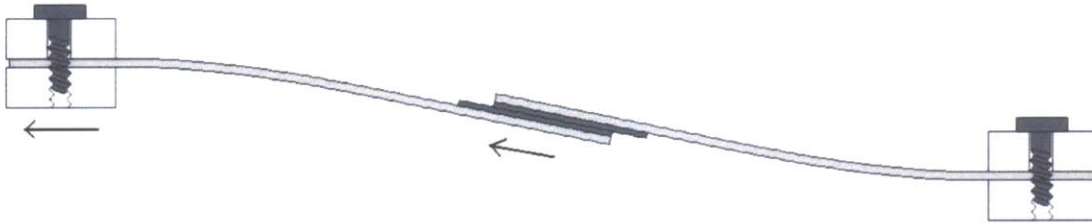
Figure 4.7- Diagram of blade flexure concept with exaggerated blade deflections
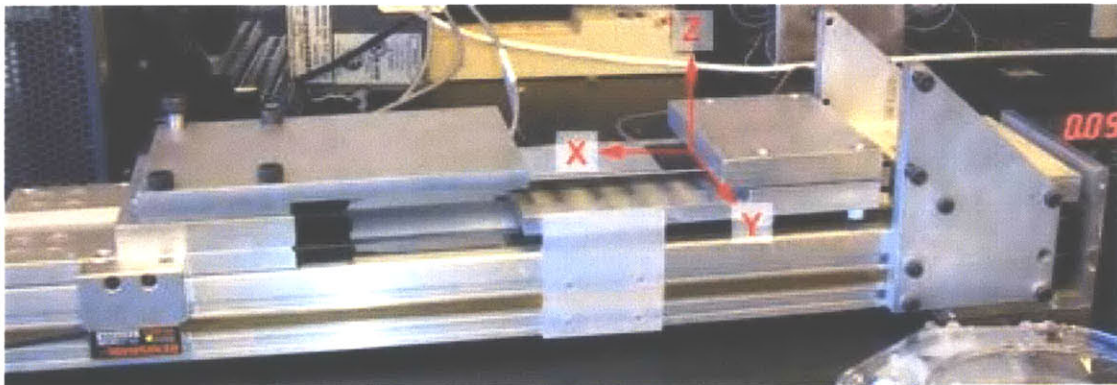
Figure 4.8- Picture of blade flexures implemented on the linear stage

Each blade was originally intended to be backed by foam over the device region. This foam, it was thought, would provide a preload that could be estimated using the stiffness of the foam and the strain introduced into the foam. Experiments later showed that the preload provided by the chosen foam was excessive (breaking chips in the extreme position). The design was then iterated to use the deflection of the blades to provide the normal force for the shear tests (as discussed in Section 3.7.1).

The force components between the silicon devices that affected the force measured by the load cell were the friction between the blades that existed in the absence of electric field, the viscous drag introduced by the ER fluid before and during application of the field, and the

additional friction introduced by the increase in normal force due to electrostatic attraction of the electrodes. Since the interesting forces in *variable impedance* composites were those than could be varied, it was desirable to minimize the friction between the blades that existed in the absence of electric field, and maximize the other dynamic forces. The added benefit of using a lower preload force (by eliminating the foam backing) was that this base frictional force between the two devices was decreased, but was still present to keep the devices in contact.

Using two of the pieces from the compression fixture, the stationary side of the blade flexure fixture was bolted to the frame of the linear stage. The force transducer was bolted to the stationary anchor on one side and to the blade clamp on the other (as shown in Figure 4.8 above). Since the force transducer was not intended to support angular loads like those created by the preload between the two blades or from the weight of the blade clamp, low-friction Teflon supports were inserted below the lower blade clamp plate. These supports were designed to carry both the weight of the blade/clamp and the force of the blade preload between the devices.

Rigorous mechanics suggests that for a true cantilevered blade flexure, the strain cones under the bolts used on either side should overlap to ensure a uniform pressure distribution across the clamped part of the blade [Slocum, 2005]. However, an order of magnitude calculation of the forces involved in this design showed that the clamping force provided by the four bolts far exceeded the load placed normal to the constraint. The simplicity of design and the ease of use of only four bolts were thus justified in this case.

4.6   Silicon Device Fabrication

A large portion of the work done for this project went into designing and implementing a *process plan* in the Microsystems Technology Laboratory (MTL) at MIT. The process plan described in the following sections is the result of many iterations and several processing experiments performed over the course of development. It is important to note that many of the steps in the process plan were introduced to correct failures. Like Edison's light bulb, this project was an exercise in iteration, refinement, and continuous "tightening" of process parameters to arrive at a working result. The following process plan represents what amounts to a final snapshot of the process, and is intended to give future researchers insight into the failure modes observed during the development of the process as well as the steps required to recreate the devices developed in

this work. Many of the following details are peculiar to the specific equipment in the MTL, but the process can be extended to other labs with similar processing equipment.

The format of the following sections gives the MTL shorthand version of the machine name, followed by a brief description of the process performed on the machine. The body of the section includes a description of the machine, including the full name where available, and a description of the overall process flow intended to read like a story. Specific recipe details like processing time, temperature, chemical compositions, etc. are included where applicable. These recipe details are outlined in bullet form for easy reading for later use in the cleanroom, where they should be used in addition to the more rigorous description of process steps given in the standard operating procedure (SOP) for each machine.

4.6.1 **RCA**- Clean wafers

The RCA clean is an industry standard set of cleaning steps to remove contaminants present on the surface of silicon wafers. The basic procedure was developed at the Radio Corporation of America (RCA) in 1965, hence the name, and has three major steps performed in succession. First, insoluble organic contaminants were removed using a solution of 1:1:5 ammonium hydroxide (NH_4OH), hydrogen peroxide (H_2O_2), and deionized (DI) water in the "SC1" clean. Second, a thin layer of silicon dioxide (where metallic contaminants may have accumulated) was removed in a dilute solution of Hydrofluoric (HF) acid (50:1 DI water to HF). Third, ionic and heavy metal contaminants were removed using a solution of 1:1:5 hydrochloric acid, hydrogen peroxide (H_2O_2) and DI water in the "SC2" clean.

Each chemical bath was followed by serial dilution in a dump rinser, where the wafer cassette (a Teflon carrier with slots to retain individual wafers in a stack, shown below in Figure 4.9a) was placed in a tank that filled with water and then "dumped" the water several times. Each time the tank filled with water, the chemicals on the wafer surface became diluted in the water bath, until all the chemicals had been removed. The process concluded with a run through a Spin-Rinse-Dry (SRD) machine that rinsed and dried the wafers and cassette while spinning the cassette at up to 2000 RPM. The RCA station and SRD machine are shown below in Figure 4.9b.

(a)   (b)

Figure 4.9- (a) Teflon wafer carrier, (b) RCA wet station (left) and SRD machines (right)

4.6.1.1   Recipe details

- 10 min SC1 clean- 1:1:5 ammonium hydroxide (NH₄OH), hydrogen peroxide (H₂O₂), and deionized (DI) water at 75-80° C
- Dump rinse (serial dilution of SC1 solution)
- 15 sec HF clean- 50:1 DI water and hydrofluoric acid (HF)
- Dump rinse
- 15 min SC2 clean- 1:1:5 hydrochloric acid (HCl), hydrogen peroxide (H₂O₂) and DI water at 75-80° C
- Dump rinse
- Spin-rinse-dry (SRD)

4.6.2 **Tube A2-WetOxBond** - Thermally grow 1 μm silicon dioxide

A 1 μm layer of silicon dioxide (SiO₂, or simply oxide) is grown at high temperature (1050 °C) in steam at atmospheric pressure in a MRL Industries Model 718 System (shown in Figure 4.10a). This "wet" oxide grew at the interface between the underlying silicon and the silicon dioxide. The oxygen atoms that formed the oxide had to travel through the growing layer of oxide to reach the underlying silicon, and the increasing diffusion distance led to an exponentially decreasing growth rate. A 1 μm layer of wet oxide was considered moderately thick, and the recipe called for 200 minutes of exposure to steam for completion. The actual recipe used in tube A2 was nine steps long including time exposed to nitrogen, oxygen, or water vapor (produced using the pyrogenic reaction of H₂ and O₂) and required around six hours to complete. Wafers were processed in a quartz boat (similar in function to a Teflon cassette, but intended for use at high temperatures) shown in Figure 4.10b below.

(a)   (b)

Figure 4.9- (a) Teflon wafer carrier, (b) RCA wet station (left) and SRD machines (right)

4.6.1.1   Recipe details

- 10 min SC1 clean- 1:1:5 ammonium hydroxide (NH_4OH), hydrogen peroxide (H_2O_2), and deionized (DI) water at 75-80° C
- Dump rinse (serial dilution of SC1 solution)
- 15 sec HF clean- 50:1 DI water and hydrofluoric acid (HF)
- Dump rinse
- 15 min SC2 clean- 1:1:5 hydrochloric acid (HCl), hydrogen peroxide (H_2O_2) and DI water at 75-80° C
- Dump rinse
- Spin-rinse-dry (SRD)

4.6.2 **Tube A2-WetOxBond** - Thermally grow 1 μm silicon dioxide

A 1 μm layer of silicon dioxide (SiO_2, or simply oxide) is grown at high temperature (1050 °C) in steam at atmospheric pressure in a MRL Industries Model 718 System (shown in Figure 4.10a). This "wet" oxide grew at the interface between the underlying silicon and the silicon dioxide. The oxygen atoms that formed the oxide had to travel through the growing layer of oxide to reach the underlying silicon, and the increasing diffusion distance led to an exponentially decreasing growth rate. A 1 μm layer of wet oxide was considered moderately thick, and the recipe called for 200 minutes of exposure to steam for completion. The actual recipe used in tube A2 was nine steps long including time exposed to nitrogen, oxygen, or water vapor (produced using the pyrogenic reaction of H_2 and O_2) and required around six hours to complete. Wafers were processed in a quartz boat (similar in function to a Teflon cassette, but intended for use at high temperatures) shown in Figure 4.10b below.

<center>(a)   (b)</center>

Figure 4.10- (a) Tube A2- WetOxBond, (b) Quartz boat with processed wafers

4.6.2.1   Recipe details

- Load wafers in quartz boat, set temperature setpoint to 1050 °C, wait for tube to reach processing temperature
- 1.0 min N_2 flow 51% (Recipe start)
- 20.0 min O_2 flow 60 % (Dry oxidation)
- 11.0 min N_2 flow 51% (Safety interlock for H_2)
- 2.0 min O_2 flow 60 % (Dry oxidation to prevent tube software fault)
- 99.9 min H_2 40%, O_2 variable (Wet oxidation by pyrogenic reaction)
- 99.9 min H_2 40%, O_2 variable (H_2 mass flow controller sets O_2 setpoint)
- 20.0 min O_2 flow 60 % (Dry oxidation)
- 30.0 min N_2 flow 51% (Anneal)
- Set temperature setpoint to 600 °C, wait for temperature to drop, remove wafers

4.6.3 HMDS- Apply photoresist adhesion promoter

HMDS (Hexamethyldisilazane), an adhesion promoter for positive photoresist (the next processing step), was a critical component in a creating a successful batch of wafers. HMDS vapor reacts with a substrate material to remove adsorbed water and reduce surface energy to increase the strength of the bond between the photoresist and the substrate. HMDS also acts to prevent etchants from undercutting the photoresist. Exposure to HMDS vapor was performed at elevated temperature under a vacuum in an oven similar to the one shown in Figure 4.11 below. After several months using HMDS recipe 4 with varying results, a change to recipe 3 was made that resulted in far superior photoresist adhesion (and superior etch results and quality). Recipe 3

<center>74</center>

used an extended exposure to HMDS vapor (60 seconds in recipe 3 vs. 20 seconds in recipe 4 or 10 seconds in recipe 5). An additional, non-standard vacuum dehydration step was also added to further drive off adsorbed water vapor and improve photoresist adhesion.

Figure 4.11- (Right) HMDS vacuum oven, (left) Photoresist spin coater

4.6.3.1 Recipe details

- Insert wafers into HMDS oven in a stainless steel boat
- Select recipe 3 (60 second HMDS) using toggle switch
- Press the start button and press the reset button when a pressure of 5 Torr is reached to hold wafers at processing temperature and low pressure for extra vacuum dehydration
- After 10 minutes, continue processing by pressing the start button
- HMDS recipe 3 runs through 39 internal steps that take ~30 minutes to complete
- Remove boat and let the wafers cool to room temperature before proceeding

4.6.4 Coater- Apply 8 μm layer of AZP4620 thick photoresist

A series of process steps was required to protect the area that would become risers in the device geometry and expose the area that would become the channels. Photoresist (PR or simply resist) is a photoactivated polymer whose chemical and mechanical properties change when exposed to light of a given wavelength. This property was exploited to selectively "harden" the PR in areas that are to be protected by shining monochromatic light through a chrome-on-quartz mask (shown below in Figure 4.12) that allowed light to shine through only in specific areas. After the adhesion promoter HMDS was applied, a layer of PR is spun onto the wafer using a Solitec Inc. model 5110 manual photoresist coater (shown in Figure 4.11 above) using centripetal forces to create a nearly uniform thickness across the spinning wafer. The spin step described in the recipe

details could be performed over a range of rotational velocities to give different film thickness (e.g. 3 krpm = 8 μm, 5 krpm = 6 μm).
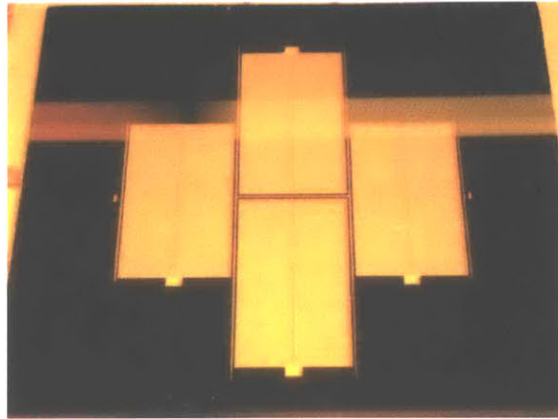
Figure 4.12- Chrome-on-quartz mask used to define channels and risers during EV1 processing

4.6.4.1   Recipe details

- Insert wafer onto the correct vacuum wafer chuck (green, 6") and turn on vacuum to secure the wafer
- Static dispense type AZP4620 photoresist (wafer not spinning) for 20 sec
- Spread resist over wafer surface for 9 sec at 1.5 krpm
- Spin resist to uniform 8 μm thickness for 60 seconds at 3 krpm (3000 rpm)
- Slow the wafer to a stop, remove PR edge bead with a cleanroom swab

4.6.5 **PrebakeOven** - Heat photoresist to 95 °C for 60 minutes

Photoresist starts out with a large volume fraction of solvents to help it flow evenly onto the wafer surface, but these solvents keep the photoresist liquid after it is dispensed. A Blue M Model DDC-146C bake oven was used to drive off these solvents at high temperature (95 °C) and solidify the resist onto the wafer.

4.6.5.1   Recipe details

- Insert wafers on Teflon cassette into oven, start timer
- Allow wafers to cool from 95 °C to room temperature before proceeding: ~5 minutes

4.6.6 **EV1**- Expose photoresist through chrome mask to define channels

The EV1 (Electronic Visions EV620 mask aligner/photolithography system) used 365-405 nm wavelength UV light generated by a 350 watt mercury lamp to expose resist-coated wafers through a mask. This recipe called for "soft contact" between the mask and wafer, which placed the mask 30 μm from the surface of the wafer (defined by the wafer thickness entered in a computer prompt) shadowing the riser area under areas of chrome on the mask. The options selected in the recipe details called for an interval exposure; this option exposes the resist to three periods of UV light, each for six seconds, alternated by six seconds of wait time. The EV1 is shown in Figure 4.13 below and many of the recipe details corresponded with the onscreen instructions given after the recipe was entered and run.

Figure 4.13- EV1 mask aligner/photolithography system

4.6.6.1 Recipe details

- Follow on-screen instructions to insert the mask holder
- Insert the mask on the mask load frame
- Adjust the mask until the mask alignment marks are shown in the on-screen optics display
- Insert wafer on vacuum chuck and align the wafer with the mask
- Expose the wafer with the following process parameters (typed into the corresponding form fields on the recipe tab of the EV1 software, or selected from pull down menus)
  - Mask holder- 7"
  - Thickness- 2.28 mm (measured using a micrometer)
  - Substrate- 6"
  - Thickness (substrate thickness)- 0.57 mm (depends on wafer manufacturer)
  - Separation- 30 μm
  - Top side exposure, transparent mask, interval exposure, soft contact
  - Exposure time- 6 seconds

- • Wait time- 6 seconds
- • Exposures- 3
- Remove wafer from chuck, insert the next wafer or press stop
- Remove the mask using the mask load frame

4.6.7 **Photo-wet-** Develop photoresist

The photoresist that was exposed to light in the EV1 was soluble in photoresist developer and washed away when submerged in this developer. The develop step was run using a Semifab Inc. model WPS 800 wet processing station and the correct color-coded lab ware (green plastic dishes).

4.6.7.1   **Recipe details**

- Gown up in the appropriate safety gear (rubber gloves)
- Place an empty Teflon cassette in the dump rinser to receive developed wafers
- Pour AZ 440 developer (the corresponding developer for the AZP4620 thick photoresist) into shallow developing container and immerse the wafer under the developer, agitate until clear
- Remove the wafer from the developer using metal tweezers and immediately place the wafer into the Teflon cassette in the dump rinser. Rinse the tweezers.
- Repeat for all wafers, changing the developer after every 3 wafers. Dispose of the developer into the water drain in the photo-wet sink.
- Once all wafers have been developed, take the Teflon cassette from the dump rinser and put it into the spin, rinse, dry machine (SRD). Rinse out the developing container.

4.6.8 Nikon fluoroscope and microscope- Inspect wafers

The Nikon Nomarski Inspection Fluoroscope (shown in Figure 4.14 below) is a tool that makes photoresist fluoresce, which facilitated inspection of the photolithography process. Care was taken to examine the thickness of resist over the pattern, the crispness of lines and corners, and any defects that may have occurred during processing. The Nikon MM-1 Measuring Microscope (also pictured in Figure 4.14 below) allowed the same inspection to be done with white light, which showed many defects on the wafer not visible through the fluoroscope. This inspection step was crucial to the successful production of working devices and revealed many of the flaws that occurred during processing.

Figure 4.14- Nikon inspection/measuring microscope and fluoroscope

Since this section of the thesis is intended in part to give an insight into the failure modes observed in the processing of silicon devices, the inspection step may reveal any of the following failures.

4.6.8.1 Poor photoresist adhesion

Characterized by brittle fracture of the photoresist over the riser areas and possible redeposition of broken pieces of resist in undesired areas, this failure was addressed by increasing the exposure time to HMDS and adding the extra vacuum dehydration step. If this failure is observed, the wafers may be "ashed" in an oxygen plasma (in the TRL Asher for 30-60 minutes depending on resist thickness) to remove the resist and return to the HMDS step.

4.6.8.2 Mask flip

The quartz mask was accidentally inserted upside-down (with the orange chrome side up) resulting in interference diffraction patterns formed in the resulting resist image (discussed in Section 6.7). This interference created risers that were much thinner than intended and eliminated the fine features on the mask alignment marks (3 µm wide lines). The resist lines remaining after such an error were easily identified as thinner than usual and the error, like all errors/failures in this section, were be fixed by ashing or stripping the resist with a 20 minute piranha etch (both described below) and starting over at the HMDS step.

4.6.8.3 Debris on mask

This failure, along with the following failure (bubbles or debris in photoresist) was characterized by defects that were generally visible to the naked eye that could be examined in more detail under the microscopes. Generally, one or two of these defects were found on each device until the process was tightly controlled and cleanliness was made paramount. It is up to the researcher doing the processing to decide whether these failures justify starting over with the photolithography sequence. Debris on the mask was found by visual inspection before each batch of exposures and was removed using the solvent wash sequence Acetone, Methanol, Isopropanol, (all three preformed over the solvent drain following the procedure outlined in the solvent SOP and in user training) DI water, blow dry.

4.6.8.4 Bubbles in photoresist

This failure yielded similar results to those found with debris on the mask. The photoresist was left in places where it should not have been, showing up in large, local defects (unlike the following two failures that tended to show up over larger areas). This failure was avoided by careful wafer handling, proper resist adhesion (to keep resist pieces from breaking off and redepositing elsewhere), keeping wafer cassettes clean, and careful attention to resist coating.

4.6.8.5 Overexposure/underexposure

Characterized by dull (not sharp) corners and line edges, an underexposure was corrected by decreasing the thickness of the resist (higher RPMs in the coater spin step) or increasing the exposure time in the EV1. Overexposure was characterized by channel areas that were wider than intended, but with the wide (~100 µm) features used in this thesis this failure was difficult to detect and preferred over underexposure or underdevelopment.

4.6.8.6 Overdevelopment/underdevelopment

Underdevelopment was characterized by a thin layer of resist remaining in a portion of the channel area (or the entire channel area in the extreme case) and could be immediately remedied by additional time immersed in resist developer. Overdevelopment, a "failure" that was never considered to be detrimental to the process, was characterized by thinning of unexposed areas of resist and widening of channel areas. Overdevelopment was often used to ensure that no

80

photoresist remained where it shouldn't be to ensure that the channels were etched to at least the desired depth.

4.6.8.7 Scratches on substrate

Scratches were seen on several wafers and nobody on the fabrication staff could explain the source of this failure. The failure was characterized by long "scratches" that ran across the bottom of the channels, but did not affect the risers, and was considered to be a benign fabrication error in that the channels could be considered at least as deep as the nominal depth. In many cases, the fear was of high spots in the channels, such that the following metallization would create regions where the opposing electrodes could short out. Overdevelopment, overexposure, scratches in the bottom of channels and fracture of photoresist (when the pieces didn't redeposit in channel areas) were thus considered benign.

4.6.9 **Postbake-** Heat wafers to 120 °C for 30 minutes

This step firmly cemented the resist remaining after the wafer had been developed. It allowed the resist to pass on to other steps with higher mechanical strength and chemical resistance. The recipe details were the same as for the prebake step, except for the time and temperature.

4.6.10 **Acid hood 2-** Etch Exposed SiO_2 for 13 minutes in BOE solution

A buffered oxide etch (BOE) solution (6:1 40% NH_4F, 49% HF) was used to isotropically etch the SiO_2 (oxide) not covered by photoresist at a rate of 0.1 μm/min. This step was inserted because the etch rate of SiO_2 in the subsequent Deep Reactive Ion Etch (DRIE) process was very low, and the DRIE greatly preferred to etch silicon over oxide (the etch selectivity of SiO_2 to Si was very high). The high etch selectivity led to fast etching of the underlying silicon where the oxide layer broke through first, resulting in an uneven etch depth in the channels. Etching the oxide in a solution with a high affinity for SiO_2, but not for Si thus broke through the oxide evenly and resulted in very little undercut of the photoresist.

4.6.10.1 Recipe details

- Gown up in the appropriate safety gear as indicated by the SOP: acid apron, face shield, arm protectors, and rubber gloves
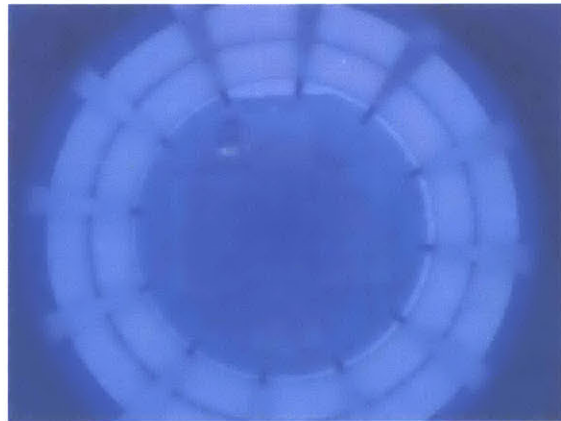
- Fill a square plastic basin with enough BOE solution to cover the wafers (BOE solution comes pre-mixed in a bottle that can be retrieved from the chemical pass-through)
- Dip wafers in Teflon carrier/cassette into the BOE solution, start the timer for 13 minutes
- When the correct time has lapsed, remove the cassette and put it into the circulating water bath (similar to a dump rinser, but without the dumping)
- Aspirate (draw off) the BOE solution with the aspirator tube by flipping the aspirator switch to the on position, and clean the plastic basin using serial dilution and the aspirator (fill and aspirate the basin with water three times)

4.6.11   **STS2-** Etch exposed Si to desired channel depth

The STS2 was an ICP (inductively coupled plasma) Deep Trench Etching System that used the Bosch DRIE process [Chang, 2005] to etch deep features into silicon with high selectivity over oxide and resist. The Deep Reactive Ion Etching (DRIE) process is an alternating series of etch (SF_6) and passivation (C_4F_8, Teflon) steps that produces high aspect ratio features in silicon with nearly vertical sidewalls.

(a) STS2 computer, load lock and chamber   (b) Etch chamber viewed through top port

Figure 4.15- STS2 (a) work station and (b) view of etch process through the top view port

4.6.11.1   **Recipe details (Recipe 2)**

- Oxide breakthrough (one time): 10 seconds, SF_6 flow rate: 70 sccm, pressure: 10 mT
- 16 sec etch cycle, 10 sec passivation cycle, 0.5 sec overlap between cycles, 36 mT primary pressure (recipe 1 used lower 31 mT primary pressure and a 15 sec etch cycle)
- Etch cycle- SF_6 gas flow rate: 140 sccm, platen power: 140 W, coil power: 600W
- Passivation cycle- C_4F_8 flow rate: 95 sccm, platen power: 0 W, coil power: 600W

4.6.12   Acid hood 2- Strip resist in 3:1 $H_2SO_4:H_2O_2$ (piranha) for 15-20 min

Once the channels had been etched to the desired depth, the photoresist was removed to reveal the patterned Si/SiO_2 surface. Complete removal of all photoresist was required before processing in Endura (a machine tool in the Integrated Circuits Laboratory), to prevent hundreds of thousands of dollars of contamination, making this step intentionally rigorous. The etch recipe called for full immersion of the wafers in a 3:1 mixture of sulfuric acid (H_2SO_4) and hydrogen peroxide (H_2O_2) in a quartz tank until all photoresist had been stripped. The recipe details were the same as for the SiO_2 BOE step in Acid Hood 2, except for the use of a quartz tank and a 15-20 minute etch time.

4.6.13   Asher- Strip Teflon in oxygen plasma for 30 min

Another step required before Al-2%Si deposition was the removal of residual Teflon left from the passivation steps (C_4F_8) in the DRIE step. Teflon remaining on the wafer hindered the adhesion of Al-2%Si, resulting in poor coverage. The wafers were placed in a quartz boat and into a barrel etcher with a high density oxygen plasma for 30 min to remove the Teflon (and any additional photoresist on the wafer). A barrel etcher creates an oxygen plasma in which oxygen ions react with organic compounds, such as photoresist, to oxidize or "ash" the compounds from the surface of the substrate. The barrel etcher used in this step put the wafers to be ashed inside a metal cage in the shape of a "barrel" that eliminated the majority of the kinetic energy of impinging oxygen ions, resulting in an anisotropic etch primarily governed by the chemical component of plasma etching (chemical and physical etching are the two primary etch mechanisms in "dry" plasma etching). Recipe details were the same as given in the SOP.

4.6.14   PreMetal-Piranha (ICL) - Metallization preparation step

The preparation for metallization in Endura included one piranha etch (a resist strip), one 30 minute ash, and a second piranha in a more pristine basin (a premetal clean). This set of steps ensured that there are no photoresist or Teflon contaminants could contaminate the expensive Endura hardware. This piranha etch was performed in the Integrated Circuits Laboratory (ICL) in the green piranha basin with an etch time of 10 minutes.

4.6.15   **Endura (ICL)** - Sputter deposit 1 μm Al-2%Si film

The Endura 5500 physical vapor deposition (PVD) system was capable of uniformly sputtering several common types of metals onto wafers. The recipe used for this process plan created a 1 μm layer of aluminum with 2% silicon. This Al-2%Si recipe provided high conductivity for the electrodes without incurring the problem of Al spiking common in depositions of pure Al (described in Section 3.4.1). The SOP and the onscreen instructions walked through the semi-automated deposition process that required very little user input or change to the process recipe.

4.6.16   **HMDS-** Apply photoresist adhesion promoter

The same recipe details and process description applied to this step as to the other HMDS recipe, including the use of recipe 3 (60 sec HMDS exposure) and the vacuum dehydration.

4.6.17   **Coater-** Apply 2 μm AZ5214 "image reversal" resist

One of the later changes to the process plan allowed for the use of a single chrome mask to define both the channels and the electrode in the bottom of the channels. Earlier in the process plan development, two masks were used to first remove resist above the channels and then to leave resist in the bottom of the channels. Careful design of a recipe using image reversal resist allowed the first mask in the set to be used for both processes.

Image reversal resist contains a special crosslinking agent that becomes active over 110 °C that acts only in exposed areas of the photoresist. By exposing the area of photoresist that was to be kept, baking the wafer at 120 °C to activate the crosslinking agent, and flood-exposing the entire wafer, the crosslinked area became insoluble in developer. The rest of the resist developed like standard, exposed positive photoresist. As discussed in Section 3.8.2, the resist did not form a uniform thickness across the wafer surface due to the channels and valleys present on the wafer surface. The alternative device cross-section presented in Section 3.8.2 would have eliminated this problem by removing the second photolithography step.

4.6.17.1   **Recipe details**

- Dynamically dispense photoresist for 10 seconds at 500 rpm. The dispensing head was held for 5 seconds at the center of the wafer before moving the head toward the outer edge for 5 seconds.
- Spread photoresist for 6 seconds at 750 rpm to get the resist into the hard to reach spots

- Spin resist to a "uniform" thickness at 1000 rpm for 30 seconds

4.6.18   PrebakeOven- Heat wafers to 95° C for 30 minutes

This step did the same thing to image reversal photoresist as it did to standard positive resist, driving off the solvents that make the resist liquid during the coating stage and preparing the resist for exposure in the EV1. After the wafers were baked in the 95 °C oven (in a Teflon cassette) for 30 minutes, they are removed and allowed to cool to room temperature before proceeding to the next step. Removing the wafers from the hot Teflon cassette and moving them to a cool cassette substantially sped this cooling step.

4.6.19   EV1- Expose resist for 10 seconds

Using the same mask as the first exposure, the resist in the bottom of the channels was exposed to UV light for 10 seconds continuously (unlike the 3 intervals used in the first exposure). This prepared the resist in the bottom of the channels to be heated to 120° C to activate the crosslinking agent that made this resist remain after developing to protect the Al-2%Si in the bottom of the channels.

4.6.19.1   Recipe details
-   Follow on-screen instructions to insert the mask holder
-   Insert the mask on the mask load frame
-   Adjust the mask until the mask alignment marks are shown in the on-screen optics display
-   Insert wafer on vacuum chuck and align the wafer with the mask
-   Expose the wafer with the following process parameters (typed into the corresponding form fields on the recipe tab of the EV1 software, or selected from pull down menus)
    -   Mask holder- 7"
    -   Thickness- 2.28 mm (measured using a micrometer)
    -   Substrate- 6"
    -   Thickness (substrate thickness)- 0.57 mm (depends on wafer manufacturer)
    -   Separation- 30 μm
    -   Top side exposure, transparent mask, <u>continuous</u> exposure, soft contact
    -   Exposure time- 10 seconds
-   Remove wafer from chuck, insert the next wafer or press stop
-   Remove the mask using the mask load frame

4.6.20   Hotplate- Heat each wafer to 120° C for 90 seconds

This step activated the special crosslinking agent in the image reversal resist that made the resist insoluble in the areas exposed to light. A slab of metal was placed in the postbake oven that remained at a constant 120 °C. One by one, wafers were set on top of this slab, the door to the oven was closed, the wafers were heated for 90 seconds, and the wafers were removed from the hotplate and allowed to cool to room temperature before further processing.

4.6.21   EV1- "Flood" expose wafer for 1 minute

Unlike other exposures in the EV1, this step was run without a mask holder or mask. By selecting the "flood exposure" option in the pull down list and selecting a 60 second exposure, the onscreen prompts walked users through the process and exposed the entire wafer for 60 seconds.

4.6.22   Photo-wet- Develop in AZ440 developer for 110 seconds

Using the same procedure as the first photoresist develop step, the wafers were submerged in developer one at a time for 110 seconds, then removed from the developer with tweezers and placed in the Teflon cassette waiting in the dump rinser. The majority of the resist cleared after 90 seconds, but the whiskers from the corners of the devices took approximately 120 sec to dissolve, so this step was run until the whiskers visually disconnected from the devices.

4.6.23   Nikon fluoroscope and microscope- Inspect wafers

Just like the first inspection, this step was crucial to ensuring high quality devices. By inspecting the wafers in the fluoroscope and the white light microscope, the thickness and continuity of the resist was examined and any defects were scrutinized. Unlike the preceding photo-lithography inspection step, defects found in this step could not be reversed by a piranha etch because the sulfuric acid would have aggressively attacked the aluminum on the wafer surface, resulting in an unstable, rapid reaction. Photoresist from this photolithography sequence had to be removed in the asher, where an oxygen plasma etched the organic components on the wafer surface (the resist) without attacking the metallic layer underneath. A 30 minute corrective ashing step was

sufficient to remove all the resist, but care to space the wafers out as much as possible improved this result.

4.6.24   **Rainbow (ICL)-** Etch the exposed Al-2%Si

The aluminum not protected by photoresist was anisotropically etched in a dry plasma in a Lam Research Rainbow 9600. The recipe used for this step was updated by the equipment technician for this tool, who should be contacted before using this machine. The endpoint of the etch was determined automatically based on a spectral analysis of the etch product gases, after which a slight over-etch was performed to ensure etch completion across the wafer surface. This process was highly automated and the recipe details varied slightly with the parameters entered by the equipment technician to compensate for the current working state of the machine.

4.6.25   **Asher-** Strip photoresist

After the aluminum was etched in the Rainbow, the protective photoresist was stripped in an oxygen plasma for at least 30 minutes. Visual inspection or inspection with the Nikon fluoroscope confirmed the complete removal of resist. This final cleanup prepared the wafers to be broken into individual devices in the die saw.

4.6.26   **DieSaw-** Cut wafers into individual devices

A Disco Abrasive System DAD-2H/6T die saw was used to cut the wafers into the final 37x65 mm devices using the SOP for the die saw. Any of the blades available for the die saw could be used with the current mask design thanks to the wide device division marks (100 μm). First, the wafer was cut along the long division marks that separated devices 1 and 3 from 2 and 4 (the devices were numbered clockwise from the flat). These four cuts were made at 37 mm intervals, and devices 1 and 3 were removed from the tape backing applied to the wafer to hold the pieces in place after they were cut apart. Devices 2 and 4 were then cut along the top and bottom using two cuts spaced at 65 mm. Devices 1 and 3 were then cut to size using three cuts spaced at 65 mm intervals to complete the separation of the four devices.

Chapter 5

Experimental Procedure

5.1 Overview

Each of the hardware platforms described in the previous chapter were designed with specific goals in mind. The compression apparatus, for example, was designed to compress foam samples filled with shear thickening fluid at strain rates not originally available to ISN team 4.3. Each platform also introduced its own software challenges and apparatus-specific calibration and testing. Chapter 5 describes in detail the experimental procedure and software used to perform the experiments on field responsive fluids in novel geometries on all three hardware platforms. Also included in Chapter 5 are descriptions of the small experiments performed along the way to the large-scale tests, especially in MTL, where much of the research went into experimenting with processing steps to create a working process plan.

5.2 Linear Stage Characterization

The existing hardware for ISN project 4.3 included a linear motion stage with a linear encoder and force transducer (MLP-10 load cell) set up to record force and position during constant velocity shear experiments. Several steps were taken to characterize the performance of the system and to calibrate the load cell before the system was used to gather data. Calibrations of the system were first checked using calibrated springs stretched between two rods in the original test fixture, then confirmed by direct loading of the force transducer with calibrated weights.

5.2.1 Spring Tests and Calibrated Weights

Recreating one of the first calibration steps from earlier work, springs with known stiffness were stretched between two rods in the original shear testing fixture. A simple calibration program was written to command the linear stage to move a specified distance at a constant velocity and record the position of the linear motion carriage and the force on the load cell. Two springs with

spring constants 0.3 lb/in and 0.6 lb/in (52.5 N/m and 105 N/m) were tested using this program at velocities of 2, 4, 8, and 16 mm/s. Trend lines were fitted through the force/position/time data to estimate the stiffness of the springs (Figure 5.1a) and the actual velocity of the moving carriage (Figure 5.1b). The measured stiffness of 97 N/m was within the specified tolerance of the calibrated spring (±0.05 lb/in).
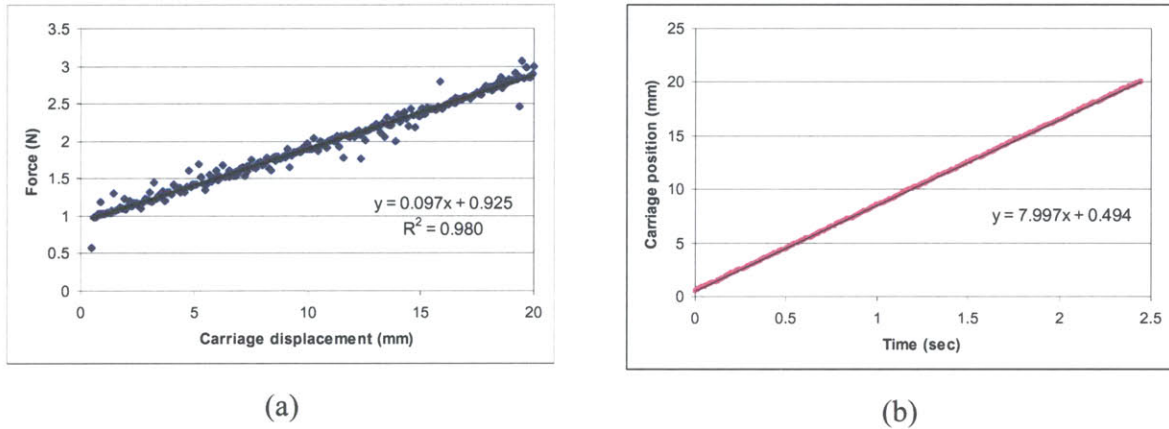

(a)   (b)

Figure 5.1- (a) Example spring force vs. displacement plot, (b) example position vs. time plot

Springs were used to calibrate the linear motion stage to replicate previous work, but a more straightforward method to test the accuracy of the load cell was to add weights in tension and compression directly to the load cell. To test the calibration of the load cell in compression, the cell was first removed from the shear testing apparatus and placed on a vibration isolating air table. Power was then applied to the load cell, and the readout from the DPM-3 load cell transducer box was set to zero (tared) once steady state was reached. Calibrated weights of 100, 200, and 500 grams were placed on top of the load cell and the value was recorded at steady state. Direct weighting of the load cell in tension was less straightforward and required the construction of a small test apparatus. Screws were inserted into both ends of the load cell and the top screw was hung from an elevated plate and the readout of the DPM-3 was tared in this position. The calibrated weights were then hung from the lower screw, the DPM-3 readout was allowed to settle, and the measurement taken. All values displayed on the DPM-3 were within 1% of the actual force applied to the load cell when the factory calibration values for the transducer were used. These measurements confirmed the more detailed characterization from [Eastman, 2004].

5.3 Flexible Electrode Characterization and Baseline Calibration

Once force and position data could be reliably measured, a baseline characterization of the original flexible electrode shear tests was performed. Strips of aluminized Mylar of the same dimensions used in the original experiments [Eastman, 2004] were mounted to aluminum rods and placed in the sample holder of the original test fixture. The wooden table used in previous tests was placed underneath the flexible electrodes, and the setup was otherwise recreated to the level of detail available from documentation and from remaining samples and hardware.

With this setup in place, a fluid sample with known rheological properties was injected onto the lower (fixed) electrode. The viscosity of this fluid, syrup, was measured to be 20 ± 1 Pa-s using a TA instruments AR1000-N rheometer in the Hatsopoulos Microfluids Laboratory (HML). This choice of calibrated liquid was made because of its use in the HML as a material of "standard" viscosity, and the similarity between the viscosity of syrup and the viscosity of homogeneous ER fluid. The volume of fluid was measured using a standard 5 mL plastic syringe, which also served as the application device for the viscous syrup. After application, the syrup tended to coalesce into a single pool with relatively uniform height. A stable perimeter of the pool was observed after the shape was initially created during application. Measurements of this pool area were taken and later used to approximate the height of the fluid.

With the fluid pool in place on the stationary electrode, the rod of the moving electrode was inserted into the fixture and the aluminized Mylar was allowed to fall onto the fluid pool. Since the syrup wet the surface of the aluminized Mylar well (a contact angle of less than 90° was observed), only a short amount of time was needed for the fluid to form a thin layer with a concave meniscus between the two electrodes. The Mylar strips were then pulled past each other using the linear stage at a constant velocity while the position and force were recorded. For the first battery of tests, the syrup was reused after each test by lifting the moving electrode after a test had been completed, commanding the linear carriage to the start position, and putting the strips back into contact. Given a short amount of time (less than five seconds), a fluid pool with the same observed dimensions and approximate thickness as the original formed between the two electrodes. The experiment was repeated after this pool had reformed.

The height of the fluid pool and the instantaneous viscosity of the fluid were estimated using Equations 5.1-5.4 below,

$$\mu = \frac{\tau h}{v} \qquad (5.1)$$

$$\tau = \frac{F}{A} = \frac{F}{w(x_0 - x)} \qquad (5.2)$$

$$h = \frac{V}{A_0} \qquad (5.3)$$

$$\mu = \frac{VF}{vA_0 w(x_0 - x)} \qquad (5.4)$$

where μ is the fluid viscosity (μPa-s), τ is the shear stress on the fluid (N/mm^2), h is the height of the fluid pool (mm), v is the velocity (mm/s), F is the force measured by the force transducer (N), A is the instantaneous area of the fluid pool (mm^2), V is the volume of fluid dispensed onto the lower electrode (mm^3), A_0 is the initial area of the fluid pool (mm^2), w is the width of the fluid pool (mm), x_0 is the initial overlap of the electrodes (mm), and x is the distance moved from the starting position (mm).

An example result of the first battery of experiments is shown in Figure 5.2. This test was the first shear test performed with syrup between flexible electrodes, and the expected linearly decreasing force due to decreasing contact area was observed with increasing carriage displacement. The data in Figure 5.2 was passed through a symmetric moving average filter that returned the result given by Equation 5.5,

$$F_i = \frac{1}{N} \sum_{j=-\left(\frac{N-1}{2}\right)}^{\left(\frac{N-1}{2}\right)} f_{i+j} \qquad (5.5)$$

where F_i is the filtered force, N is the size of the window (an odd integer, always 5 in this thesis), and f_{i+j} are the individual force measurements around and including f_i. The moving average filter is the optimal finite impulse response (FIR) filter for reducing random noise while retaining a sharp step response. This filter decreases the magnitude of the noise in a data set by the square root of N [Smith, pp. 278-279].
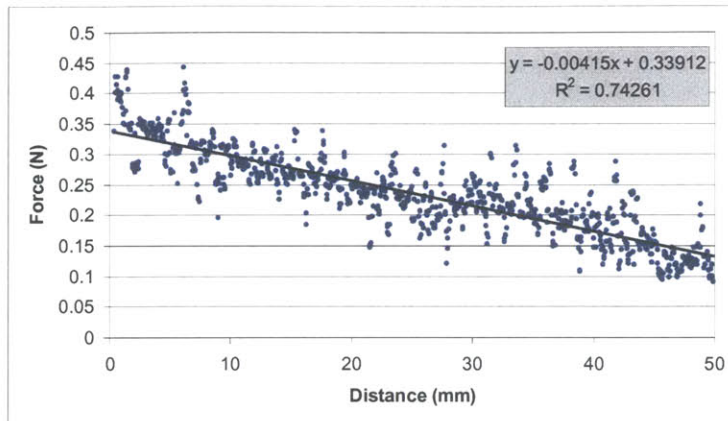
Figure 5.2- Force versus displacement data for syrup in the original shear fixture (filtered, N=5)

The viscosity of the fluid from this test was calculated to be 19.3 Pa-s (this value remained unchanged between the raw and filtered data), which fell within the range measured using the AR1000 rheometer of 20±1 Pa-s. Tests performed reusing the same sample, however, did not produce calculated viscosities around 20 Pa-s; in fact, the calculated viscosity of the sample was found to increase linearly with the number of tests run using the fluid sample. Figure 5.3 below shows this increase in viscosity with the number of reuses.
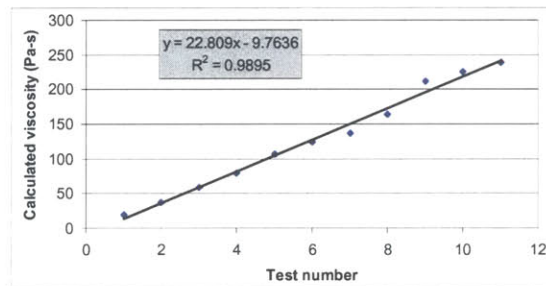
Figure 5.3- Viscosity versus test number for syrup between flexible electrodes

Two of the four variables in Equation 5.1 above were not directly measured: the viscosity of the fluid and the height of the fluid pool. For the observed trend to occur, the viscosity of the fluid had to increase, the height of the fluid pool had to decrease, or the viscosity had to follow an equation other than Equation 5.1. Neglecting non-Newtonian behavior, an increase in fluid viscosity or a decrease in pool height were both considered to be potential explanations of this phenomenon. Researchers in the HML used the AR1000 rheometer to study syrup at steady state,

93

where it was found to act like a Newtonian fluid across varying strain rates and test durations, supporting the conclusion that substantial non-Newtonian behavior could be discounted.

Over the course of several tests, the viscosity could potentially increase as components of the fluid evaporated or the rheological properties of the fluid changed after being in contact with air or heat (viscous heating). Conversely, the height of the fluid pool could have decreased due to either a loss of volume of the fluid (possibly due to evaporation) or an increase in the pool area. Since the pool area was monitored visually between tests and the volume of the fluid was not observed to decrease by the factor of twelve required to explain the effect, the increase in fluid viscosity over multiple tests was attributed primarily to an increase in the actual fluid viscosity. This increase may have been due to evaporation of some component, an increasingly strong bond to the flexible electrode, or a change in the chemical structure of the sugars in the syrup in response to air or heat. Several batteries of tests were subsequently run using a new procedure where the syrup sample was changed between each test. The results of these tests are discussed in Section 6.1.2.

The important lesson learned from the first set of syrup tests was that individual samples of a fluid may change between tests, and the results from subsequent tests reusing a fluid sample should be examined to ensure consistent fluid properties. This lesson was relevant to the experiments run both with STF between flexible electrodes and with ER fluid in the silicon devices. In a deployed application, fluid would likely be sealed inside a desired geometry where the issue of fluid evaporation/oxidation/etc. would be diminished by the protective layers surrounding the fluid. In such a contained environment, properties of the composite could potentially change with temperature, wear, etc. but are likely to reach a steady state such that the performance can be repeatably characterized. This is a topic for future research, beyond the scope of this thesis.

5.4 Shear Thickening Fluid Between Flexible Electrodes

Similar to the motivation behind using the linear stage to test STF-filled foam samples in compression, the desire to test shear thickening fluid in the flexible electrode geometry was seen as a way to extend the capability of an existing piece of hardware. Like the syrup experiments, an attempt was made to "spread" shear thickening fluid onto the stationary electrode, place the top electrode in contact with the fluid pool, and run shear experiments with unconstrained

boundary conditions. Unlike the syrup experiments, however, the STF did not "spread" or coalesce into a pool of uniform height. Nor was it possible to measure the volume of the STF using a plastic syringe. Any exposure to high strain rates (such as drawing the STF into a syringe or attempting to spread the fluid into a thin layer) caused the fluid to harden, making it very difficult to create repeatable samples of STF on the electrodes.

The technique that was used to put STF onto the lower electrode involved dipping a metal spatula into a bottle of shear thickening fluid and pulling a slug of STF from the bottle. By applying the right combination of fast and slow hand movements when pulling the STF slug, it was possible to pull approximately 1-5 mL of fluid onto the spatula. The STF was drizzled onto the lower electrode from the spatula as the fluid began to liquefy in a low strain rate flow under the pull of gravity. Once the fluid had been drizzled onto the electrode, small perturbations were applied with the spatula to spread the STF into an approximation of the uniform rectangular fluid pool created during the syrup experiments. The top electrode was set on top of the fluid pool, where further small perturbations were applied tangential to the flexible electrodes in small left/right shearing motions to allow the fluid to wet both electrodes. This entire process of getting STF in between the electrodes was successful to varying degrees, producing relatively unique samples with varying strain histories.

The volume of the shear thickening fluid on the lower electrode was estimated using the mass and the viscosity of the fluid. The mass of the electrode was measured both before and after the fluid was applied, and the difference in these mass measurements was used as the mass of the STF. The average height of the fluid pool was then estimated using Equation 5.6,

$$h = \frac{m}{\rho w l} \tag{5.6}$$

where ρ is the density of the shear thickening fluid (2.2 g/cm^3), m is the mass of the fluid in grams, and w and l are the width and length of the fluid pool in cm. The estimated height of the fluid was substituted into Equation 5.1 to calculate the instantaneous viscosity of the fluid.

Once the fluid had been weighed and the area of the fluid pool measured, the experiments proceeded like the syrup tests with the top electrode pulled past the bottom electrode in a constant velocity shearing motion. These experiments, in general, produced highly variable

results that were inconsistent from one test to another. Examples of the results from these experiments are shown in Figure 5.4 below. The variability between tests was primarily attributed to the difference between the individual fluid samples used for each test. Differences in the shear history of neighboring particles were thought to lead to localized effects that quickly grew to dominate the net shear force between the electrodes.

<table>
<tr><td>(a)</td><td>(b)</td><td>(c)</td></tr>
</table>
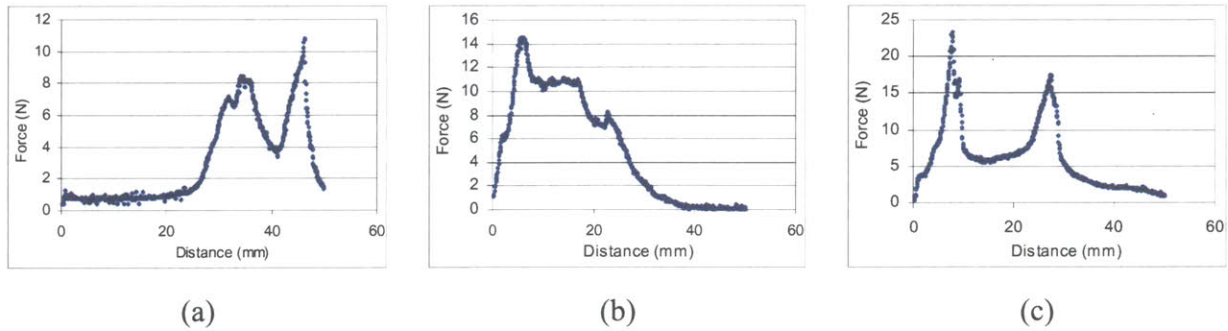
Figure 5.4- Example plots of STF between flexible electrodes, all run at 5 mm/s with similar fluid mass

For example, one area of the fluid on the lower electrode may not have been relaxed as much as the neighboring area and this area of the fluid might tend to harden first under applied shear stress. Such localized bands of hardened fluid were observed to fracture and slide along the surface of the electrode. Great effort in previous research with STF in shear geometries [Bettin, 2004] was taken to match the surface roughness of the shear surfaces with the particle size of the STF particles to prevent the type of surface slip observed in these flexible electrode tests. Future research could attempt something similar with flexible electrodes to improve the repeatability of these tests. The matter was not pursued further in the work reported here.

5.5   Compression Apparatus Experiments

The compression apparatus created to test STF-filled foam was used to test cylindrical foam samples 6-8 mm thick and 7-13 mm in diameter at strain rates as high as 15 s^{-1}. The forces generated in these small samples exceeded the capacity of the small MLP-10 load cell used for shear testing (±10 lbs), and a larger MLP-100 (±100 lb/ ±445 N) force transducer was installed for the compression tests. As discussed in Section 4.4.2, one of the requirements for testing these samples was that they undergo constant strain rate compression. This requirement increased the

complexity in programming the linear stage to produce a changing velocity synchronized with the position of the linear stage.

These experiments were drastically different from either the syrup or STF shear tests in several ways. First, the speed at which the carriage was moving increased from the range of 0-16 mm/s to as high as 120 mm/s (for an 8 mm sample tested at 15 s^{-1}). Second, this high velocity had to be updated rapidly to approximate a continuous exponential velocity decay, instead of the single velocity command given to the GT6K controller for the constant velocity experiments. Third, the issue of "crashing" the linear stage, or commanding the stage to a position beyond the physical limits imposed by the compression fixtures, came into play. Crashing the linear stage could easily damage the force transducer, the fixtures, or the linear stage itself (especially the ballscrew). These issues necessitated a new set of programs and safety measures to protect the linear stage and produce the desired exponential trajectory. Programs based on feed-forward velocity commands, velocity following, and onboard programming of the GT6K were implemented.

5.5.1 Feed-Forward Design

The first successful attempt at generating an exponentially decreasing carriage velocity came in the form of a feed-forward program called "Exponential gutted.vi" shown in Figure 5.5 below. Using a user specified sampling rate in Hz, initial velocity in mm/s, run time, and exponential time constant (sec), the program created an array of command velocities at evenly spaced time intervals. These velocity commands were sent to the GT6K controller over Ethernet one at a time until the array was completed. One limitation of this program was the lack of synchronization of position and velocity. In an ideal constant strain rate compression program, the strain rate should match the corresponding strain (the velocity should match the corresponding position) according to Equation 4.2. The lack of time or position synchronization meant that the distance traveled by the carriage depended on the number of velocity commands in the array, the transmission time of the velocity commands, and other factors.
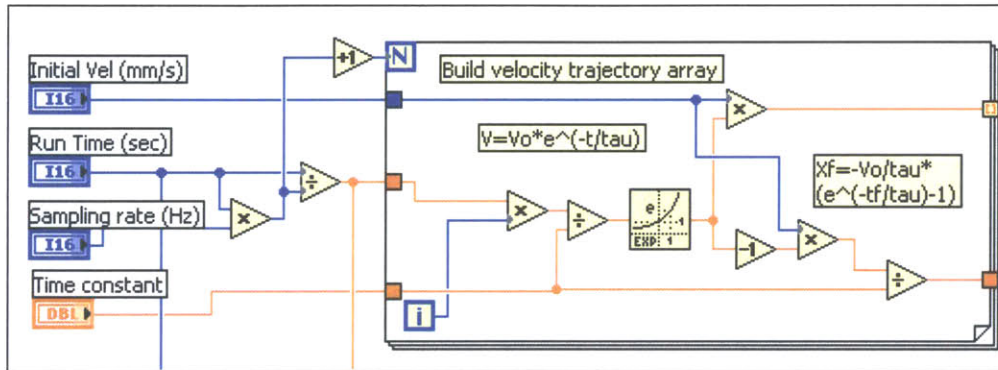
Figure 5.5- LabVIEW for loop used to generate an array of exponentially decreasing velocities

In light of this variable run distance, the feed-forward program was only run in free space, away from the fixed compression plate where it could crash and damage the hardware. The evenly spaced string of velocity changes was a large conceptual jump from the constant velocity commands issued by previous generations of programs. The key to changing the velocity mid-move was to issue a pair of commands before commanding the first nonzero velocity. Once the commands comexc1: and mc1: had been issued, any commands in the form of v10 (where 10 is an example desired command velocity in mm/s) would change the velocity at which the stage was moving. Later tests showed that the time to update this velocity became increasingly important at high velocities.

5.5.2 Compression Experiments

Based on the success of the feed-forward design, a user-friendly version of the feed-forward compression program was implemented with force and position safety features. This program, "CompressionV2.vi", had a force-based position zeroing subroutine, followed by a program break for sample insertion, and a ramp up to the initial velocity before the exponentially decaying velocity profile. The zeroing subroutine gave the program the positional synchronization that was missing in the first program and allowed compression tests to be run in close proximity to the fixed compression surface. The transition from the constant initial velocity (V_0) into exponential velocity decay was triggered when the compression surfaces were separated by the height of the sample. Two parallel loops ran during the exponential velocity decay portion of the compression test. The first loop was programmed to update the velocity of the carriage to the exponential command trajectory. The second loop monitored the force

98

transducer and linear encoder and commanded the stage to stop if either the force exceeded the maximum allowable force or the position exceeded the maximum desired strain.

This advanced program allowed testing of both empty foam samples and samples filled with glycerol or STF. The user first entered several parameters including sample height, maximum allowable force, strain rate, maximum desired strain, and sampling rate. The program then asked the user to manually position the compression plates within 2 mm of each other and hit a "find zero" button. The program found the point at which the force transducer registered contact between the plates and retracted the carriage to the sample height plus enough distance to get the carriage up to speed before contacting the sample. After verifying that the user had inserted the sample via a dialogue box, the program ran through the velocity trajectory generated based on the experimental parameters, collecting data until the maximum desired strain was reached or the force on the transducer exceeded the specified maximum. The results of the experiments run using this program are discussed in Section 6.2.

5.5.3 Update Rate Experiments

The limits of this program were tested and found to be more restrictive than originally anticipated based on the literature and simple experiments with LabVIEW. This unexpected performance prompted an inquiry into the limiting factors of the apparatus. Early experiments showed jumps in the position reported by the GT6K controller that looked like individual steps of the stepper motor at first glance (see Figure 5.6c below). Closer inquiry into the size of the stepper motor steps showed that the microstepping performed by the controller should produce steps of less than 1 μm, whereas these tests showed steps of 12 μm (shown in Figure 5.6b below). The result of the inquiry into this discrepancy, showed that the steps observed in the position array (Figure 5.6a) were not due to microstepping of the motor, but rather to a zero order hold onboard the GT6K that was updated every 11-13 milliseconds.
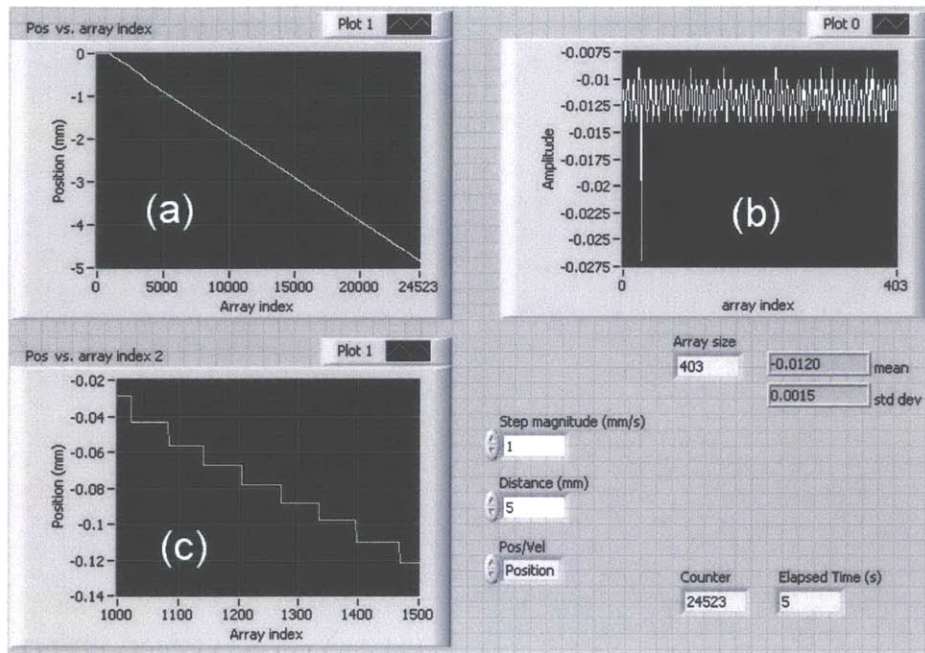
Figure 5.6-Rapid encoder querying after a single velocity command, (a) Position values reported by the GT6K controller for the entire run, (b) height of each step in position shown in (c) a close-up of the position array

All the parameters that could be queried from the GT6K were observed to update every 11-13 ms, and the steps in the position reported by the GT6K were shown to be nearly equal to the carriage velocity multiplied by 11 to 13 milliseconds. An example of this refresh rate can be seen in Figure 5.7 below, where two constant velocity tests were run with the same high sampling rate (16734 samples in 3 seconds, or a LabVIEW sampling rate of around 5000 Hz). The slow velocity test (1 mm/s, shown in Figure 5.7a) had position steps on the order of 10-15 µm, whereas the high velocity test (200 mm/s, shown in Figure 5.7b) had jumps in the reported position of as large at 2.5 mm.
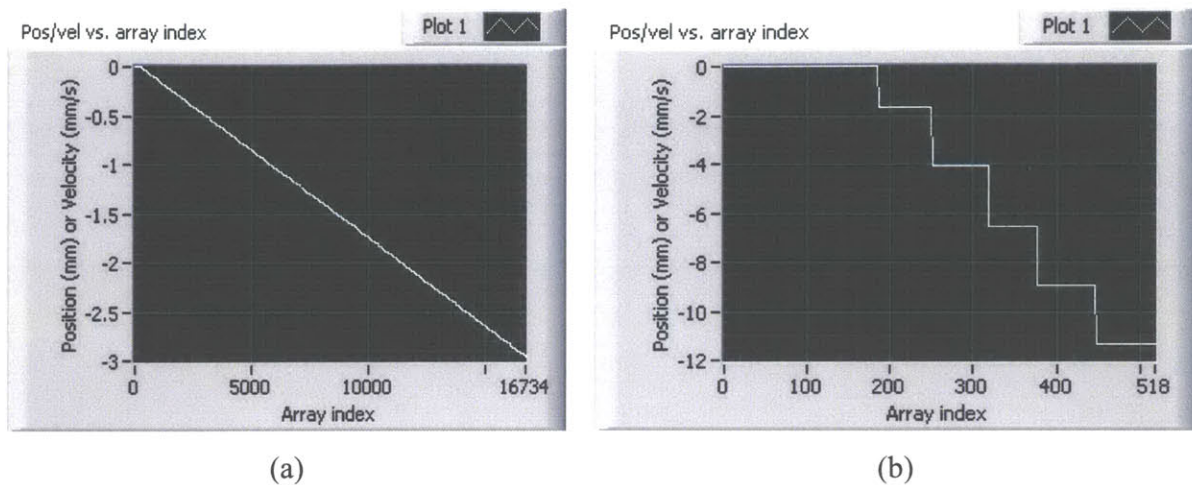
Figure 5.7- Constant velocity tests with (a) 1 mm/s for 3 mm (b) 200 mm/s for 20 mm

5.5.4 GT6K Resident Programs

Given the slow update rate of the position and velocity of the GT6K controller, an alternative was sought to improve the performance of the system. One alternative to communicating with the GT6K over Ethernet was to move the control program onto the GT6K, where motion programs could be stored in a resident programming language for later execution. Other possible solutions included changing the motor to a DC servo (ideal for velocity control and higher speeds), reading the linear encoder directly instead of waiting for the GT6K to update its cache, or implementing a control system without the GT6K at all. The least expensive option was to create programs that could be stored and run directly from the GT6K controller without communication delays or problems with update rates.

A LabVIEW program, "Compiled motion.vi", was written to take the same inputs as earlier compression programs (sample height, maximum strain, strain rate, etc.) and convert the resulting array of desired positions and velocities into a program that could be downloaded onto the GT6K. The format of this program called for the controller to wait until the carriage reached a desired command point, at which point the velocity of the carriage was updated. One such command line was created to read "wait(pc>=10.000); V20.000; go;". After the stage had reached a position greater than 10 mm relative to the start of the move, the velocity was commanded to change to 20 mm/s. Once a GT6K program had been created in LabVIEW and downloaded to the GT6K, "Compiled motion.vi" called the resident program to start the motion and recorded the position and force data output from the GT6K and the load cell. Although this

101

approach did not solve the problem of recording the position data at a rate higher than the refresh rate of the controller's cache, it did vastly improve the performance of the exponential velocity following. The results of the experiments performed using the final compression program are discussed in Section 6.3.

5.5.5 Texture Analyzer and Sample Preparation

Soon after the completion of the GT6K resident programming effort and initial testing of STF-filled foams with these advanced compression programs, the method used to fabricate the foam samples came to the attention of the research group. For years, the cylindrical foam samples were punched from thin sheets of foam using circular punches. These thin sheets were cut from a large block of foam by hand using a razor blade [Bettin, 2004]. The limit to the thinness of the sheet was dictated by the skill of the person with the razor blade and sample thickness was inherently variable.

When this manufacturing process came to light, a superior solution was quickly implemented using a bandsaw to produce the thin foam sheets from which the samples were punched. This technological "leap" allowed much thinner samples to be manufactured with high thickness uniformity across samples. The existence of thinner samples allowed testing to be performed at a lower maximum velocity than previously achievable. For example, the maximum speed in a test with a constant strain rate of 5 s^{-1} dropped from 50 mm/s for a 10 mm thick sample to 25 mm/s for a 5 mm thick sample. The availability of thinner samples allowed significantly higher strain rates to be tested using the Texture Analyzer (discussed in Section 4.4). The Texture Analyzer (TA) had a limited maximum speed, but a higher force and acceleration capability than the linear stage. With lower maximum speeds needed to test STF filled foam samples at the desired strain rates, the data from the TA proved superior to the data from the linear stage in terms of sampling rate, load cell conditioning, user interface, etc., rendering the compression setup on the linear stage obsolete. A comparison of the data from the linear stage and the TA is presented in Sections 6.2.2, 6.2.3, and 6.3. The fact that the TA had been designed to do variable speed compression (and tension) tests directly from the factory made it a superior alternative to the custom compression apparatus.

102

5.6   Blade Flexure Tests

Unlike the sophisticated programs developed for the compression apparatus, tests run with blade flexures used the same, relatively simple LabVIEW programming as the flexible electrode syrup experiments. This program commanded the linear stage to ramp to a constant velocity with the maximum acceleration and hold this velocity until a final position was reached. The program recorded the force output of the force transducer for the duration of the run.
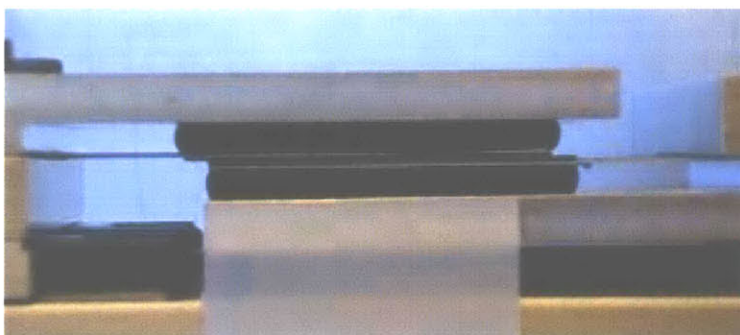
Figure 5.8- Assembled blade flexure fixture with foam preload behind the silicon devices

The hardware setup required for these blade flexure tests was more complicated than either the compression tests or the flexible electrode tests. Each blade was secured between two clamping blocks (shown in Figure 5.8 above) to provide the cantilevered beam boundary condition on which blade flexures were premised. Changing samples required the removal and subsequent reinsertion of eight bolts to remove and replace the stationary and moving blades. The full setup procedure was as follows (provided in list form for readability):

- Position the fixed blade using the alignment features on the lower clamping block
- Secure the fixed blade in the correct position between the two clamping blocks (Figure 5.9)
- Move the carriage into the preload calibration position
- Align and secure the moving blade (Figure 5.10)
- Adjust the preload of the blades by bending the blades (Figure 5.11)
- Unclamp and remove the moving blade
- Move the carriage into the overlapped position (Figure 5.12)
- Apply ER fluid (if required) (Figure 5.13)
- Align and secure the moving blade (now in contact with the lower blade) (Figure 5.14)
- Attach alligator clips
- Turn on electric field (if required)
- Run constant velocity program and record the shear force until completion

- Turn off electric field
- Remove alligator clips
- Unclamp both blades
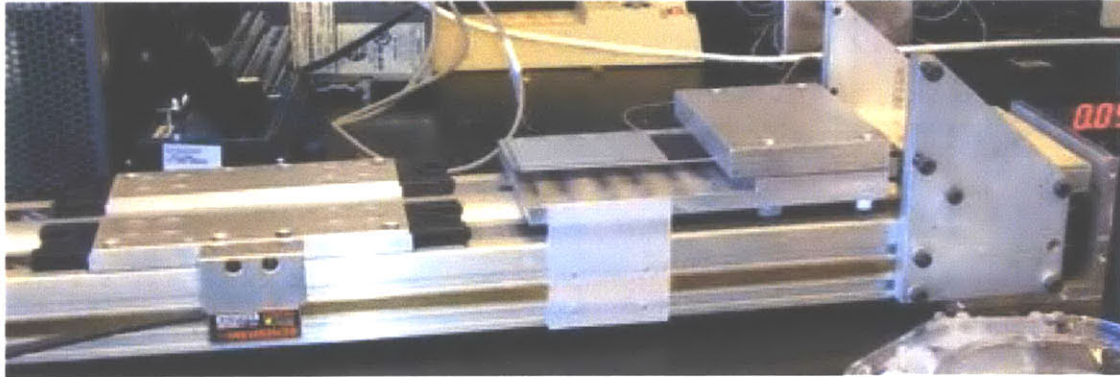
Figure 5.9- The fixed blade was clamped between two blocks and bolted to the fixed end
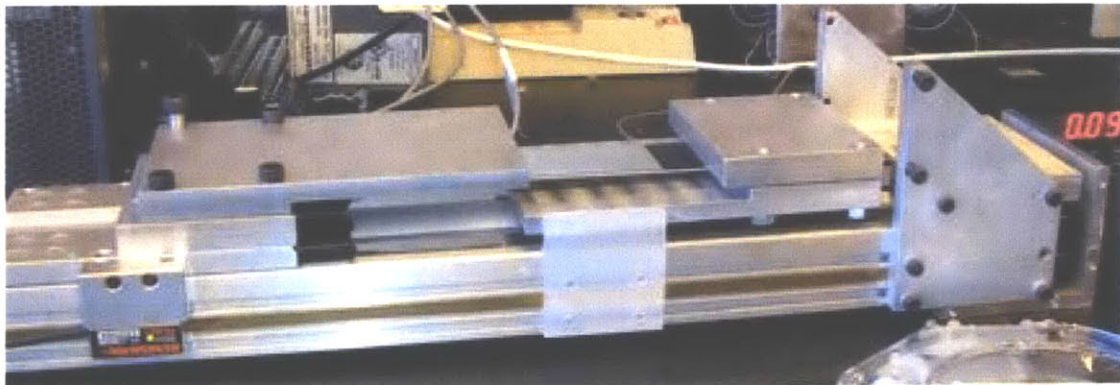
Figure 5.10- The moving blade was clamped to the carriage of the linear stage and the blades were aligned
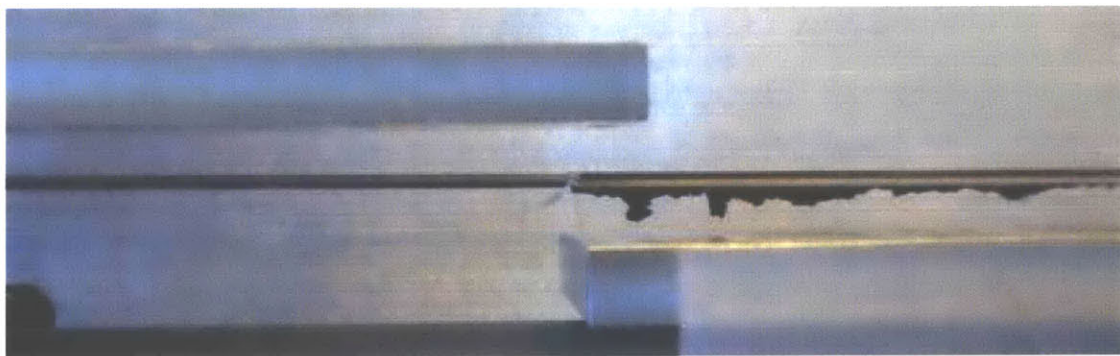
Figure 5.11- Close-up of the alignment position for the opposing blades
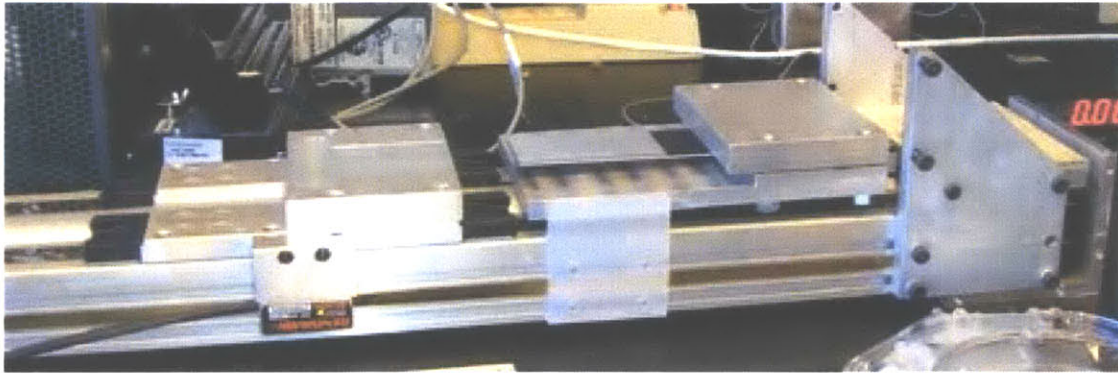
Figure 5.12- The moving blade was removed and the carriage was moved into position

Figure 5.13- ER fluid was injected onto the chip (subsequently spread with a spatula/squeegee)
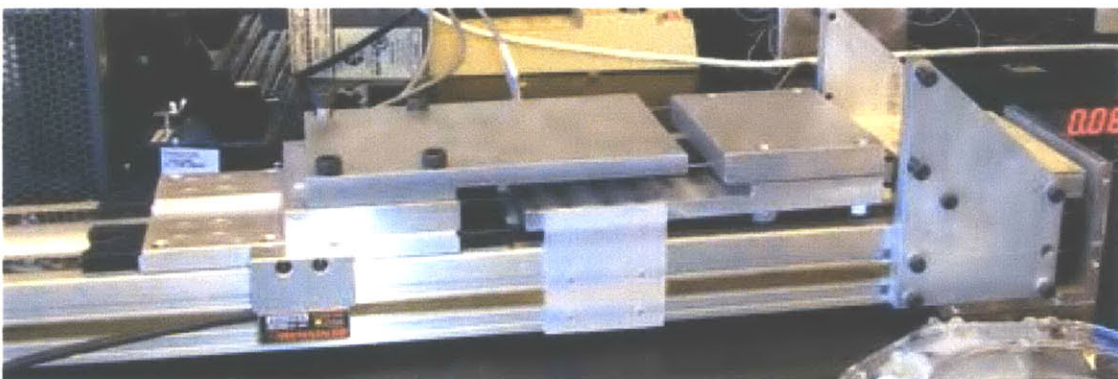
Figure 5.14- The moving blade was clamped into position in contact with the fixed blade
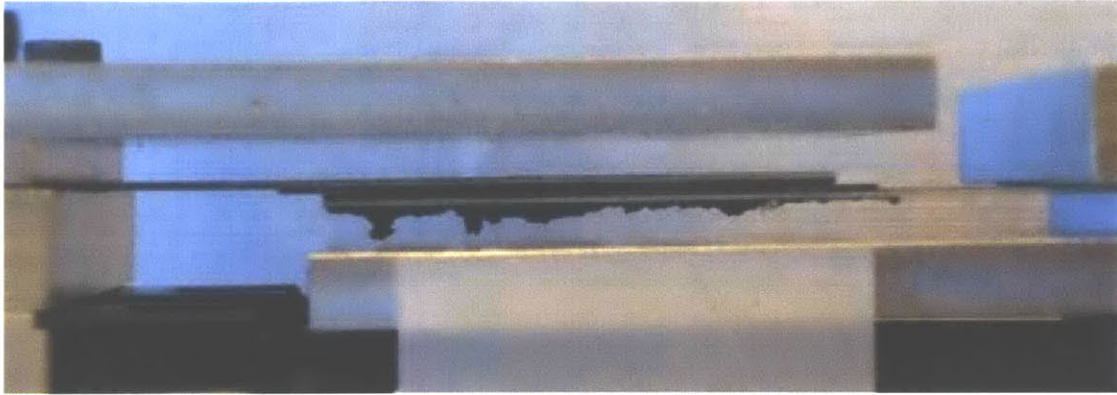
Figure 5.15- Blades in contact with a noticeable preload

Figure 5.16- ER fluid left on the moving blade after an experiment

Figure 5.8 above shows the blade flexures backed with foam. Without the foam in place, the aluminum overhangs shown in many of the figures here are unnecessary, and future hardware revisions to this setup could remove them for the sake of weight and simplicity. The black residue on the back of the lower blade in Figure 5.11 and Figure 5.15 is part of the foam that could not be removed from the blade after the majority was removed. Other blades did not come with this "extra" feature.

If the tests were run back-to-back without changing the devices, the alternate procedure was to pull the blades apart vertically at the end of a run (illustrated by Figure 5.16 above), drive the carriage back into the starting/overlapped position, let the blades come back into contact and run the next experiment from here. The problem with this approach was that pulling the devices apart and putting them back together was observed to introduce tiny bubbles. The high viscosity of homogeneous ER fluid prevented bubbles from working their way out of the channels. The

presence of these bubbles may have had an unaccounted for effect on the measured shear force, but there was no way to discern what portion of the change in shear force was due to bubbles. The bubbles may have introduced an uncontrolled source of variability into the data, but quantifying their presence, amount, and effect was neglected for the first round of experiments.

A variation on this test-reload-test setup was to simply drive the carriage back into the starting position once a run had been concluded. This procedure did not introduce any bubbles in between the devices, but as the wafers pushed past each other, there were no features designed to compress the fluid exposed to the atmosphere back into the channels. Like pushing a putty knife instead of pulling it, the edges of the advancing wafers pushed any fluid above the channel surface back to the starting position. In some experiments, this scraping effect was intentionally used to remove all the fluid outside of the channels. This led to increased electrical shorting in some devices, and the preferred method of testing was to pull the devices apart at the end of a run, move the carriage back into the starting position and run the next test. The best method in terms of eliminating bubbles and minimizing electrical shorting, although most work-intensive and wasteful of ER fluid, was to unload the blades, rinse off the old ER fluid with acetone, and reload the devices using new ER fluid.

5.7   Homogeneous ER Fluid Contact Angle

Experiments were performed before the first batch of silicon wafers were completed to ensure that homogeneous ER fluid wet the surface of silicon, oxide, and aluminum. These experiments were run on a VCA-2000 (video contact angle) Contact Angle Surface Analysis System by AST Products, Inc. The experimental procedure for these tests was relatively simple. First, a sample of ER fluid was drawn into a special syringe purchased specifically to fit the VCA-2000 system. A 90 degree bent needle was inserted onto the end of the syringe and the syringe was loaded into the VCA system. A sample of the substrate in question was then loaded onto the adjustable viewing stage and a drop of the ER fluid was dropped onto the surface from the syringe. The brightness and contrast of the computer output of the VCA software were adjusted and a snapshot of the droplet was taken. With the push of a button, the VCA software determined the contact angle of the droplet, which was recorded for later analysis. The results of these tests are given in Section 6.6, but the homogeneous ER fluid was shown to wet all three types of substrate.

5.8 Resistance Testing and Process Change

The results of the resistance tests performed using devices from the prototype wafer batch are discussed in Section 6.5. One of the results that introduced a significant change to the device design and process plan was the low resistance between opposing electrodes in contact both with and without ER fluid. This low resistance precluded the use of high enough electric fields to activate the ER effect and required that an insulating layer be added somewhere in the device geometry to stop the flow of current through the risers and between chips.

The experimental procedure for these tests was simply to measure the resistance between two points on the same device, between points on a device and the attached blade, or between devices in contact (with and without ER fluid). The low resistances measured in these experiments prompted a calculation of the theoretical resistance of the devices, and inspired subsequent addition of a 1 μm thick insulating layer of SiO_2 on top of the risers to dramatically increase the resistance between devices.

5.9 Microfabrication Process Experiments

5.9.1 Photolithography Recipes

5.9.1.1 OCG 825 Thin Resist

Experiments were run to find a working recipe for the application of thin resist (OCG 825) to a blank silicon wafer. The standard recipe produced poor results in several instances where wafers were irreparably burned in places the resist was supposed to protect in the STS2 or in instances where the resist didn't adhere to the substrate. The procedure usually involved an application of HDMS recipe 5 (10 sec HMDS exposure, 30 min run time), varying the coater spin speeds and times, 30 min softbake, exposure in the EV1, and development. When these steps produced consistent coverage and good resist coverage, they were processed in the STS2 where any defects were etched into the silicon. Enough of these experiments failed that a more robust resist, thick resist AZP4620, was used to replace the thin OCG 825 resist. The result of these experiments was a working process, described in Section 4.6.4.

5.9.1.2 AZP4620 Thick Resist

Experiments were run using several AZP4620 thick resist recipes before a working result was found. Early experiments began by finding the right combination of speed and time to give uniform coverage of the wafer without dry spots or excessive buildup of resist in device corners. These experiments produced more robust results than the thin resist experiments, although unintentional resist liftoff remained a problem with some of the processed wafers until the HDMS step was improved. Use of thick resist for the second photolithography pass (coating a 3D surface with deep channels) was much more challenging and required extensive experimentation to get a recipe that coated the bottom of the channels somewhat uniformly. Again, these experiments involved passing wafers through the process plan until a failure occurred, stripping away steps back to a stable wafer state (or throwing the wafer away where the failure was irreversible), and reiterating the process with slightly different parameters. The result of these experiments was a working process, described in Section 4.6.4.

5.9.1.3 AZ5214 Image Reversal

When the diagonal channel and dot array device geometries were introduced, a plan to use a single mask instead of the two used in the original process plan was instituted. This change required the use of image reversal resist and the same mask used in the first photolithography pass (used to define the channels) to leave resist in the bottom of the channels instead of removing resist over the channels. The test wafers were run through the process designed with the help of MTL staff until failures were recorded, at which point the cycle of inspect, strip, restart began anew. The result of these experiments was a working process, described in Section 4.6.17.

5.9.2 DRIE Depth Characterization

Experiments were also run to characterize the etch depth of the STS2 deep reactive ion etching (DRIE) tool using two etch recipes. Etch depth measurements were taken at various points across each wafer for all three device geometries with different combinations of continuous and cumulative etch time. Depths were measured using the interference optics on a Nikon inspection microscope after processing in the DRIE, but before the photoresist was stripped from the wafers. Results from these experiments are presented in Section 6.8 with tolerances of ± 0.5 μm

where the data reveals etch depths that were not uniform across the wafer surface. The etch depth was observed to increase at the edge of the wafer where the reaction temperature may have been higher in the region of the wafer chuck. The back side of every wafer was cooled with helium impinging on the center of the wafer, but the helium could not cool the edge of the wafer covered by the wafer chuck. Combined with local competition for etch gasses, this temperature gradient may have led to the "edge-fast" etch depth profile presented in Section 6.8.

Chapter 6

Results

6.1 Flexible Electrode Characterization and Baseline Calibration

6.1.1 Syrup Tests with Reused Samples

As discussed in Section 5.3, one important result from the baseline characterization of the flexible electrode setup indicated that the number of tests performed on a single fluid sample could have a pronounced effect on the measured properties of the sample. This result is illustrated by Figure 6.1 below, where the calculated viscosity of a reused sample of syrup is shown to increase linearly with the number of tests performed using the sample. The first test in this series produced a viscosity of 19.3 Pa-s, within the bounds of the actual 20±1 Pa-s measured using a conventional rheometer. Possible explanations for the increasing viscosity are discussed in Section 5.3.
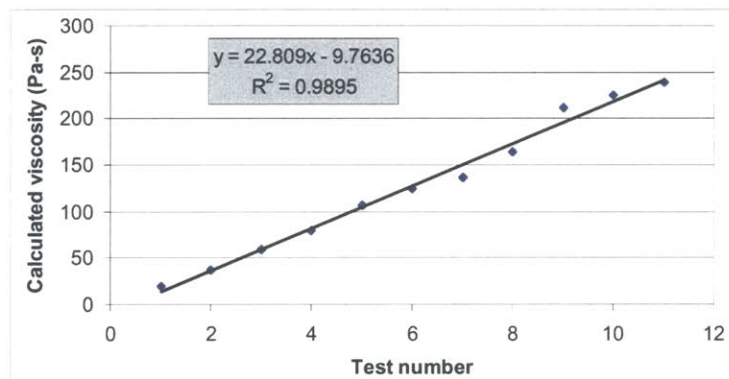
Figure 6.1- Measured viscosity versus number of reuses of syrup sample

6.1.2 Syrup Tests with Fresh Samples

A battery of tests was run using a new syrup sample for each test. To test the assumption that the syrup was a Newtonian fluid, these tests were performed across a range of linear velocities

(strain rates). For a given fluid volume and corresponding fluid pool height, increasing velocity leads to linearly increasing strain rate. Newtonian fluids exhibit a constant viscosity across strain rates, and a deviation from this is considered non-Newtonian behavior. The results of these "fresh" syrup tests are summarized in Table 6.1 below. Table 6.1a displays the test results in the order that they were taken, showing the velocity and corresponding viscosity calculated using Equation 5.4. Table 6.1b summarizes the test results by the velocity used in each test, and shows the average viscosity for all tests performed at one velocity. The average viscosity of all 19 fluid samples was 23.2 Pa-s, higher than the viscosity measured using a conventional rheometer.

Table 6.1- Measured viscosity for fresh syrup test grouped by (a) day, and (b) velocity

(a)

Date	Test #	Velocity (mm/s)	Viscosity (Pa-s)
1/13/2005	1	5	19.3
1/14/2005	1	5	19.1
	2	5	21.1
	3	10	19.9
	4	10	17.3
	5	20	15.4
	6	20	15.6
1/31/2005	1	2	30.1
	2	2	35.2
	3	2	29.5
	4	5	23.9
	5	5	25.4
	6	5	28.6
	7	10	21.2
	8	10	21.0
	9	10	19.0
	10	20	20.0
	11	20	20.4
	12	20	21.0

(b)

Velocity (mm/s)	Viscosity (Pa-s)	Average viscosity
2	30.1	31.6
	35.2	
	29.5	
5	19.3	22.9
	19.1	
	21.1	
	23.9	
	25.4	
	28.6	
10	19.9	19.7
	17.3	
	21.2	
	21.0	
	19.0	
20	15.4	18.5
	15.6	
	20.0	
	20.4	
	21.0	

Average viscosities calculated for tests performed at a given velocity showed wide variation. While tests performed at 10 mm/s produced viscosities within 3 Pa-s of the actual 20 Pa-s, tests performed at 2 mm/s produced viscosities as high as 35 Pa-s. This variation is indicative of non-Newtonian behavior, and Figure 6.2 and Figure 6.3 below elaborate on this trend by displaying the calculated viscosity of fresh syrup samples against test number and grouped by velocity. Figure 6.2 does not show the same linear increase of viscosity as Figure 6.1

above, possibly due to the use of fresh samples with every test, but reflects variability in the calculated viscosity that was not expected to occur in a Newtonian fluid.
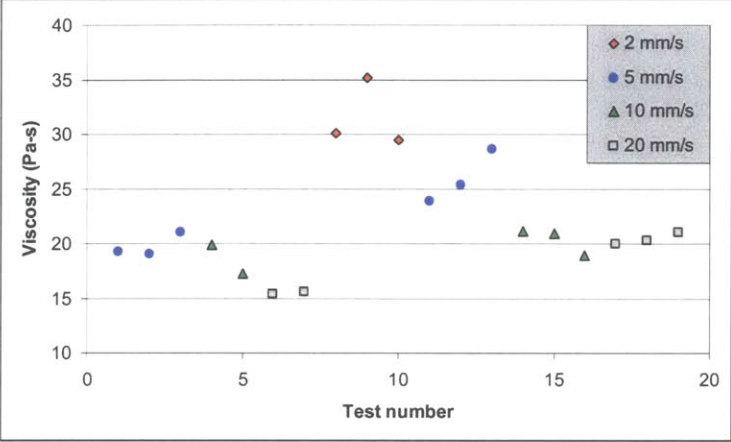
Figure 6.2- Viscosity versus test number for fresh syrup tests

6.1.3 Non-Newtonian, Rate Dependent Viscosity

Figure 6.3 below addresses the issue of changing viscosity over different strain rates directly by plotting the viscosity vs. velocity for each test along with the average viscosity for all the tests performed at each velocity. The average viscosity tends toward the actual 20 Pa-s with increasing velocity, but the figure shows a variability that should not exist in a standard Newtonian fluid. This variation could be attributed to variation in the fluid pool height at different velocities, but the arguments used to explain the linearly increasing fluid viscosity with test number (temperature, time and fluid composition in Section 5.3) do not readily apply in this case. Conclusive determination of the specific properties of this fluid is beyond the scope of this thesis and is left for future work.

113
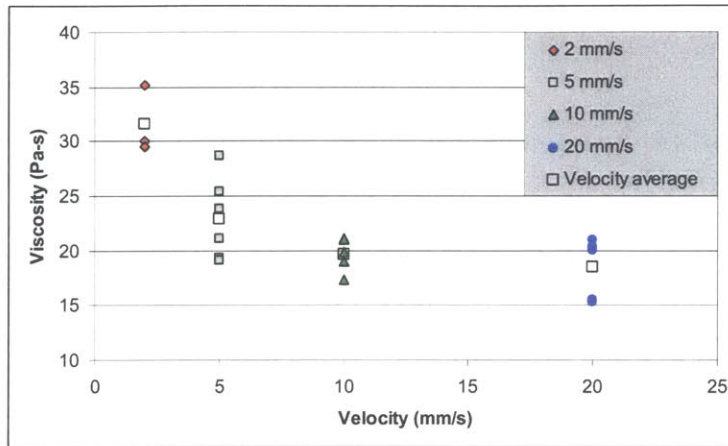
Figure 6.3- Viscosity versus velocity for all fresh syrup tests showing rate-dependent viscosity

6.1.4 Signal to Noise Ratio

One result observed in many of the experiments performed using the linear stage, not only the syrup tests, was a correlation between linear stage velocity and the signal to noise ratio of the recorded force data. As the linear carriage velocity increased, the noise visible in a force vs. displacement plot appeared to decrease significantly. Figure 6.4 below shows four syrup tests that are representative of this effect.
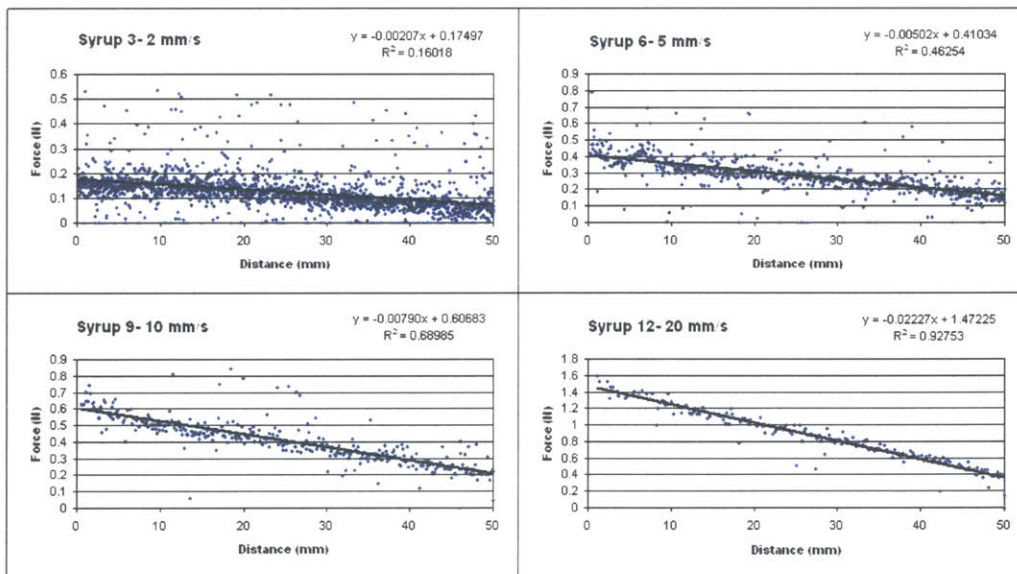
Figure 6.4- Syrup shear tests at 2, 5, 10, and 20 mm/s

The four tests shown in Figure 6.4 were run at 2, 5, 10, and 20 mm/s and are all from the same batch of tests. One indicator of the amount of noise found in each test is the root mean square (RMS) of the residuals from the least squares trend line fit to the data. The RMS of the residuals increased from a low 0.069 at 2 mm/s to a high of 0.095 at 20 mm/s as shown in Figure 6.5a below, matching the upward trend introduced in previous noise characterization for this system [Eastman, p. 58]. The fact that the data was actually getting noisier was masked by the increasing magnitude of the signal. A simple measure for the magnitude of this increasing signal magnitude is the average force over a test. The signal to noise ratio (S/N) was calculated using the average force and the RMS of the residuals (shown in Figure 6.5 below), showing an increasing S/N with increasing velocity. As discussed in Section 6.4, the S/N also increased with increased normal force between shear surfaces.

(a)	(b)
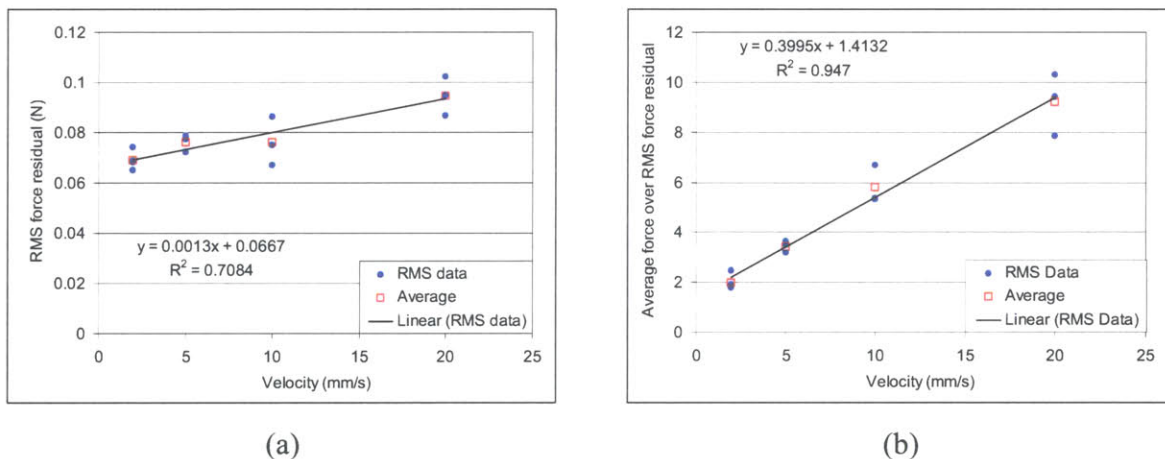
Figure 6.5- Plots of (a) RMS of force residuals and (b) ratio of average force to RMS force residual

6.2 Compression Apparatus Experiments

6.2.1 Empty Foam

Constant strain rate compression experiments were run using the new compression apparatus and testing procedure described in Sections 5.5.2. Results from compression tests run on empty open-cell reticulated foam at constant strain rates of 0.5, 1, 2, and 4 s^{-1} are shown in Figure 6.6 below.

The raw data from these tests were recorded as force and displacement, which was transformed into stress and strain shown in the figure using the diameter of the cylindrical foam sample.

(a) Strain rate = 0.5 s^{-1}

(b) Strain rate = 1 s^{-1}

(c) Strain rate = 2 s^{-1}
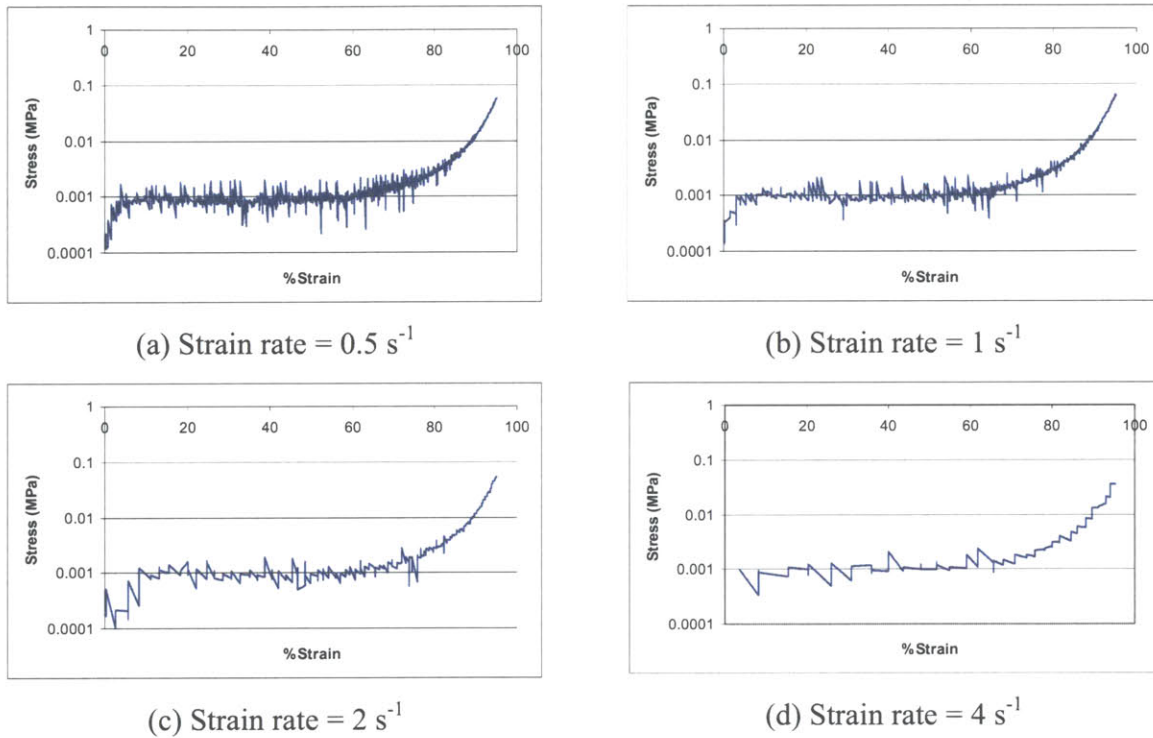
(d) Strain rate = 4 s^{-1}

Figure 6.6- Raw compression data from empty foam samples at strain rates 0.5, 1, 2, and 4 s^{-1}

The stress-strain traces for tests at each of the four strain rates shown in Figure 6.6 are similar. The test run at 4 s^{-1} is rough compared to the test at 0.5 s^{-1} due to the limited sampling rate of the compression apparatus. All four tests show the same general trend including an increasing stress at low strain up to a plateau from strains of approximately 10 to 60 percent, followed by another rise in stress above 60 percent strain. This trend matches the idealized patterns shown in Figure 6.7 below for compression of an elastomeric foam.
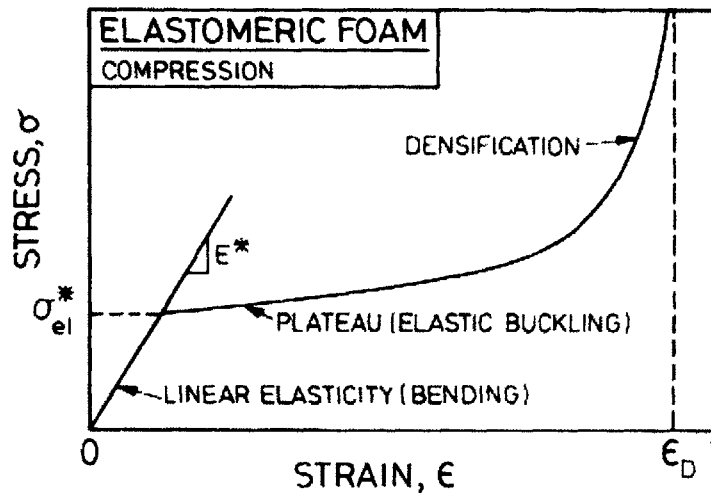
Figure 6.7- Compression of elastomeric foam [Gibson, 1988]

The physical phenomena governing the behavior in each of the three regions of strain are illustrated in Figure 6.7 above. The first region, linear elasticity, occurs when the cell walls of the foam elastically bend. This region transitions into elastic buckling as the cell walls exceed their buckling strength. The elastic buckling region represents the largest area of energy absorption in the compression of open cell foams as individual cells throughout the foam buckle. At some point in the compression, the walls of the buckled cells start to interfere with one another and the foam enters the densification region of compression, where the stress approaches that found in a solid sample of the foam material.

The data in Figure 6.6 above reports several values of stress for an individual value of strain, an effect of sampling the position cache of the GT6K controller at a higher rate than it was updated (12 ms update rate for GT6K cache, 2 ms sampling time). This oversampling resulted in several force readings from the continuous force signal between updates of the GT6K cache. The data in Figure 6.8 and Figure 6.9 below were "filtered" by averaging all the force data points reported at a single position and show similar plateau stresses and transition points from elastic buckling to densification. The primary differences between the results of the four tests are a slight difference in the bending modulus (E*) and the transition from linear elasticity to elastic buckling. Figure 6.8d, for example, indicates a low bending modulus and a transition to elastic buckling around 12 percent strain, whereas Figure 6.8a indicates a high modulus and a transition

to elastic bending around 8 percent strain. The disparity is likely caused by the decreasing quality of the data at low strain where the velocity of the linear carriage is highest.

(a) Strain rate = 0.5 s^{-1}

(b) Strain rate = 1 s^{-1}

(c) Strain rate = 2 s^{-1}
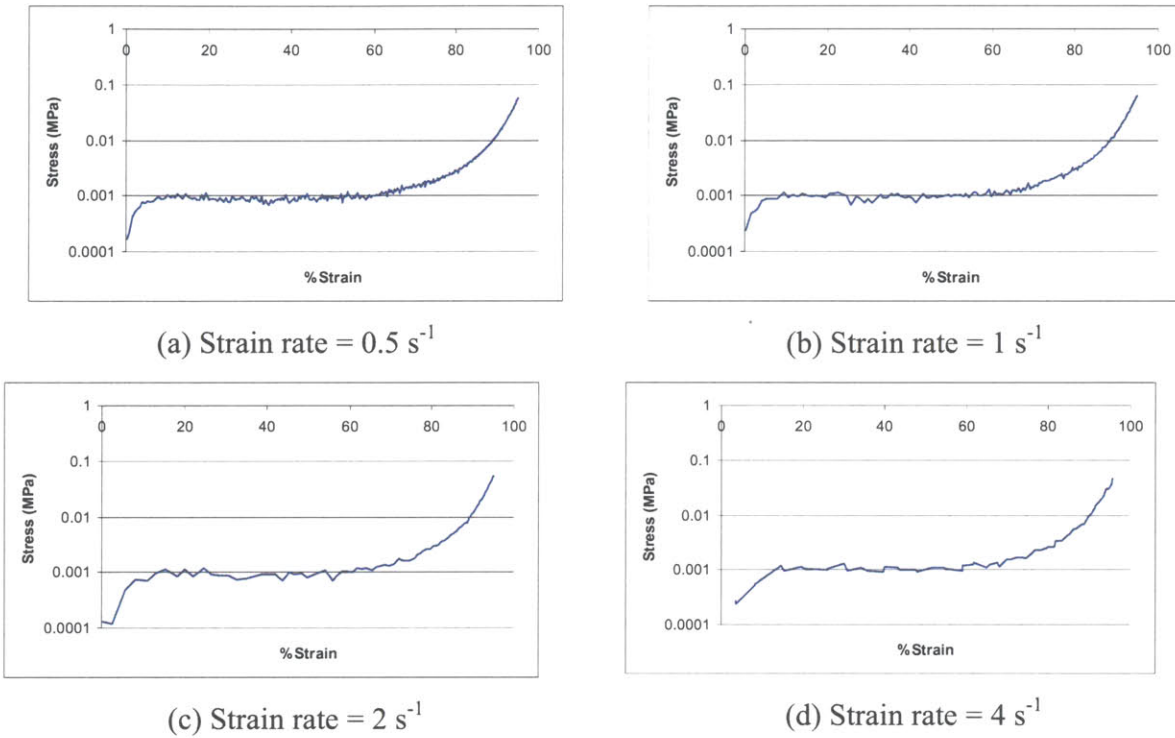
(d) Strain rate = 4 s^{-1}

Figure 6.8- Empty foam in compression at strain rates 0.5, 1, 2, and 4 s^{-1} (filtered)

The data shown in the 4 s^{-1} strain rate plot above is the combination of data points from two consecutive compression tests, done to increase the number of data points in the linear elasticity range of the tests where the compression stage was at its maximum velocity and minimum sample density (samples/mm). Despite this combination, there are only seven data points below 20% strain in the 4 s^{-1} plot, compared to the eight points shown in the 2 s^{-1} test or the sixteen in the 1 s^{-1} test. Figure 6.9 below superimposes the four strain rates for closer comparison. There is a small amount of variation in the plateau stress between the tests (shown below in Table 6.2), and the data taken at the maximum stage speed is sparse for the high strain rate tests. Otherwise, the results appear the same for all of the compression rates.
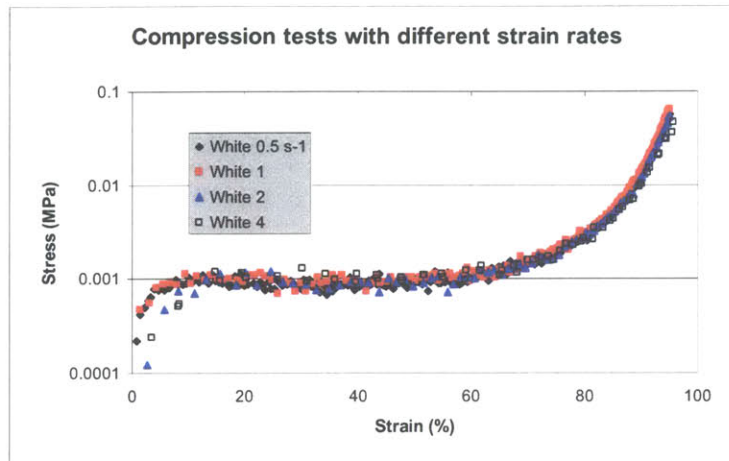
Figure 6.9- Superimposed stress data from empty foam tests

The average plateau stress for the four strain rate compression tests is displayed in Table 6.2 below. The value of the plateau stress was calculated by averaging the values of stress over the range of strains from 20 to 60 percent. Although a slight increase is observed in the average plateau stress with increasing strain rate, the increase is less than the observed noise in each of the tests.

Table 6.2- Average plateau stress for empty foam compression at four strain rates

	0.5 s^{-1}	1 s^{-1}	2 s^{-1}	4 s^{-1}
Average plateau stress (20-60% strain)	0.000906	0.000990	0.000927	0.001061

In comparison with earlier results published for constant strain rate compression of empty foam [Bettin, 2004] the results in Figure 6.9 above are similar to those shown in Figure 6.10 below. The primary difference in the earlier results is a higher plateau stress, which may be due to a difference in the bulk material properties of the foam constituent. The samples of foam tested in this thesis were given without specification of material, cell density, etc. The size of the samples used to determine the stress-strain response of the polyurethane foam in Figure 6.10 below (relative density of 0.03 and ES = 70MPa) was not reported, preventing a quantitative comparison.

119
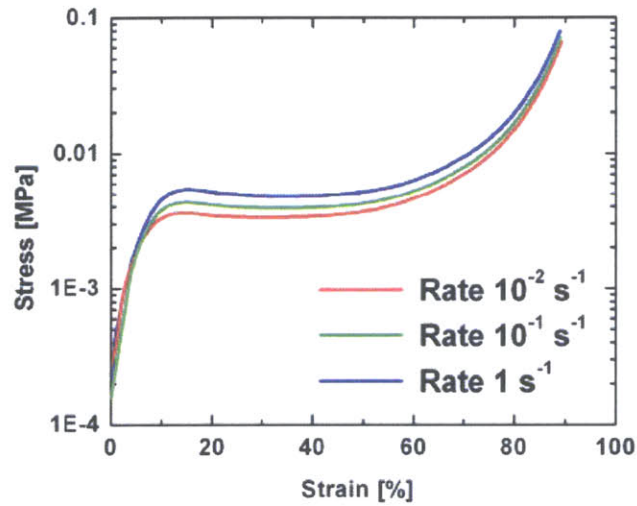
Figure 6.10- Empty foam test results [Bettin, 2004]

6.2.2 Glycerol-Filled Foam

Further tests were performed to extend the range of strain rates used in glycerol-filled and STF-filled foam compression tests. Previous research tested these types of samples up to a strain rate of 1 s^{-1}, while this research attempted strain rates as high as 15 s^{-1} for glycerol-filled foams and 10 s^{-1} for STF-filled foams. Figure 6.11 below shows the results of four compression tests on samples of glycerol-filled foam at strain rates of 1, 5, 10, and 15 s^{-1}. Once again, the slow 12 ms update rate of the GT6K controller can be seen in the higher strain rate plots, as well as the lower spatial sampling rate at low values of strain where the velocity of the carriage is highest.

(a) Strain rate = 1 s^{-1}

(b) Strain rate = 5 s^{-1}

(c) Strain rate = 10 s^{-1}
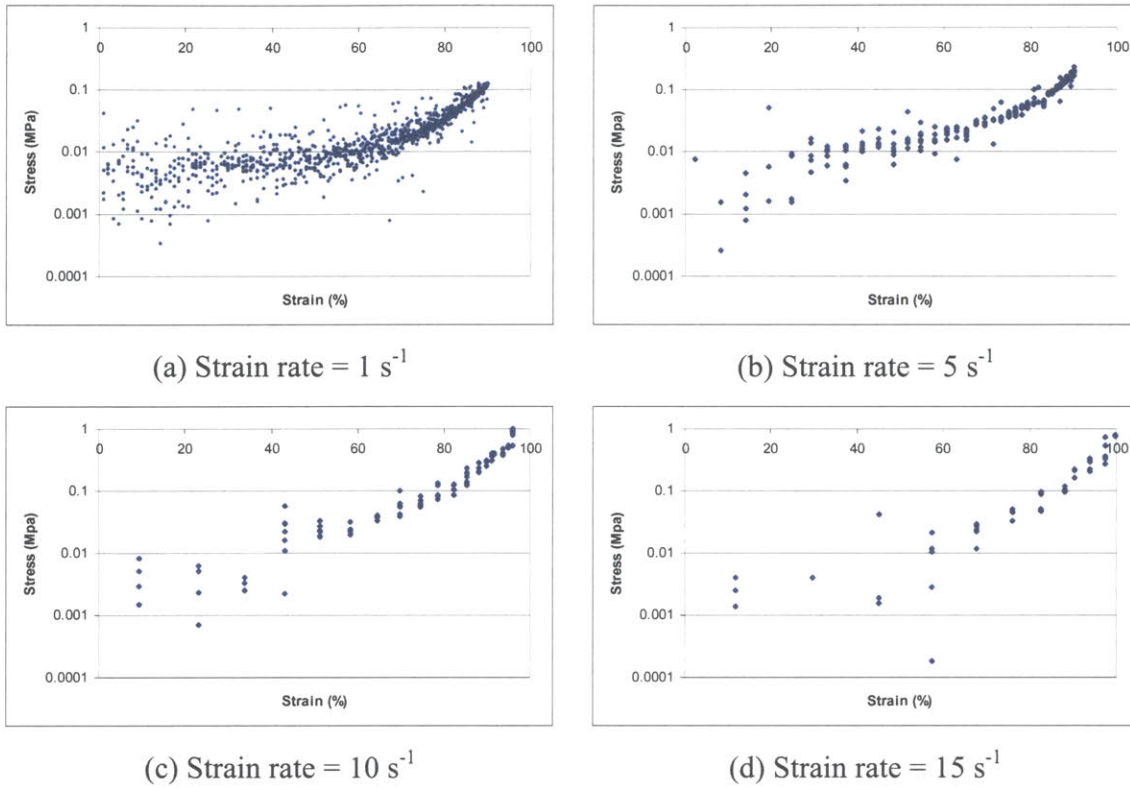
(d) Strain rate = 15 s^{-1}

Figure 6.11- Glycerol-filled foam in compression at strain rates 1, 5, 10, and 15 s^{-1}

These new results superimposed in Figure 6.12a below compare well with previous results at lower strain rates shown in Figure 6.12b below, although the resolution of the force transducer and data acquisition system used to obtain the new results did not allow the force at low strains to be measured as thoroughly. The tests performed at higher strain rates continued the upward trend in the stress seen in Figure 6.12b, with maximum stresses of 1 MPa seen in both the 10 s^{-1} and 15 $^{-1}$ compression tests.

(a)   (b)
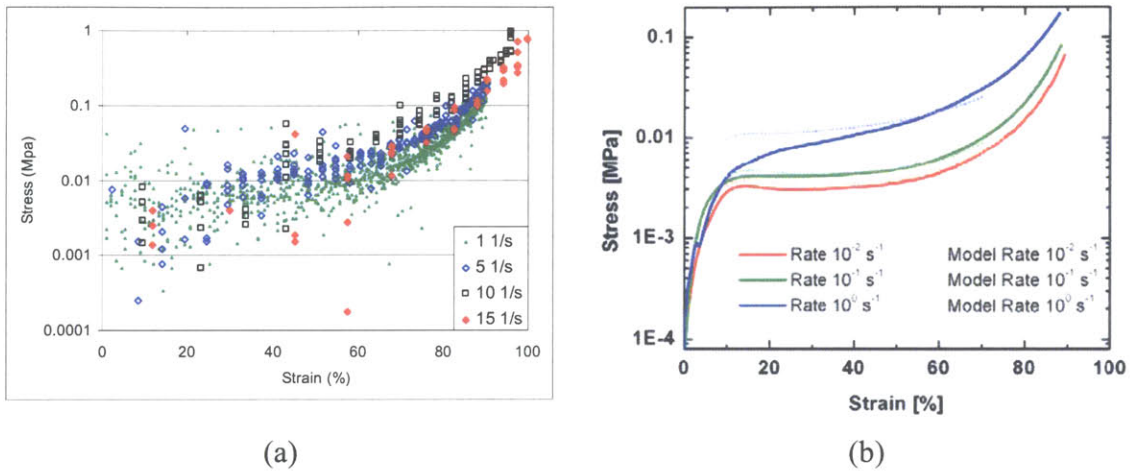
Figure 6.12- Glycerol-filled foam in compression at (a) 1, 5, 10, and 15 s^{-1} and (b) 0.01, 0.1, and 1 s^{-1} [Bettin, 2004]

6.2.3 Shear Thickening Fluid-Filled Foam

Several sets of experiments were run to test STF-filled foam in the new compression apparatus. The results of one set of tests is shown in Figure 6.13 below. These data were taken using a compression program run from a host PC that sent commands to the GT6K motor controller via Ethernet. The update rate limitation discussed in Section 5.5.3 led to performance limitations at high speed, as shown in Figure 6.13b and Figure 6.13c. As shown in Figure 6.13c, the linear stage became unstable at values of strain as low as 10 percent, possibly due to mechanical limits or time delay in the feedback loop.

(a) Strain rate = 1 s⁻¹

(b) Strain rate = 10 s⁻¹

(c) Strain rate = 10 s⁻¹ close-up
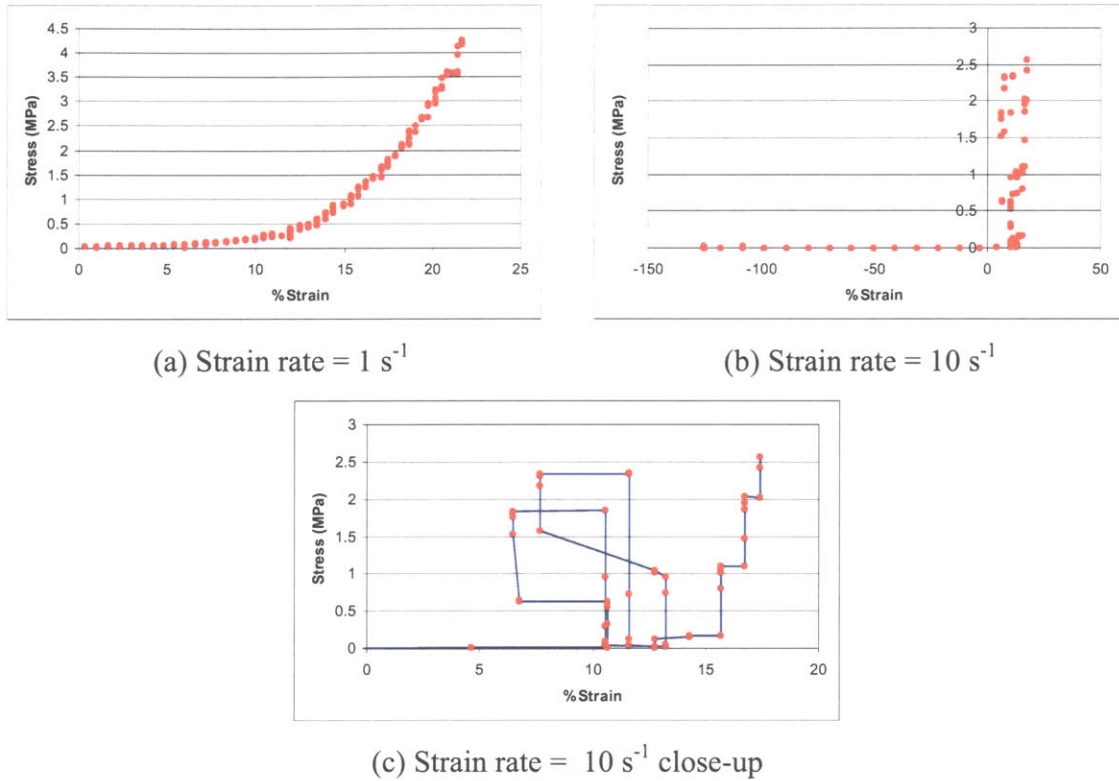
Figure 6.13- STF-filled foam compression tests at 1 and 10 s⁻¹

6.3 GT6K Resident Programs

The speed capacity of the linear stage was increased by about five times by programming the GT6K controller directly, bypassing the need for control commands to be sent over Ethernet before they were executed. The following data also used a new method of sample preparation which increased the uniformity across samples by using a bandsaw instead of a razor blade to cut the sheet from which the samples were punched. After a sheet of foam was cut from the large block of foam, the samples were individually punched from the sheet with a punch set containing several punch sizes.

Three experiments were run using the resident programming on the GT6K to test STF-filled foam at strain rates of 1, 5, and 10 s⁻¹. STF-filled foam tests were more challenging than empty foam or glycerol-filled foam, requiring higher force/speed capacity than other tests. In addition, filling the foam samples with STF was more complicated and variable than the

123

preparation of other types of samples. Plots of STF-filled foam compression tests at three strain rates (1, 5, and 10 s^{-1}) are shown in Figure 6.14a-f on both linear and logarithmic axes. Comparing the results in Figure 6.13a above with Figure 6.14a below, the increase in number of samples per unit strain using the new control program can be seen, as well as the increased force and strain stability of the apparatus indicated in Figure 6.14e and f.

(a) Strain rate = 1 s^{-1} (b) Strain rate = 1 s^{-1}

(c) Strain rate = 5 s^{-1} (d) Strain rate = 5 s^{-1}

(e) Strain rate = 10 s^{-1} (f) Strain rate = 10 s^{-1}
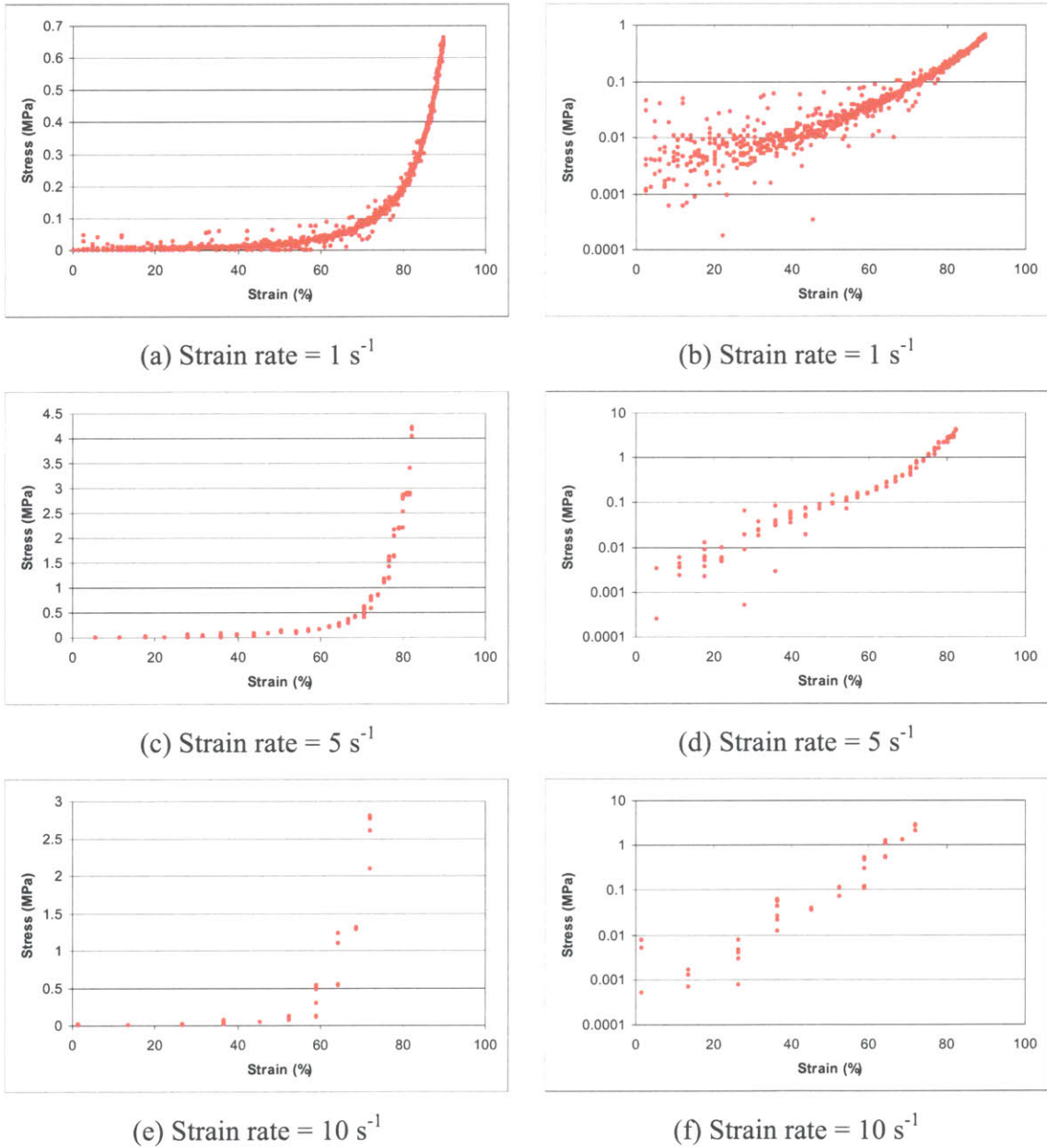
Figure 6.14- STF-filled foam compressed at 1, 5, and 10 s^{-1} using GT6K resident programming

With increasing strain rate, the magnitude of the stress in the STF compression tests increased for a given strain. The stress at 70% strain, for example, increases from 91 kPa in Figure 6.14a, to 590 kPa in (b), to 2800 kPa in (c). Comparing the new data to the data taken from the texture analyzer (shown in Figure 6.15) is difficult due to the different strengths of the two testing platforms. The Texture Analyzer, with a lower force capability and higher force resolution, gave detailed data on compression at low strains (less than 30 percent strain for a test at a strain rate of 1 s^{-1}), and no data at high strain. Conversely, the linear stage compression apparatus gave more complete data at high strain where the high force capability and low speed requirement were more suited to the test platform. The overlap in the data, namely the test at a strain rate of 1 s^{-1}, appears to be two orders of magnitude higher at a strain of 30 percent in the data from the Texture Analyzer (0.4 MPa vs. 0.007 MPa).

(a)   (b)
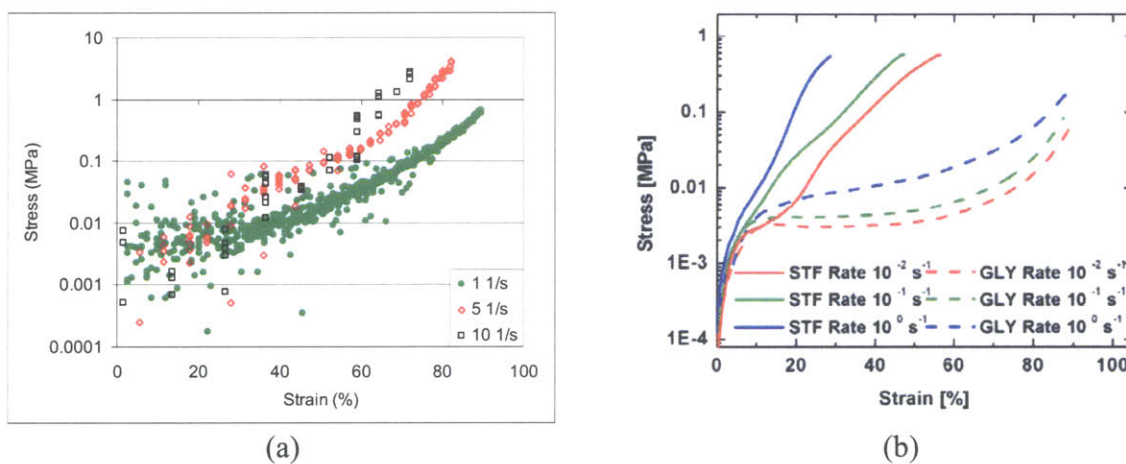
Figure 6.15- STF-filled foam in compression at (a) 1, 5, and 10 s^{-1} and (b) 0.01, 0.1, and 1 s^{-1} [Bettin, 2004]

A maximum stable strain of 72 percent was achieved by the resident GT6K programs at 10 s^{-1}, where the previous tests achieved a maximum of 12 percent. The system instability is shown in Figure 6.16 below where the strain was observed to increase to a point and rebound. Possible reasons for this breakdown include the test exceeding the mechanical limits of the stepper motor, the driver reaching the desired position and releasing the holding torque, or system instability due to time delay or high gains in the system.

125
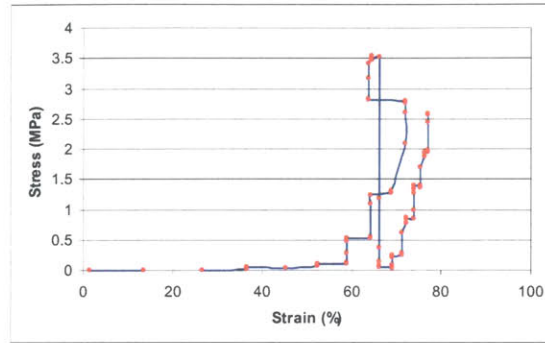
Figure 6.16- Instability of the GT6K compression of STF-filled foam at 10 s^{-1}

6.4 Blade Flexure Tests

Preliminary tests were performed using the first batch of completed silicon devices in the blade flexure setup both with and without ER fluid between the devices. Figure 6.17 below shows the results from tests without ER fluid (dry tests with chips in direct contact) at 1 mm/s with and without foam backing on the blade flexures. The tests were run first in tension, then compression, resulting in the two sets of lines on each plot. The top line is the part of the test run in tension and reads from left to right, whereas the bottom line shows compressive forces as the devices return to the home position (30 mm back to zero). Figure 6.17a superimposes the results from three dry tests, while Figure 6.17b shows only one test.
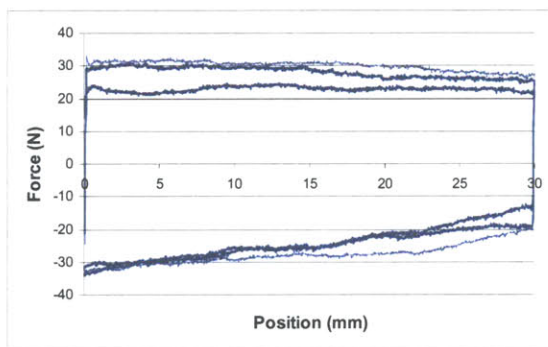
(a) Foam preload
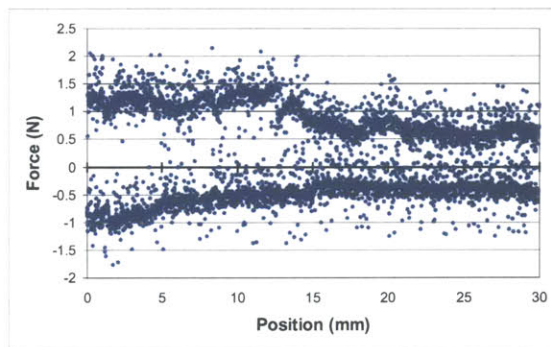
(b) No foam preload

Figure 6.17- Blade flexure device tests: Dry, 1 mm/s, patterned against planar, with and without foam preload

The foam backing applied to preload the chips together created a much higher normal force between the devices, indicated by the difference between Figure 6.17a and Figure 6.17b. The tests without foam preload exhibited forces between 0.5 and 2 N, and the signal to noise ratio tended to be lower than the tests with foam preload. The noise in the two signals is shown in Figure 6.18 below, where the average force from the entire test has been subtracted from the signal. The figure shows a similar noise level for the two tests, whose widely different average forces lead to the difference in signal to noise ratio. Although the tests with foam preload exhibited a much higher signal to noise ratio, the large force between devices tended to damage the surface of the devices and on one occasion resulted in a broken chip when the devices were pulled completely past each other. Beyond these initial tests, foam preload was abandoned to decrease the proportion of the force signal created by friction.
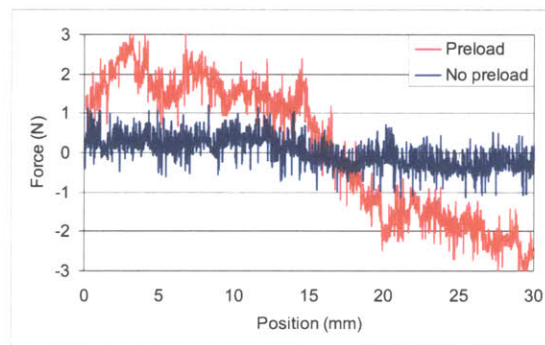
Figure 6.18- Noise in the 1 mm/s dry device tests with and without foam preload

Figure 6.19 below shows two blade fixture tests with ER fluid between the opposing devices, without an applied voltage or foam preload at 1 and 5 mm/s. The first few millimeters of most "wet" tests show a transient from a higher force before approaching a decreasing linear trend, as seen in both Figure 6.19a and Figure 6.19b. The magnitude of the force at 5 mm/s is approximately four times higher than the force in the 1 mm/s test, although the relative decrease in the force from the home position to the extreme position (30 mm) is similar. The decrease in force for each test was approximately one fifth to one seventh of the initial value.
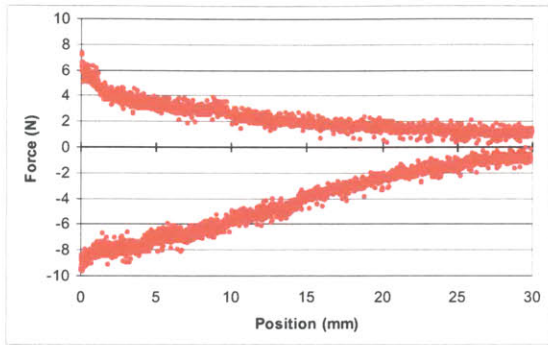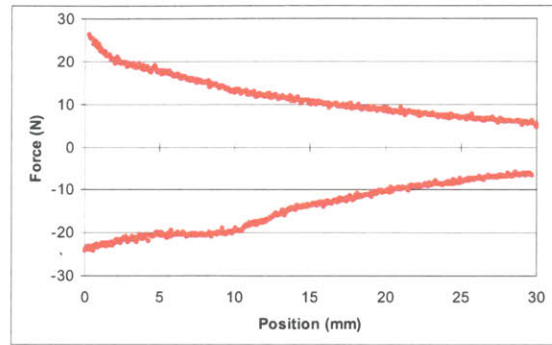
(a) Velocity = 1 mm/s   (b) Velocity = 5 mm/s

Figure 6.19- Blade flexure device tests: Wet, 1 and 5 mm/s, patterned against planar, no foam preload

6.5 Electrical Resistance Measurements

The first batch of silicon devices was unable to support the required electric field in ER fluid due to a low resistance between devices. Several measurements were taken to characterize this low resistance, including resistances of individual chips, resistance from the conducting surface of chips to the attached blade, and from one chip to another. The voltage required to create the maximum electric field of 5 kV/mm across the largest channel depth anticipated, 100 μm, was calculated to be 500V. To maintain a leakage current less than 50 mA, the resistance from the contact terminal of the patterned device to the planar electrode needed to be at least 10 kΩ. As shown in Table 6.3 below, this resistance was measured to be as low as 0.6 kΩ, requiring some effort to increase the resistance as discussed in Section 3.4.1.

Table 6.3- Measured resistances across several points in the first batch of devices

Description	Resistance
Corner to corner of planar electrode (Al)	2-3 Ω
Corner to corner of Aluminum blade	0.5-1.5 Ω
Corner to corner of anodized blade	NA
Contact terminal to riser surface	6-8 kΩ
Contact terminal to planar electrode	0.6 kΩ

128

6.6   Homogeneous ER Fluid Contact Angle

Before the completion of the first batch of silicon devices, tests were run to examine the wettability of contact surfaces with homogeneous ER fluid. A contact angle of zero would indicate a perfectly wettable surface, while a contact angles as high as 70° or 90° would signify low wettability. High wettability (low contact angle) was desired in the silicon devices to achieve high fluid retention and good force transmission from the liquid to the substrate. Using the VCA2000 video contact angle measurement system described in Section 5.7, the data in Table 6.4 was taken using a brightness setting of 100% and a contrast setting of 60%.

Table 6.4- Contact angle data for water and homogeneous ER fluid on various substrates

	Water	Homogeneous ER fluid
Dark Silicon	90°, 92°, (91° average)	38°, 42°, 39°, 39° (39° average)
Untouched Silicon	50°, 48°, 55°, 53° (52° average)	37°, 39°, 34°, 35° (36° average)
Aluminum, 2% Silicon	80°, 80° (80° average)	34°, 37°, 30°, 35° (34° average)

The results of any contact angle test depend on several factors and the values are accurate to within about ±10°, but the values measured using the VCA2000 system were repeatable within ±4°. ER fluid was observed to wet all three types of surfaces tested: dark silicon etched during the DRIE process, pristine silicon unetched by any process, and Al-2%Si. With contact angles less than 40°, the homogeneous ER fluid wet all three surfaces better than water and the devices were considered feasible from a fluid retention and compatibility standpoint.

6.7   Microfabrication Process Experiments

During the development of the process plan in the Microsystems Technology Lab (MTL), individual process steps were run with varied parameters. The results of several failed process attempts are shown in microscopic images in Figure 6.20 below taken from an angle normal to the water surface (top view). One such processing mistake, mentioned in Section 4.6.8.2, was the exposure of wafers during the first photolithography step with the chrome side of the mask facing up rather than down. This mistake allowed light to diffract over the 2.28 mm thickness of the mask before reaching the photoresist surface, resulting in exposed photoresist in regions of the wafer intended to be masked. Figure 6.20a and b show the narrow risers created by this

diffraction. Figure 6.20c and d show a different kind of diffraction pattern in the photoresist remaining after development where the thickness of the photoresist increased from the edge of the channel in Figure 6.20c toward the nominal thickness away from the channel edge. Figure 6.20d shows the thin, washed-out alignment marks on one of the affected devices, where one would usually find crosshairs that intersected at the center of the design.
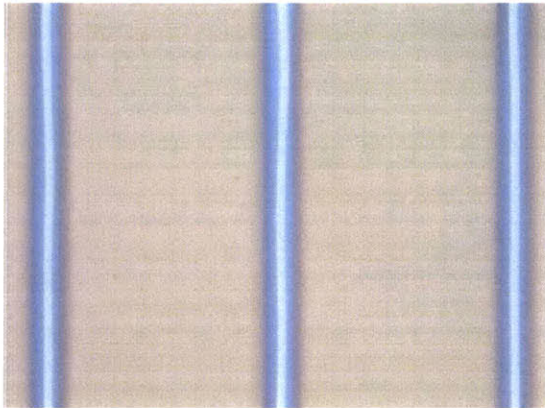
(a) Thin risers caused by mask diffraction
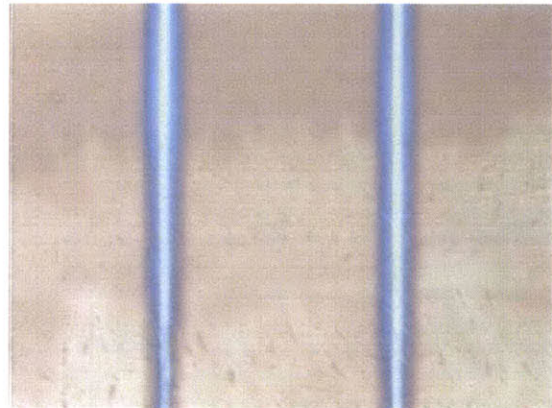
(b) Thin risers and unknown crystal defect
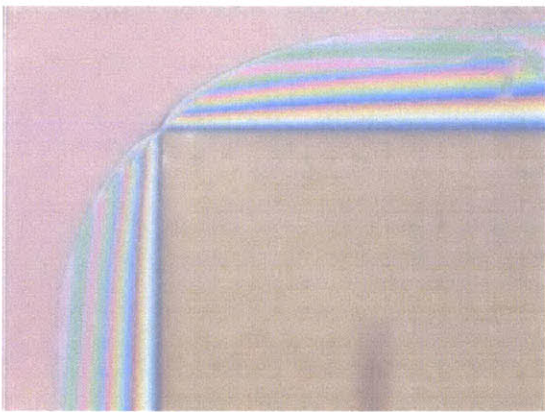
(c) Diffraction through varied PR thickness
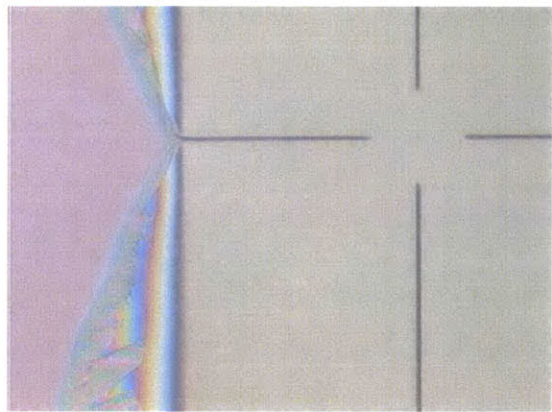
(d) Washed-out alignment marks

Figure 6.20- Various pictures of mask inversion error

Unlike the photolithography error that caused the problems in Figure 6.20 above, a problem with the etch recipe in the deep reactive ion etch (DRIE) step created the "black silicon" seen in Figure 6.21 below. The DRIE process called for a series of alternating etch and passivation steps to anisotropically etch channels into the silicon. If the passivation step in this sequence was too long or the etch step too short, not all the Teflon used to protect the channel

sidewalls was removed from the bottom of the channel surface. Any remaining speck of Teflon then masked a small area of the channel bottom, resulting in a rough surface indicative of black silicon. The magnitude of this micromasking effect varied spatially with the availability of etch and passivation gasses, resulting in the transition from black silicon to "healthy" silicon shown in Figure 6.21b.

(a) Black silicon formed after DRIE etch (b) Transition from black silicon to clean Si
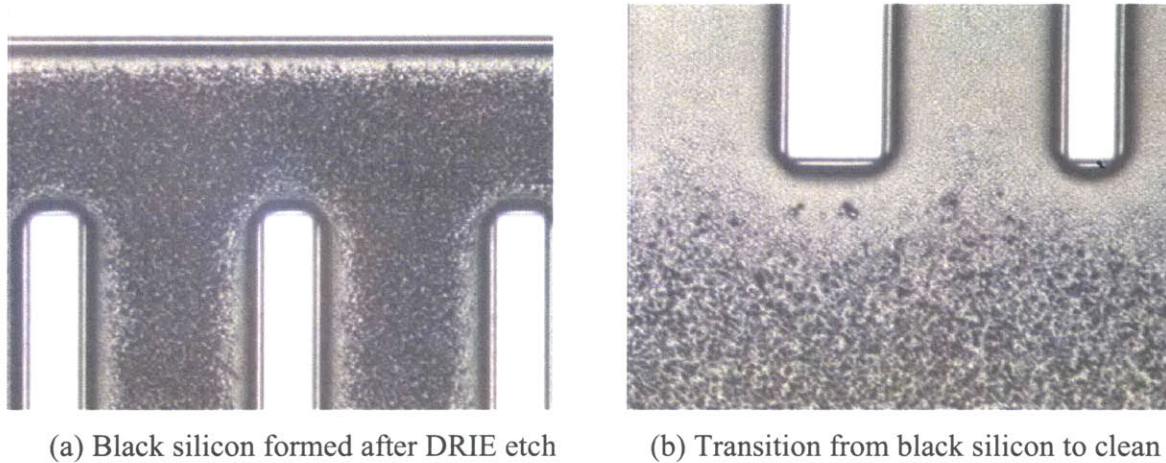
Figure 6.21- Images of channel damage from early STS2 recipe resulting in black silicon

An example of another common process failure, poor photoresist (resist) adhesion, is shown in Figure 6.22 below. Residual stresses in the resist (shown with a purple hue in Figure 6.22a) cause the edges of the resist to peel up. In the dot array geometry, this created small cups of resist resting on the substrate with a small area at the center of the cup anchored to the substrate protecting the surface from etchants. This protected area shows up as a smaller circle in Figure 6.22a-d. Ideally, any residual stress in the resist would be counteracted by surface adhesion forces to keep the resist anchored to the substrate across the resist disc. Factors including elevated humidity during processing, insufficient HDMS exposure time, or extended time between HMDS and resist coating may have detrimentally affected adhesion of the resist. Good resist adhesion is especially important when the resist is subjected to rigorous use. The devices in Figure 6.22, for example, underwent a long buffered oxide etch (BOE) followed by a long DRIE recipe. The BOE isotropically etched underneath the photoresist cups, resulting in the smaller protected circles seen in Figure 6.22a, b, and d.

(a)   (b)

(c)   (d)
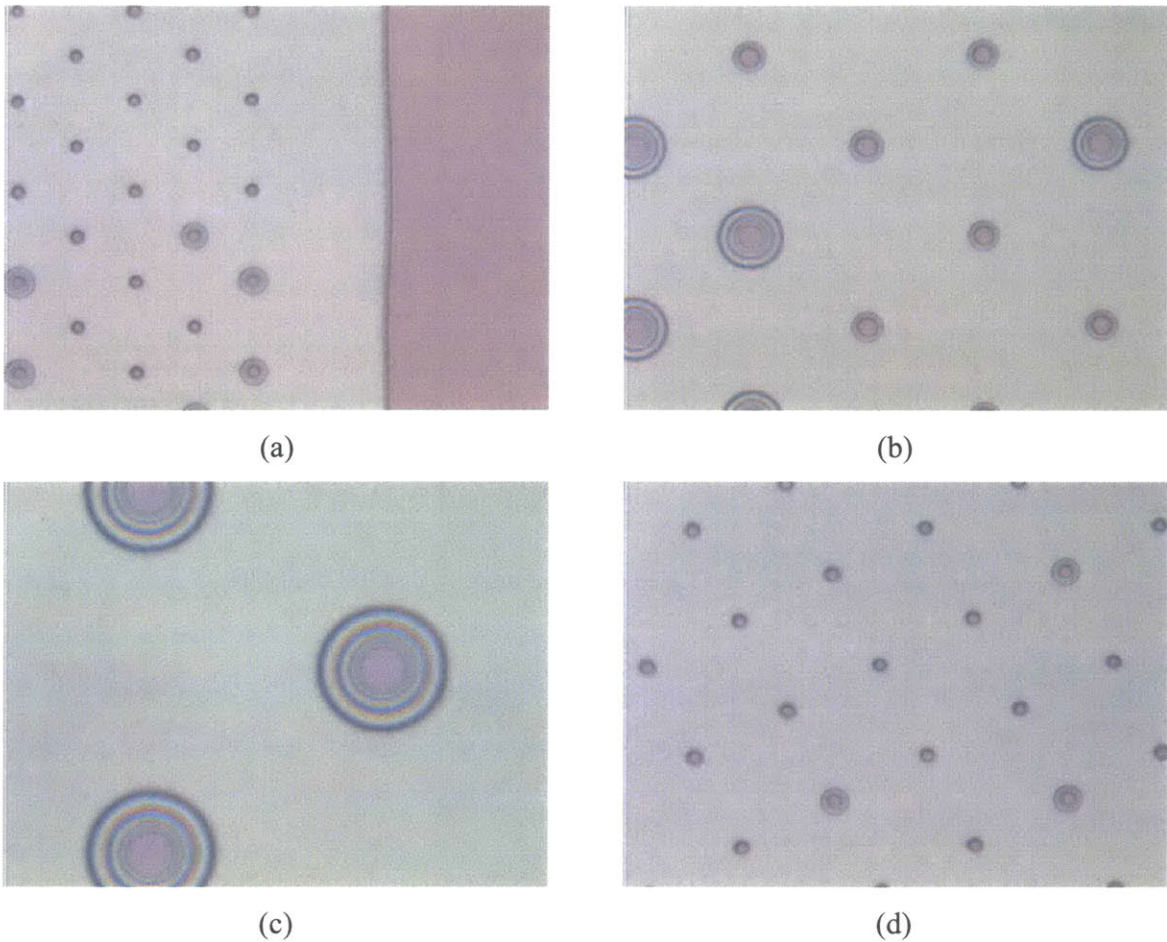
Figure 6.22- Various pictures of damage resulting from photoresist liftoff on dot array devices

The device shown in Figure 6.22a, b, and c above had a high density dot array with the same raised area as the parallel channel device design, whereas the device in Figure 6.22d used a less dense dot array described in Section 3.4.6. In terms of photoresist adhesion, both the high and low density devices were affected equally. The related problem with the parallel channel design (not shown) resulted in the liftoff of resist starting at the free end of risers. Figure 6.22a above shows the free end of the risers, the usual site for the initiation of resist liftoff. Curls of photoresist were observed in the parallel channel design, and frequently these curls of resist broke away from the substrate and redeposited elsewhere on the wafer, resulting in unintentional masking in later processing.

Figure 6.23 below shows a wafer that had successfully passed through the process plan up through the deposition of Al-2%Si. Clean, sharp edges are observed in both images, with no

evidence of black silicon or roughness on the channel bottom or the riser. This wafer was subjected to one processing error whose result is shown in the irregular areas of Figure 6.23b. The passivation step in the DRIE process can leave a slight Teflon residue on the wafer surface. The process plan calls for 30 minutes in an oxygen plasma to remove this residue before the Al-2%Si deposition, but this step was omitted in the wafers shown below. The result was intermittent areas of lower thickness Al-2%Si in the otherwise uniform film, where the lower adhesion rate of Al-2%Si to the Teflon residue impeded the deposition.

(a)   (b)
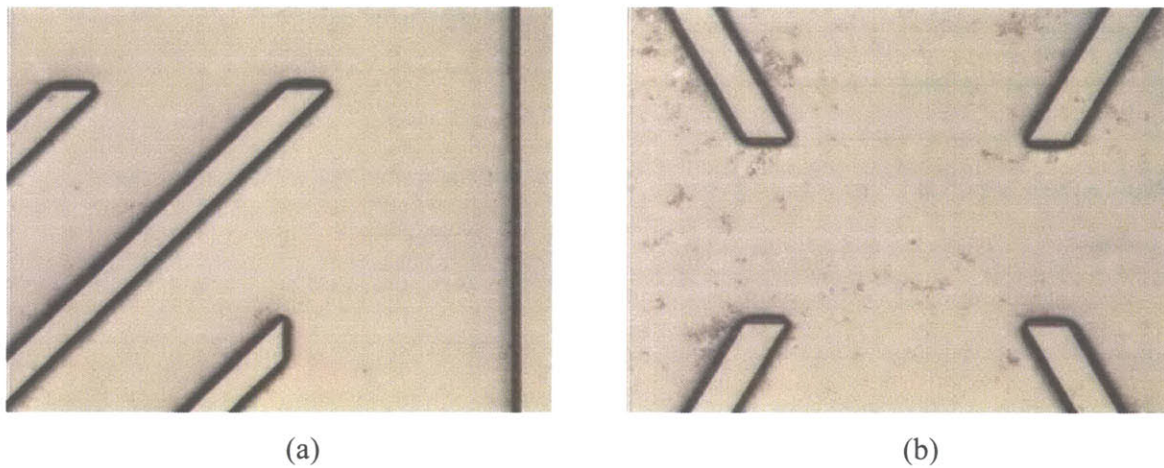
Figure 6.23- Pictures of successful diagonal line devices ready for the second photolithography step

6.8   DRIE Depth Results

Measurements were taken with interference optics on a Nikon inspection microscope to characterize the etch depth of the reactive ion etch (RIE or DRIE) process. As discussed in Section 5.9.2, the STS2 equipment used for DRIE is an edge-fast etch, resulting in the etch depth profile shown in Figure 6.24 below. Figure 6.24 shows the depth profile of channels processed using the first and second etch recipes, with increased depth after increased etch time. Each of the lines in the figure correspond to a different total etch time. Figure 6.24a shows a maximum depth at a radius of 55 mm from the center of the wafer, with a decrease in depth at higher radius for three of the sets of measurements. The data point at 65mm in the 10, 20, and 30 minute etch wafers was taken from the same point on each wafer, at the top of the electrical contact terminal. The etch depth at this location was lower than the average etch depth for this radius because of

133

the large etch area surrounding this point. The concentration of etch gas per etch area was decreased in this location and resulted in a systematically lower etch depth.

(a) Recipe 1   (b) Recipe 2
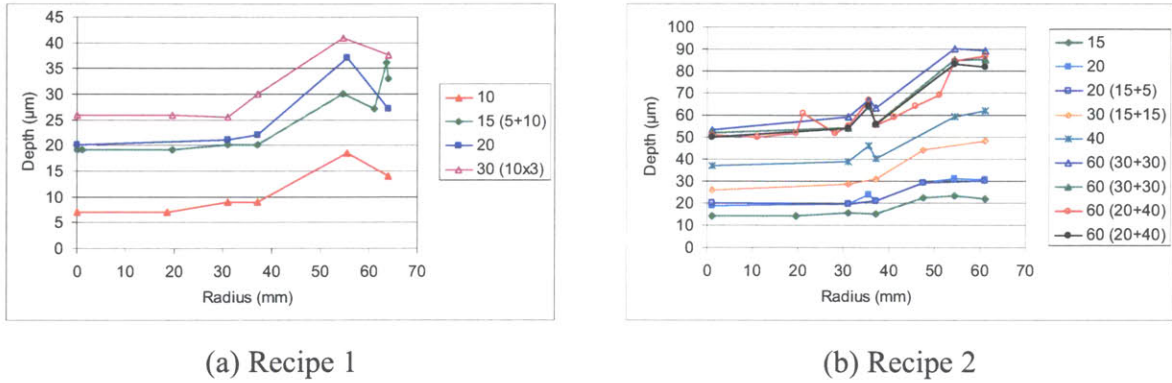
Figure 6.24- Channel etch depth vs. radius from wafer center at different etch times for both recipes

The etch depth profile shown in Figure 6.24b is a more accurate representation of the true depth versus radius relation due to better selection of measurement points around the wafer. This plot shows the same increasing depth with increasing etch time seen in the wafers processed with recipe 1, as well as exhibiting some repeatability in the etch depth between several wafers at 20 and 60 minutes total etch time. Local effects may have also played a part in the prevalent depth spike at a radius of 35 mm. A large proportion of the area of the wafer was etched to the minimum depth, which was deemed the "characteristic depth" of a wafer. This depth was used to estimate the electric field in the device since the devices tested with ER fluid overlapped primarily at this depth.

The average minimum depth for all measured wafers at a given total etch time is shown in Figure 6.25 below. The wafers processed using both the first and second recipes fall on the same line, indicating that the characteristic depth of a wafer increased linearly with etch time. Similarly, Figure 6.25a shows that the ratio of maximum measured depth to the characteristic depth (only wafers processed with recipe 2 are plotted) also increased linearly with etch time, resulting in a linearly increasing maximum etch depth. The exception was one wafer, processed for 30 minutes in the STS2 that had a significantly higher max/min depth ratio than any of the other eleven sets of measurements. The maximum depth of this outlier was four microns higher than the expected value.

134

| (a) Max/min depth ratio | (b) Minimum depth |
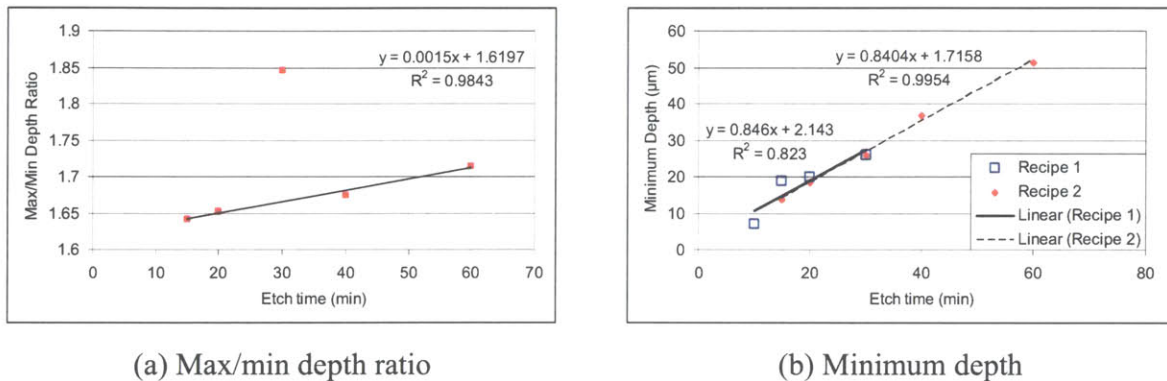
Figure 6.25- Maximum to minimum etch depth ratio and minimum depth vs. DRIE etch time

The topology of the channel bottom was observed to be radially symmetric. This symmetry resulted in two devices with symmetry across the long axis of the device and two devices with symmetry along the short side of the device. The two devices in the center of the wafer (with symmetry about the center channel in parallel channel devices) were exclusively used for ER fluid microchannel tests, to prevent off-axis asymmetry that might pull a device laterally during a test. These devices were referred to as type 1/3, for the number of the device counted clockwise from the wafer flat (devices 2 and 4 were located at 3 o'clock and 9 o'clock with the flat facing up). In retrospect, the design and implementation of a device with the cross-section described in Section 3.4.1 (the planar electrode device with superimposed risers in Figure 3.7b) would have had superior depth uniformity to the implemented process plan and allowed use of all four devices. Future researchers would be wise to consider this alternative to remove one of the undesirable features of this design.

6.9   ER Fluid Microchannel Results

To begin, previous research had suggested that the ER effect may not be obtained at small length scales (discussed in Section 1.2). In the tests reported below, application of an electrical field increased the shear force between ER microchannel devices by up to 350% in devices with channels as shallow as 20 microns. Further, electrical fields of sufficient strength could readily be created with microchannel devices and breakdown occurred at approximately the same 5 kV/mm field strength as in prior tests with larger gap sizes. Finally, though improvements in the

135

processing may be desirable, the feasibility of manufacturing recessed electrode silicon devices in large quantities using standard silicon processing techniques was demonstrated.

6.9.1 Device Composition

Figure 6.26 below shows the results from a set of 20 tests in a four by five combinatorial matrix of applied voltage and test velocity. A test was performed at every combination of the four voltages and five velocities in randomized order reusing a single sample of ER fluid. Individual force traces are referred to by figure number, subplot and velocity in the form 26b8, referring to the test shown in Figure 6.26, subplot b, at 8 mm/s. Figure 6.26 below reports the results from a standard parallel channel device with an Al-2%Si electrode and channel depth of 20-35 μm.

(a) 90 V

(b) 60 V

(c) 30 V

(d) 0 V
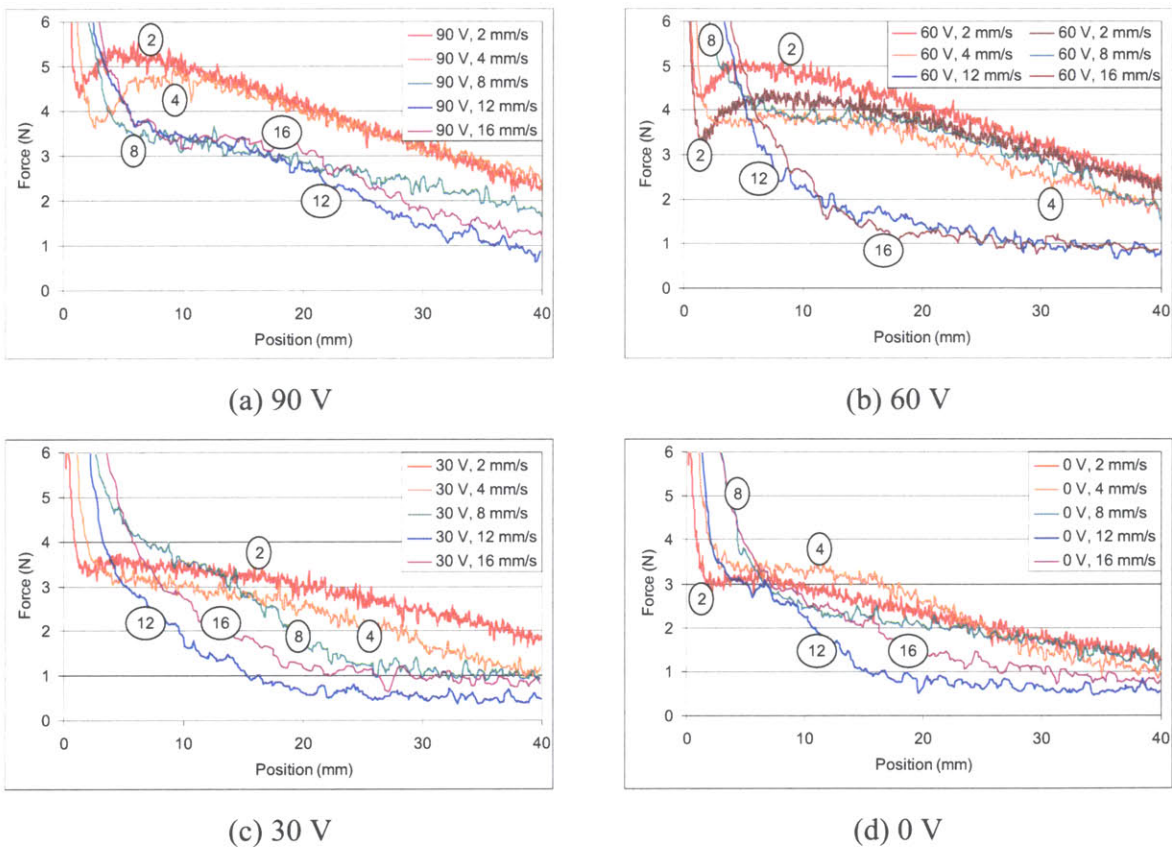
Figure 6.26- Summary of ER tests from 20-35 μm depth, Al-2%Si chip from 0-90 V

All of the plots in Figure 6.26, Figure 6.27, and Figure 6.28 were filtered using the type of 5-point, symmetric moving average filter discussed in Section 5.3. The results show that tests performed at lower velocities generated higher forces. This effect could have been due to the light shear thinning observed in ER fluid reported in [Wissbrun, 1981; Adolf, 1994], a difference in the efficiency of chain formation between high and low shear rate, or an effect similar to hydrodynamic lubrication at high velocity.

Figure 6.27 below summarizes the second set of randomized voltage/velocity tests for a silicon device with Al-2%Si electrodes and a larger amount of recessed channel area. This device was the result of the upside-down mask error described in Sections 4.6.8.2 and 6.7 that decreased the width of the risers to approximately 50 μm (half of the width of the risers in the device summarized in Figure 6.26 above). The area of the electrode in these devices remained unchanged from the upside-down mask error because the electrodes were defined by a separate patterning step. In fact, the quality of the electrode in this "thin riser" type of device may have been superior to the devices conforming to the process plan due to better removal of metal from the channel walls during patterning. The results of tests with the thin riser device show similar trends across voltage and velocity as the baseline parallel channel device, although the forces are lower in general.
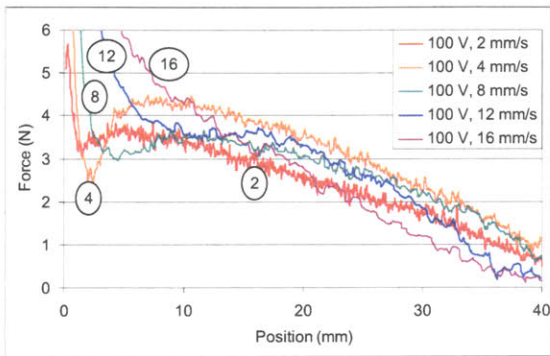
(a) 100 V
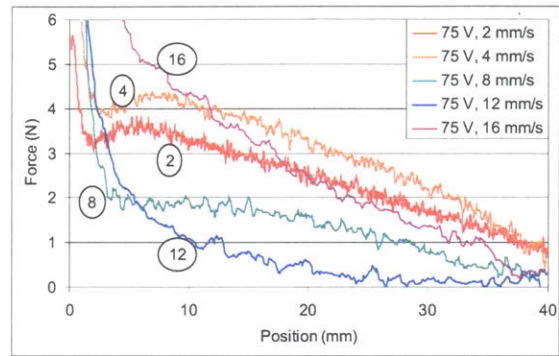
(b) 75 V
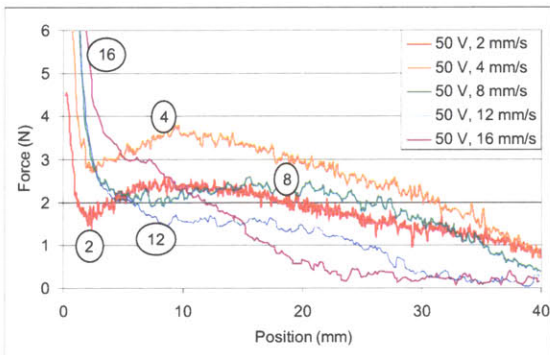
(c) 50 V
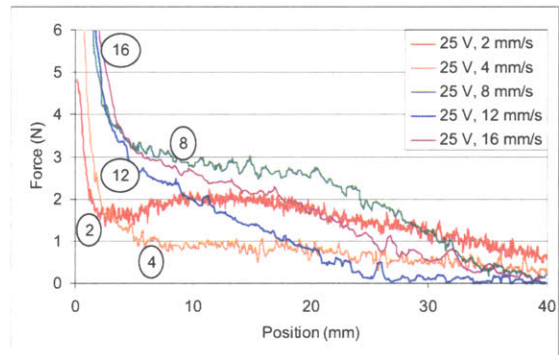
(d) 25 V
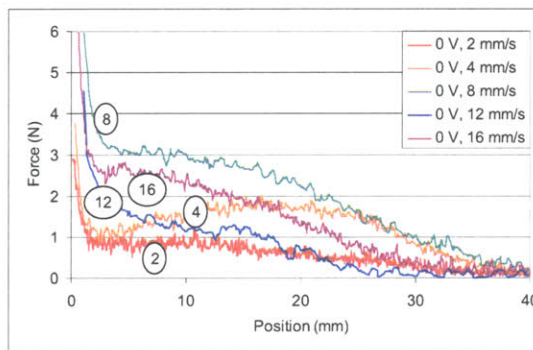
(e) 0 V

Figure 6.27- Summary of ER tests from 26-48 μm depth, thin riser Al-2%Si chip from 0-100 V

At high voltage (90 or 100V for the standard or thin riser devices), both types of devices show a tight band of force response with the low velocity (2 and 4 mm/s) tests slightly above the high velocity (12 and 16 mm/s) tests. The high voltage tests also trend toward the same slope across velocities for the majority of the test, unlike the low voltage tests where different

velocities have varied shapes. It is possible that the high voltage tests pulled the electrodes to a more consistent depth resulting in higher uniformity of the force vs. position trace, where the low voltage tests may have allowed the electrode gap to be influenced by fluid flow. Modeling of the forces created by fluid flow is an issue that could be addressed in future work. The high velocity tests in general have a larger force response at small displacement, and the high velocity, high voltage tests get an added boost at small displacement. In medium and low voltage tests, many of the high velocity curves look like an exponential decay (26b12, 26b16, 26c12, 26c16, 26d16, 27b12, 27c16, 27d12), some with a single superimposed bump at varying positions (26c8, 26d12, 26c12, 26d16).

The low velocity tests show a nearly universal transient dip at small displacements that does not show up in high velocity tests. As the voltage decreases, the magnitude of the dip in the low velocity tests tends to decrease and the length of the dip tends to increase. This trend approaches a plateau in some tests, including tests 26b4, 26c2, 26c4, 26d4, 26b8, 27d4, 27d8, and 27e8. The low velocity, low voltage tests in the standard device (26c2, 26c4, 26d2, and 26d4) are shown to be 2-3 times higher than the same "off state" tests with the thin riser device (27d2, 27d4, 27e2, and 27e4). Despite the overall lower forces, this gives the thin riser devices the advantage of a higher ratio of "on force" to "off force" at low velocity, which is important if low forces are desired in the off state.

Figure 6.28 below shows the results from the third randomized voltage/velocity test series with a device without an aluminum electrode. This type of device was cut from a series of wafers after they had been etched in the DRIE process step, but before the metallization step. This decision was based on the realization that the low resistivity of the silicon substrate that caused the first batch of devices to fail could be used as a benefit by using the substrate as the patterned electrode. The layer of SiO_2 added to the surface of the wafer before etching the channels insulated the substrate from the planar electrode. The response of this type of device is comparable with the two discussed above, with maximum (non-transient) forces between 5 and 6 N at high voltage and between 1 and 3 N at low voltage.

(a) 90 V

(b) 60 V

(c) 30 V

(d) 0 V
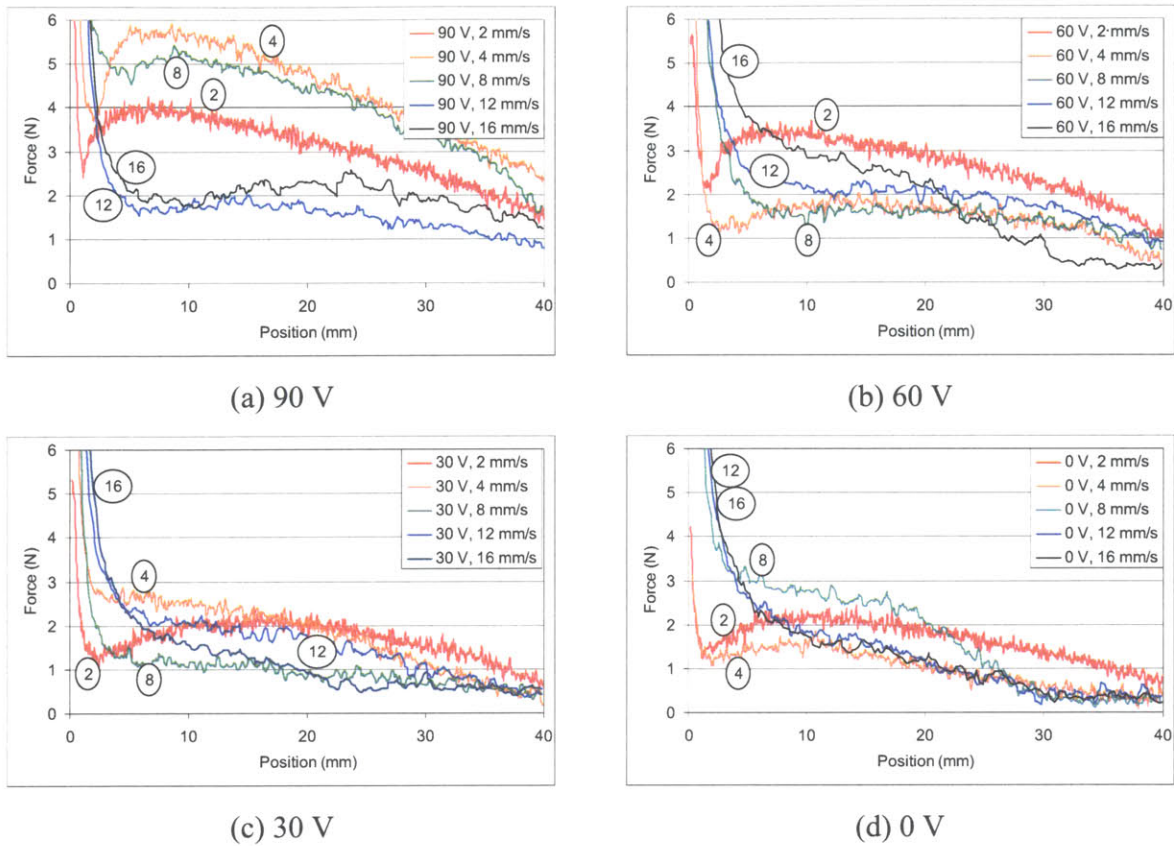
Figure 6.28- Summary of ER tests from 20-38 μm depth chip without Al-2%Si from 0-90 V

The force traces at high voltage (Figure 6.28a) are more spread out than in either of the other two device compositions, primarily because the high velocity tests don't receive the same boost at low displacement as in the other devices. Test 28a2 is another notable departure from the expected high voltage, low velocity test, being significantly different than the 4 mm/s test at the same voltage, which usually follows the 2 mm/s test closely. As in the other two device compositions, the 2 mm/s test is very similar in the two high voltages and again in the two low voltages, and represents the most repeatable test seen in these experiments. The high velocity tests are also similar to those seen in the two other device compositions; decreasing without a noticeable transient dip, with increased mid-test forces at lower voltage.

Figure 6.29 below summarizes the four combinations of high and low voltage and high and low velocity for all three device compositions. The combination of high voltage and high speed, shown in Figure 6.29a, produced clean data that were consistent for four of the six tests, excluding the tests from the non-metal device, which had a low force response at low

140

displacement. The combination of low voltage and high speed (Figure 6.29b) produced plots that looked like exponential decay, with forces lower than the high voltage, high speed tests. The high voltage, low speed tests shown in Figure 6.29c showed a consistent dip at low displacement, followed by decreasing linear behavior beyond 7-10 mm. The low voltage, low speed results summarized in Figure 6.29d were the most inconsistent data, with several behaviors including force plateaus, dips at low displacement, and concave down curves.
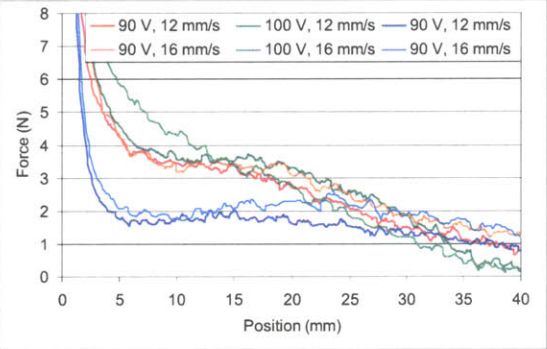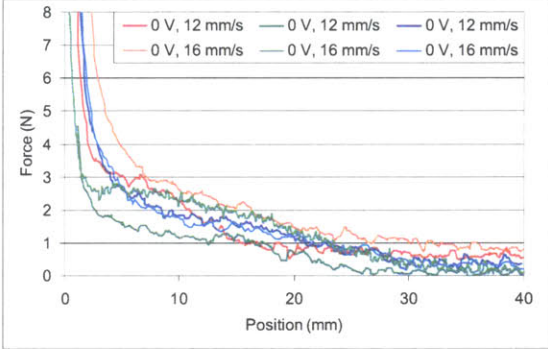
(a) High voltage, high speed   (b) Low voltage, high speed
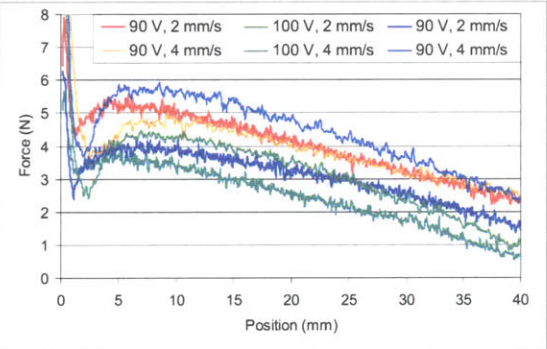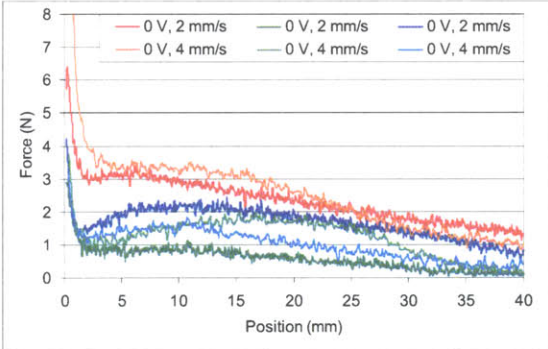
(c) High voltage, low speed   (d) Low voltage, low speed

Figure 6.29- Summary force response plots for all three device compositions grouped by voltage and velocity

The reuse of ER fluid samples was justified by the results shown in Figure 6.30 below. Unlike the syrup tests, there was very little correlation between pull force and test number (Figure 6.30a with Pearson's correlation coefficients, R = A: 0.358, B: 0.361, C: 0.338) or between the work absorbed by the fluid and test number (Figure 6.30b) when reusing a sample of ER fluid. The choice to use the y-intercept of the linear regression to the force vs. position data

as a measure of the ER effect was motivated by the model of the fluid viscosity given in Equation 5.2. The model predicted that the viscous force should scale with the viscosity of the fluid and the contact area, which decreased linearly with increasing position. Thus, the slope of the force vs. position data was a measure of the viscosity of the ER fluid. The slope of the data, however, was negative and small and a more intuitive feel for the magnitude of the viscosity was available from the y-intercept of a linear regression applied to a portion of the force-position data. The start and end points used to fit the least squares trend line, slopes, y-intercepts, and all other data for the tests are tabulated in Appendices D.4.1, D.5, and D.6.

(a) Y intercept vs. test number   (b) Work vs. test number
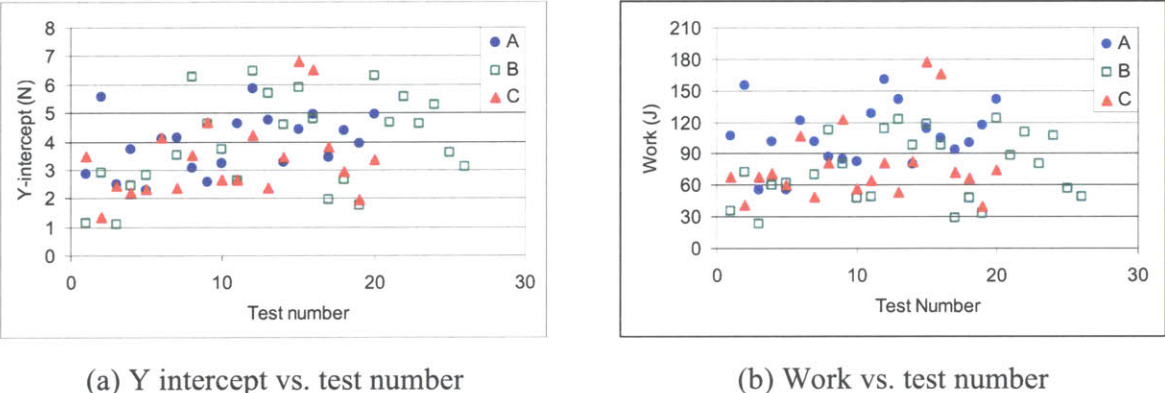
Figure 6.30- Force-position linear regression y-intercept and work absorbed for all three device compositions

The work absorbed by the fluid is another intuitive measure of the "effective viscosity" of the fluid. The work absorbed is a more aggregate measure of the energy absorption characteristics of a test, is more independent of the shape of the force-position response, and reflects roughly the same pattern of points (Figure 6.30b) as the y-intercept data. The plot of work versus test number also shows very little correlation for all three types of devices (Pearson's correlation coefficients, R = A: 0.222, B: 0.236, C: 0.227). The work for all the ER microchannel data reported above was calculated by numerically integrating the filtered force-position data using the trapezoid rule. These values were further used to calculate the average power absorbed by the fluid by dividing the work input to the fluid by the run time of a test (the distance of the pull divided by the velocity). The results of work and power absorbed by the ER fluid are shown in Figure 6.31 below.

142
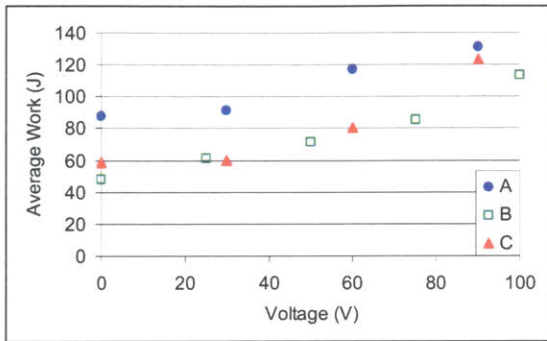
(a) R = (A: 0.968, B: 0.980, C: 0.920)
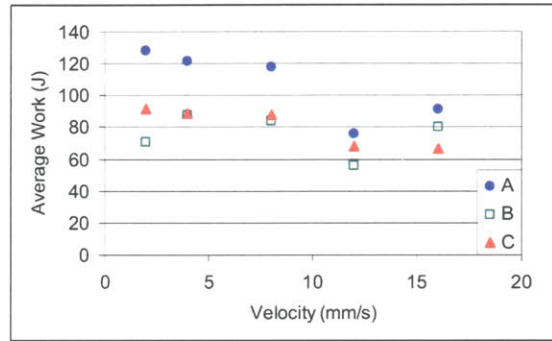
(b) R = (A: -0.853, B: -0.205, C: -0.932)
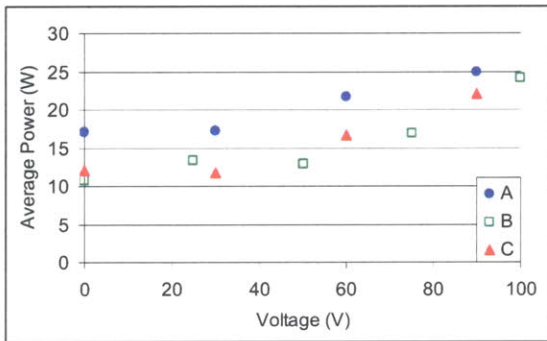
(c) R = (A: 0.954, B: 0.913, C: 0.928)
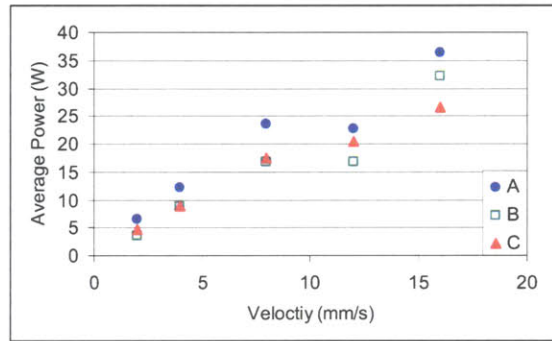
(d) R = (A: 0.960, B: 0.954, C: 0.985)

Figure 6.31- Average work absorbed by ER devices plotted for tests at the same (a) voltage, and (b) velocity. Average power plotted for tests at the same (c) voltage, and (d) velocity.

The correlation coefficients for data series given in the captions for Figure 6.31 above were calculated for individual device compositions. The data series labeled "A" represent the standard riser width parallel channel devices without metal. Similarly, "B" and "C" series corresponded to thin riser and non-metal device compositions. With the exception of the thin riser device, the work absorbed by the ER devices showed high correlation with voltage and velocity. The average work increased with increasing voltage and decreased with increasing velocity (as indicated by the plots above). The average power, on the other hand, increased with both voltage and velocity and showed high correlation for all device compositions. The linear relationship between velocity and test time (used to calculate power from work) contributed in part to the high correlation between average power dissipation and velocity.

6.9.2 Breakdown

Two sets of tests were performed to examine the breakdown characteristics of the standard metallized and the nonmetal device compositions. The first set of tests, on a standard 20-35 um parallel channel, Si/SiO2/Al-2%Si device with ER fluid was run until visible or audible sparks were observed. Small sparks were recorded at 84 and 93 volts before a large spark was observed at 101 V. The voltage set point was reset to zero and ramped up a second time where a small spark was observed at 93 volts on the way to another large spark at 101 V. In both tests, voltages above 93 V were stable, but voltages above 100 V resulted in frequent sparks. 100 V was considered the breakdown limit of this type of device after an initial break in. The corresponding electric field at this voltage was estimated to be 5 kV/mm (100 V across 20 μm), assuming that the planar electrode was in direct contact with the top of the risers.

The second set of tests was more exhaustive and included a record of the current supplied by the 500 V, 250 mA power supply. The same type of slow voltage ramp was applied to a nonmetal device, and the current versus voltage curve is shown in Figure 6.32a below. The power supply allowed simultaneous maximum current and voltage set points, one of which was the independent variable in determining the power to the device. The current set point on the power supply was set to 18 mA while the voltage was ramped up in the first test, and when the device shorted at 150 volts, the current jumped to 18 mA and the voltage dropped to 131 V. A second test with the same device showed a much more rapid increase in the current (and corresponding power output shown in Figure 6.32b), possibly along the circuit path created during the breakdown in the first test. The second test shorted at 130 V and 18 mA. The second test showed an approximately linear (V=I*R) path, with a resistance of approximately 7 kΩ.

144
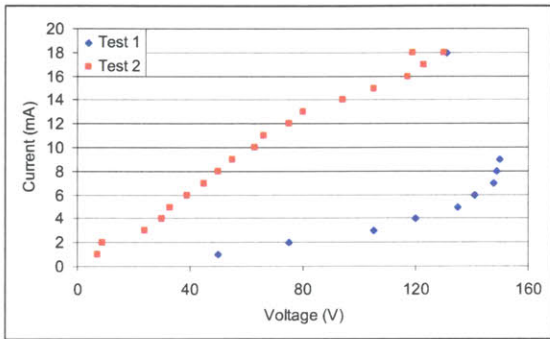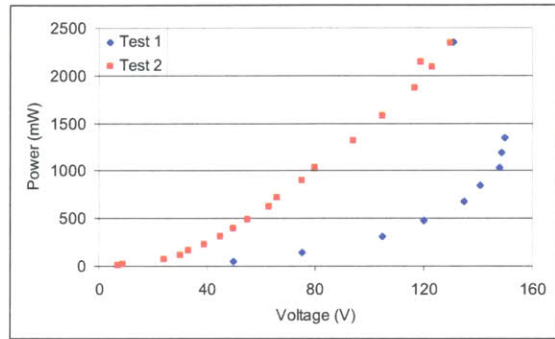
Figure 6.32- Breakdown tests of a nonmetal device plotted with (a) current vs. voltage and (b) power vs. voltage

Many other tests performed on ER microchannel devices showed leakage currents of 2 to 3 mA at the maximum test voltage of 90 or 100 V, even if breakdown was observed prior to the measurement. This effect was attributed to subsequent moving of the chips that erased the circuit through which the current flowed in the breakdown. The electrodes in both sets of breakdown tests on nonmetal devices were not moved between voltage ramps.

Chapter 7

Conclusion

This thesis focused on the development and testing of several field responsive fluid composites including shear thickening fluid-filled foams and electrorheological fluid microchannel devices. Hardware, including a compression stage and a blade flexure fixture, was designed and constructed to allow testing of these composites at a range of strain rates previously unavailable to researchers on ISN project 4.3. Silicon microchannel devices were designed and fabricated with several device compositions and pattern geometries that successfully sustained electric fields of 1-5 kV/mm over electrode gaps between 18 and 85 μm. The ER effect was shown to exist at these length scales with homogeneous ER fluid, with on/off force ratios in the range of 3.5:1. The results of this work are briefly summarized below, followed by suggestions for future work and a discussion of the factors considered to be important in the design of deployable, flexible ER composites.

7.1   Linear Stage Characterization

Springs and calibrated weights were used to verify the calibration of the force transducer used with the linear stage. The spring stiffness calculated from the slope of a linear regression fit to the force versus displacement data in constant velocity spring tests matched the ideal spring stiffness within a tolerance of ±0.05 lb/in. Measurements of calibrated weights were within 1% of the nominal value. Confirmation of the reported velocity was achieved using the stage position reported by the GT6K stepper controller and a LabVIEW time signal. The accuracy of the reported position was not examined directly.

7.2   Flexible Electrode Characterization and Baseline Calibration

New experiments with high viscosity syrup in the type of flexible electrode experiments described by [Eastman, 2004] yielded unexpected results. Although the viscosity of the syrup

147

had been measured to be 20±1 Pa-s using a conventional rheometer across a range of strain rates, the flexible electrode fixture generated viscosities between 15.4 and 35.2 Pa-s. The viscosity of a single sample of syrup reused in multiple tests showed a linear increase with the number of tests run using the same sample. Additionally, the measured viscosity of "fresh" samples was observed to decrease with increasing strain rate, a non-Newtonian behavior. Increasing strain rate (linear stage velocity) was also observed to produce higher signal to noise ratios in all experiments performed.

7.3 Shear Thickening Fluid Between Flexible Electrodes

Experiments using shear thickening fluid in the flexible electrode setup produced forces that varied widely between similar experiments. The low reproducibility of these experiments was attributed to the difficulty of preparing repeatable samples. Difference in strain history from one area of the fluid sample to another led to localized hardening at different points in the test, resulting in sample-dependent force peaks. Poor adhesion between the flexible electrodes and the STF also played a role in the variable results.

7.4 Compression Apparatus Experiments

A compression apparatus was constructed to extend the testing capability of the linear motion stage. Several programs were also created to perform constant strain rate compression on samples of open-cell reticular foam filled with glycerol, STF, or no fluid (empty foam) to compare with previous research [Bettin, 2005]. Constant strain rate testing required creation of exponentially decaying velocity profiles, the quality of which increased dramatically with the development of software designed to be loaded directly onto the GT6K stepper motor controller. Further improvements to the compression apparatus were forgone after the production of thin samples with uniform, repeatable thickness. The new samples allowed tests with improved force resolution and sampling rate to be performed on a TA.XT Plus Texture Analyzer.

 Compression tests on empty foam matched the trends found in previous results, although the measured plateau forces were 1 kPa versus 2-5 kPa reported by Bettin. The data density at low percent strain (high stage velocity) was lower than that at high strain due to the fixed sampling rate of the compression apparatus. The high sampling rate of the TA ameliorated this

problem. The results of glycerol-filled foam tests matched previous experimental results and successfully extended the rate of these tests to 15 s^{-1} (up from 1 s^{-1} in previous work). Tests on STF-filled foam achieved strains as high as 90% (up from 57%), stresses as high as 4.5 MPa, and stable compression at 10 s^{-1} up to a strain of 72%. The STF-filled foam tests performed using the linear stage generated lower forces than those produced by the TA, although the results followed the same trends with increasing strain and strain rate. Further characterization of the nature of this discrepancy was forgone in light of the superior performance of the TA.

7.5   Microfabrication Process Experiments

Solutions were found to problems including poor photolithography definition, mask errors, black silicon, photoresist adhesion, and STS2 Teflon removal. Photolithography recipes were iterated for three primary types of photoresist: thin (OCG 825), thick (AZP 4620), and image reversal (AZ 5214), resulting in successful patterning using all three types of resist. Exposing wafers through an upside-down chrome mask was shown to produce thin risers and diffraction patterns in the exposed photoresist. The issue of black silicon formation was solved by increasing the ratio of etch cycle time to passivation cycle time. Photoresist adhesion was dramatically improved with increased exposure time to HMDS. Teflon residue from the DRIE process was shown to impede the adhesion of Al-2%Si to the wafer surface, but easily corrected by removing the Teflon in an oxygen plasma prior to metallization.

Characterization of the spatial distribution and etch time dependence of channel depth produced by DRIE was performed using measurements taken using the interference optics on a Nikon inspection microscope. These results illustrated the edge-fast nature of the DRIE process, which was attributed to the temperature distribution across the wafer. The results also indicated a linear correlation between total etch time and channel depth. Silicon devices at the center of the wafer were selected for ER fluid testing based on the depth symmetry across the width of the devices, with a long section of relatively uniform channel depth at the distal end of the devices.

7.6   Contact Angle and Resistance Measurements

The first batch of silicon devices were subjected to several tests to check the feasibility of their use with homogeneous ER fluid and high voltages. Contact angle tests of homogeneous ER fluid

149

on the three types of surfaces in the wafer (etched silicon, unetched silicon and Al-2%Si) indicated that ER fluid wet the surfaces better than water. The small contact angles indicated that fluid retention and force transmission from the ER fluid to the substrate would be acceptable. Resistance tests of the first batch of devices indicated insufficient resistance between opposing electrodes to produce the required electric field. The device design was iterated to include a layer of insulating silicon dioxide to augment this resistance.

7.7   ER Fluid Microchannel Results

A blade flexure fixture was designed and implemented to approximate the degrees of freedom of previous tests with unconstrained boundary conditions. This design originally called for foam backing on each blade to apply a preload force between the devices. Foam backing on dry devices produced sufficiently excessive normal force and friction to damage the silicon devices, and the use of foam backing was discontinued in favor of using cantilever deflection forces to preload the devices. Tests with ER fluid applied between the devices (no E field) increased the shear force over dry tests without foam backing, especially at high speed, where the force increased by a factor of four from tests at 1 mm/s to those at 5 mm/s.

Randomized combinations of voltage and velocity were tested on all three types of device compositions: standard Si/SiO$_2$/Al-2%Si devices, thin riser devices with Al-2%Si, and nonmetallic Si/SiO$_2$ devices. Velocities of 2, 4, 8, 12, and 16 were tested in combination with four or five voltages between 0 and 100 V, depending on the composition. The standard device composition generated the highest forces (on average) compared to the thin riser or nonmetallic devices, while force trends seen at comparable velocity and voltage were similar between all the devices. The total work absorbed by ER devices was observed to increase with increasing velocity, but decrease with increasing velocity. The average power dissipation calculated using the total work absorbed, increased with both voltage and velocity for all three device compositions.

Unlike the syrup tests that showed a linear correlation between calculated viscosity and number of tests performed using a single fluid sample, the tests using ER fluid showed minimal dependence on the number of tests performed with a sample of fluid. Neither the y-intercepts of the linear regression to force-position data or the work absorbed by the fluid showed more than

minimal correlation with the number of fluid reuses, indicating that fluid reuse did not significantly affect the experimental results.

7.8 Flexible ER Fabric Future Work

The rigid silicon devices created in this research were a small step toward the larger vision of flexible ERF composites. These rigid devices should be used in future work to closely examine the effect of etch depth and geometry on the effectiveness of FRF composites (an intended result of this research not achieved due to time constraints). Following in-depth characterization of the rigid devices, new devices based on flexible substrates and conductors should be developed. Several factors should be considered when integrating these new flexible devices into deployable prototypes, including individual layer thickness, tensile strength of an individual layer, bidirectional operation, ER fluid retention, delamination prevention, mass manufacturability and force transmission to a user's skin.

7.8.1 Flexible Electrode Stack

Each pair of devices separated by ER fluid (a shear pair) can absorb the same amount of energy under similar operating conditions. Integration of multiple shear pairs into a stack would thus increase the energy absorbing capacity of the composite per unit area. A shear stack would also have a higher force capacity and be robust to the failure of any single shear pair. The thickness of each individual shear pair in a stack becomes an important design variable, balancing the tensile strength of a single flexible layer with the thickness of a stack of N layers. Decreasing the thickness of each electrode (without compromising the strength of an electrode) would allow more layers to fit in a desired total thickness.

7.8.2 Electrode Tensile Strength

The strength of individual layers could be increased by incorporating tensile elements into each layer. Like rebar in a concrete column or carbon fibers in a composite matrix, materials designed to carry the tension in a composite allow higher performance than the analogous homogeneous systems. The tensile strength of individual layers dictates how large a shear area each layer can support. The compressive strength of individual layers is not important because, like trying to

151

push a rope, pushing thin/flexible films results in buckling. This fact brings up another important feature of a successful multi-foliate ERF composite: bidirectional operation.

7.8.3 Bidirectional Operation and Return Mechanisms

The rigid devices developed in this thesis allowed bidirectional testing (tension and compression), but the flexible counterpart of these devices would buckle in compression. In a deployed prototype, this "one way" behavior would only work for closed paths like concentric bands. Intended applications like joint immobilization require linear elements with a finite range of motion that travel back to a home position after extension. One solution to this requirement is a multi-foliate geometry with a return mechanism. Figure 7.1 below shows two possible versions of such a return mechanism using an elastic shell (Figure 7.1a) or elastic "springs" attached to the free end of each layer (Figure 7.1b). An elastic return mechanism tethered to an anchor on either end would keep individual layers in tension across the range of motion of the composite stack.

| (a) External elastic shell | (b) Internal elastic return mechanism |
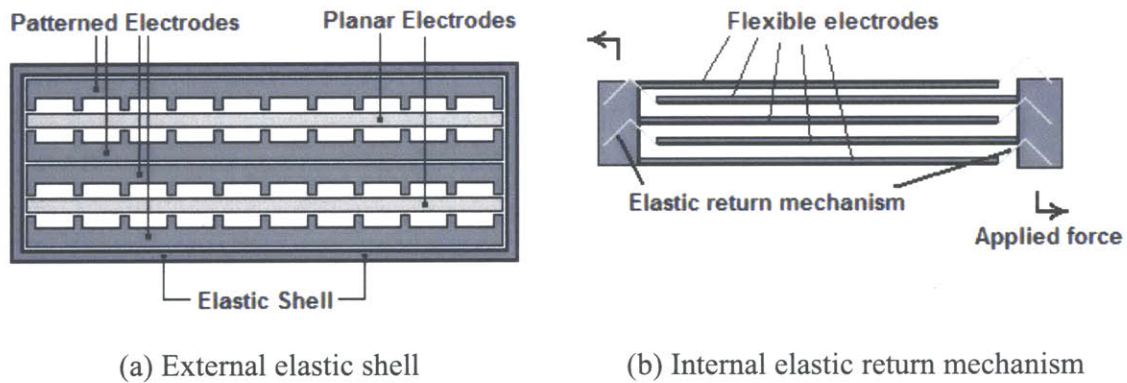
Figure 7.1- External and internal elastic return mechanisms

7.8.4 Fluid Retention and Delamination Prevention

Fluid retention is another design requirement that needs to be addressed. In combination with environmental robustness, this requirement calls for packaging that allows device flexibility while keeping the ER fluid in and the environment out. The correct selection of an elastic shell like the type shown in Figure 7.1 above would address the problem, but an airtight shell might create a vacuum during extension, for better or worse. This vacuum might address the problem

of delamination, where individual layers separate, resulting in a loss of force transmission. Delamination could also be addressed by intermittent ribs, like cross-bracing in a truss, illustrated in Figure 7.2a below or rivets like those that dimple the surface of a mattress (Figure 7.2b).

(a) Ribs   (b) Rivets
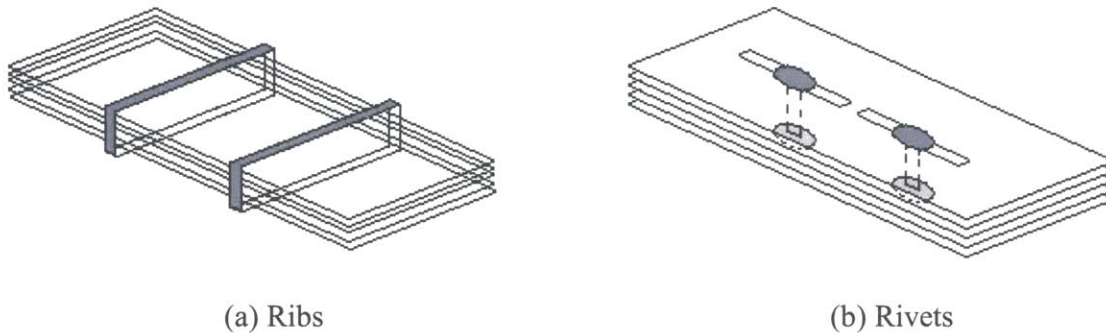
Figure 7.2- Two potential solutions to prevent delamination

7.8.5 Manufacturing

Mass manufacture of flexible microscale patterned electrodes could be made possible by several existing and emerging technologies. Technologies including micro plastic injection molding (μPIM), hot embossing, and interference lithography could allow mass manufacture of patterned films. New technologies, like the MEMS equivalent of continuous casting, could replace the serial processes of photolithography and DRIE with a continuous roller-based impression process. This is speculation, but a pattern-on-roller could theoretically transfer a desired 2D pattern onto a thin layer of molten plastic. The manufacturing scheme is illustrated in Figure 7.3 below.
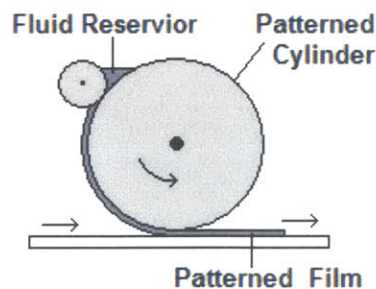
Figure 7.3- An idea for continuous thin film production with microscale features

153

7.8.6 Force Transmission to a Force Source

One final consideration in the design of flexible ERF composites is the issue of force transmission to the user. Even the best energy absorbing material would be useless without transferring the force absorbed by the composite to the structure creating the force. Joint immobilization by a shirt sleeve, for example, would be difficult with a loosely fitting sleeve, where the user is allowed movement before engaging the energy absorbing material. This requirement calls for tightly fitted materials or devices that can be selectively tightened at the points of force input (like the anchor shown in an early conceptual drawing in Figure 7.4 below). Tightly fitted materials could cause discomfort, for example by limiting moisture or heat dissipation, etc. if these concerns were not properly addressed. Selectively tightened devices, such as those with straps, may potentially forfeit the benefit of situational readiness or remote activation.
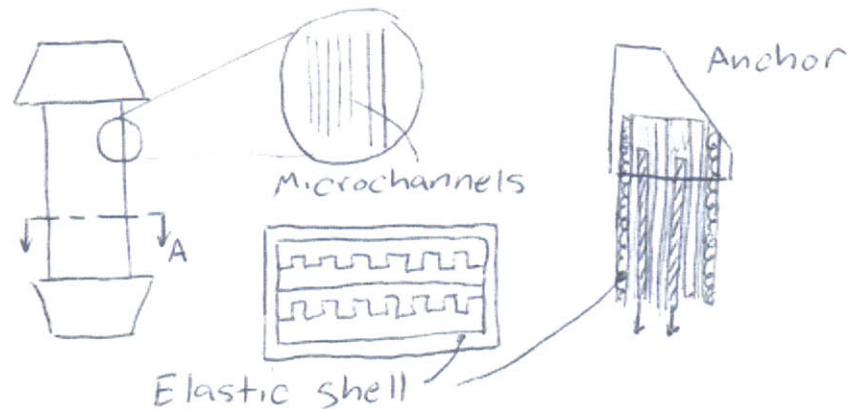
Figure 7.4- Early conceptual drawing incorporating stacked microchannel shear pairs with an external elastic return mechanism and anchors for force transmission to the user

7.9   Device-Level ERF Composite Geometries

As mentioned briefly in Sections 3.8.2 and 6.8, several manufacturing difficulties could be avoided by switching from the device cross-section in Figure 7.5a below to that in Figure 7.5b. This second device cross-section calls for continuous electrodes on both sides, with a patterned electrode separating layer deposited on one electrode. This design has the benefit of guaranteed

electrode separation, where the design implemented in this thesis may have allowed some of the metal intended to only exist in the bottom of channels to remain on the walls of the channels after processing. The magnitude of this sidewall contamination (illustrated in Figure 7.5c) was not examined in this thesis, but the potential existence of this parasitic effect may have decreased the performance of the fabricated devices below their ultimate potential.
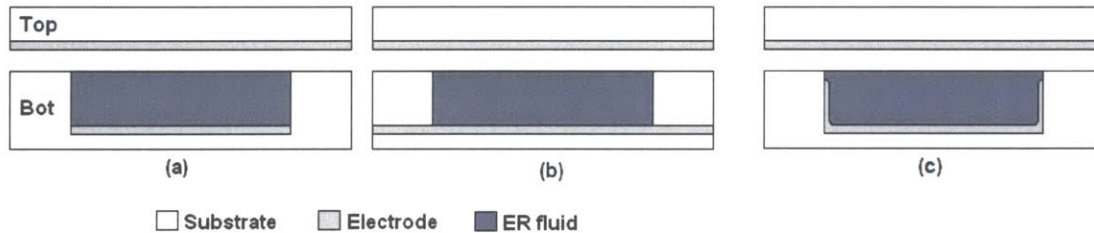
Figure 7.5- Three device cross-sections: (a) Electrode in channel, (b) continuous electrode, (c) channel sidewall contamination

Another alternative at the device level is to incorporate a device separation layer not fixed to either electrode. Like the separate spacers used in Eastman's work, this spacer would keep electrodes from coming into contact. Unlike the continuous spacer used in that research, the envisioned spacer could be a mesh-type structure with large openings to allow uninterrupted chain formation between electrodes, while maintaining a periodic minimum electrode gap. The maximum mesh spacing would be governed by the stiffness of the electrodes, the height of the mesh, and the stiffness of the mesh. The friction and tribological characteristics of this spacer material could be selected to provide higher or lower static friction and long device life.

A composite incorporating a mesh spacer operated in shear mode would ideally have isotropic stiffness. One of the first device-level ideas generated in this project, shown below in Figure 7.6a and b, was intended to create a material with anisotropic stiffness. Instead of one patterned electrode and one planar electrode, this implementation called for two patterned electrodes in contact. The material allowed very little motion in the transverse direction and gross motion along the channels. Multiple "shear directions" could be added to allow motion along any axis (including rotations) as shown in Figure 7.6b below.

155

(a) Interlocked risers	(b) Preferential shear directions
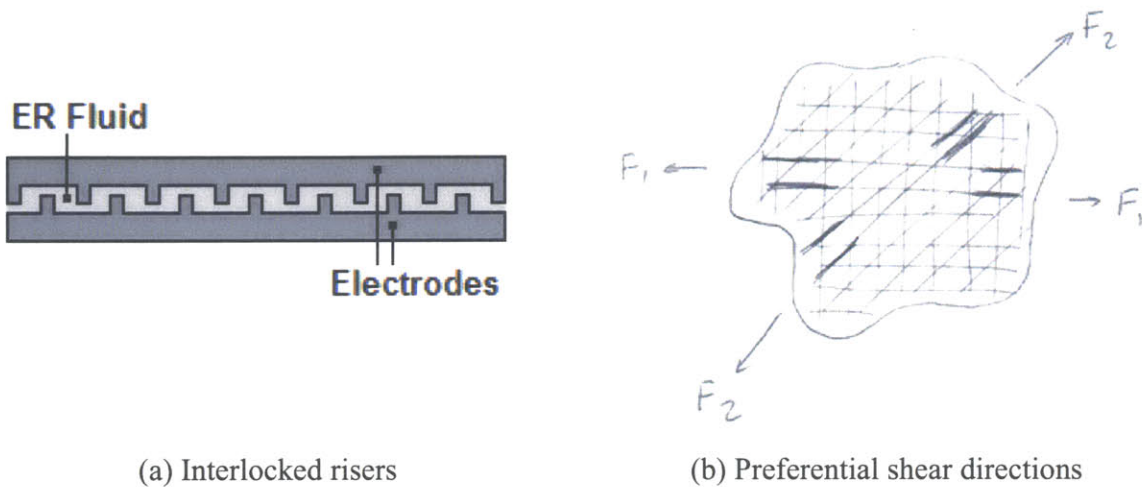
Figure 7.6- Anisotropic material with (a) interlocked risers and (b) preferential shear directions

7.10 Traumatic Brain Injury and Blast Lung

The U.S. Center for Disease Control (CDC) lists four basic mechanisms of blast injury. Primary blast injuries are attributed to the supersonic blast overpressurization wave caused by high explosives impacting body tissues. Air filled organs including the middle ear and lung are the most susceptible to this type of injury, although traumatic brain injury (TBI) is also included in this category. Secondary injuries are those attributed to flying debris and bomb fragments, while tertiary injuries occur when an individual is thrown. Quaternary injuries encompass all other injuries experienced due to a blast. STF-filled foam has been suggested as a solution to both primary and tertiary blast injury.

Primary blast injury occurs from an interaction of the blast overpressurization wave with body tissues to cause a pressure differential at the interface between tissues with different densities such as the inner ear or lung. Pressure differentials at the boundary of the lung can lead to the rupture of alveoli, causing a condition called "blast lung". Fluid-filled cavities such as the brain and spine are also susceptible to primary blast injury [Elsayed, 1997; Mayorga, 1997]. Traumatic brain injury (TBI) is a condition that can be caused by both the primary overpressurization wave or tertiary collisions with walls, etc.

According to National Institute of Neurological Disorders and Stroke (NINDS), "Traumatic brain injury (TBI), also called acquired brain injury or simply head injury, occurs when a sudden trauma causes damage to the brain. TBI can result when the head suddenly and

156

violently hits an object, or when an object pierces the skull and enters brain tissue" [NINDS, 2006]. The use of Kevlar helmets and body armor have increased the overall survival rate of soldiers and have decreased the incidence of penetrating injuries, but Kevlar helmets don't prevent the type of "closed brain injuries" common in blast exposure [Mayorga, 1997; DVBIC, 2005].

STF-filled foam has been suggested as a solution to primary blast injuries by providing an energy absorbing layer with a large density difference (paired with high density Kevlar body armor, for example) outside the body, dissipating the high velocity pressure waves before they have a chance to enter the body. STF-filled foams also have the potential to "stretch" the pressure wave imparted to the skull through a helmet, resulting in lower trauma caused by primary or tertiary blast impacts. Current research at ISN is examining the feasibility of STF-filled foams in these complex energy absorbing roles, with encouraging initial results.

Appendix A

Syrup in Flexible Electrodes

A.1 Reused Syrup Tests

Table A.1- Summary of slopes, y-intercepts, coefficients of determination, and viscosities of reused syrup tests in the flexible electrode geometry

Test number	Velocity (mm/s)	Slope	y- intercept (N)	R squared	Viscosity (Pa-s)
1	5	-0.0041	0.339	0.391	19.3
2	5	-0.0131	0.807	0.772	36.7
3	5	-0.0219	1.316	0.890	58.1
4	5	-0.0295	1.772	0.906	78.9
5	5	-0.0333	2.185	0.920	106.1
6	5	-0.0398	2.589	0.952	123.9
7	2	-0.0175	1.158	0.855	136.8
8	5	-0.0549	3.468	0.953	163.4
9	5	-0.0676	4.379	0.931	211.0
10	10	-0.1632	9.976	0.944	225.1
11	20	-0.3715	22.167	0.942	238.7

Syrup 1 y = -0.00414x + 0.33863 R² = 0.39118

(a) v = 5 mm/s

Syrup 2 y = -0.0131x + 0.807 R² = 0.7724

(b) v = 5 mm/s

Syrup 3 y = -0.02194x + 1.31622 R² = 0.88999

(c) v = 5 mm/s

Syrup 4 y = -0.02948x + 1.77243 R² = 0.90634

(d) v = 5 mm/s

Syrup 5 y = -0.03333x + 2.18486 R² = 0.91967

(e) v = 5 mm/s

Syrup 6 y = -0.03977x + 2.58919 R² = 0.95181
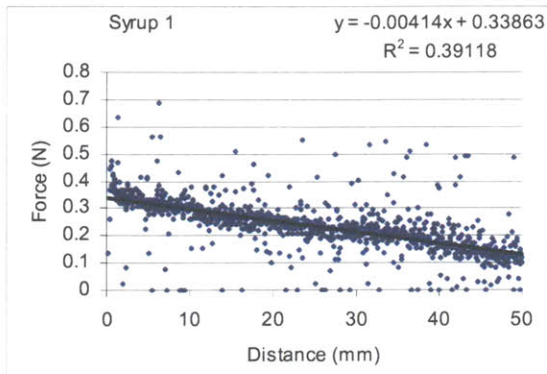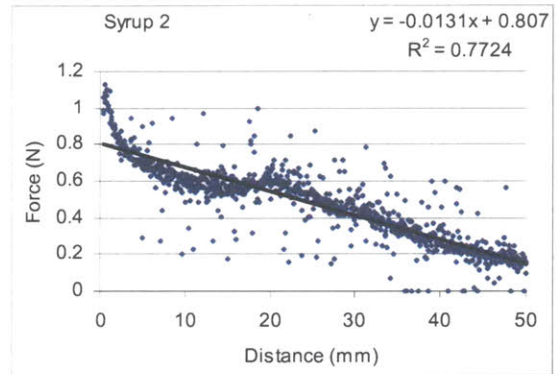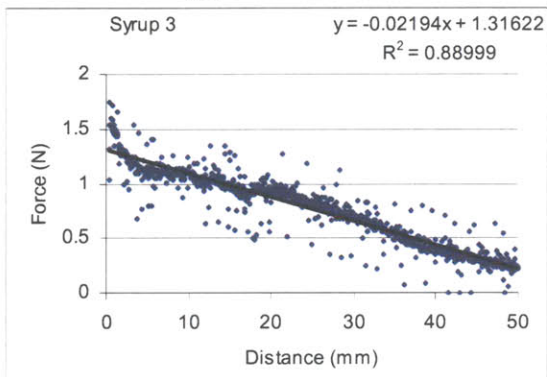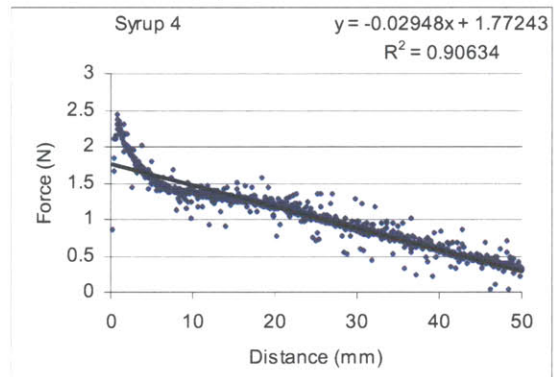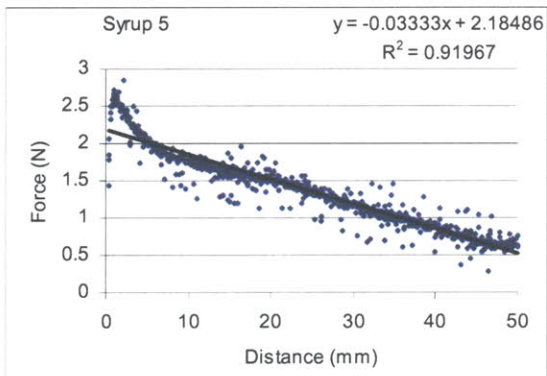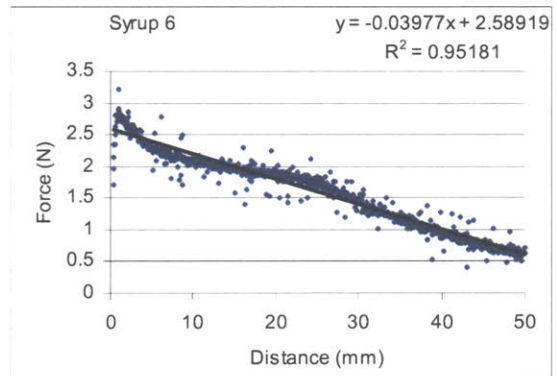
(f) v = 5 mm/s

Figure A.1- Plots of the first six syrup tests with a reused sample at v= 5 mm/s
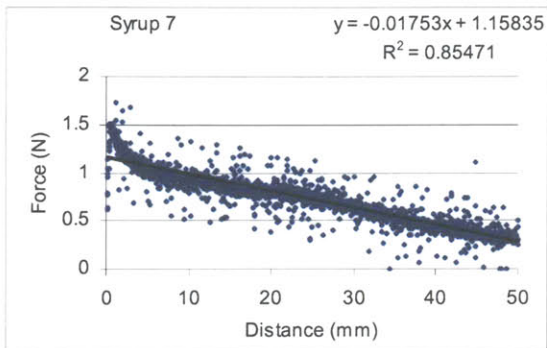
(g) v= 2 mm/s
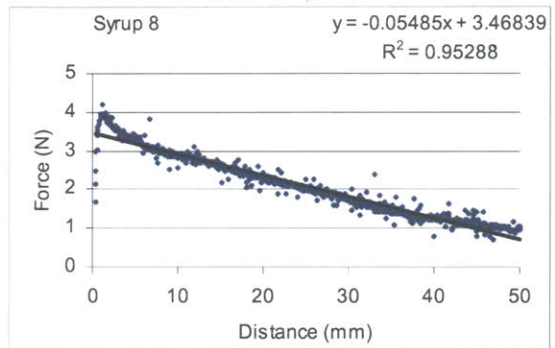
(h) v = 5 mm/s
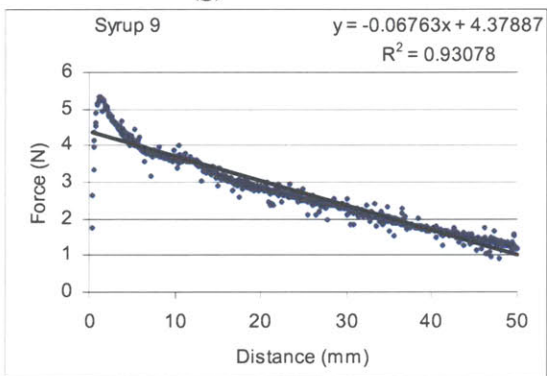
(i) v = 5 mm/s
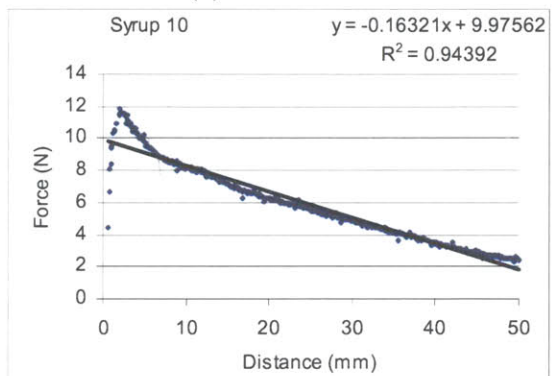
(j) v = 5 mm/s
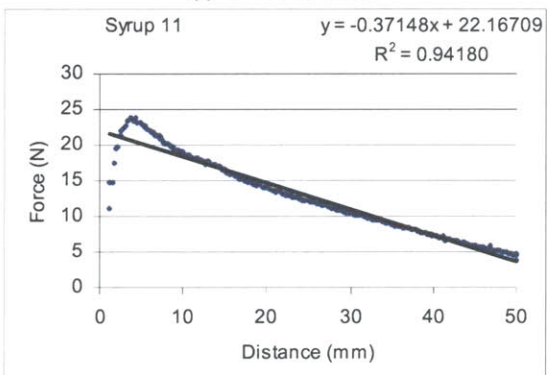
(k) v = 10 mm/s
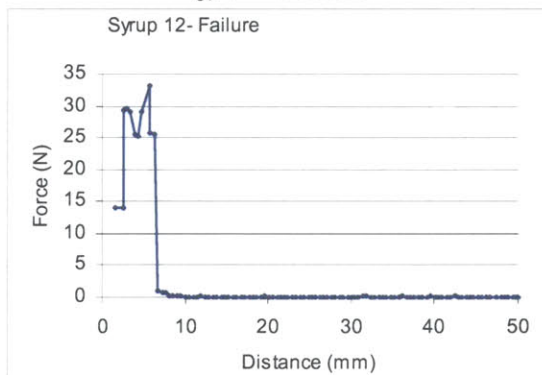
(l) v = 20 mm/s

Figure A.2- Plots of the second six syrup tests with a reused sample at v= 2, 5, 10, and 20 mm/s

A.2 Fresh Syrup Tests

Table A.2- Summary of viscosities, noise (RMS of residuals), average forces, and signal to noise ratios (average force over RMS) of fresh syrup tests in the flexible electrode geometry

Test	Velocity (mm/s)	Viscosity (Pa-s)	Average Viscosity	RMS of Residuals	Average RMS	Average Force (N)	F/RMS Ratio	Average F/RMS
1	2	30.07		0.0688		0.124	1.81	
2	2	46.71	35.41	0.0743	0.0706	0.184	2.47	2.03
3	2	29.46		0.0686		0.124	1.81	
4	5	23.87		0.0725		0.255	3.52	
5	5	25.37	25.96	0.0786	0.0763	0.253	3.22	3:47
6	5	28.64		0.0777		0.285	3.66	
7	10	21.17		0.0864		0.462	5.35	
8	10	20.97	20.37	0.0672	0.0763	0.451	6.71	5.81
9	10	18.98		0.0753		0.406	5.39	
10	20	20.03		0.1025		0.808	7.88	
11	20	20.35	20.47	0.0949	0.0947	0.895	9.43	9.21
12	20	21.03		0.0866		0.894	10.33	
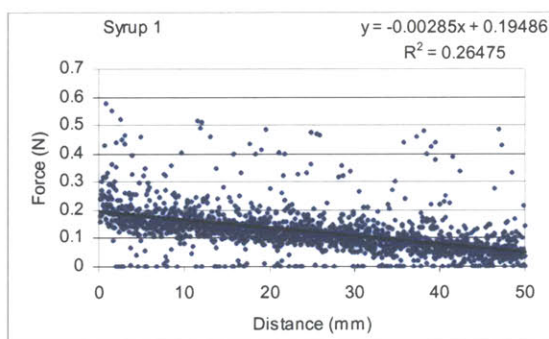
(a) v = 2 mm/s
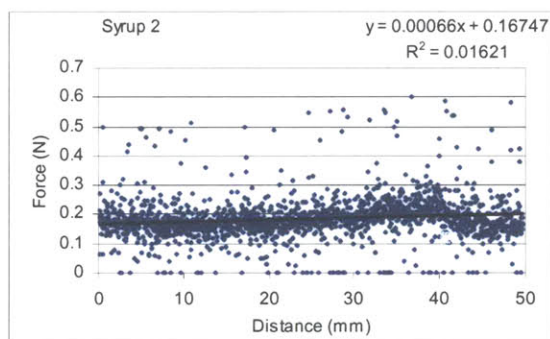
(b) v = 2 mm/s
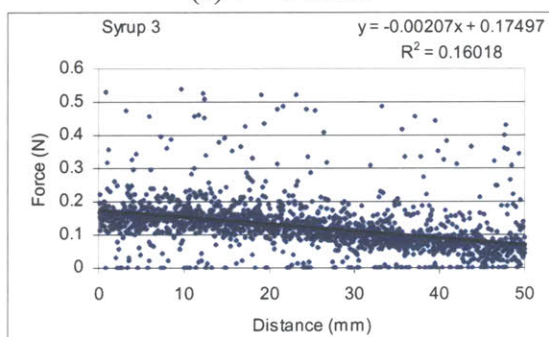
(c) v = 2 mm/s
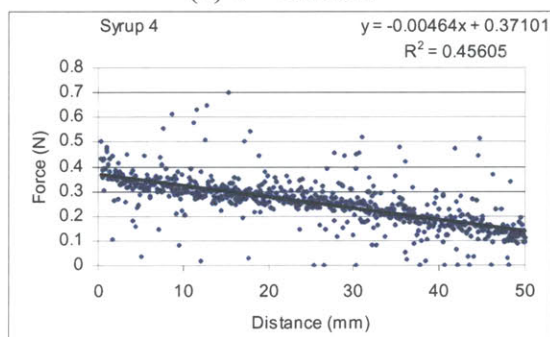
(d) v = 5 mm/s

Figure A.3- Plots of the first four fresh syrup tests with v= 2 and 5 mm/s

162
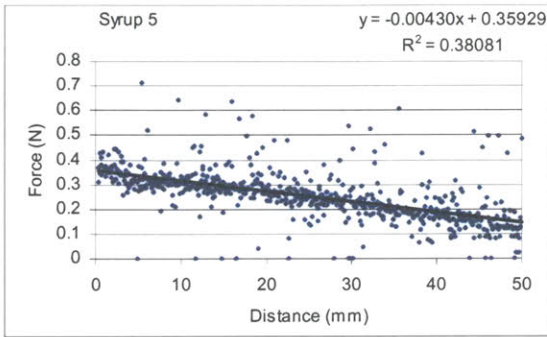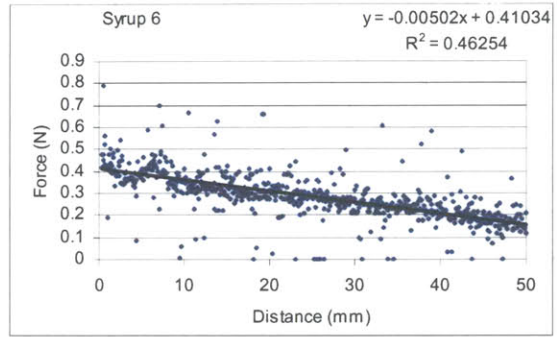
(e) v = 5 mm/s

(f) v = 5 mm/s
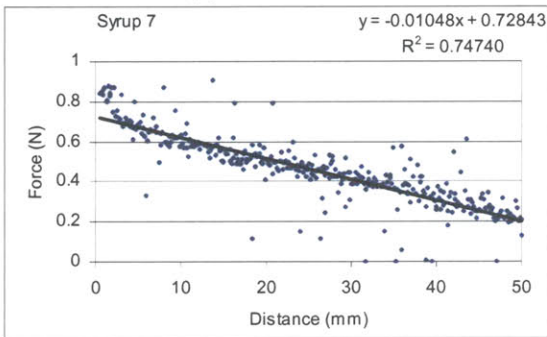
(g) v = 10 mm/s
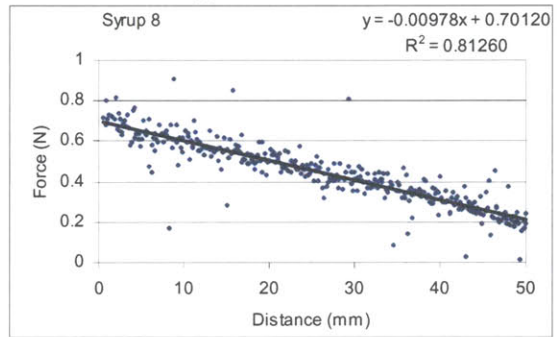
(h) v = 10 mm/s
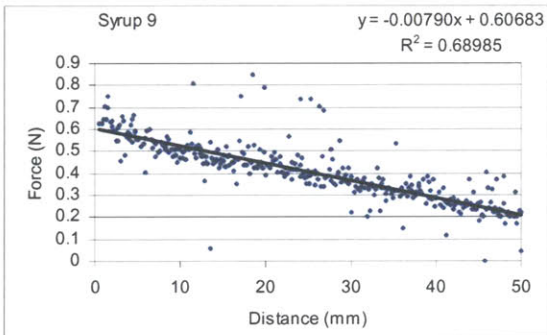
(i) v = 10 mm/s
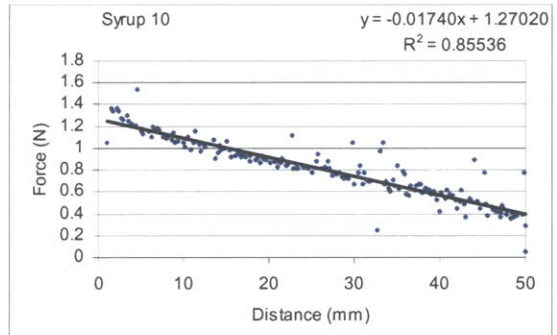
(j) v = 20 mm/s
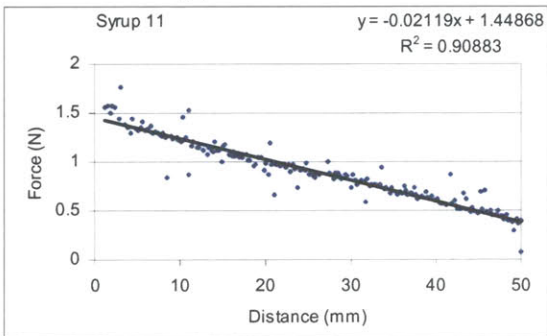
(k) v = 20 mm/s
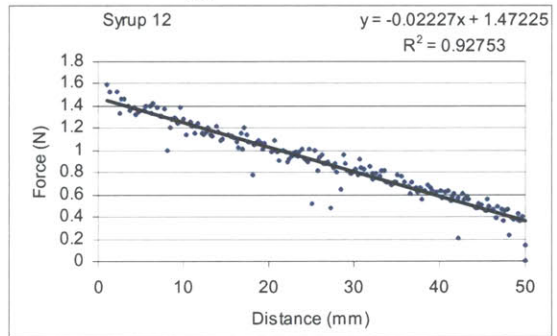
(l) v = 20 mm/s

Figure A.4- Plots of the remaining eight fresh syrup tests with v= 5, 10 and 20 mm/s

Appendix B

STF Between Flexible Electrodes

(1) m= 1.0667 g, v= 5 mm/s

(2) Reuse sample, v= 5 mm/s

(3) m= 0.9405 g, v= 5 mm/s

(4) Reuse sample, v= 5 mm/s

(5) m= 0.9469 g, v= 5 mm/s

(6) Reuse sample, v= 5 mm/s
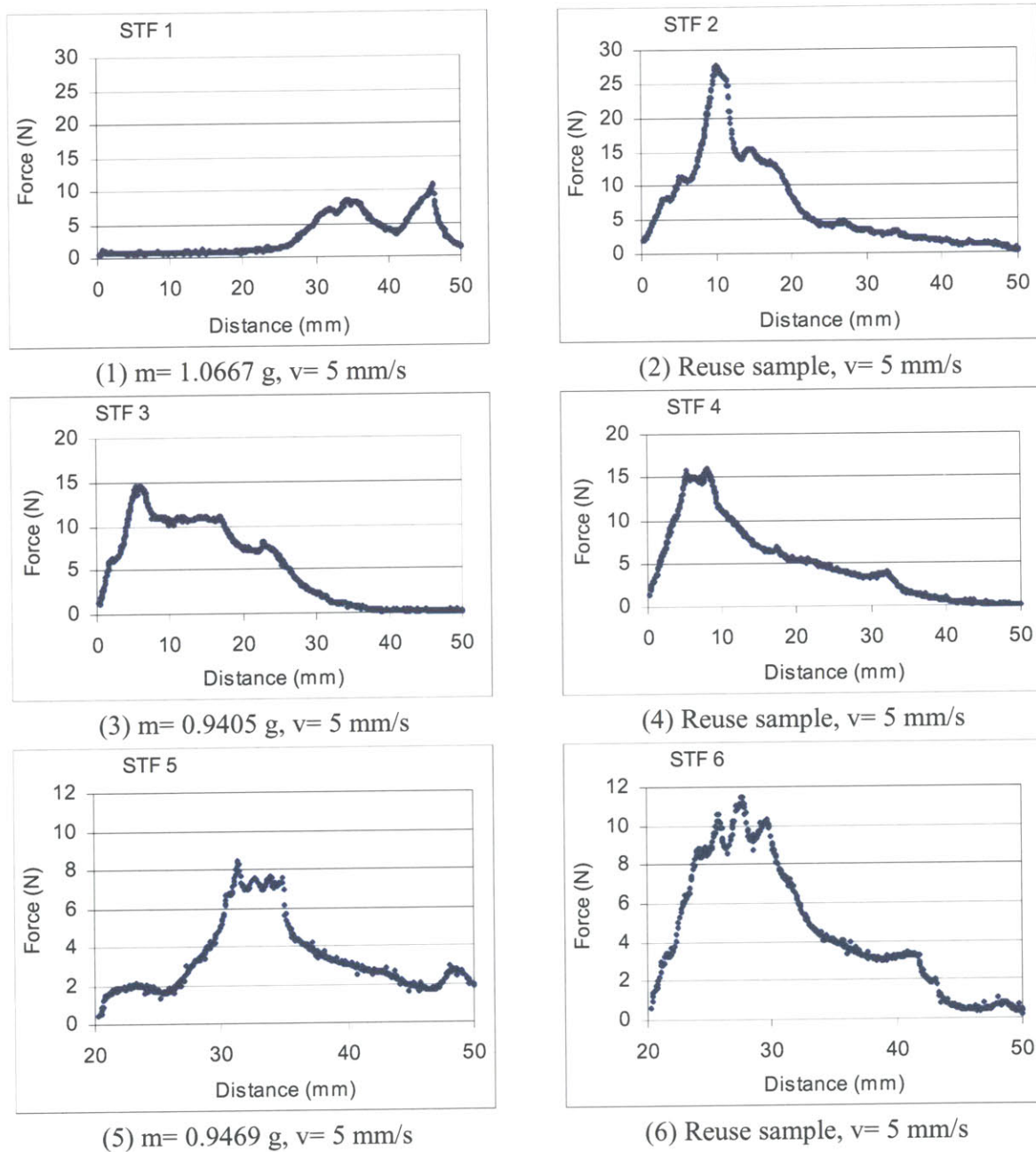
Figure B.1- Plots of the flexible electrode STF tests 1-6 (even tests reused fluid sample)
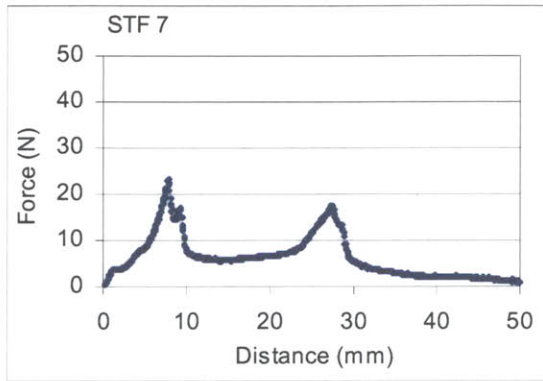
(7) m= 2.9688 g, v= 5 mm/s
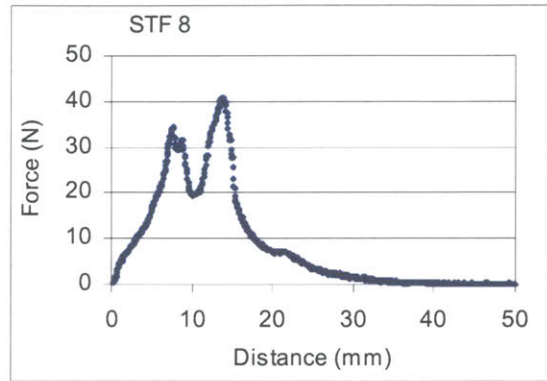
(8) Reuse sample, v= 5 mm/s
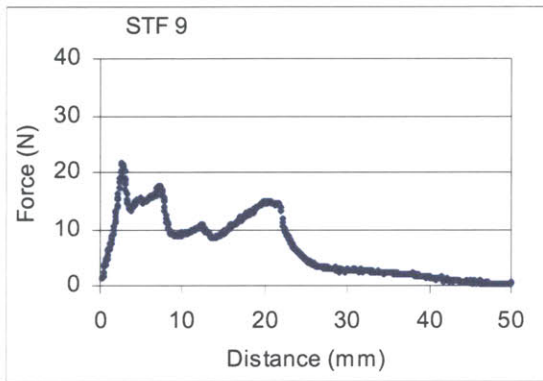
(9) m= 1.9966 g, v= 5 mm/s
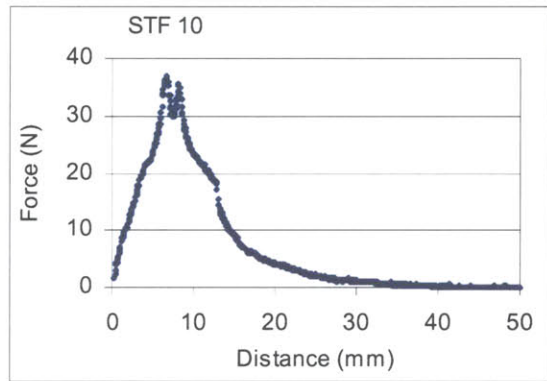
(10) Reuse sample, v= 5 mm/s
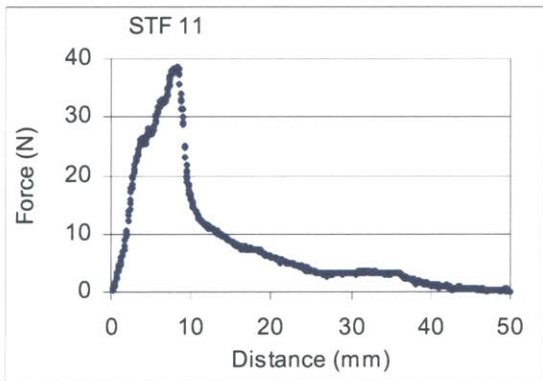
(11) m= 3.2197 g, v= 5 mm/s
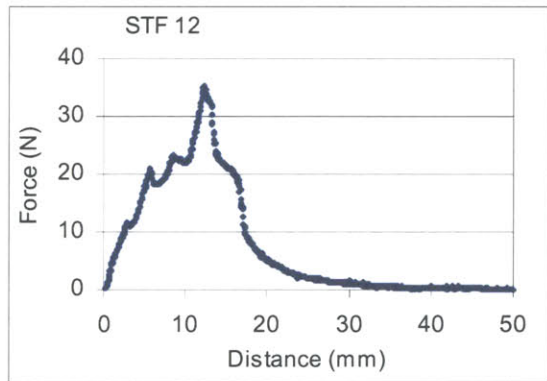
(12) Reuse sample, v= 5mm/s

Figure B.2- Plots of flexible electrode STF tests 7-12 (even tests reused fluid sample)
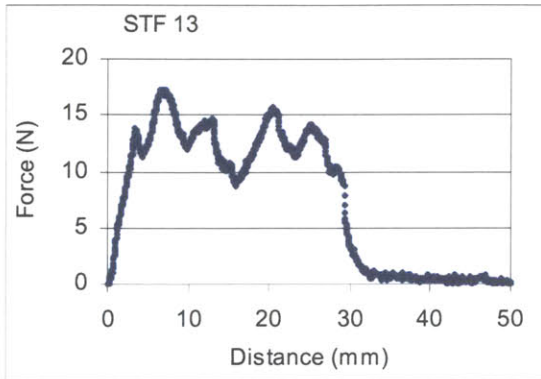
(13) m= 2.3668 g, v= 2 mm/s
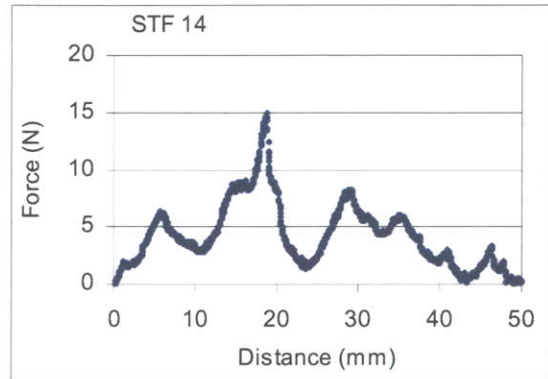
(14) Reuse sample, v= 2 mm/s
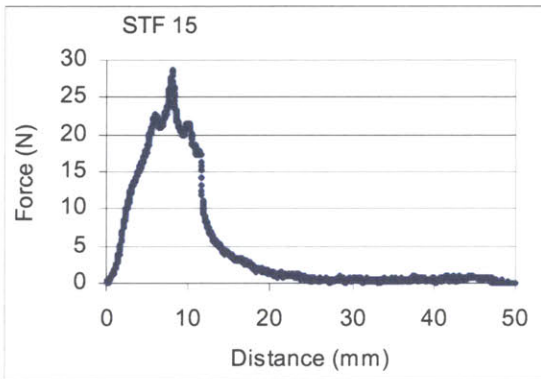
(15) m= 1.8965 g, v= 2 mm/s
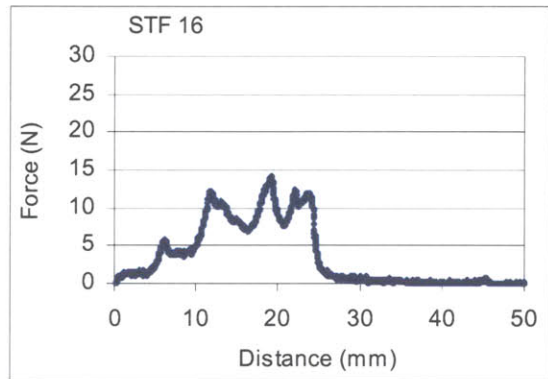
(16) Reuse sample, v= 2 mm/s
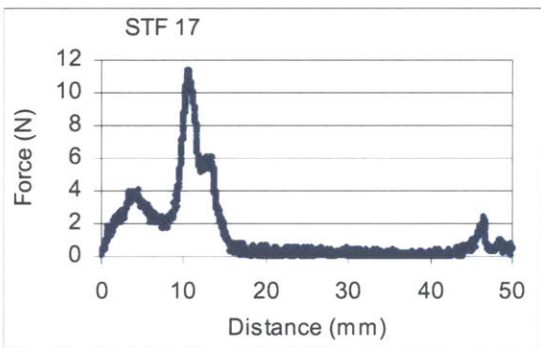
(17) m= 2.1140 g, 1 mm/s
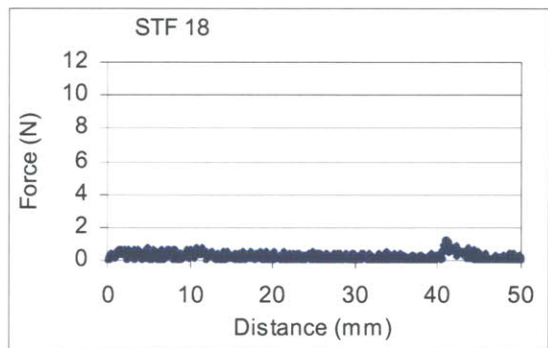
(18) Reuse sample, 1 mm/s

Figure B.3- Plots of flexible electrode STF tests 13-18 (even tests reused fluid sample)

Appendix C

Foam Compression Results

C.1 GT6K Program Performance Characterization

C.1.1 Effect of Increasing Command Sampling Rate (4 s^{-1} strain rate)

(a) 4 s^{-1}, 30 Hz

(b) 4 s^{-1}, 60 Hz

(c) 4 s^{-1}, 90 Hz

(d) 4 s^{-1}, 120 Hz

(e) 4 s^{-1}, 150 Hz

(f) 4 s^{-1}, 180 Hz
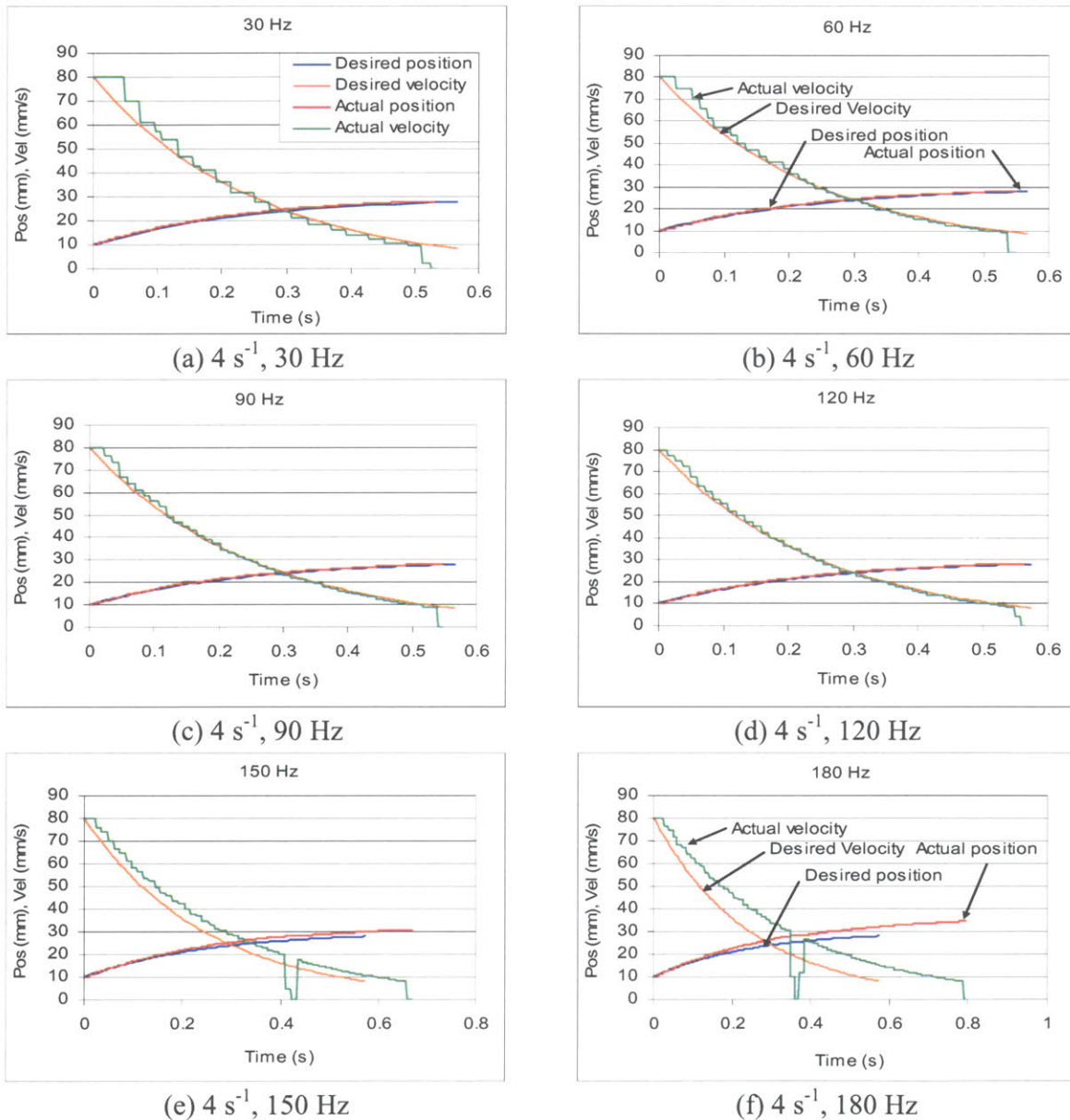
Figure C.1- Plots comparing desired and actual position and velocity at a strain rate of 4 s^{-1} and command sampling rates of 30, 60, 90, 120, 150, and 180 Hz

C.1.2 Effect of Increasing Strain Rate (120 Hz command sampling rate)

(a) 120 Hz, 2 s^{-1}

(b) 120 Hz, 4 s^{-1}

(c) 120 Hz, 6 s^{-1}

(d) 120 Hz, 8 s^{-1}

(e) 120 Hz, 10 s^{-1}

(f) 120 Hz, 12 s^{-1}
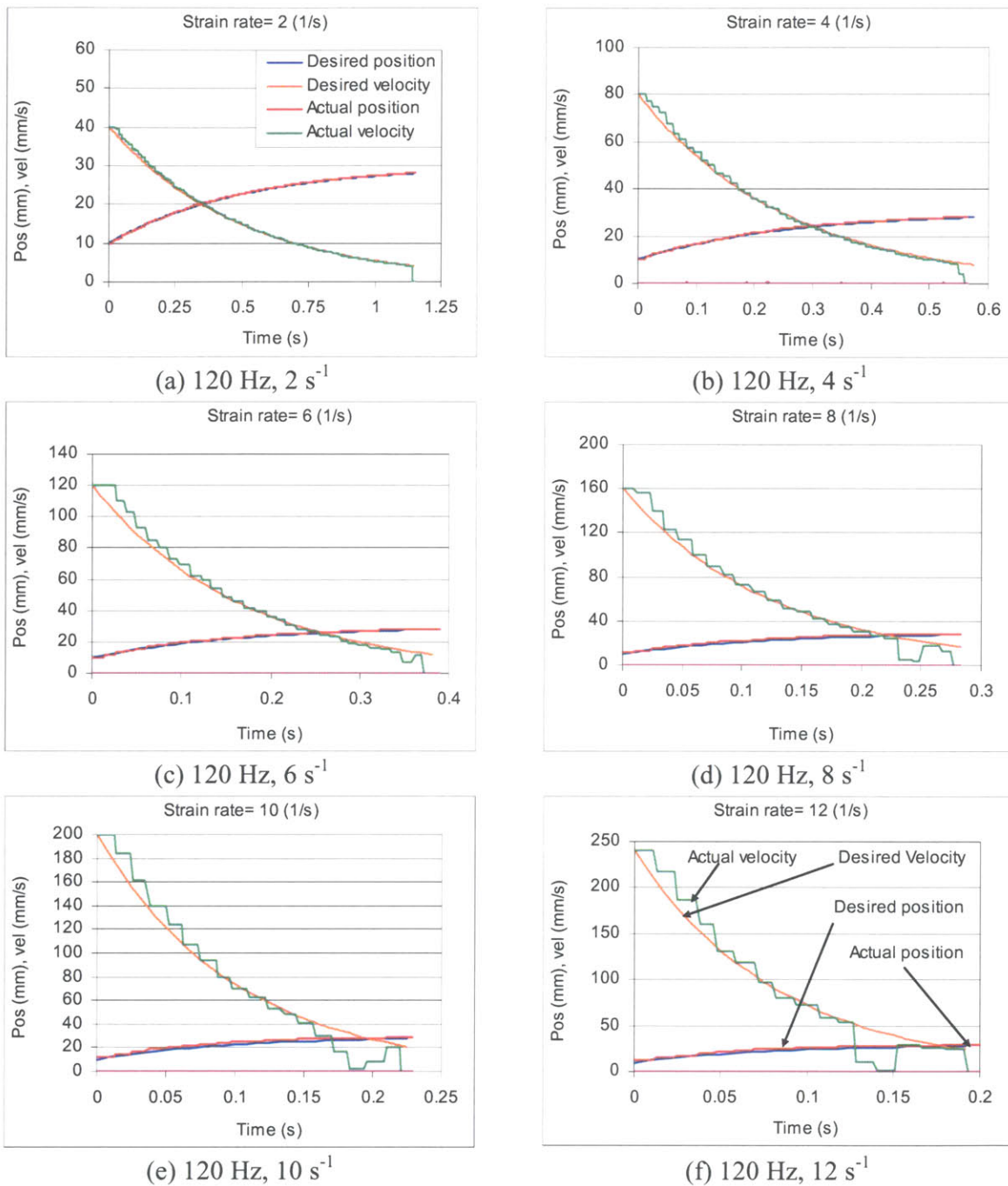
Figure C.2- Plots comparing desired and actual position and velocity at a command sampling rate of 120 Hz and strain rates of 2, 4, 6, 8, 10, and 12 s^{-1}

C.2 Empty, Glycerol-filled, and STF-filled Foam Tests (120 Hz)
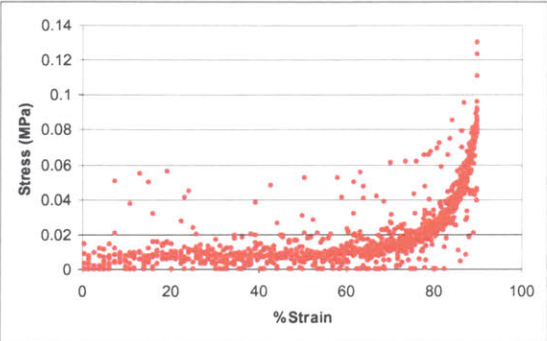
(a) Empty foam, h= 7.1 mm, 1 s^{-1}
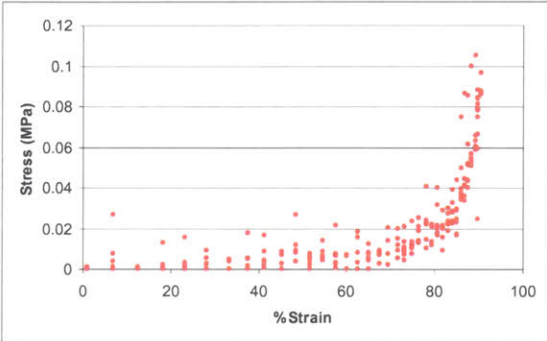
(b) Empty foam, h= 7.1 mm, 5 s^{-1}
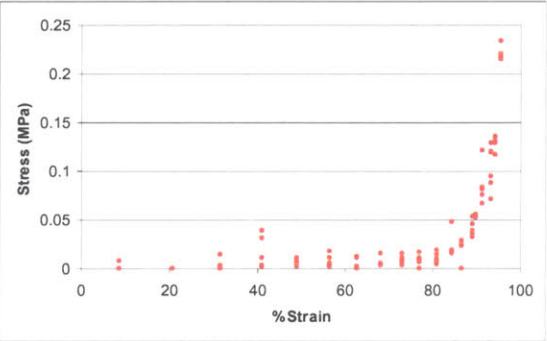
(c) Empty foam, h= 7.1 mm, 10 s^{-1}
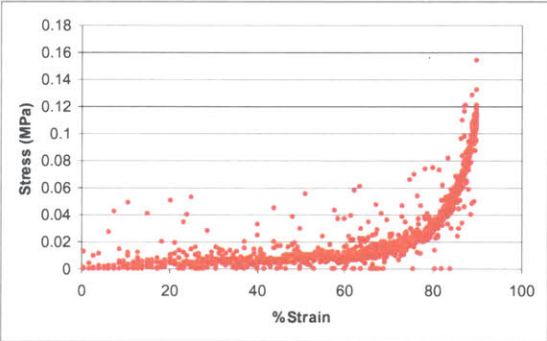
(d) Glycerol foam, h= 5.8 mm, 1 s^{-1}
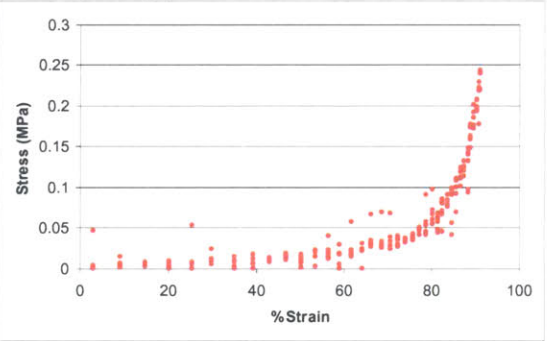
(e) Glycerol foam, h= 6.3 mm, 5 s^{-1}
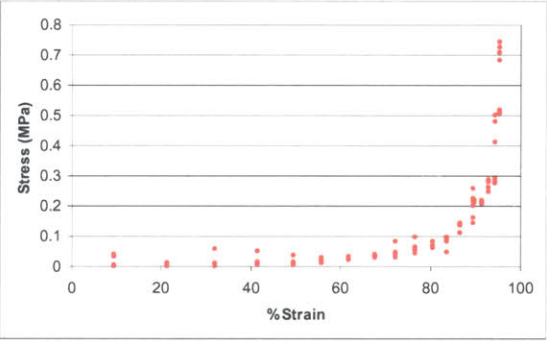
(f) Glycerol foam, h= 6.1 mm, 10 s^{-1}

Figure C.3- Stress vs. strain plots for empty and glycerol-filled foam samples at strain rates of 1, 5, and 10 s^{-1}
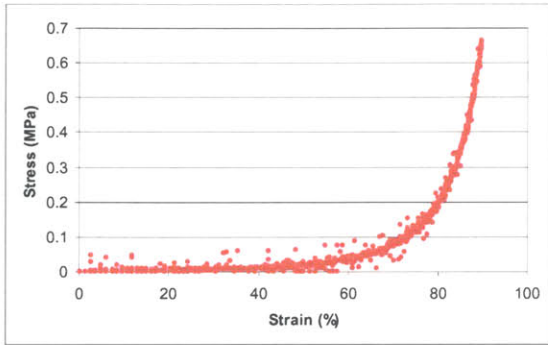
(g) STF-filled foam, h= 6.8 mm, 1 s^{-1}
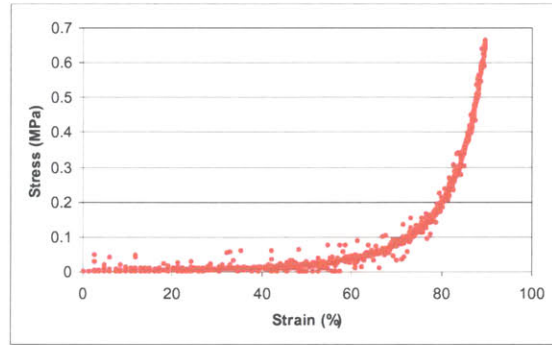
(h) STF-filled foam, h= 6.8 mm, 5 s^{-1}
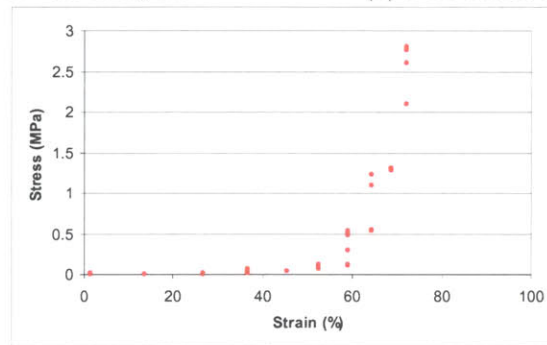
(i) STF-filled foam, h= 6.8 mm, 10 s^{-1}

Figure C.4- Stress vs. strain plots for STF-filled foam samples at strain rates of 1, 5, and 10 s^{-1}

Appendix D

ER Microchannel Devices

D.1 Summary of Work and Power

Table D.1- Summary of work and power averaged for all tests at one voltage or velocity for each device composition. Correlation coefficients for the quantity in question and the independent variable also given.

Velocity (mm/s)	Work (J)	R	Power (W)	R
2	128.54		6.43	
4	121.66		12.17	
8	117.79	-0.853	23.56	0.960
12	75.55		22.66	
16	91.10		36.44	
2	70.97		3.55	
4	87.87		8.79	
8	84.13	-0.205	16.83	0.954
12	55.80		16.74	
16	80.68		32.27	
2	91.07		4.55	
4	88.08		8.81	
8	87.84	-0.932	17.57	0.985
12	68.16		20.45	
16	66.15		26.46	

Voltage (V)	Work (J)	R	Power (W)	R
0	87.83		17.06	
30	91.58	0.968	17.24	0.954
60	116.94		21.73	
90	131.35		24.98	
0	47.73		10.74	
25	61.28		13.45	
50	71.64	0.980	12.96	0.913
75	85.59		16.91	
100	113.21		24.12	
0	57.97		12.07	
30	59.55	0.920	11.63	0.928
60	80.44		16.57	
90	123.08		21.99	

(a) Summary of work and power averages for all the tests performed at a single velocity for each type of device composition. Plotted in Figure 6.31b and d.

(b) Summary of work and power averages for all the tests performed at a single voltage for each type of device composition Plotted in Figure 6.31a and c.

D.2 Device Composition A (Standard Riser Width, Al-2%Si)

Table D.2- Summary of data taken on 5-24-06 with a standard riser width, metallized silicon device

| #	Test ID	Voltage (V)	Velocity (mm/s)	Start (mm)	End (mm)	Slope (N/mm)	Intercept (N)	R squared	Work (J)	Power (W)
17	A.16_57	0	2	5	40	-0.0540	3.43	0.87	94.20	4.71022
7	A.16_15	0	4	5	40	-0.0831	4.15	0.92	101.09	10.1094
1	A.15_47	0	8	10	40	-0.0402	2.88	0.75	107.45	21.4906
3	A.15_57	0	12	5	40	-0.0603	2.49	0.65	55.66	16.6976
14	A.16_44	0	16	5	40	-0.0733	3.29	0.83	80.73	32.2908
19	A.17_04	30	2	5	40	-0.0505	3.95	0.83	116.91	5.84573
4	A.16_02	30	4	5	40	-0.0654	3.73	0.89	101.22	10.122
18	A.17_02	30	8	5	40	-0.1024	4.37	0.85	100.33	20.0659
5	A.16_04	30	12	5	40	-0.0578	2.32	0.66	56.29	16.8869
10	A.16_34	30	16	5	40	-0.0739	3.24	0.71	83.16	33.2621
20	A.17_07	60	2	7	40	-0.0650	4.98	0.87	142.09	7.10432
11	A.16_36	60	4	7	40	-0.0698	4.66	0.88	128.78	12.8779
13	A.16_42	60	8	5	40	-0.0661	4.76	0.86	141.96	28.3916
9	A.16_29	60	12	7	40	-0.0504	2.60	0.72	84.85	25.4544
8	A.16_26	60	16	5	40	-0.0694	3.09	0.60	87.03	34.8127
12	A.16_38	90	2	5	40	-0.0890	5.89	0.93	160.95	8.04771
2	A.15_56	90	4	10	40	-0.0778	5.57	0.91	155.53	15.5528
6	A.16_12	90	8	5	40	-0.0503	4.11	0.83	121.40	24.28
16	A.16_53	90	12	5	40	-0.0947	4.95	0.94	105.39	31.6175
15	A.16_46	90	16	5	40	-0.0816	4.44	0.89	113.48	45.3902
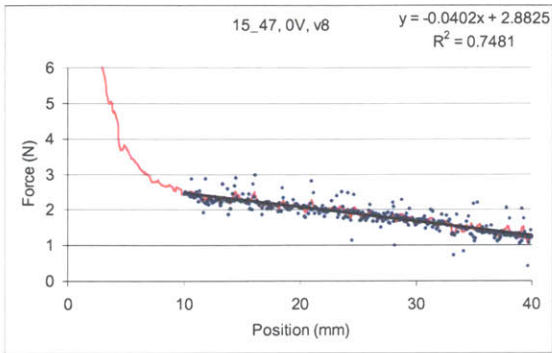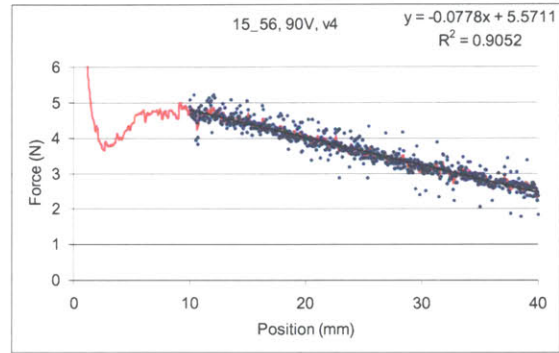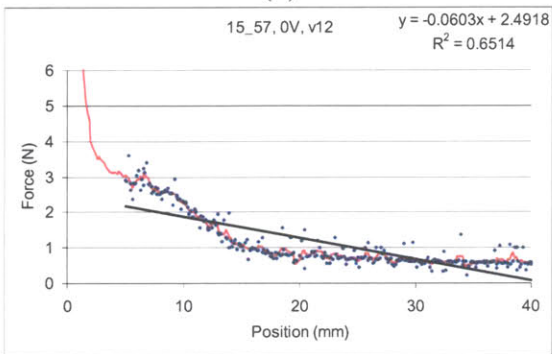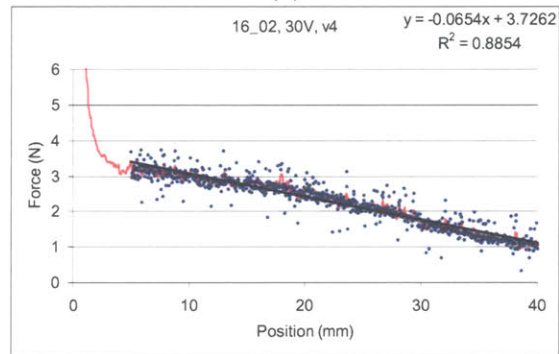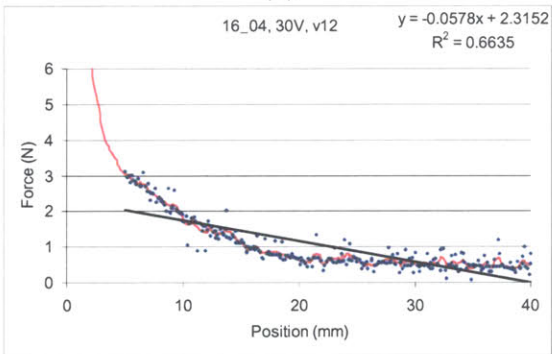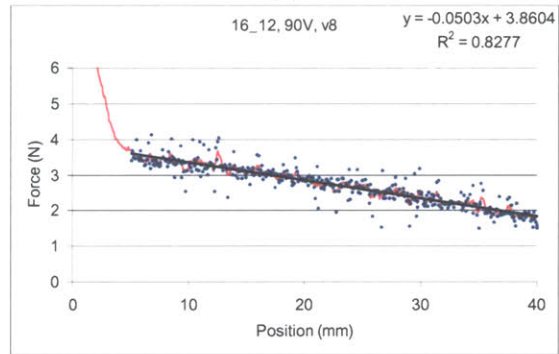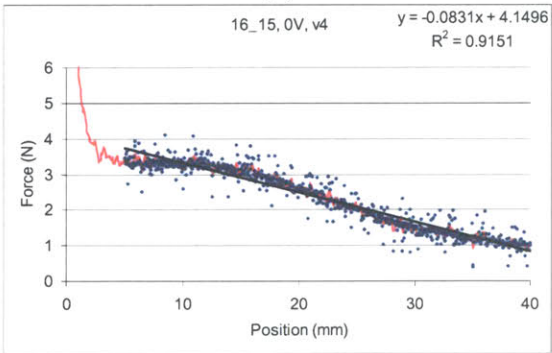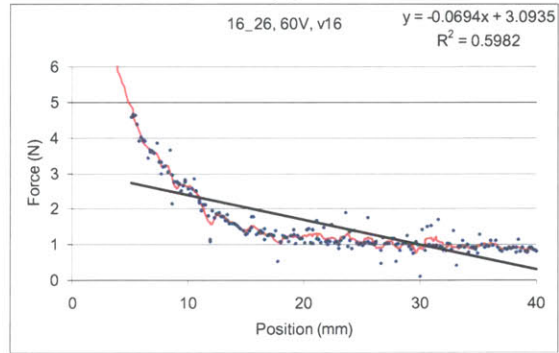
(1)   (2)   (3)   (4)   (5)   (6)   (7)   (8)
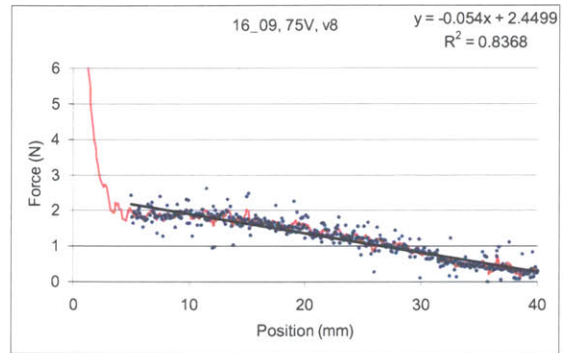
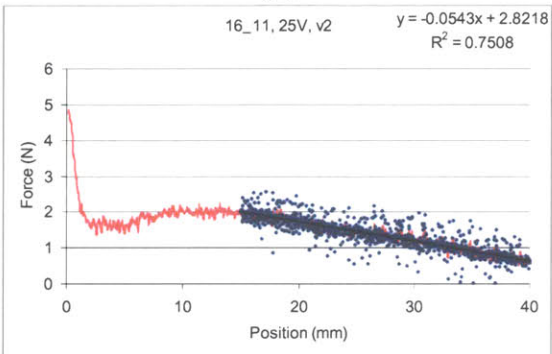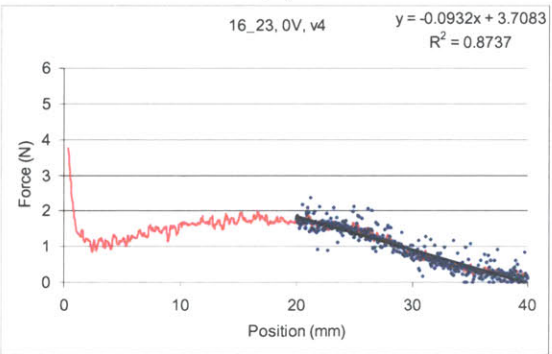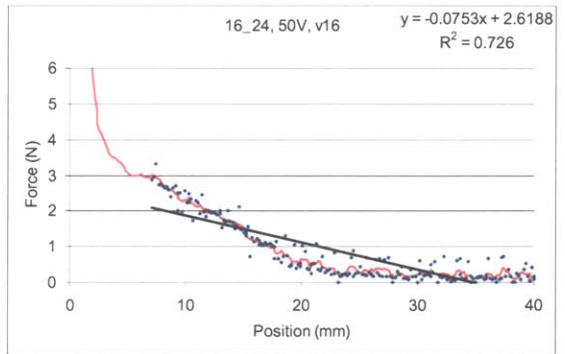Figure D.1- Force vs. position plots of randomized voltage/velocity tests 1-8 (device A)

16_29, 60V, v12   y = -0.0504x + 2.601
                   $R^2 = 0.7235$

(9)

16_34, 30V, v16   y = -0.0739x + 3.2382
                   $R^2 = 0.7052$

(10)

16_36, 60V, v4   y = -0.0698x + 4.6554
                   $R^2 = 0.8849$

(11)

16_38, 90V, v2   y = -0.089x + 5.8856
                   $R^2 = 0.9334$

(12)

16_42, 60V, v8   y = -0.0661x + 4.7575
                   $R^2 = 0.8559$

(13)

16_44, 0V, v16   y = -0.0733x + 3.2913
                   $R^2 = 0.8251$

(14)

16_46, 90V, v16   y = -0.0816x + 4.4362
                   $R^2 = 0.8922$

(15)

16_53, 90V, v12   y = -0.0947x + 4.4782
                   $R^2 = 0.9432$
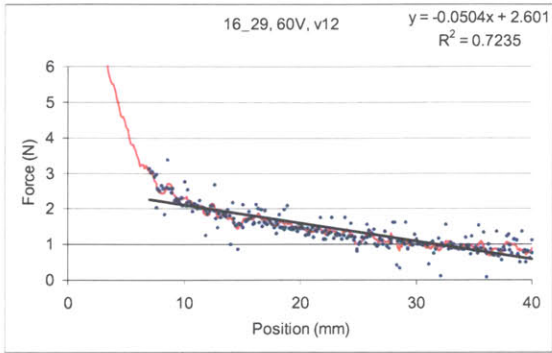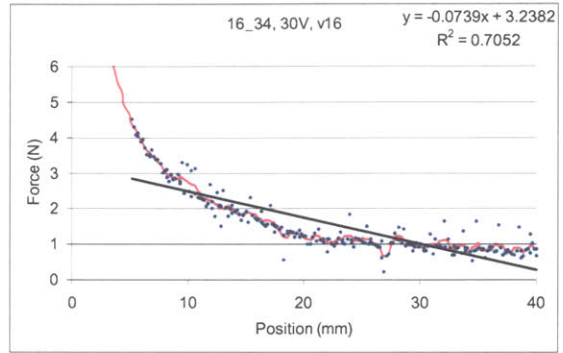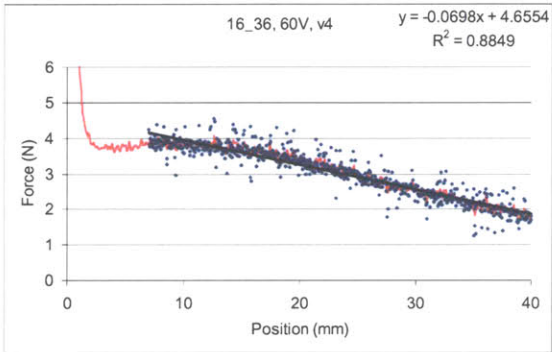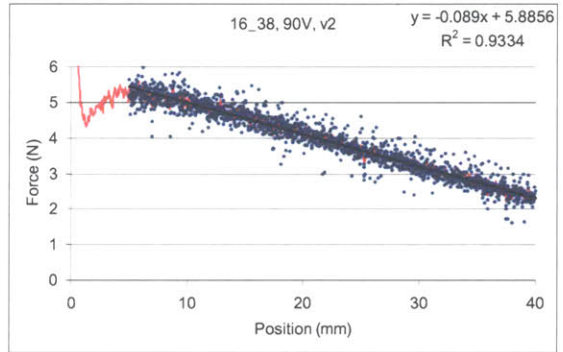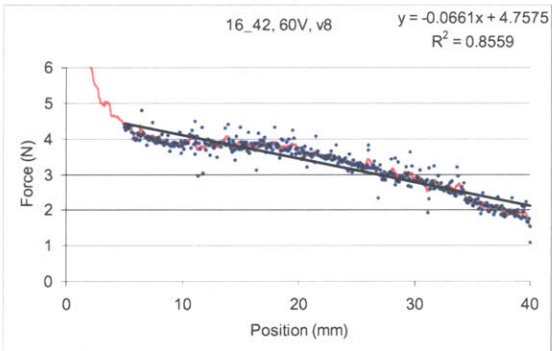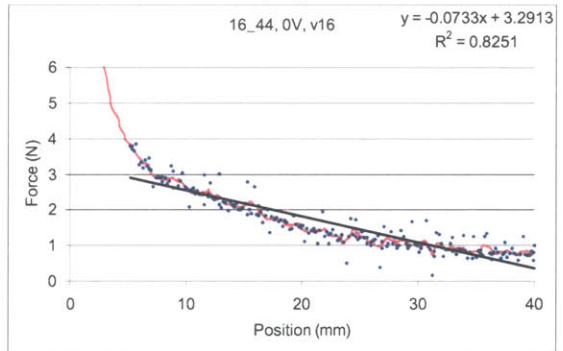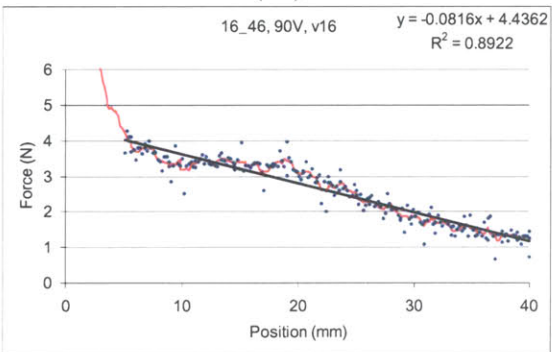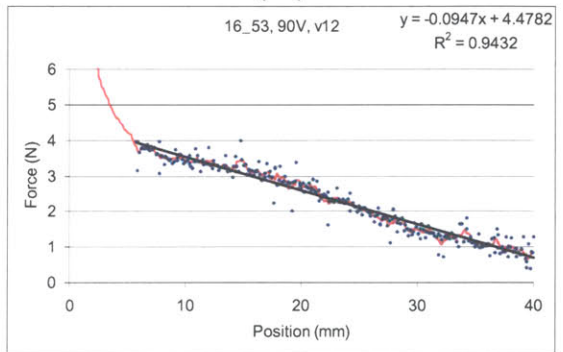
(16)

Figure D.2- Force vs. position plots of randomized voltage/velocity tests 9-16 (device A)
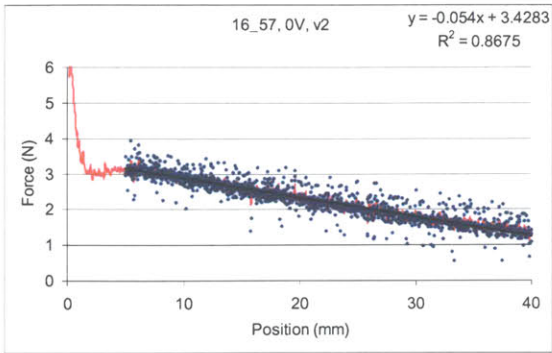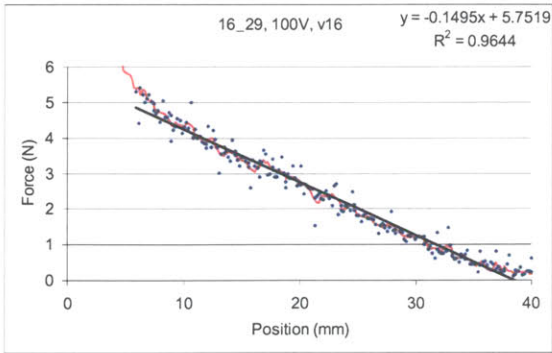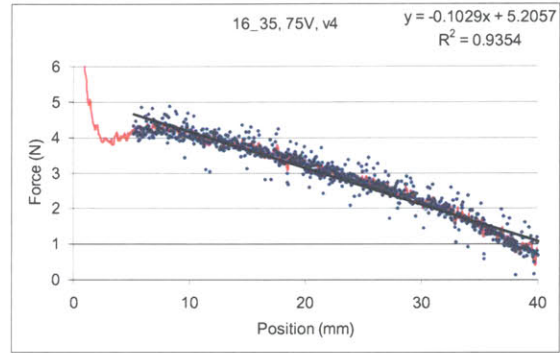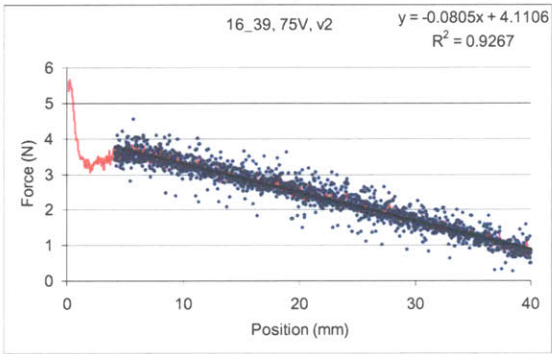
(17)
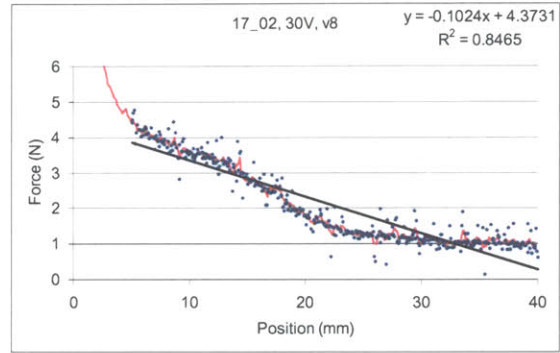
(18)
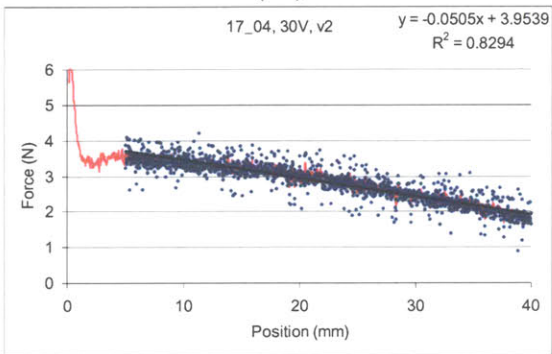
(19)
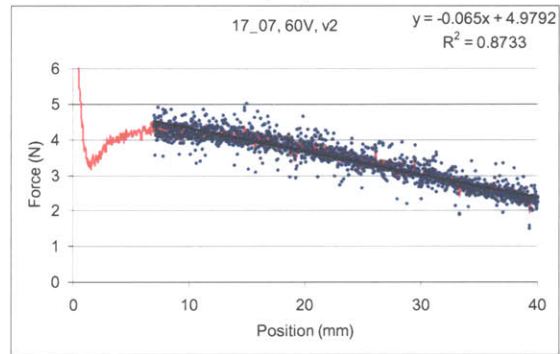
(20)
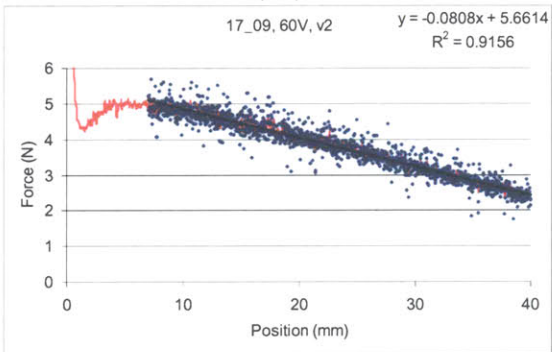
(21)

Figure D.3- Force vs. position plots of randomized voltage/velocity tests 17-21 (device A)

D.3 Device Composition B (Thin Risers, Al-2%Si)

Table D.3- Summary of data taken on 5-25-06 with a thin riser, metallized silicon device

#	Test ID	Voltage (V)	Velocity (mm/s)	Start (mm)	End (mm)	Slope (N/mm)	Intercept (N)	R squared	Work (J)	Power (W)
3	B.16_07	0	2	5	40	-0.0260	1.09	0.62	23.25	1.16
10	B.16_23	0	4	20	40	-0.0938	3.72	0.87	48.56	4.86
23	B.17_01	0	8	7	40	-0.0987	4.65	0.94	80.41	16.08
17	B.16_50	0	12	5	40	-0.0489	1.98	0.78	29.49	8.85
25	B.17_05	0	16	5	40	-0.0840	3.59	0.92	56.94	22.77
5	B.16_11	25	2	15	40	-0.0543	2.82	0.75	62.48	3.12
1	B.16_03	25	4	5	40	-0.0202	1.14	0.81	35.99	3.60
21	B.16_57	25	8	5	40	-0.0974	4.69	0.90	88.51	17.70
26	B.17_06	25	12	5	40	-0.0803	3.13	0.84	49.53	14.86
7	B.16_15	25	16	5	40	-0.0918	3.52	0.94	69.90	27.96
2	B.16_05	50	2	7	40	-0.0498	2.91	0.82	72.27	3.61
24	B.17_03	50	4	10	40	-0.0918	5.29	0.92	107.31	10.73
9	B.16_21	50	8	20	40	-0.1035	4.62	0.87	80.78	16.16
18	B.16_52	50	12	5	40	-0.0592	2.68	0.84	48.50	14.55
11	B.16_24	50	16	7	40	-0.0758	2.62	0.72	49.31	19.73
14	B.16_39	75	2	4	40	-0.0805	4.59	0.93	98.16	4.91
13	B.16_35	75	4	4	40	-0.1029	5.72	0.94	123.00	12.30
4	B.16_09	75	8	5	40	-0.0540	2.45	0.84	60.31	12.06
19	B.16_53	75	12	5	40	-0.0430	1.75	0.69	33.25	9.97
8	B.16_19	75	16	5	40	-0.1405	6.27	0.95	113.21	45.29
16	B.16_48	100	2	5	40	-0.0874	4.80	0.93	98.67	4.93
20	B.16_56	100	4	9	40	-0.1120	6.31	0.94	124.49	12.45
22	B.17_00	100	8	13	40	-0.0985	5.58	0.90	110.66	22.13
15	B.16_45	100	12	5	40	-0.1167	5.89	0.90	118.22	35.47
12	B.16_29	100	16	4	40	-0.1495	6.50	0.96	114.03	45.61
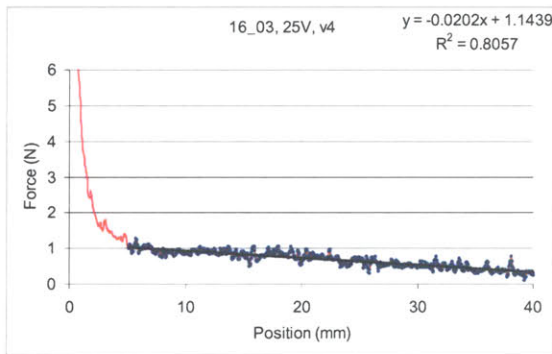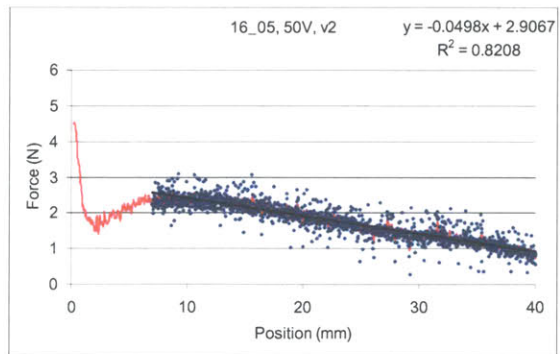
(1)   (2)

Figure D.4- Force vs. position plots of randomized voltage/velocity tests 1-2 (device B)
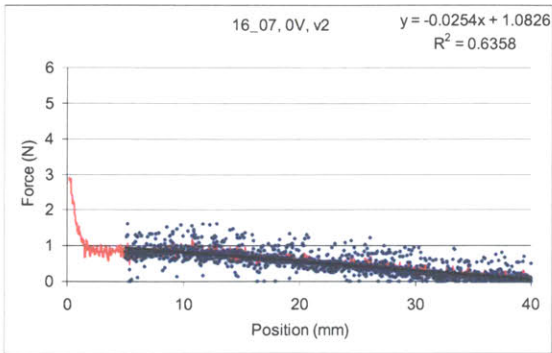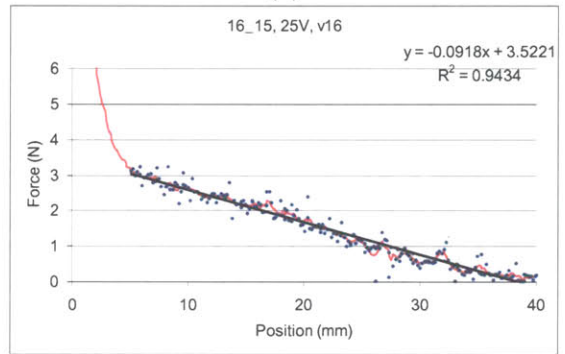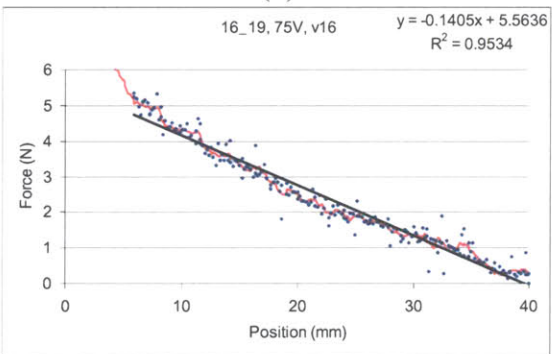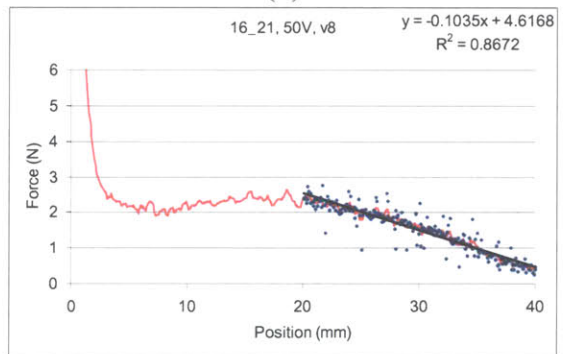
Figure D.5- Force vs. position plots of randomized voltage/velocity tests 3-10 (device B)

(11)

(12)

(13)
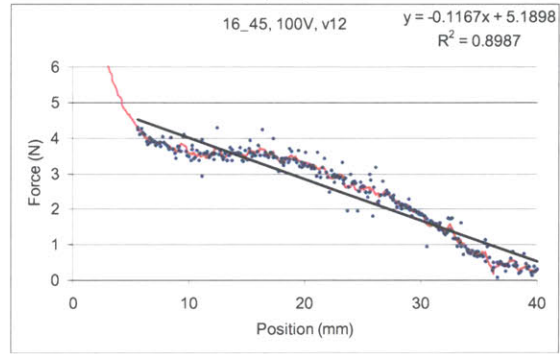
(14)
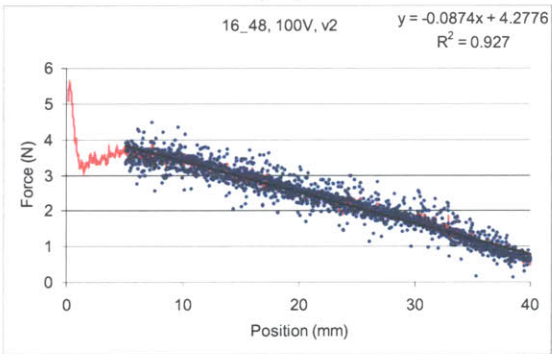
(15)
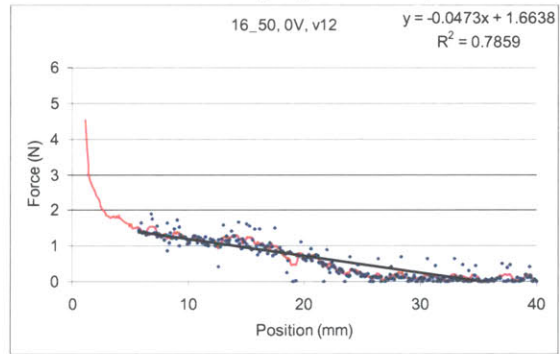
(16)

(17)

(18)

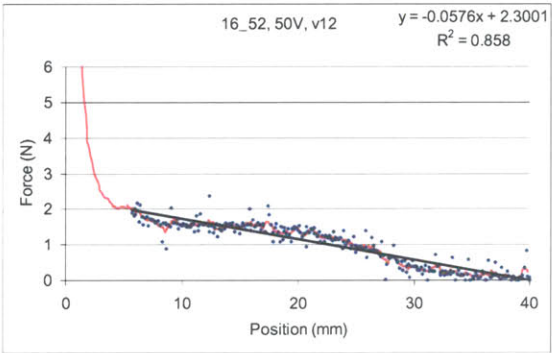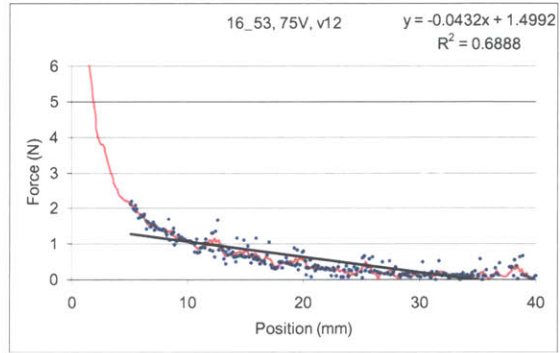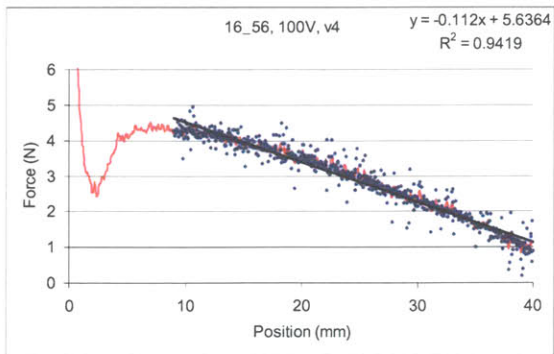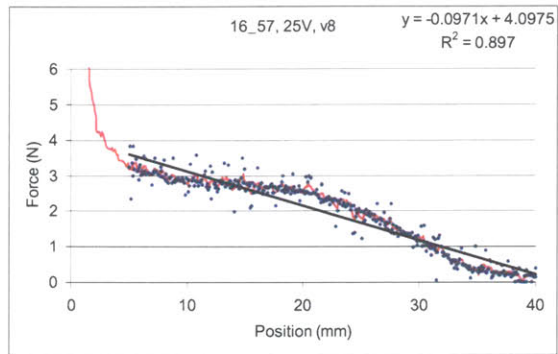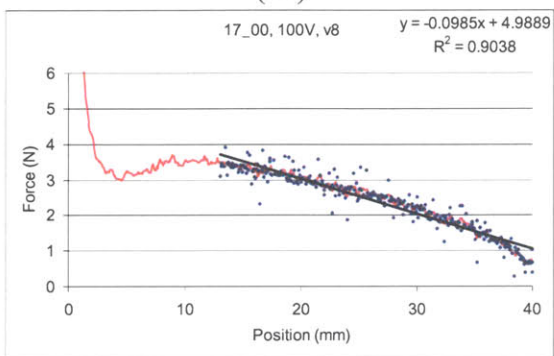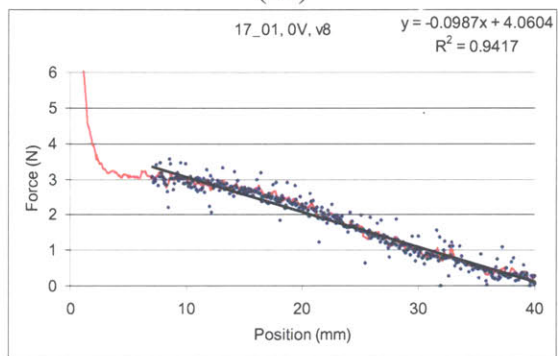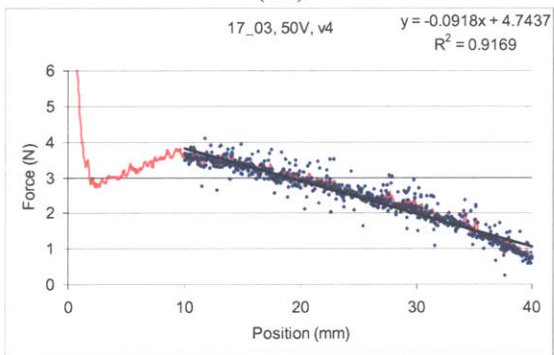Figure D.6- Force vs. position plots of randomized voltage/velocity tests 11-18 (device B)
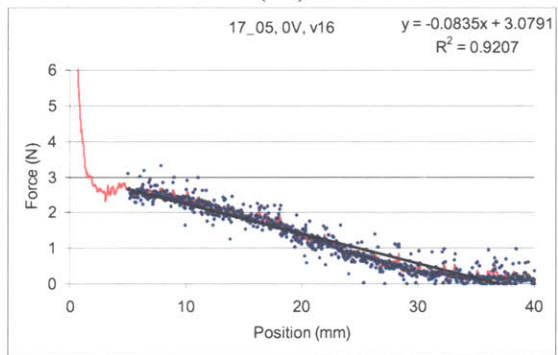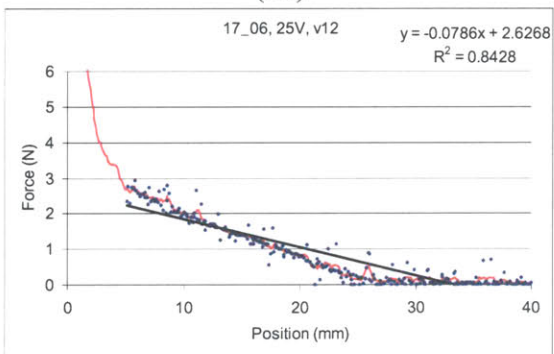
(19)

(20)

(21)

(22)

(23)

(24)

(25)

Figure D.7- Force vs. position plots of randomized voltage/velocity tests 19-25 (device B)

## D.4 Device Composition C (Standard Riser Width, No Al-2%Si)

Table D.4- Summary of data taken on 5-26-06 with a standard riser width, non-metallized silicon device

| #	Test ID	Voltage (V)	Velocity (mm/s)	Start (mm)	End (mm)	Slope (N/mm)	Intercept (N)	R squared	Work (J)	Power (W)
18	C.14_35	0	2	15	40	-0.0540	2.95	0.77	66.56	3.33
19	C.14_36	0	4	10	40	-0.0447	1.98	0.75	39.98	4.00
17	C.14_33	0	8	5	40	-0.1005	3.81	0.91	72.83	14.57
10	C.14_24	0	12	7	30	-0.0758	2.68	0.85	57.41	17.22
13	C.14_28	0	16	5	40	-0.0589	2.37	0.84	53.08	21.23
1	C.14_04	30	2	20	40	-0.0664	3.48	0.75	68.15	3.41
20	C.14_39	30	4	7	40	-0.0741	3.35	0.90	74.71	7.47
2	C.14_08	30	8	5	40	-0.0224	1.37	0.57	40.90	8.18
11	C.14_25	30	12	5	40	-0.0547	2.67	0.86	64.89	19.47
7	C.14_18	30	16	5	25	-0.0740	2.38	0.83	49.09	19.64
6	C.14_17	60	2	7	40	-0.0667	4.14	0.85	106.88	5.34
5	C.14_15	60	4	15	34	-0.0330	2.34	0.41	60.26	6.03
4	C.14_14	60	8	15	40	-0.0293	2.21	0.49	71.33	14.27
14	C.14_29	60	12	10	40	-0.0382	2.74	0.63	82.58	24.78
12	C.14_26	60	16	5	32	-0.1134	4.24	0.92	81.12	32.45
9	C.14_23	90	2	7	40	-0.0737	4.67	0.88	122.69	6.13
15	C.14_30	90	4	7	40	-0.1063	6.80	0.93	177.39	17.74
16	C.14_32	90	8	10	40	-0.1085	6.54	0.93	166.28	33.26
3	C.14_09	90	12	13	40	-0.0390	2.47	0.71	67.74	20.32
8	C.14_20	90	16	20	40	-0.0541	3.53	0.60	81.30	32.52
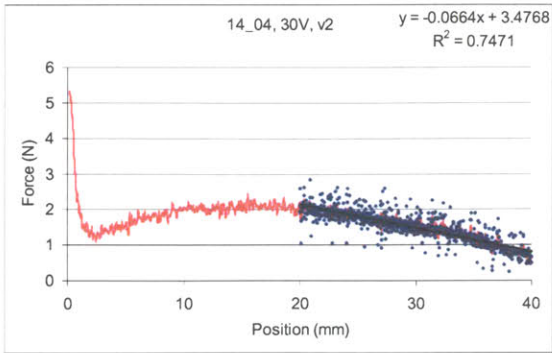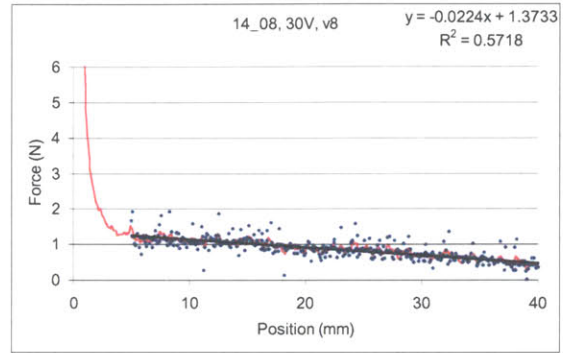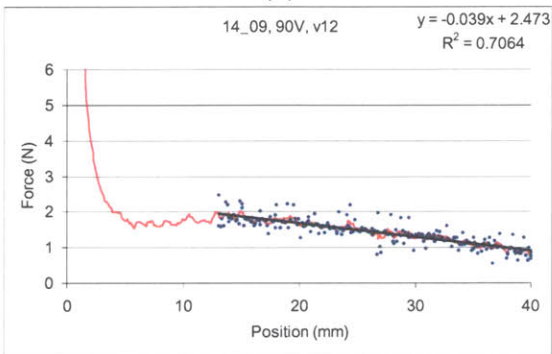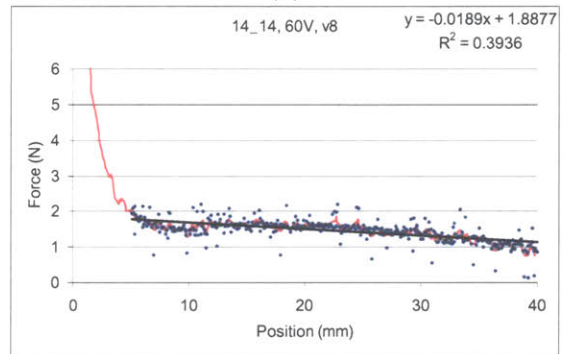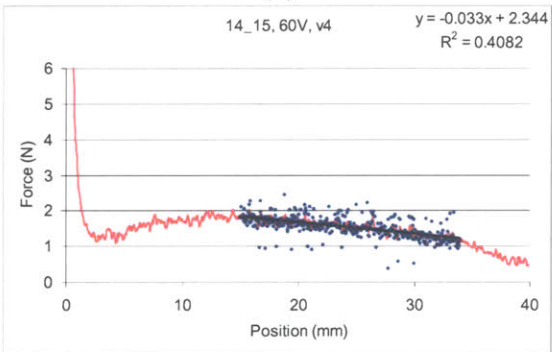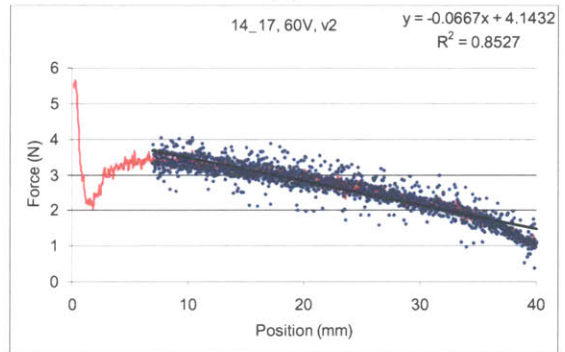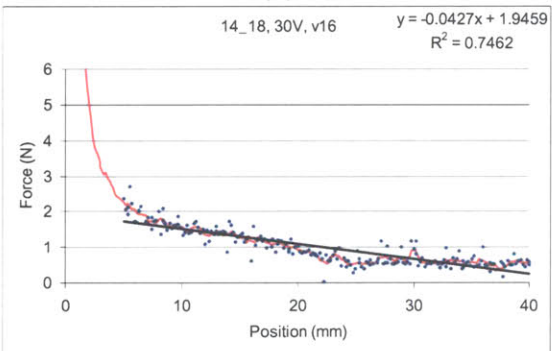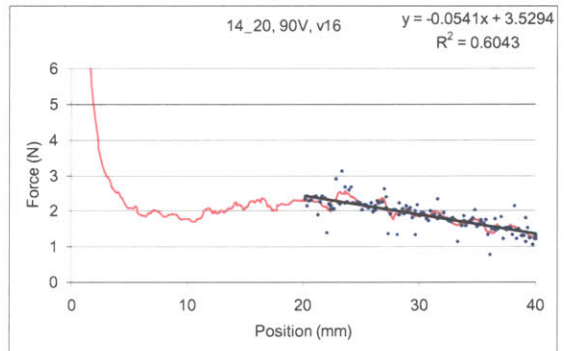
Figure D.8- Force vs. position plots of randomized voltage/velocity tests 1-8 (device C)
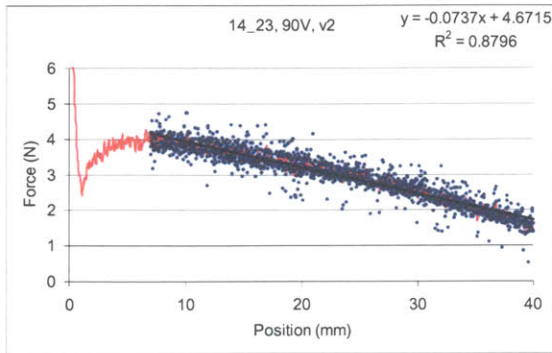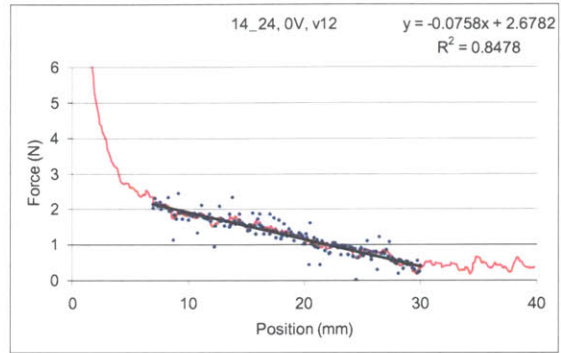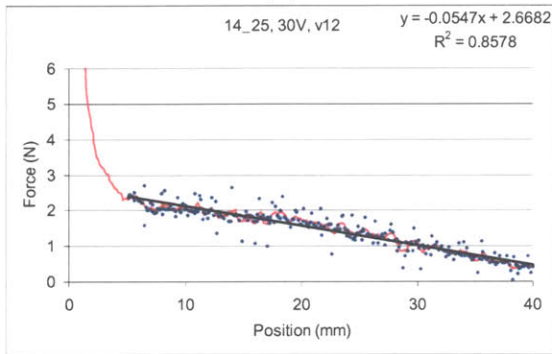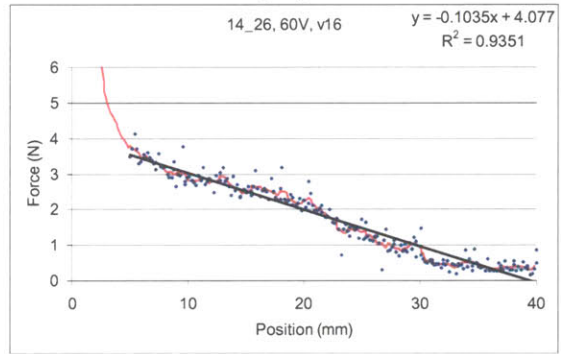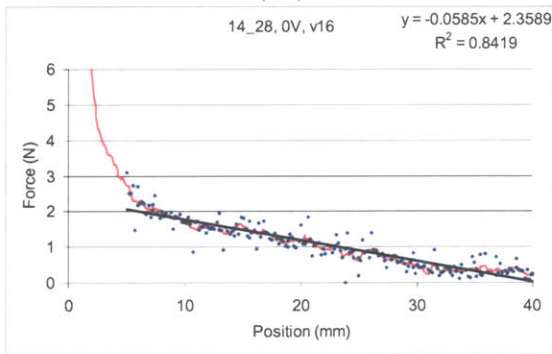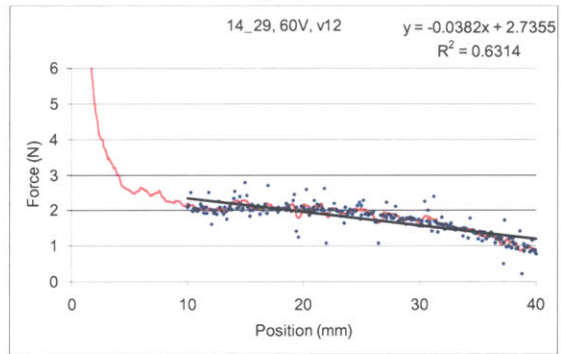
Figure D.9- Force vs. position plots of randomized voltage/velocity tests 9-16 (device C)

(17)

(18)

(19)

(20)

Figure D.10- Force vs. position plots of randomized voltage/velocity tests 17-20 (device C)

185

Bibliography

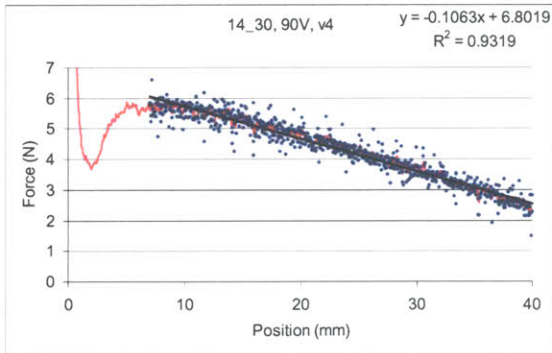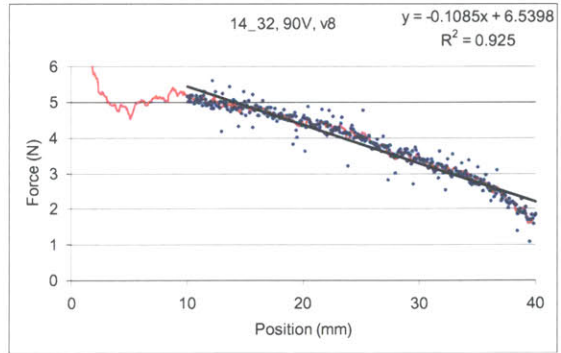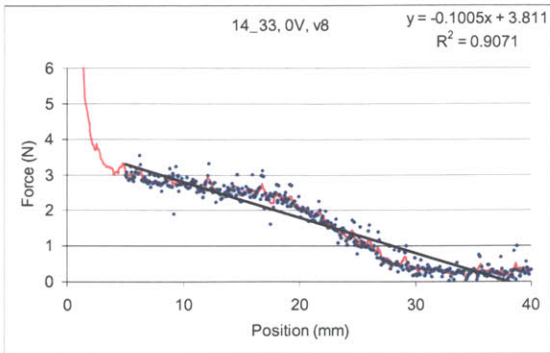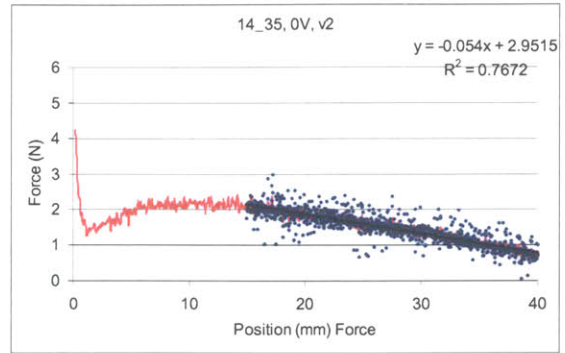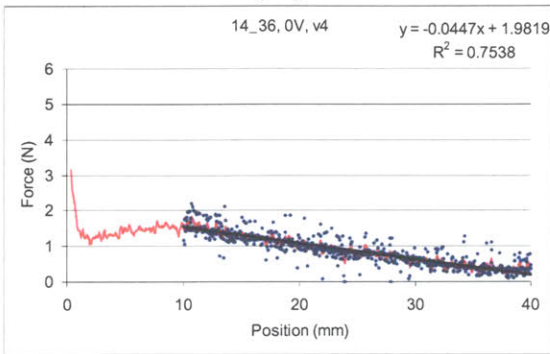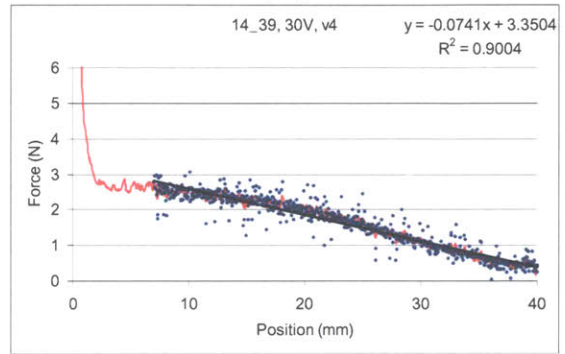Adolf, 1995- Douglas Adolf, Terry Garino, and Brad Hance, "Permittivity of Electrorheological Fluids under Steady and Oscillatory Shear", *Langmuir*, **11**(1): 313-317 (1995)

Bender, 1996- J. W. Bender and N. J. Wagner, "Reversible shear thickening in monodisperse and bidisperse colloidal dispersions", *Journal of Rheology*, **40**: 899-916 (1996)

Bettin, 2005- Giorgia Bettin, "Energy Management Devices using Composites Impregnated with Shear-Thickening Fluids", S.M. Thesis, Dept. of Mechanical Engineering, MIT; Supervisor: Prof. G. McKinley (Dec 2004)

Bonnecaze, 1991- R. Bonnecaze and J. Brady, "Dynamic simulation of an electrorheological fluid", *J. Chem. Phys.*, **96**(3): 2183-2202 (Feb 1992)

Brady, 1985- Brady, J. F. and G. Bossis, "The rheology of concentrated suspensions of spheres in simple shear flow by numerical simulation", *J. Fluid Mech.* **155**: 105-129 (1985)

Britannica, 2006- "Electrostriction", *Encyclopædia Britannica*, 2006, Encyclopædia Britannica Premium Service, 19 April 2006 <http://www.britannica.com/eb/article-9032346>

Catherall, 2000- Alan Catherall, John Melrose, "Shear thickening and order-disorder effects in concentrated colloids at high shear rates", *Journal of Rheology*, **44**: 1-25 (2000)

Chang, 2005- Chienliu Chang, Yeong-Feng Wang, Yoshiaki Kanamori, et al., "Etching submicrometer trenches by using the Bosch process and its application to the fabrication of antireflection structures", *J. Micromech. Microeng*, **15**: 580-585 (Jan 2005)

Choi, 2001- Hyoung J. Choi, Min S. Cho, Ji W. Kim, Chul A. Kim and Myung S. Jhon, "A yield stress scaling function for electrorheological fluids", *Appl. Phys. Lett.*, **78**(24): 3806-3808 (June 2001)

Choi, 2005- S. B. Choi, T. H. Lee, Y. S. Lee and M. S. Han, "Control performance of an electrorheological valve based vehicle anti-lock brake system, considering the braking force distribution", *Smart Mater. Struct.*, **14**: 1483-1492 (2005)

D3o, 2005- www.d3o.com

Dassanayake, 2000- U. Dassanayake, S. Fraden, and A. van Blaaderen, "Structure of electrorheological fluids", *Journal of Chemical Physics*, **112**(8): 3851-3858 (Feb 2000)

Devil CAAT, 2003- U.S. Army Center for Army Lessons Learned, Task Force Devil Combined Arms Assessment Team (Devil CAAT), "The Modern Warrior's Combat Load", Coalition Task Force 82, Coalition Joint Task Force 180, April - May 2003

DVBIC, 2005- "Blast Injury", *Defense and Veterans Brain Injury Center*, March 14, 2005, <http://www.dvbic.org/blastinjury.html>

Eastman, 2004- Douglas E. Eastman IV, "Design of Semi-active Variable Impedance Materials Using Field-Responsive Fluids", S.M. Thesis, Dept. of Mechanical Engineering, MIT; Supervisor: Prof. N. Hogan (June 2004)

Egres, 2004- R. G. Egres, M. J. Decker, C. J. Halbach, Y. S. Lee, J. E. Kirkwood, K. M. Kirkwood, E. D. Wetzel, and N. J. Wagner, "Stab resistance of shear thickening fluid (STF)-Kevlar composites for body armor applications", *Proceedings of the 24th Army Science Conference,* Orlando, FL. Nov. 29 - Dec. 2, 2004

Gibson, 1988- Gibson, L.J. and Ashby, M.F., "Cellular Solids: Structure and Properties", *Pergamon Press*, Oxford (1988)

Hanaoka, 2002- R. Hanaoka, M. Murakumo, H. Anzai, and K. Sakurai, "Effects of Electrode Surface Morphology on Electrical Response of Electrorheological Fluids", *IEEE Transactions on Dielectrics and Electrical Insulation*, 9(1): 10-16 (Feb 2002)

Hayes, 1995- Hayes, Wilson C.; Robinovitch, Stephen N.; McMahon, Thomas A., "Bone fracture prevention method", *US Patent* 5,545,128 (1995).

Hoffman, 1972- Hoffman, R. L., "Discontinuous and dilatant viscosity behavior in concentrated suspensions. I. Observation of flow instability", *Journal of Rheology*, 16(1): 155-173 (March 1972)

Johnson, 1995- R.F. Johnson, J.J. Knapik, D.J. Merullo, "Symptoms during load carrying: effects of mass and load distribution during a 20-km road march", *Percept. Mot. Skills.*, 81(1): 331-8, (Aug 1995)

Kay, 1955- H. F. Kay, "Electrostriction", *Rep. Prog. Phys.* 18: 230-250 (1955)

Klingenberg, 1990- D. J. Klingenberg and C. F. Zukoski, "Studies on the Steady-Shear Behavior of Electrorheological Suspensions", *Langmuir*, 6(1): 15-24 (1990)

Knapik, 2004- Joseph J. Knapik, Katy L. Reynolds, Everett Harman, "Soldier Load Carriage: Historical, Physiological, Biomechanical, and Medical Aspects", *Military Medicine*, 169(1): 45-56 (Jan 2004)

Kohl, 2000- M. Kohl, "Fluidic actuation by electrorheological microdevices", *Mechatronics*, 10: 583-594 (2000)

Kondoh, 1997- Yutaka Kondoh and Shinichi Yokota, "Micro In-Pipe Mobile Machines by Making Use of an Electro-Rheological Fluid", *Proc. IROS 1997, IEEE*, pp. 1672-1677

Lee, 2002- Y. S. Lee, E. D. Wetzel, R. Egres and N. J. Wagner. "Advanced Body Armor Utilizing Shear Thickening Fluids", *Proceeding of 23rd Army Science Conference*, 2002

Liu, 2005- Liyu Liu, Xixiang Huang, Cai Shen, Zhengyou Liu, Jing Shi, Weijia Wen, and Ping Sheng, "Parallel-field electrorheological clutch: Enhanced high shear rate performance" *Appl. Phys. Lett.*, 87, 104106 (2005)

Makris, 1996- Nicos Makris, Scott A. Burton, Davide Hill, Mabel Jordan, "Analysis and Design of ER Damper for Seismic Protection of Structures", *Journal of Engineering Mechanics*, 122(10): 1003-1011 (Oct 1996)

Mayorga, 1997- M. A. Mayorga, "The pathology of primary blast overpressure injury", *Toxicology*, 121: 17-28 (1997).

Nakamura, 2002- Taro Nakamura, Norihiko Saga, Masaru Nakazawa, "Impedance Control of a Single Shaft-type Clutch Using Homogeneous Electrorheological Fluid", *Journal of Intelligent Material Systems and Structures*, 13: 465-9 (July/Aug 2002)

Nava, 1997- R. Nava, M. A. Ponce, L. Rejón, S. Víquez and V. M. Castaño, "Response time and viscosity of electrorheological fluids", *Smart Mater. Struct.* 6: 67-75 (Feb 1997)

NINDS, 2006- "Traumatic brain injury", *National Institute of Neurological Disorders and Stroke*, June 19, 2006, <http://www.ninds.nih.gov/disorders/tbi/tbi.htm>

Otsubo, 1998- Yasufumi Otsubo, Kazuya Edamura, "Viscoelasticity of a dielectric fluid in nonuniform electric fields generated by electrodes with flocked fabrics", *Rheol. Acta*, 37(5): 500-507 (Nov 1998)

Otsubo, 1999- Yasufumi Otsubo, Kazuya Edamura, "Electric effects on the rheology of insulating oils in electrodes with flocked fabrics", *Rheol. Acta*, 38: 137-144 (1999)

Slocum, 2005- Alexander Slocum, FUNdaMENTALS of Design, "Topic 3, FUNdaMENTAL Principles", MIT 2.007. <http://pergatory.mit.edu/2.75/2_007 Lectures/Topic 3 Fundamental Principles.pdf> (2005)

Smith, 1997- Steven W. Smith, "The Scientist and Engineer's Guide to Digital Signal Processing", *California Technical Publishing* (1997)

Takesue, 2002- Naoyuki Takesuea, Junji Furusho, and Akio Inoue, "Electro-rheological effects of liquid crystalline polymer on one-sided pattern electrodes", *Journal of Applied Physics*, **91**(3): 1618-1623 (2002)

Taylor, 1996- P.M Taylor, A. Hosseini-Sianaki, C.J. Varley, "Surface Feedback for Virtual Environmental Systems Using Electrorheological Fluids", *Int. Jour. Modern Phys*, **10**(23,24): 3011-3018 (1996)

Taylor, 1998- P.M. Taylor, D. M. Pollet, A. Hosseini-sianaki, and C.J. Varley, "Advances in an electrorheological fluid based tactile array", *Displays*, **18**:135-141 (1998)

Wissbrun, 1981- Kurt F. Wissbrun, "Rheology of Rod-like Polymers in the Liquid Crystalline State", *Journal of Rheology*, **25**(6): 619-662 (1981)

Webb, 1998- Gregory M. Webb, "Exercise apparatus and associated method including rheological fluid brake", *US Patent 5,810,696* (1998)

Wen 1997- W. Wen, H. Ma, W. Y. Tam, and P. Sheng, "Frequency and water content dependencies of electrorheological properties", *Physical Review E*, **55**(2): 1294-1298 (1997)

Werely, 2004- Norman M. Wereley, Jason Lindler, Nicholas Rosenfeld and Young-Tai Choi, "Biviscous damping behavior in electrorheological shock absorbers", *Smart Mater. Struct.*, **13**: 743-752 (2004)

Yoshida, 2002- K. Yoshida, M. Kikuchi, J.-H. Park, S. Yokota, "Fabrication of micro electro-rheological valves (ER valves) by micromachining and experiments", *Sensors and actuators*, A, **95**: 227-233 (2002)

Zhang, 2000- Guoguang Zhang, Junji Furusho, Masamichi Sakaguchi, "Vibration Suppression Control of Robot Arms Using a Homogeneous-Type Electrorheological Fluid", *IEEE/ASME Transactions on Mechatronics*, **5**(3): 302-309 (Sept 2000)